FINAL REPORT

for

the

SERDP Project

CU-1125

Influence of Groundwater Constituents on Longevity of Iron-Based Permeable Barriers

Submitted by:

Professor A. Lynn Roberts – Project PI

Professors William P. Ball, Peter Searson, and Howard Fairbrother – Project Co-PIs

Dr. Peter J. Vikesland and Dr. Jörg Klausen – Postdoctoral Researchers

Tamar Kohn, Roopa Kamath, and Hubert J. Zimmermann – Graduate Students

The Johns Hopkins University

Dr. David Burris, Project Co-PI

Air Force Research Laboratory, Tyndall AFB, FL

Submitted: May 31, 2002

TABLE OF CONTENTS

CHAPTER 1 INTRODUCTION 1-1

Motivation 1-1
Prior Longevity Studies 1-3
Potential Effects of Solutes on Iron Reactivity and on HRT 1-4
Scope of Present Investigation 1-6
Organization of Report 1-9

CHAPTER 2 EXPERIMENTAL PROCEDURES 2-1

Column Setup and Operation 2-1
Column Design and Construction 2-1
Loading of Columns: Media Properties and Loading Technique 2-3
Characterization of Initial Conditions 2-5
Conditions of Continuous Operation 2-8
Column Feed Water and Chemical Addition 2-9
Quantification of solutes 2-11
CHC Quantification 2-11
NAC quantification 2-12
Silica Analysis 2-13
Fe(II) and Fe_{tot} Quantification 2-14
Carbon Measurement 2-16
Calcium Measurement 2-17
pH Measurement 2-17
Tracer Studies 2-18
Tracer Tests With Tritiated Water 2-18
Tracer Tests With Sulfur Hexafluoride (SF_6) 2-21
Batch Studies with SF_6 2-24
Electrochemistry 2-25
Open-Circuit (Corrosion) Potential 2-27
Impedance Spectroscopy 2-29
Surface characterization 2-29
Auger Electron Spectroscopy (AES) 2-29
X-ray Diffraction 2-30
Electron Microscopy 2-31
Raman Spectroscopy 2-33

CHAPTER 3 EVALUATION OF TRANSPORT PROPERTY VARIABILITY 3-1

Tritiated Water Experiments 3-1
Data Analysis 3-1
Effluent Port Sampling of Columns A-F: HRTDs and Modeling Results 3-5
Effluent Port Sampling of Columns A-F: Estimates of Water Volume and Precipitate Mass 3-16
Port Sampling of Columns G-J 3-24
Tracer Tests with Sulfur Hexafluoride 3-45
Column Studies 3-45

Batch Studies 3-49
CHAPTER 4 CHANGES IN COLUMN REACTIVITY 4-1
Data Analysis 4-2
Calculation of Rate Coefficients 4-2
Mass Transfer Considerations 4-3
Results 4-4
Variations in Geochemical Parameters of Columns G-J 4-4
Variation in Porewater pH Values 4-5
Reduction of Chlorinated Alkanes 4-11
Reduction of TCE 4-13
Products of CHC Degradation 4-19
Reduction of Nitroaromatic Compounds 4-19
Discussion 4-22
Comparison of Results Obtained at JHU and AFRL 4-22
Effect of Influent pH on Reactivity 4-24
Effect of Continuous vs. Intermittent TCE Exposure on Granular Iron Reactivity 4-24
Effect of Co-Solutes on Granular Iron Reactivity 4-27
NAC Reduction 4-38
Comparison of the Reactivity of CHCs to NACs 4-38
Reactivity Losses at the Proximal End 4-40
CHAPTER 5 SURFACE SPECTROSCOPIC RESULTS 5-1
Auger Electron Spectroscopy 5-2
Characterization of Raw Master Builder Iron 5-2
Characterization of Contaminant-Exposed Iron Grains 5-5
X-Ray Diffraction 5-9
Sample Preparation and Analysis 5-9
Characterization of Raw Master Builder Iron 5-10
Characterization of Exposed Grains 5-13
Characterization as a Function of Column Age 5-18
Electron Microscopy 5-18
Sample Extraction and Analysis 5-20
Characterization of Raw Master Builder Iron 5-21
Characterization of Exposed Grains 5-24
Characterization as a Function of Position in the Column and Column Age 5-46
Micro-Raman Spectroscopy 5-49
Sample Extraction and Analysis 5-49
Data Analysis – Spectral Deconvolution and Raman Band Identification 5-50
Characterization of Raw Master Builder Iron 5-56
Interfacial Composition as a Function of Position in a Column 5-56
Interfacial Composition as a Function of Column Age. 5-73
CHAPTER 6 ELECTROCHEMICAL PROBE RESULTS 6-1
In-Situ Electrochemical Probes 6-1
Open-Circuit Potential Measurements 6-1
Impedance Spectroscopy 6-21

Ex-Situ Electrochemical Probe Results 6-23
Overview of Electrochemical Probe Development..... 6-25

CHAPTER 7 IMPLICATIONS OF RESULTS TO BARRIER DESIGN 7-1

Overview..... 7-1
Projections of the relative Impacts on Performance Owing to Changes in Solute Transport..... 7-2
Impacts of Co-Solutes on TCE Degradation 7-9

REFERENCES CITED..... APPENDIX-1

TABLE OF FIGURES

Figure 2.1 Schematic of experimental setup with mixing chambers in place. 2-4

Figure 2.2 Experimental setup for tracer studies with ^3H_2O 2-20

Figure 2.3: Experimental setup for tracer studies with SF_6 2-23

Figure 2.4 Schematic of electrochemical probe 2-26

Figure 2.5 Schematic of *ex situ* electrochemical probe design. 2-28

Figure 3.1 ^3H_2O breakthrough curves as a function of age for Columns A-F 3-7

Figure 3.2 Comparison of single- and dual-region model fits for ^3H_2O test on Column F (day 554) 3-12

Figure 3.3 Calculated dispersivities (α_m) for columns A-F. Dispersivity = D_m/v_m. 3-13

Figure 3.4 Comparison of normalized water filled porosity estimates determined for Columns A-F using gravimetric data ($s_{grav}(t)$) to those determined using the ^3H_2O tracer data ($s_{tracer}(t)$). △ = $s_{tracer}(t)$ and • = $s_{grav}(t)$ 3-18

Figure 3.5 Calculated mass of precipitated solute materials as a function of column age.. 3-23

Figure 3.6 ^3H_2O breakthrough curves obtained by sampling from five different ports along the length of column G. 3-30

Figure 3.7 ^3H_2O breakthrough curves obtained by sampling from five different ports along the length of column H 3-31

Figure 3.8 ^3H_2O breakthrough curves obtained by sampling from five different ports along the length of column I. 3-32

Figure 3.9 ^3H_2O breakthrough curves obtained by sampling from five different ports along the length of column J 3-33

Figure 3.10 Variation in A) Pore water velocity, B) Dispersivity, C) Dispersion coefficient, and D) Immobile water content for ports 1, 5, 7, 10, and 13 of Column G..... 3-37

Figure 3.11 Variation in A) Pore water velocity, B) Dispersivity, C) Dispersion coefficient, and D) Immobile water content for ports 1, 5, 7, 10, and 13 of Column H..... 3-39

Figure 3.12 Variation in A) Pore water velocity, B) Dispersivity, C) Dispersion coefficient, and D) Immobile water content for ports 1, 5, 7, 10, and 13 of Column I 3-41

Figure 3.13 Variation in A) Pore water velocity, B) Dispersivity, C) Dispersion coefficient, and D) Immobile water content for ports 1, 5, 7, 10, and 13 of Column J 3-43

Figure 3.14 Column C - SF_6-tracer test (pulse input) - experimental data..... 3-46

Figure 3.15 Column D - SF_6-tracer test (pulse input) - experimental data 3-47

Figure 3.16 SF_6 batch set #1 with predictions for vial 1 and 2 based on batch set #2 3-48

Figure 4.1 Fe(II) profiles for columns G-J 4-6

Figure 4.2 Inorganic carbon profiles for columns G-J. 4-7

Figure 4.3 Variation in porewater pH values for columns G-J. 4-9

Figure 4.4 Calcium retention within Column G 4-10
Figure 4.5 1,2,3-TCP profiles for column C 4-12
Figure 4.6 TCE profiles for 1) column C, 2) column E, and 3) column N 4-14
Figure 4.7 Pseudo first-order kinetic coefficients for TCE reduction in columns C-E 4-15
Figure 4.8 Pseudo first-order kinetic coefficients for TCE reduction in columns G-J 4-16
Figure 4.9 Pseudo first-order kinetic coefficients for TCE reduction in columns K-O continually exposed to a mixture of CHCs 4-17
Figure 4.10 Pseudo first-order kinetic coefficients obtained during the 'TCE probe' tests for columns A-F 4-18
Figure 4.11 Nitroaromatic compound (NAC) profiles for column F for A) 117, B) 170, C) 197, D) 264, E) 401, and F) 1050 days 4-20
Figure 4.12 Pseudo first-order rate coefficients for reduction of nitroaromatic compounds 4-21
Figure 4.13 Comparison of pseudo first-order rate coefficients obtained with columns D, J (operated at JHU) and K (operated at AFRL) 4-23
Figure 4.14 Example illustrating the initial variability of k_{obs} values obtained during a typical 'TCE-probe' experiment 4-26
Figure 4.15 Dissolved silica profiles for column B 4-31
Figure 4.16 Silica porewater concentrations within column H as a function of time 4-32
Figure 4.17 Comparison of the reactivity of column B (fed silica) to column A (not fed silica) 4-34
Figure 5.1 AES analysis of raw Master Builder iron indicates that the cast iron surface is coated by an iron oxide layer (17.0 % iron, 28.0 % oxygen). 5-3
Figure 5.2 AES maps for raw Master Builder iron.. 5-4
Figure 5.3 Depth profile of Master Builder iron particle. 5-6
Figure 5.4 Average atomic compositions of grains extracted from port 1 for columns G-J in July 2000, February 2001, and August 2001. 5-7
Figure 5.5 Attempted depth profile on a grain from column G 5-8
Figure 5.6 XRD pattern of the oxide layer of raw Master Builder iron. 5-12
Figure 5.7 XRD patterns of the oxide layer of raw Master Builder iron and of grains from the influent end of columns B-J. 5-15
Figure 5.8 XRD pattern of the oxide layer in column D. Fe = iron, G = graphite, GR = green rust, Mg = magnetite, Si = silicon, W = wustite, ? = unidentified peak. 5-16
Figure 5.9 (a) Cross section of a raw Master Builder iron grain. (b) Close-up on a pore... 5-22
Figure 5.10 Elemental map of oxygen, sulfur, silicon and iron of a pore of in raw Master Builder iron grain 5-23

Figure 5.11 (a) Cross section of a grain from the effluent end of column D. (b) Second grain from column D at higher magnification, showing wide pores partially filled with intact oxides. 5-26

Figure 5.12 TEM image of ion milled sample J12. 5-27

Figure 5.13 EDS analysis of green rust platelet. 5-28

Figure 5.14 EELS spectra of green rust showing the chemical shift due to differences of iron valence state before and after damage from the electron beam. 5-29

Figure 5.15 TEM image of fine-grained iron oxides in sample D2. 5-30

Figure 5.16 (a) Close-up on the metal/oxide interface of a grain from column D. (b) Close-up on the metal/oxide interface of picture (a). 5-32

Figure 5.17 (a) Compositional map of the region shown in figure D (a). (b) Compositional map of a second region on the same grain, showing MnS and silicon slabs 5-33

Figure 5.18 (a) Cross section of a grain from the influent end of column J. (b) Close-up on the holes in the grain of figure (a). 5-35

Figure 5.19 TEM image of the metal/oxide interface in sample J12 5-36

Figure 5.20 STEM images of sample J12. DF = dark field image. 5-37

Figure 5.21 STEM image of Si-rich fayalite near the metal/oxide interface. Labels are as in Fig. 5.20 5-38

Figure 5.22 Compositional map of the oxide layer of a grain from column B. 5-40

Figure 5.23 Compositional map of a grain from the influent end of column G. 5-41

Figure 5.24 Compositional map of a pore in a grain from column H.. 5-42

Figure 5.25 (a) Cross section of a heavily reacted grain from the influent end of column E. (b) Close-up on the lower left part of the grain shown in (a). 5-44

Figure 5.26 (a) Cross section of a grain from the influent end of column H. The dark inclusions in the oxide layer are a silicon slags. (b) Close-up on the oxide layer and the slags in figure (a). 5-47

Figure 5.27 Two grains from the effluent end of column J. 5-48

Figure 5.28 Example Raman spectra for the 180-800 cm^{-1} region 5-52

Figure 5.29 Representative Raman spectra for goethite, green rust, hematite, lepidocrocite, aragonite, and albite 5-55

Figure 5.30 Raman spectrum for as-received Master Builder iron 5-57

Figure 5.31 Raman spectroscopic results for column G. 5-59

Figure 5.32 Raman spectroscopic results for column H.. 5-63

Figure 5.33 Raman spectra for albite grains extracted from ports 1, 4, and 5 from column H. 5-67

Figure 5.34 Raman spectroscopic results for column I. 5-68

Figure 5.35 Raman spectroscopic results for column J. 5-71
Figure 5.36 Comparison of representative Raman spectra for column F. 5-74
Figure 6.1 Electrochemical results – probe G1. 6-3
Figure 6.2 Electrochemical results – probe G2 6-4
Figure 6.3 Electrochemical results – probe G3. 6-5
Figure 6.4 Electrochemical results – Probe H1 6-6
Figure 6.5 Electrochemical results – Probe H2 6-7
Figure 6.6 Electrochemical results - Probe H3 6-8
Figure 6.7 Electrochemical results – Probe I1 6-9
Figure 6.8 Electrochemical results - Probe I2 6-10
Figure 6.9 Electrochemical results - Probe I3 6-11
Figure 6.10 Electrochemical data – Probe J1 6-12
Figure 6.11 Electrochemical data - Probe J2 6-13
Figure 6.12 Electrochemical data – Probe J3 6-14
Figure 6.13 Electrochemical results - comparison of Probes G1, G2, and G3 (Grain 1 vs. reference) 6-16
Figure 6.14 Electrochemical results - comparison of Probes H1, H2, and H3 (Grain 1 vs. reference) 6-17
Figure 6.15 Electrochemical results - comparison of Probes I1, I2, and I3 (Grain 1 vs. reference) 6-18
Figure 6.16 Electrochemical results - comparison of Probes J1, J2, and J3 (Grain 1 vs. reference) 6-19
Figure 6.17 Comparison of differential voltages for Grain 3 (vs. Grain 1) and Grain 2 (vs. Grain 1) 6-20
Figure 6.18 Nyquist plot of an impedance measurement on an in situ probe 6-22
Figure 6.19 Ex-situ probe experimental results 6-26
Figure 6.20 Ex-situ probe results: Effect of silica addition on the open circuit potential. 6-27
Figure 6.21 Comparison of the open circuit potentials of a grain exposed to 50 mg/L silica and a grain exposed to no silica over the course of 10 days. 6-28
Figure 6.22 Open circuit potentials of two iron grains in solutions of high (20 mM) and low (4 mM) bicarbonate concentration. 6-29
Figure 7.1 Simulations of steady state TCE concentrations through a 10 m thick iron (Master Builder) PRB 7-6
Figure 7.2 Variation in TCE removal over time as a result of surface passivation and the formation of an apparent unreactive zone near the column inlets. 7-10

TABLE OF TABLES

Table 2.1 Approximate locations (± 1 mm) of aqueous sampling ports for columns A-F, G-J, and K-O. 2-1

Table 2.2 Locations (± 0.1 mm) of solid sampling ports for columns G-J. 2-1

Table 2.3 Characteristics of the fresh iron columns 2-1

Table 2.4 Composition of Feedwater for Columns A-F (operated for 1100 days at JHU), G-J (operated for 475 days at JHU), and K-O (operated for 407 days at AFRL) 2-1

Table 2.5 Input characteristics for the SF_6 tracer tests 2-1

Table 2.6 Vial composition for the batch SF_6 test 2-1

Table 3.1 Parameters obtained from first moment analyses and CXTFIT dual region model 3-9

Table 3.2 Parameters obtained from CXTFIT dual region model for columns G-J. 3-26

Table 3.3 Results from batch test #2 3-51

Table 3.4 Measured and calculated loss of SF_6 mass during the column tracer tests 3-51

Table 4.1 Organic carbon extracted using 5-6 pore volumes of pH 12 NaOH 4-37

Table 5.1 High intensity XRD peaks of selected species for a CuKα1 anode. 5-11

Table 5.2 High intensity Raman bands of selected species in the 200-2000 cm^{-1} region.. 5-51

Table 7.1 Input parameters for model simulations of TCE transport and reaction within an iron PRB. PRB thickness = 1000 cm, K_d = 6.3 L/g. 7-7

CHAPTER 1 – INTRODUCTION

MOTIVATION

Recent work has demonstrated the utility of iron permeable reactive barriers (PRBs) for the *in situ* treatment of chlorinated hydrocarbons (Gillham and O'Hannesin, 1994; Matheson and Tratnyek, 1994; Roberts et al., 1996; Scherer et al., 1997; Arnold and Roberts, 2000; Farrell et al., 2000). In these systems, the surface of the granular iron acts as an electron donor with the reducible contaminant acting as an electron acceptor, thereby leading to corrosion of the metal. Although the exact mechanisms involved have not been fully elucidated, field demonstrations indicate that the reactions are rapid under environmentally relevant conditions (O'Hannesin and Gillham, 1998; McMahon et al., 1999; Puls et al., 1999). At the time of this writing, granular iron PRBs for the degradation of VOCs in groundwater have been installed at over 70 sites, including 53 sites located within the United States (Envirometal Technologies Inc., 2002). Questions remain, however, concerning the longevity of effective contaminant removal at such installations.

From a design standpoint, the long-term success of iron treatment walls is critically dependent on their ability to maintain a reactive surface and appropriate hydraulic residence times (HRTs) for treatment. Deteriorations in the performance of iron-based treatment processes may occur if either the *chemical reactivity* of the solid surface diminishes or if the mean *hydraulic residence time* of the porous medium is reduced. Moreover, changes in the hydraulic residence time distributions (HRTDs) of the porous medium may affect treatment efficiency in a manner that is strongly dependent on the nature of the reaction kinetics (Fogler, 1999).

At present, the relationships between the iron surface composition, reaction mechanisms, and reactivity are imperfectly understood. Although some studies (Orth and Gillham, 1996; O'Hannesin and Gillham, 1998) have indicated little change over time in iron reactivity for chlorinated hydrocarbons, other investigations have demonstrated that specific groundwater constituents can act over the long term to either diminish or to enhance the reactivity of the iron's interfacial region towards certain species (Reardon, 1995; Farrell et al., 2000; Vikesland et al., 2000; Klausen et al., 2001).

As groundwater flows through a PRB, constituents in the liquid, gas, and solid phases are subject to processes of oxidation, reduction, dissolution, adsorption, and precipitation. For example, reducible solutes can oxidize Fe(0) or Fe(II) at the particle-water interface, leading to the formation of higher valence iron species (Fe(II) or Fe(III), respectively). A variety of iron surface complexes and precipitates involving Fe(II) and Fe(III) may then form. Depending upon the pH and redox characteristics of the system, some of the partially oxidized iron species produced may be highly reactive. Potential reactive species include: adsorbed Fe(II) (Klausen et al., 1995; Charlet et al., 1998; Haderlein and Pecher, 1998; Buerge and Hug, 1999; Liger et al., 1999; Amonette et al., 2000; Pecher et al., 2002; Vikesland and Valentine, 2002), mixed valence iron (hydr)oxides such as magnetite (Klausen et al., 1995; Odziemkowski et al., 1998; Farrell et al., 2000), or green rust compounds (Erbs et al., 1999; Bonin et al., 2000a; Williams and Scherer, 2001). Other more highly oxidized (hydr)oxides such as goethite (Blowes et al., 1997; Bonin et al., 2000a), lepidocrocite (Gu et al., 1999), maghemite (Farrell et al., 2000), or akaganéite (Phillips et al., 2000) may also form under appropriate conditions. In carbonate-bearing porewaters, ferrous carbonate precipitates (siderite, $FeCO_3$) have been detected (Agrawal and Tratnyek, 1996; Phillips et al., 2000). Finally, because of changes in Eh and pH within the iron

wall, precipitates other than iron (hydr)oxides or siderite may form. Some precipitates that have been previously identified include aragonite ($CaCO_3$; Phillips et al., 2000) and makinawite (Fe_9S_8; Gu et al., 1999). Other precipitates involving calcium and sulfur, as well as silicon and magnesium, can also develop.

H_2 gas can be generated within the porous medium through reduction of water or protons by the iron (Matheson and Tratnyek, 1994; Reardon, 1995; Sorel et al., 2001). This H_2 gas may accumulate and hence contribute, together with the precipitated solids, toward the creation of preferential paths of water flow through the porous media. Such "short-circuiting" can alter HRTDs within the barrier and may limit contaminant access to some fraction of the iron surface.

PRIOR LONGEVITY STUDIES

In light of the potential impact of solid precipitation and gas pocket formation on permeable barrier HRTDs, a number of researchers have conducted laboratory studies to examine the implications of such processes (Eykholt et al., 1995; Mackenzie et al., 1999; Casey et al., 2000; Devlin et al., 2000). These prior studies were of comparatively short duration, however, and changes to the porous media that may occur as a result of longer-term processes were not specifically investigated.

Studies by Sivavec and co-workers (Sivavec et al., 1995; Sivavec and Horney, 1996; Mackenzie et al., 1999) and by Farrell et al. (2000) have identified some of the factors associated with barrier longevity. Sivavec demonstrated that the reactivity of iron towards trichloroethylene (TCE) decreased upon exposure of the iron to 420 pore volumes of carbonate-buffered water. Because experiments were conducted at flow velocities (~ 806 cm/d) considerably higher than those observed in the field, pH and other geochemical gradients that are expected to develop within a PRB may not have become established. This could have repercussions on surface

speciation (and hence reactivity), as well as on mineral precipitation (and thus contaminant residence time). Such factors complicate extrapolation of their results to field conditions.

Farrell et al. (2000) also noted a significant decline in reactivity of iron towards TCE over the course of 667 days (~704 pore volumes) in column studies conducted at a flow velocity (50 cm/d) more representative of field conditions. Rate coefficients for TCE degradation were found to be a function of its concentration, as well as of the co-solute composition and column age. This suggests that site-specific differences in groundwater chemistry may affect PRB longevity. Nevertheless, because these researchers used inorganic matrices that were primarily composed of sulfate, chloride, or nitrate, the results may not relate to the carbonate systems more commonly encountered in groundwater. Moreover, it is difficult to assess the extent to which alterations in average flow velocity, resulting from precipitate formation, may have contributed to the deterioration in treatment efficiency reported by Farrell et al.

POTENTIAL EFFECTS OF SOLUTES ON IRON REACTIVITY AND ON HRT

Prior studies of iron corrosion and passivation indicate that reactivity may be a complex function of the inorganic and organic composition of the groundwater. Not only could contaminant type and concentration affect longevity, but the types and amounts of co-solutes present could also play a role. Carbonate, silica, chloride, and natural organic matter (NOM) have been identified as common groundwater constituents that could potentially affect the reactivity of iron towards chlorinated hydrocarbons (CHCs) and nitroaromatic compounds (NACs). These solutes could deactivate the interfacial region by altering the local electronic environment of the reductants, by limiting access to reactive sites, or by competing with contaminants for reactive sites. Alternatively, some solutes could assist in maintaining reactivity within the PRB, either by facilitating breakdown of passivating Fe(III) (hydr)oxide coatings or

by enabling the formation of new reactive phases. Other solutes could promote precipitate formation, altering flow velocities and HRTDs. Individual solutes may concurrently serve different roles, and the net effect could vary with solute concentration.

Carbonate, for example, can either serve to enhance or inhibit iron corrosion, depending on its concentration (Gui and Devine, 1995; Reardon, 1995; Agrawal and Tratnyek, 1996; Gu et al., 1999). Its presence leads to precipitation of mineral phases such as carbonate green rust (Bonin et al., 2000b), siderite ($FeCO_3$; Agrawal and Tratnyek, 1996; Phillips et al., 2000), calcite ($CaCO_3$; Vogan et al., 1999), or aragonite ($CaCO_3$; Phillips et al., 2000; Yabusaki et al., 2001). These precipitates may reduce the porosity of the permeable media (Mackenzie et al., 1999; Roh et al., 2000; Yabusaki et al., 2001); they could inhibit contaminant access to the iron surface (Reardon, 1995; Agrawal and Tratnyek, 1996); and in the case of carbonate green rust, they could provide a redox-active phase.

Chloride acts as a corrosion promoter, and its presence could thus enhance the reactivity of iron. Chloride destabilizes the passive film present on the iron surface, and this can induce corrosion pit formation (MacDougall and Graham, 1995; Gotpagar et al., 1999). Such effects have been hypothesized to produce the rate enhancement observed in reduction of CCl_4 (Johnson et al., 1998) and TCE (Gotpagar et al., 1999). Using an input-output column, we have previously shown that addition of chloride initially led to increased reactivity towards 2-nitrotoluene (2-NT) reduction by Master Builders iron (Klausen et al., 2001). Reactivity nonetheless declined as the column aged, indicating that the rate-enhancing effect may be relatively short-lived.

Silica is a known corrosion inhibitor (Sastri, 1998) that may compromise PRB longevity through the formation of surface complexes at the particle-water interface. Typical concentrations in groundwater are in the range of 116-749 μM (7-45 mg/L as SiO_2; see Davis et

al., 2001), and field measurements have shown that dissolved silica concentrations decrease abruptly within an iron PRB (Sass et al., 2001). Although the effect of silica adsorption on contaminant degradation within full-scale column reactors has not been previously addressed, preliminary results have indicated a strong detrimental effect on the reactivity of iron towards both TCE (Deng et al., 1998) and NACs (Klausen et al., 2001).

Despite the ubiquity of natural organic matter (NOM), little is known about its effects on PRB efficacy. Results from a column study suggest, however, that high total organic carbon (TOC) concentrations (> 500 mg/L) can adversely affect tetrachloroethylene degradation rates (Duran et al., 2000). Tratnyek et al. (2001) observed slight declines in reactivity toward CCl_4 in the presence of three isolated humic acids; in contrast, the four fulvic acids tested did not significantly influence CCl_4 reduction rates.

SCOPE OF PRESENT INVESTIGATION

The principal technical objectives of the present investigation were to evaluate the impact of groundwater composition on the long-term performance of zero-valent iron (Fe) barriers and to develop a prototype electrochemical probe for monitoring reactivity changes at either the field or laboratory scale. Specific objectives were:

(1) to understand the effects of groundwater chemistry on long-term barrier performance, including delineation of the impacts of chemical reactivity changes and alterations in transport properties;

(2) to develop an electrochemical probe that could be used to continuously assess the ongoing performance of a reactive barrier, either in laboratory columns or *in situ* in the field;

(3) to develop a fundamental understanding of the causes of alterations in reactivity through studying its relationship to the changing composition of the iron surface;

(4) to incorporate the results of our studies into a set of guidelines that could be used to qualitatively or quantitatively predict the impact of groundwater solutes on PRB performance.

To address these issues, the present studies employed long-term laboratory column studies of TCE and NAC reduction by a commercial grade of zero-valent iron, Master Builder iron. During this investigation, alterations in the reactivity of the interfacial region were decoupled from changes in the mean hydraulic residence time (HRT) that stemmed from mineral precipitate and H_2 gas pocket formation within the porous media.

Fifteen columns, filled with Master Builder iron and continually fed solutions containing various organic and inorganic solutes, were operated concurrently for up to 1100 days. Two sets of columns were housed at Johns Hopkins (columns A-F, run for 1100 days; columns G-J, run for 475 days), and the third was maintained at the Air Force Research Laboratory (K-O, run for 407 days). At a flow rate of 0.5 mL/min (220 cm/d), these operation times correspond to up to 4500 pore volumes. We believe these zero-valent iron column experiments to be the longest of any reported to date.

Thirteen of these columns were continuously exposed to mixtures of contaminant species, and contaminant concentrations were determined in sampling ports at periodic intervals. The remaining two columns were only periodically exposed to TCE so as to test the effect of co-solutes and water (as opposed to TCE) on iron passivation. Rate constants were obtained by fitting the resulting contaminant profiles to an exponential decay model. Target mixtures included three CHCs: TCE, 1,2,3-trichloropropane, and 1,1-dichloroethane; and three NACs: 2-

nitrotoluene, 4-nitroacetophenone, and 4-nitroanisole. Although the reactivities of many of these species with iron have previously been examined, long-term effects of solute composition on Fe^0 reactivity towards mixtures of these compounds have not been investigated. The principal experimental variables included the type and concentration of co-solutes (bicarbonate, chloride, silica, and NOM).

Periodic measurements were also conducted to determine the concentrations of important (pH; total organic carbon and total inorganic carbon; dissolved silica; dissolved Fe(II); dissolved calcium). Particular emphasis was placed in obtaining such data for columns G-J.

For ten columns (A-J), periodic tracer tests were conducted with tritiated water (^3H_2O). (Because the AFRL is not licensed for use of tritium by the Nuclear Regulatory Commission, such studies were restricted to columns operated at JHU). These ^3H_2O tracer studies enabled precise determination of the mean HRT, enabling a delineation of the effects of altered HRT from changes in the reactivity of the interfacial region on overall system performance. For columns A-D, tracer tests were also attempted using the gas partitioning tracer, SF_6.

Four columns (G-J) were equipped with three *in situ* electrochemical probes each installed at different distances along each column. Each probe consisted of five isolated grains of Master Builder iron, a platinum counter electrode, and an Ag/AgCl reference electrode. Electrochemical measurements that were conducted included continuous measurement of open circuit (corrosion) potential and intermittent impedance spectroscopic measurements. These electrochemical measurements provide information concerning the state of passivation of the reactive iron material. A more limited array of electrochemical measurements were also conducted using *ex situ* electrochemical probes (also constructed of individual grains of Master Builder iron).

Granular iron samples were obtained from eleven of these columns (A-J), and were subjected to various types of analyses to characterize the evolving composition of the interfacial region. Techniques employed included Auger electron spectroscopy (both to assess variations in composition at the interfacial region and, in conjunction with Ar^+ ion sputtering, to determine profiles of composition as a function of depth); X-ray diffaction (XRD) analyses of mineral phases formed; scanning electron microscopic (SEM) imaging (complemented by energy dispersive spectroscopic (EDS) and wavelength dispersive spectroscopic (WDS) analysis); transmission electron microscopic (TEM) analysis (in conjunction with selected area electron diffraction (SAED), EDS, and electron energy loss (EEL) spectroscopic analyses); and micro Raman spectroscopic analysis.

ORGANIZATION OF REPORT

This report is organized into seven chapters. Chapter 2 provides detail pertaining to the experimental procedures employed. Chapter 3 reports on our findings concerning changes in mean HRT and HRTDs over time. Chapter 4 describes changes that occurred over time in each column towards the reactivity of Master Builder iron towards NACs and TCE, in response to exposure to varying solutes. Chapter 5 presents the results of our analyses of grains and precipitates obtained from various columns. Chapter 6 summarizes the results we obtained with electrochemical probes (operated both in an *in situ* mode and in an *ex situ* mode). Finally, Chapter 7 provides our guidelines as to how information pertaining to local groundwater composition will affect longevity and hence should be factored into PRB design.

Some of the sections of this report represent somewhat expanded versions of papers that have been (or are in the process of being prepared for submission to) scientific journals, including the *Journal of Contaminant Hydrology* and *Environmental Science and Technology*.

For example, Chapter 3 represents an expanded version of a paper that has been accepted (pending revisions) by the *Journal of Contaminant Hydrology*. Preliminary findings obtained in this study have been presented at a number of national meetings of professional societies and meetings of industry groups. These include a panel discussion presented at the Remediation Technologies Development Forum (RTDF) Permeable Reactive Barriers Action Team Meeting held in Oak Ridge, TN, November 1998; a poster presented at the European Geophysical Society XXV General Assembly, Nice, France, April 2000; the August 2000 National Meeting of the American Chemical Society held in Washington, D.C.; the Spring 2001 meeting of the American Geophysical Union held in Boston, MA in May 2001; posters at the Gordon Research Conference on Environmental Science: Water held in June 1998 and June 2000; a platform presentation at the IWA Second World Water Congress held in Berlin, Germany in October, 2001; two posters at the American Geophysical Union national meeting held in San Francisco, CA in December 2001; and a platform presentation at the Third International Conference on the Remediation of Chlorinated and Recalcitrant Compounds held in Monterey, CA in May 2002. In addition, various presentations of our findings were made at universities (University of Virginia, April 2000; EAWAG-ETH (Switzerland), May 2000; Ohio State University, May 2000; Colby College, October 2000; University of California-Berkeley, 2001; Virginia Tech, 2001).

CHAPTER 2 – EXPERIMENTAL PROCEDURES

Fifteen columns (divided into three sets), filled with granular iron and continually fed solutions containing various organic and inorganic solutes, were operated concurrently. Two sets were operated at Johns Hopkins (columns A-F, run for 1100 days; columns G-J, run for 475 days), and the third set was maintained at AFRL (K-O, run for 407 days). At an approximate flowrate of 0.5 mL/min, these operation times correspond to ~ 4500 pore volumes fed to columns A-F, ~ 1560 pore volumes fed to columns G-J, and ~ 1430 pore volumes fed to columns K-O.

COLUMN SETUP AND OPERATION

Column Design and Construction

The fifteen columns utilized in this study were constructed using Plexiglas tubes with dimensions of either ~ 390 mm × 30 mm inner diameter (columns A-F) or ~ 350 mm × 35 mm inner diameter (columns G-J, K-O). Sampling ports were installed at 12 locations in each column, distributed over the entire column length as indicated in Table 2.1. These sampling ports were composed of 1/16" stainless steel tubes driven radially to the centerline of the columns and epoxy sealed at the column walls. The external ends of these tubes were sealed using removable Valco caps. The sampling ports were arranged radially so that the flow pattern in the porous medium upgradient of any sampling port was minimally altered. In addition to the aqueous sample ports, five solid sampling ports were installed in columns G-J to enable the periodic removal of iron grains from the columns (Table 2.2). These ports consisted of removable 1/4" delrin plugs, cut so that their ends were flush with the interior column wall.

Table 2.1 Approximate locations (± 1 mm) of aqueous sampling ports for columns A-F, G-J, and K-O. Flow direction was from port 1 to 13.

Columns	Port #												
	1	**2**	**3**	**4**	**5**	**6**	**7**	**8**	**9**	**10**	**11**	**12**	**13**
	Location of Aqueous Sampling Port (mm)												
A-F	9.5	19.5	29	39	49	78	117	156	195	234	273	324	392
G-J	9.5	19.5	29.5	40	49.5	79.5	119.5	159.5	199.5	240	289.5	339.5	346.5
K-O	9.5	19.5	29.5	40	49.5	79.5	119.5	159.5	199.5	240	289.5	339.5	346.5

Table 2.2 Locations (± 0.1 mm) of solid sampling ports for columns G-J. Flow direction was from port 1 to 5.

Column	Port #				
	1	**2**	**3**	**4**	**5**
	Location of Solid Sampling Port (mm)				
G	4.5	29.5	79.5	199.5	339.5
H	5.0	30.0	80.0	200.0	340.0
I	4.5	29.0	79.5	199.0	340.0
J	4.5	29.0	80.0	199.5	339.5

Three electrochemical probes were installed in each of columns G-J. These probes were permanently attached to each column at distances of approximately 6.5, 140, and 369 mm from the column inlet. These probes are fully described in the electrochemistry section later in this chapter.

Flow to all fifteen columns was provided using multichannel peristaltic pumps (Ismatec IPC, Cole Parmer Instrument Co., Chicago, IL) that withdrew fluid from individual feedwater reservoirs. The flow to each column was maintained at approximately 0.5 mL/min throughout the duration of the study. A syringe pump (Harvard Apparatus Co., South Natick, MA) provided flow of organic contaminant-laden water to each column, at a rate of 2.7 μL/min per column, or approximately 0.5% of the primary peristaltic pump rate. Concentrated stock solutions were used in the syringe pumps in order to avoid unreasonably large syringe sizes or frequent syringe filling. Concentrations in excess of normal aqueous solubility were achieved through the use of methanol as a cosolvent (50% v/v). The mole fraction of methanol in the combined feed never

exceeded 2.4×10^{-3} and was therefore below the level where co-solvent effects occur (Munz and Roberts, 1986; Schwarzenbach et al., 1993). Initial results obtained with this setup yielded irregular input concentrations in columns A-F. This was corrected by introducing 37 mL mixing chambers after the first 100 days of operation. Experiments with columns G-J and K-O were initiated with the mixing chambers in place. Except for short and infrequent periods of maintenance and repair, the flow to the columns was continuous over the full duration of this work. A diagram of the experimental setup is provided in Fig. 2.1

Loading of Columns: Media Properties and Loading Technique

The iron used in this study was commercial grade GX-27 granular iron obtained from Master Builders, Inc. (Cleveland, OH). Previous analysis of this material has shown that it is approximately 90% Fe with small amounts of other metals (< 5% Mn, < 3% Cu, and < 2% Cr) and ~ 2.4% carbon (Hardy and Gillham, 1996). Nitrogen BET analysis suggests that the specific surface area is approximately 1 m^2/g (Devlin et al., 1998). The iron grains were sieved using standard brass-mesh sieves and sieve-tapping equipment (W.S. Tyler, Inc., Mentor, OH) prior to column packing. The final size distribution was: 355-500 μm (13.2% by weight), 500-700 μm (33.9%), 700-1000 μm (40.3%), and 1000-1400 μm (12.6%).

Columns A-F, G, I-J, and K-O were packed with 100% iron, whereas column H was packed with a mixture consisting of 92% Master Builder iron – 8% Amelia albite (w/w). Amelia albite ($NaAlSi_3O_8$), an aluminosilicate mineral, was obtained from Ward Scientific (Rochester, NY). The albite was crushed using a mortar and pestle, and was subsequently sieved to obtain a final size distribution of 0.35 to 1.4 mm.

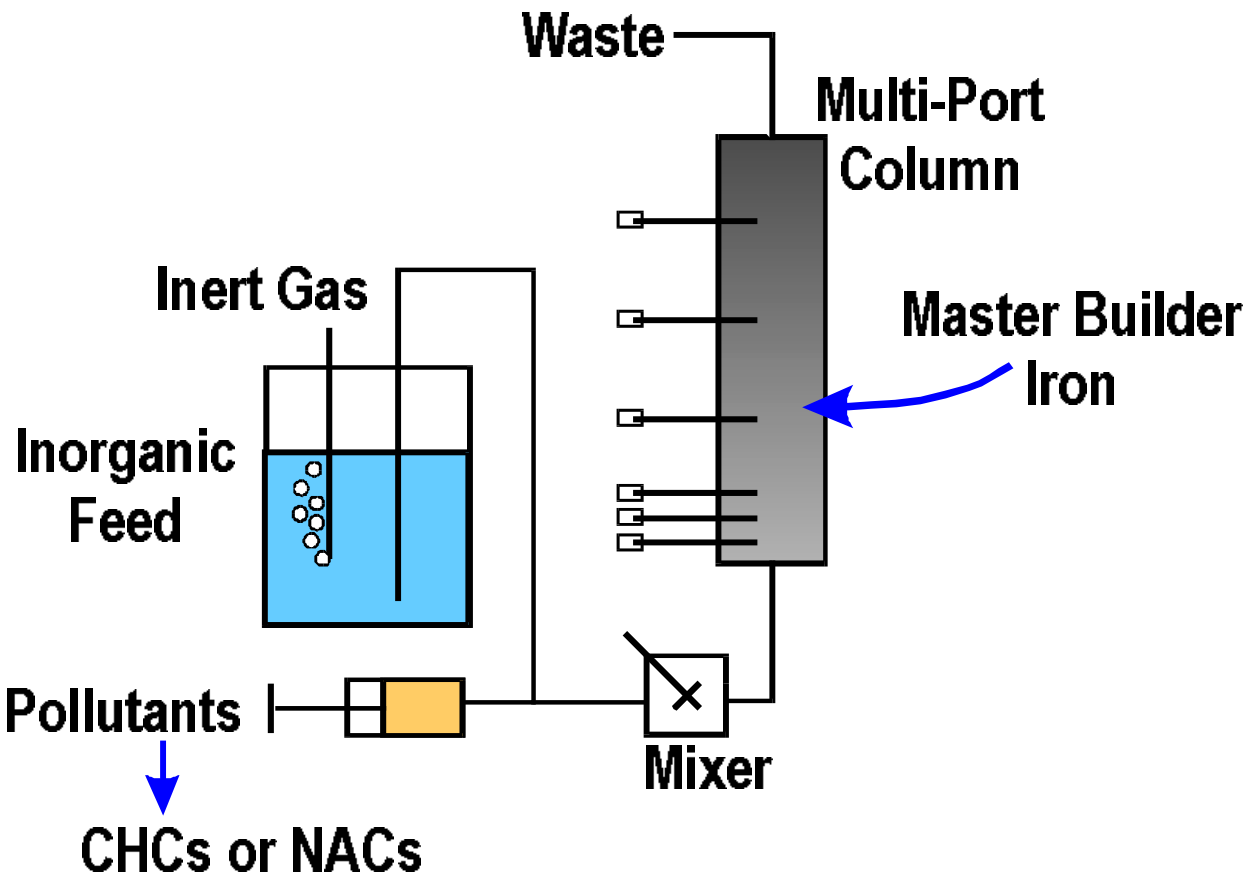

Figure 2.1 Schematic of experimental setup with mixing chambers in place. Note that these mixing chambers were added to Columns A-F after the first 100 days of operation; all other column experiments were initiated with these mixing chambers in place at the outset.

Each column was packed using either iron grains or an iron grain/albite mixture. A quantity of iron grains sufficient to fill the columns was initially split into smaller units of approximately 125 g each using a 16-way spinning riffle splitter (Model SP-201, Gilson, Worthington, OH). For the 100% iron columns these lofts were then individually poured into the vertically positioned columns. The lofts for the albite/iron column were produced by mechanically mixing a riffle split iron loft with a riffle split albite loft until a homogeneously distributed mixture was obtained. These mixed lofts were then carefully poured into the vertically positioned column. After adding each loft, the columns were lightly tapped to achieve a uniform distribution. It was not possible to tamp down the lofts, as it was observed that this led to non-uniform particle size distributions. Once the column was filled, the top column end cap was screwed in place, and the column was sealed. The mass of the dry filled and sealed column was determined gravimetrically. Comparison with the previously determined mass of the empty sealed column enabled the determination of the mass of porous medium within each column.

Characterization of Initial Conditions

Column Startup

Columns A-F and K-O were filled with feedwater by first evacuating the pore space using a faucet aspirator, and then initiating bottom-up feed of de-aerated solutions. The pore space in Columns G-J was saturated with 100% CO_2 gas and was then filled with feedwater in a similar manner. Feed solutions were maintained under either continuous nitrogen-carbon dioxide (N_2/CO_2) or continuous nitrogen (N_2) purge. The water reservoirs for columns A-F were initially pressurized with 10 psi of N_2. This led to concerns that the overpressure could lead to N_2 degassing during column filling and initial operation, potentially accounting in part for the

undersaturation of the porous medium of columns A-F at the beginning of operation. We minimized such overpressure by removing the check-valves on the influent reservoirs after ~ 110 days of operation. Columns G-J and K-O were initiated without these check valves present. The normalized water-filled porosity (see below) values in columns G-J were lower than those of columns A-F. This suggests that N_2 degassing does not contribute significantly to the gas phase that accumulates within the columns.

Once filled, columns A-F were initially operated using a horizontal orientation in an attempt to simulate a permeable reactive barrier in the field, and with the hope that gas accumulation would reach steady-state without bubble rise. Within the first two weeks of operation, however, we observed that gas had accumulated along the upper walls of the column and that gas volumes in the beds were not steady. In response, we changed the column orientation to vertical (flow from bottom to top) after 13 days. Columns G-J and K-O were operated using a vertical orientation throughout their operation lifetimes.

Characterization of Initial Pore Volumes

To accurately measure changes in flow conditions and the relative water-phase and gas-phase saturations of the columns as a function of column age, it was necessary to fully characterize the initial pore volume of each column. The volume of each empty column (V_{column} [cm^3]) was determined based on the weight of an empty column (m_{empty} [g]), the weight of the column filled with H_2O ($m_{\text{empty+H}_2\text{O}}$ [g]), and the density of water ($\rho_{\text{H}_2\text{O}}$ [$\text{g}\cdot\text{L}^{-1}$]):

$$V_{column} = \frac{m_{empty+H_2O} - m_{empty}}{\rho_{H_2O}} \tag{2.1}$$

The total initial pore volume ($V_{V,initial}$ [cm^3]) of a fresh column at startup was determined by subtracting the volume of the porous medium from the volume of the empty column (V_{column} [cm^3]):

$$V_{V,initial} = V_{column} - V_{medium,initial} = V_{column} - \frac{m_{Fe,initial}}{\rho_{Fe}} - \frac{m_{albite,initial}}{\rho_{albite}} \tag{2.2}$$

Mass of iron in the column ($m_{Fe,initial}$) was calculated as previously noted and its solid density (ρ_{Fe} = 7.000 ± 0.001 g·cm^{-3}) was determined using a Micromeritics (Norcross, GA) AccuPyc 1330 Pycnometer. The mass of albite in column H ($m_{albite,initial}$) was determined by accounting for the number of lofts of albite/iron added and the total mass of albite in each (NB: For the other columns this term was equal to zero). The density of albite (ρ_{albite} = 2.6 g·cm^{-1}) was obtained from the literature. Total initial porosity ($\theta_{tot,initial}$ [-]) was defined as the ratio between the total pore volume of a fresh column and its empty volume:

$$\theta_{tot,initial} = \frac{V_{V,initial}}{V_{column}} \tag{2.3}$$

The initial linear velocity (v_{inital} [m·d^{-1}]) and the initial hydraulic retention time ($\tau_{initial}$ [d]) are based on the assumption that the columns were fully saturated when operation started and are defined as follows:

$$v_{initial} = \frac{Q}{A\theta_{tot,initial}} \tag{2.4}$$

$$\tau_{initial} = \frac{V_{V,init}}{Q} \tag{2.5}$$

where Q [cm^3·d^{-1}] is the volumetric flow rate and A [cm^2] as the cross-sectional area of the column.

Using these definitions, the volume of each empty column (V_{column} [cm^3]), the porous medium mass ($m_{\text{medium,initial}}$ [g]), the initial pore volume ($V_{\text{V,initial}}$ [cm^3]), and the cross sectional area (A [cm^2]) for columns A-F and G-J were calculated; results are tabulated in Table 2.3. (Because detailed ^3H_2O tracer studies were not conducted on columns K-O, the values of the parameters for these columns are not included here.) In addition, calculated values for total initial porosity ($\theta_{\text{tot,initial}}$ [-]), initial linear velocity (v_{initial} [md^{-1}]), and initial hydraulic retention time (τ_{initial} [d]) are also listed.

Table 2.3 Characteristics of the fresh iron columns

Column	V_{column} [cm^3]	$m_{media,initial}$ [g]	V_V [cm^3]	A [cm^2]	$\theta_{tot,initial}$ [-]	$v_{initial}$ [m·d^{-1}]	$\tau_{initial}$ [d]
A	266.7	791.9	153.6	6.79	0.576	1.84	0.213
B	300.4	891.2	173.1	7.65	0.576	1.63	0.240
C	283.1	839.0	163.2	7.18	0.577	1.74	0.228
D	266.1	790.0	153.3	6.82	0.576	1.83	0.213
E	273.7	812.4	157.6	6.98	0.576	1.79	0.219
F	286.6	850.3	165.1	7.29	0.576	1.71	0.229
G	336.3	911.6	206.1	9.71	0.613	1.21	0.286
H [a]	337.0	836.3	202.7	9.71	0.602	1.23	0.282
I	338.2	910.0	208.2	9.77	0.616	1.20	0.289
J	332.1	888.7	205.1	9.58	0.618	1.22	0.285

[a]For this column the mass includes both iron (m_{iron}) and albite (m_{albite}). The void volume calculation takes the different particle densities into account.

Conditions of Continuous Operation

The volumetric flow rate (Q [mL·min^{-1}]) in the columns was typically in the range of 0.4-0.5 mL·min^{-1} and was periodically measured at the effluent end of the columns. This flow rate provided a linear porewater velocity in the range of 1.2 to 1.8 m·d^{-1} and an initial hydraulic retention time in the fresh columns of 0.21 to 0.29 days at full saturation (see Table 2.3). Porewater velocities were determined periodically, and for columns A-F and G-J were based on independent estimates of normalized water-filled porosity and flow rate. For columns K-O the

calculated porewater velocities were based solely on the measured flow rates. The hydraulic head loss through the columns was not determined.

Column Feed Water and Chemical Addition

The column feed solutions were prepared in 9 L flasks using distilled and purified water (Milli-Q Plus UV, Millipore). These solutions were then deoxygenated for 3-4 hours by sparging with either purified N_2 (columns A-F, J, K-O) or a 5% CO_2/95% N_2 mixture (columns G-I). A continuous purge was maintained to prevent oxygen from being drawn into the reservoirs when the water level dropped in the flasks. To address the role of influent pH and ionic composition on the reactivity of the iron, we varied the chemical compositions of the fifteen feed reservoirs, as summarized in Table 2.4.

Of the fifteen columns studied in this work, the CHCs were continuously introduced to twelve (columns C-E, G-J, and K-O). The CHCs (TCE and 1,2,3-TCP) were fed at nominal initial concentrations of 100 μM each. 1,1-DCA (also at ~ 100 μM) was fed to columns C-E from day 1 to day 197; because it underwent negligible transformation, it was removed from the feed to those columns after 197 days. The 1,2,3-TCP fed to columns K-O was discontinued after 148 days, leaving TCE as the sole contaminant.

Column F was primarily fed a mixture of two NACs throughout the duration of the study. The NAC feed contained 2-NT and either 4-NA or 4-NAP, each at a nominal concentration of 100 μM. The switch from 4-NA to 4-NAP after 301 days of operation was made to examine if the large difference in one-electron reduction potential between 4-NA and 4-NAP would result in substantial differences in the relative reactivity of these compounds (Klausen et al., 1995; Devlin et al., 1998).

Table 2.4 Composition of Feedwater for Columns A-F (operated for 1100 days at JHU), G-J (operated for 475 days at JHU), and K-O (operated for 407 days at AFRL)

	COLUMN														
	A	**B**	**C**	**D**	**E**	**F**	**G**	**H**	**I**	**J**	**K**	**L**	**M**	**N**	**O**
Influent pH =>	**9.3**	**9.3**	**9.3**	**9.3**	**9.3**	**9.3**	**7.5**	**7.5**	**7.5**	**9.3**	**9.3**	**9.3**	**9.3**	**9.3**	**9.3**
Co-solutes (shown are the times (in days) during which the feed was added)															
2 mM $NaHCO_3$	1-1100	1-1100	1-1100	1-1100		1-1100				1-475	1-290	1-290	1-290	1-290	1-290
2.4 mM $CaCO_3$[a]							1-475								
3.1 mM $NaHCO_3$[b]								1-475	1-475						
20 mM $NaHCO_3$					1-1100										
10 mM NaCl		1-1100		313-409											
500 µM Na_2SiO_3		875-1100	409-538			183-300									
5 mL HCl, 37%					400										
20 mg/L AHA[c]												1-240			
2 mg/L AHA[c]													1-240		
2 mg/L SRHA[d]														1-240	
2 mg/L GDS NOM[e]															1-240
pH 12 NaOH											345-346	345-346	345-346	345-346	345-346
Organic Contaminants[f] (shown are the times (in days) during which the feed was added)															
TCE	134-158 264-291 446-513 789-848 918-1100	134-158 264-291 446-513 789-848 918-1100	1-1085	1-1085	1–508 624-1100	134-158 264-291 401-446 509-623 789-848	1-475	1-475	1-475	1-475	1-345 346-407	1-345 346-407	1-345 346-407	1-345 346-407	1-345 346-407
1,2,3-TCP			1-1100[g]	1-1100[g]	1-508[g] 624-1100[g]		1-475	1-475	1-475	1-475	1-148	1-148	1-148	1-148	1-148
1,1-DCA			1 – 197	1 – 197	1–197										
2-NT					509-623	1-1100[h]									
4-NA						1-301[h]									
4-NAP					509-623	301-1100[h]									

[a] Set using a saturated $CaCO_3$/0.5% CO_2 buffer.
[b] Set using a $NaHCO_3$/ 0.5% CO_2 buffer
[c] Aldrich Humic Acid
[d] Suwannee River Humic Acid
[e] Great Dismal Swamp Natural Organic Matter
[f] Nominal concentration for all compounds 100 µM
[g] During periods when 'TCE probe' experiments were conducted, the TCP feed was suspended
[h] During periods when TCE was fed, NAC feed was suspended

TCE alone (~ 100 μM) was fed on an intermittent basis to columns A-F for short periods. These periodic "TCE probe" experiments were conducted to compare the reactivity of different columns at a given point in time. This enabled a comparison of the reactivity of the columns not normally fed TCE (A, B, and F) to those that were continually fed CHCs (C-E, G-J, K-O), and additionally provided information pertaining to the effect of the co-contaminants, 1,2,3-TCP and 1,1-DCA, on rates of TCE degradation in columns C-E.

QUANTIFICATION OF SOLUTES

During the course of these experiments, samples were periodically taken from the columns by allowing fluid to flow under hydraulic pressure from the sampling ports into headspace-free syringes. These syringes were used to transfer samples to other containers as appropriate, without exposing the samples to the ambient atmosphere. The collected samples were analyzed by gas chromatography (GC) for the chlorinated hydrocarbon (CHC) samples, by high-pressure liquid chromatography (HPLC) for the nitroaromatic compound (NAC) samples, by colorimetric methods for the quantification of silica and ferrous/ferric iron, by a carbon analyzer to quantify the organic and inorganic carbon content, and by atomic absorption (AA) spectroscopy to measure calcium. In addition, periodic samples were also taken to measure the column porewater pH. Procedures for each of these measurements are described in the sections that follow.

CHC Quantification

At JHU: Aqueous 1 mL samples obtained from the sampling ports were transferred to 2.5 mL autosampler vials. Headspace samples (200 μL) were analyzed by gas chromatography (GC 8000 by Fisons Instruments, Beverly, MA) with flame-ionization detection (FID) using

either a 30 m × 0.53 mm ID GS-Q PLOT column or a 60 m × 0.32 mm ID GASPRO PLOT column (Agilent Technologies, Palo Alto, CA). Prior to injection, each sample was equilibrated at 60 °C for 30 minutes in the oven of a Fisons HS 850 headspace autosampler.

Five-point calibration curves for TCE, the three dichloroethylene (DCE) isomers, vinyl chloride, 1,1-DCA, and 1,2,3-TCP were generated using aqueous standards prepared in 20 mL glass syringes. These standards were analyzed using the same method as the aqueous samples and spanned a concentration range of 2-100 μM. The minimum detection limits (MDL) were calculated using the method of Hubaux and Vos (1970) and were between 0.5 and 4 μM for all chlorinated solvents.

Acetylene, ethylene, ethane, propylene, propane, 1-butene, n-butane, n-pentane, 1-pentene, n-hexane, and 1-hexene were calibrated using commercially available gas standards (Scott Specialty Gas). Aqueous concentrations were calculated using Henry's Law constants determined via a modified EPICS method at 60 °C (Arnold, 1999).

At AFRL: 0.40 mL aqueous samples were added to 1.2 mL acetonitrile (containing 1,4-dichlorobenzene as an internal standard) and were analyzed by GC on a 15 m × 0.53 mm DB-1 column. Detection was by ^{63}Ni electron capture detection.

NAC quantification

The nitroaromatic compounds and their corresponding aniline daughter products were determined by HPLC analysis on a RP-18 reversed-phase column (125 × 4 mm) equipped with a precolumn (4 × 4 mm; both LiChroCART stainless steel cartridge, 5 μm spheres; Merck AG, Darmstedt, Germany) connected to a Waters 515 HPLC pump (Millipore Corp., Milford, MA) and a Waters 486 variable-wavelength UV/VIS detector set to 220-280 nm. The system was

supplemented by a Waters 717Plus autosampler. The mobile phase was phosphate buffered (15 mM, pH 7.0) methanol/water (55/45 v/v).

Aqueous 1 mL samples obtained from a given column and a given sampling port were transferred to autosampler vials and were analyzed using the HPLC system. The MDL was found to be between 4 and 8.5 μM for all compounds and their daughter products. Each time the system was operated, it was calibrated using aqueous standards that spanned the range of concentrations typically observed in the samples.

Silica Analysis

Silica analyses were conducted using the heteropoly blue method (Greenberg et al., 1992). This is a sensitive colorimetric technique for detection of molybdate-reactive silica and is typically recommended for samples containing between 0.6 and 33 μM SiO_2. The heteropoly blue method is based on the reaction between silica and ammonium molybdate at pH 1.2 to produce molybdosilicic acid. The solution is then treated with oxalic acid to destroy any molybdophosphoric acid that may have formed through the reaction of the molybdate reagent with trace amounts of phosphate. After treatment with oxalic acid, the yellow molybdosilicic acid complex is reduced to a heteropoly blue complex by adding 1-amino-2-naphthol-4-sulfonic acid. The blue complex has a more intense color and is more stable than the yellow molybdosilicate complex, and therefore quantification of the heteropoly blue complex is preferred. The blue complex is stable for up to 12 hours (Bunting, 1944; Boltz and Mellon, 1947; Carlson and Banks, 1952).

The silica concentration in the porewater samples was quantified by adding 0.1 mL of 1+1 HCl and 0.2 mL ammonium molybdate reagent (10 g $(NH_4)_6Mo_7O_{24}\bullet 4H_2O$ in 100 mL water

pH adjusted to 7.5; Fisher Scientific # LC11250) to a 5 mL sample. The sample was rapidly mixed for a minute and then was left to stand for 5 to 10 minutes. A 0.2 mL aliquot of 7.5% (w/w) oxalic acid solution (Fisher Scientific # LC18060) was added, the solution was rapidly mixed, and was then allowed to react for a period of at least five but no more than fifteen minutes. After this reaction period, 0.2 mL of the reducing agent (0.042 mM 1-amino-2-naphthol-4-sulfonic acid ($H_2NC_{10}H_5(OH)SO_3H$) in 7.94 mM sodium sulfite ($NaSO_3$); Fisher Scientific # LC10890) was added and the solution was mixed thoroughly. Once the color had developed (typically 5-10 minutes), absorbance measurements at 815 nm were obtained using a UV-visible spectrophotometer (Shimadzu UV-160; Columbia, MD) and plastic 1 cm path length cuvettes.

The spectrophotometer was standardized using secondary standards (0-16.7 μM) produced by diluting a primary standard solution of sodium metasilicate nonahydrate ($Na_2Si_2O_3 \bullet 9H_2O$). The standards were found to be stable for periods of up to one week. All reagents had shelf lives of less than 6 months and were replaced accordingly. To prevent any form of external contamination, all reagents, samples, and standards were stored in plastic bottles and all reagents were specially produced for silica quantification. The MDL for silica was determined to be 77.4 nM by using the U.S. EPA approach (Mac Berthouex and Brown, 1994).

Fe(II) and Fe_{tot} Quantification

A modified FerroZine® (Stookey, 1970) technique was employed to quantify both ferrous and ferric iron. The procedure was originally developed by Lovley and Phillips (1986) to measure the reduction of ferric iron by microorganisms. Their approach was then further

modified by Roden and Zachara (1996) to include the measurement of ferrous iron adsorbed to particle surfaces. The procedure of Roden and Zachara was utilized in these experiments.

This method employs the use of 3-(2-pyridyl)-5,6-bis (4-phenylsulfonic acid)-1,2,4-triazine disodium salt (FerroZine®) to complex ferrous iron. The complex has a relatively high molar absorptivity thereby making it amenable to trace level determinations. The magenta complex formed is quite stable.

Solution Preparation

The FerroZine® reagent solution was prepared by dissolving 1 g of FerroZine® (Aldrich Chemical Company; St. Louis, MO) in 1 L of 50 mM HEPES (4-[2-hydroxyethyl]-1-piperazine ethanesulfonic acid) buffer. The pH of this solution was then raised to 7.0 by adding 2 M NaOH. The prepared FerroZine® reagent was stored in an amber auto-dispenser bottle. This solution was stable for one month, after which it was discarded. A 10% hydroxylamine hydrochloride solution was prepared by dissolving 10 grams of hydroxylamine hydrochloride in 100 mL of water. This solution was used to reduce ferric iron (Fe(III)) to the ferrous state (Fe(II)).

An Fe(II) stock solution (1 or 10 mg Fe/mL) was prepared by adding ferrous sulfate ($FeSO_4 \bullet 7H_2O$) to deionized water. The water was de-aerated by bubbling N_2 through it for twenty minutes. Ferrous sulfate was then added and the solution pH was reduced to 2.0 by the addition of 1 M HNO_3. This Fe(II) stock was stored in an anaerobic chamber where it was stable indefinitely.

Analytical Technique

Dissolved Fe(II) concentrations ($Fe(II)_{soln}$) were determined by passing a sample aliquot (0.1-10 mL) through a 0.22 μm syringe filter into 5 mL of FerroZine® reagent, followed by

measuring the absorbance of this solution in a 4 cm cuvette at 562 nm. Total dissolved iron {Fe(II) + Fe(III)} concentrations were then determined by adding 250 μL of 10% hydroxylamine hydrochloride to the vial. These reduced samples were equilibrated for 24 hours, after which the absorbance was measured at 562 nm. The difference between the concentration determined in the unreduced samples and in the reduced samples corresponds to the soluble or colloidal ferric iron concentration. The MDL for this technique was found to be 0.286 μM (15.95 μg/L) using a 10 mL sample aliquot and a 1 cm cell.

Carbon Measurement

At JHU: A Phoenix 8000 carbon analyzer (Tekmar-Dohrmann, OH) was used to measure the dissolved inorganic carbon (IC) concentration of column porewater samples. The carbon analyzer operates by first acidifying a sample and then sparging it to liberate the inorganic carbon as CO_2 gas. The CO_2 produced is transported via a carrier gas to a non-dispersive infrared analyzer that quantifies the amount of CO_2 produced and converts it to a carbon concentration based on the volume of the injected sample (Greenberg et al., 1992). Because the samples are not oxidized, any organic carbon present in the samples was not converted to CO_2 and was therefore not quantified.

The inorganic carbon content of the column porewater was determined by transferring 5 mL samples taken from individual ports to 40 mL amber glass vials that were previously filled with 35 mL deionized water. These headspace free vials were tightly sealed and were subsequently analyzed using the carbon analyzer. The system was calibrated using a five-point calibration curve. The standards were prepared by diluting a primary standard of deionized water and $NaHCO_3$. The MDL was found to be 0.1 mM.

At AFRL: The organic carbon content of porewater samples obtained from columns K-O was determined using a Shimadzu 5000 carbon analyzer (Columbia, MD). This instrument employs a platinum catalyst to oxidize the organic carbon to CO_2. The CO_2 was then quantified via non-dispersive infrared analysis.

Calcium Measurement

The calcium concentration in the porewater samples from column G was measured using atomic absorption (AA) spectroscopy (Greenberg et al., 1992). A 5 mL sample from the column was acidified with 1 mL of 1.1 M HNO_3, was diluted to 10 mL with deionized water, and was analyzed using a Perkin-Elmer Aanalyst 100 spectrophotometer. The excitation wavelength was set to 422.7 and the slit width to 0.7 nm. Prior to use, the system was calibrated using secondary standards. These standards were produced by diluting a primary standard of acidified calcium carbonate. A range of secondary standards (0.1-1 mM) was used to obtain a calibration curve, and the MDL was found to be 0.07 mM.

pH Measurement

The pH of the porewater samples was measured by removing aliquots from the sampling ports using headspace free syringes. The filled syringes were then attached to a flow-through cell containing an Orion Scientific combination reference/analytical electrode. The solution pH was measured using a Cole-Parmer (Vernon Hills, IL) pH 100 meter. The pH meter and electrode underwent a three-point calibration using standard buffer solutions from Fisher Scientific (Pittsburgh, PA) each time they were used.

TRACER STUDIES

Tracer studies for the measurement of solute transport properties were performed using two different agents: tritiated water ^3H_2O (Sigma Chemical Co., St. Louis, MO) in columns A-J, and sulfur hexafluoride SF_6 (Allied Chemical Co., New York, NY). The latter tracer was employed in columns A-D only.

Tracer Tests With Tritiated Water

Tritium-labeled water is a non-reactive tracer with perfect miscibility with normal water. A very low detection limit and a very precise analysis by liquid scintillation counting are achieved as a result of the nuclear decay of ^3H_2O. Because density change and solubility are not an issue, $^3H_20$ can be added in highly concentrated spikes so that accurate quantitation can be obtained even after substantial dilution and dispersion (Young and Ball, 1997a).

Pulses of tritiated water (30 μL with an activity of 5.5-8.5 × 10^4 DPM/μL) were injected onto a given Fe(0) column using an HPLC injection valve (Rheodyne Corp., Cotati, CT). A high-precision syringe pump (ISCO Inc., Lincoln, NE), containing feed solution of the same chemical composition as that normally fed to the column, was used to drive the ^3H_2O pulse onto the columns at a controlled flow rate of 0.500 mL·min^{-1}.

The 30 μL injection volume represents ~ 0.02% of a given column's pore volume. Within the timescale of effluent ^3H_2O measurement, this injection approximates an instantaneous input. The application of high concentrations in essentially instantaneous pulses can be expressed in terms of the Dirac delta function ($\delta(t)$ [d^{-1}]), which describes a unit impulse function with respect to time (t [d]). The Dirac function vanishes for all nonzero values of its argument in

such a way that the integral of this function over an interval containing the origin is equal to unity (Roos, 1969):

$$\int_0^\infty \delta(t)dt = 1 \tag{2.6}$$

The normalizing concentration (c_0 [dpm/mL]) is as traditionally assumed for a Dirac pulse input (i.e., the concentration of the solute that would result if the whole mass were dissolved in one pore volume of the column; (Young and Ball, 1997a)):

$$c_0 = \frac{\sum {}^3H_2O}{V_{column}\theta_w} \tag{2.7}$$

Previous work has shown that Dirac inputs are more effective at illustrating the effects of mass transfer limitations, large scale spatial heterogeneities, and other sources of non-Fickian dispersion than are either finite duration pulses or step inputs (Young and Ball, 1997a).

^3H_2O samples were collected either from the outlet end of the columns by using an automated fraction collector (ISCO Inc., Lincoln, NE) or from individual sample ports by manually withdrawing samples using a gas tight syringe. The ^3H_2O activity in the samples was determined using liquid scintillation counting (Beckman Inst., Fullerton, CA). Results are automatically corrected for any quenching effect by the instrument's software, using the following relationship

$$dpm = [\frac{cpm}{E}] \times 100 \tag{2.8}$$

where dpm are the decays of ^3H isotopes per minute and cpm are the counts of light photons registered per minute. The efficiency E [%] is based on the response efficiency of ^3H decay correlated to the spectral index of the sample (first moment of the pulse height distribution), as obtained by comparison of response with an external radiation source. Sample counts on the

scintillation counter were performed for either 30 minutes or until a relative error of ± 2% for the mean of the counts was achieved. The relative error (s/I [-]) is defined as the ratio

$$\frac{s}{I} = \sqrt{\frac{1}{tI}} = \sqrt{\frac{1}{N}} \tag{2.9}$$

in which s [cpm] is the standard deviation of the mean of the number of counts per minute, I [cpm] defines the counts per minute for one sample, t [min] is the time interval of counting performed, and N [-] is the number of counts done for one sample. A typical background activity concentration of 80-130 dpm per mL of scintillation fluid was experienced over the time range of the different ^3H_2O test series. Fig. 2.2 shows the experimental setup for the ^3H_2O tracer tests used in the lab.

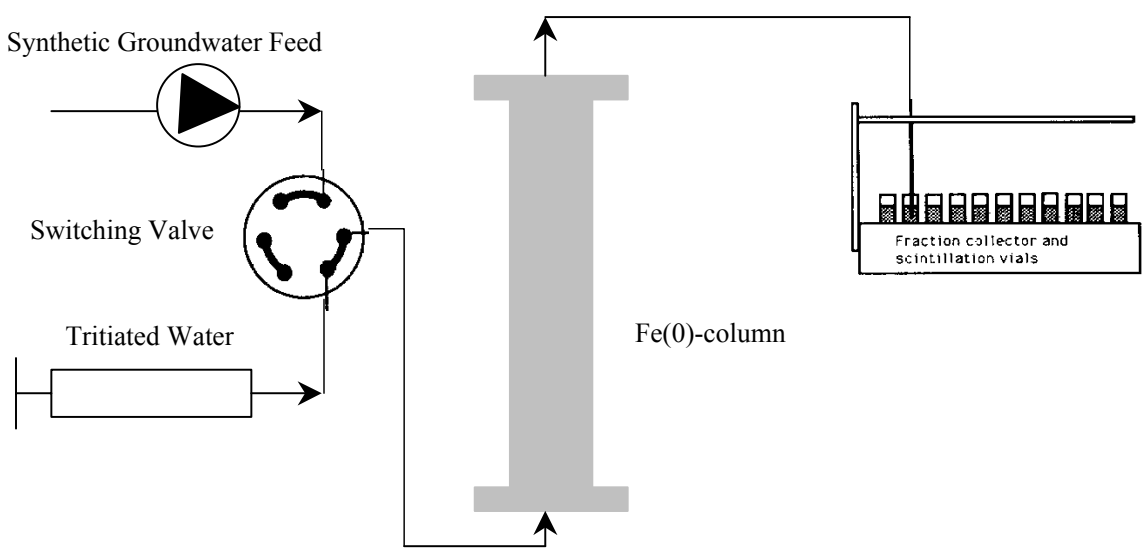

Figure 2.2 Experimental setup for tracer studies with ^3H_2O

Tracer Tests With Sulfur Hexafluoride (SF_6)

Sulfur hexafluoride (SF_6), a colorless and incombustible gas at room temperature, is often used in gas-partitioning tracer studies due to its low level of reactivity. Wilson and Mackay (1993) report an aqueous solubility of 37.5 mg·L^{-1} and a nondimensional Henry's law constant (H_c [-]) of 160.9 at 22 ^{o}C.

$$H_c = \frac{C_G}{C_L} \tag{2.10}$$

where C_G is the concentration of SF_6 in the gas phase (in moles·L^{-1}) and C_L is the equilibrium concentration in the aqueous phase (in moles·L^{-1}). It was our hope that tracer studies with this volatile solute would enable us to quantify gas volumes in the columns. Advantages of SF_6 as a potential gas-partitioning tracer include not only its high volatility, but also its high fluorine content, which allows for sensitive detection using an electron capture detector (ECD) on a gas chromatograph (GC).

For SF_6 injection into columns A-D, a 50 mL gastight syringe (Hamilton Inc., Reno, NV) was filled with approximately 40 mL Milli-Q water that had been sparged with N_2 gas for 30 minutes. SF_6 gas was then added to the syringe by attaching it to the regulator of a gas tank. After the syringe was filled, the outlet valve was opened to expel water (and was then quickly closed), such that the gas and water in the syringe were at approximately atmospheric pressure. The syringe was then fixed on a shaker table and was mixed horizontally to allow mass transfer from the gas phase into the aqueous phase. Once the SF_6 solutions had equilibrated, they were loaded onto a calibrated syringe pump (Sage Model 355, Orion Research, Inc., Beverly, MA) that was used to drive the SF_6-laden solutions into the columns for a specified application time

(pulse width). Aqueous concentrations and application times for the pulse inputs in these experiments are reported in Table 2.5.

Both liquid and gaseous samples for SF_6 analysis were collected at the effluent end of the columns (Fig. 2.3). Liquid samples were collected in 10 mL flow-through glass vials that were periodically removed and analyzed. In addition, the effluent tube of the liquid sampling vial was connected to a 50 mL gas-tight syringe that was initially filled with water. Any gas eluting from the column passed through the liquid sampling vial and accumulated in the headspace of the syringe. Gas samples from the headspace were taken periodically and were analyzed.

The liquid samples were stored upside down and were submerged in a water bath to prevent loss of SF_6 through the septa. For GC analysis, a headspace was generated in the sample vials by withdrawing liquid and simultaneously allowing ambient air to enter the vessel via a separately inserted small-diameter syringe needle. The syringe needles were removed, and the gas and water phases were then allowed to equilibrate for 30 seconds under vigorous shaking.

Table 2.5 Input characteristics for the SF_6 tracer tests

	Column A	Column B	Column C	Column D
Approximate initial volumetric ratio r [-] of gas/liquid in syringe	1:1	1:1	1:4	1:4
Time on shaker table [d]	16.0	16.0	1.7	1.7
Pulse application time t [min]	30.0	28.3	30.0	36.0
Aqueous concentration C_L [mg/L]	20.9	27.6	28.5	28.5
Standard error σ [mg/L]	0.13	0.86	0.47	0.47
Injected mass m [μg]	314	391	428	514

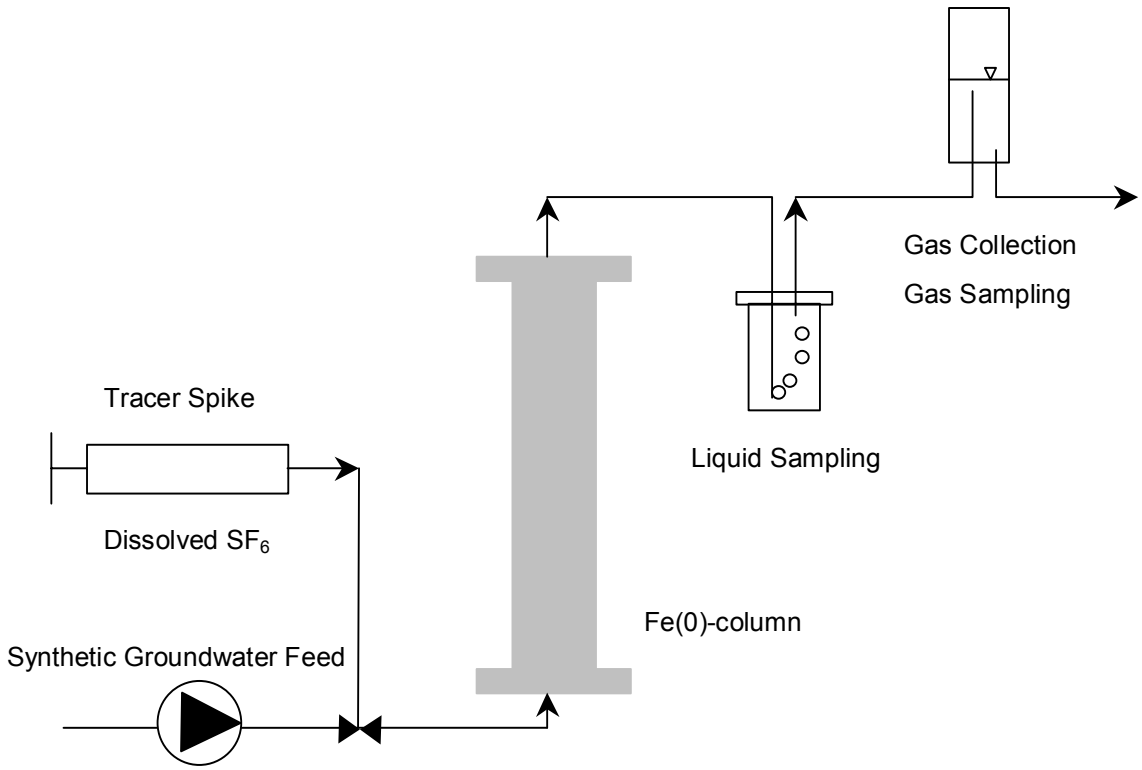

Figure 2.3: Experimental setup for tracer studies with SF_6

Analysis of gas-phase concentrations was accomplished using a Fisons GC 8000 series gas chromatograph (Fisons Instruments, Beverly, MA) that contained a 30 m × 0.32 mm ID PLOT column (Agilent Technologies, Palo Alto, CA). Because of its sensitivity to halogenated compounds, a ^{63}Ni electron capture detector (ECD) was used to quantify SF_6.

BATCH STUDIES WITH SF_6

At the outset of these experiments it was expected that SF_6 would act as a non-reactive tracer. To test this hypothesis, a set of batch tests was performed to examine the stability of SF_6 in the presence of granular iron. For this test, 60 mL glass vials were used. Four samples were set up with similar ratios between the gas, liquid, and solid phases as shown in Table 2.6. The liquid used in the samples was a deaerated 2 mM $NaHCO_3$ solution (the same solution used to feed columns A, C-D, F, J, and K-O). To prevent overpressure due to H_2 evolution over time, 5 mL of gas was withdrawn from the headspace in each vial.

Table 2.6 Vial composition for the batch SF_6 test. V_G [L^3] is the volume of headspace in the vials, V_L [L^3] is the volume of bicarbonate solution, and m_{Fe} [M] is the mass of iron added to the vials. C_G [ML^{-3}] is the initial concentration of SF_6 in the headspace.

	V_G [mL]	V_L [mL]	m_{Fe} [g]	C_G [μg/L]
Average vial	18.3±0.5	26.9±0.1	117.6±4.9	50

The vials for the batch tests were shaken on a shaker table. Gas samples were regularly taken from the headspace to determine the SF_6 concentration as a function of time. When it was determined that SF_6 was lost from the aqueous phase (presumably owing to either reaction or to sorption to the solid phase), an apparent first-order rate coefficient in the three phase system ($k_{eff,batch}$ [d^{-1}]) was calculated:

$$k_{eff,batch} = \frac{k_{SF_6}}{R_{d,batch}} \tag{2.11}$$

in which k_{SF_6} [d^{-1}] is the first-order rate coefficient for reaction/sorption of SF_6 on the iron surface, and R_d [-] is the distribution coefficient defined as

$$R_d = 1 + \frac{H_c V_G}{V_L} \tag{2.12}$$

where H_c [-] is the dimensionless Henry's law constant of partitioning, V_G [mL] is the volume of headspace in the batch vials, and V_L [mL] is the volume of liquid.

The reaction/sorption rate coefficient obtained from the batch samples was used to predict the first-order loss of SF_6 in the column ($k_{eff,column}$ [d^{-1}]). This was done by taking the different distribution coefficients and iron mass-liquid volume ratios in the two systems into account:

$$k_{eff,column} = k_{eff,batch} \frac{R_{d,batch}}{R_{d,column}} \frac{(m_{Fe}/V_L)_{column}}{(m_{Fe}/V_L)_{batch}} \tag{2.13}$$

in which m_{Fe} [g] is the mass of iron. A first-order decay process estimates the theoretical mass of SF_6 that could then be recovered from the columns at time t:

$$\frac{M(t)}{M_0} = \exp^{-k_{eff,column}t} \tag{2.14}$$

in which $M(t)$ [g] is the mass of SF_6 recovered after hydraulic residence time t [d] and M_0 [g] is the mass of SF_6 injected for the tracer studies.

ELECTROCHEMISTRY

Two types of electrochemical experiments were conducted. The first utilized *in situ* electrochemical probes mounted within columns G-J. As shown in Fig. 2.4, each of these

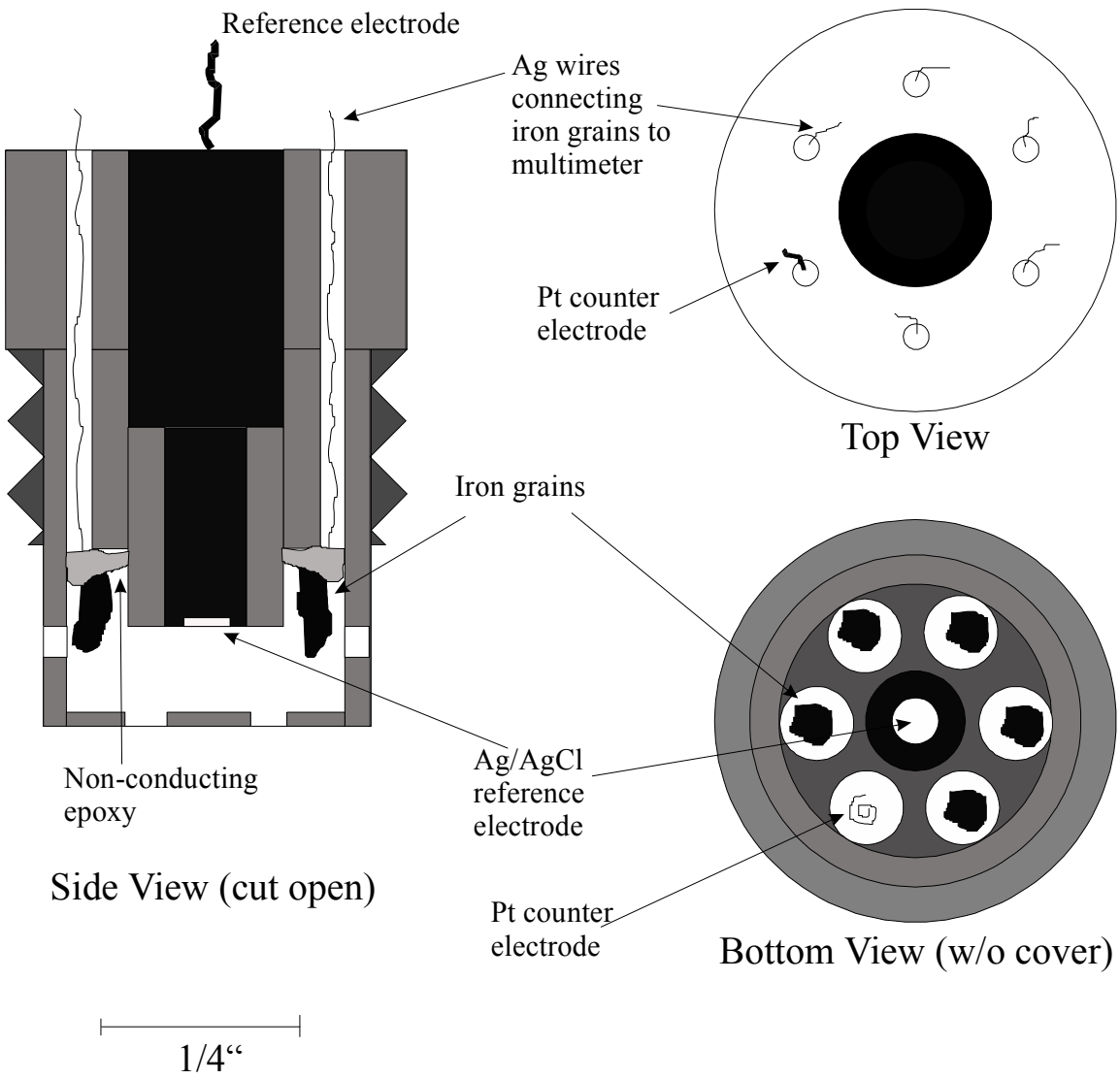

Figure 2.4 Schematic of electrochemical probe. Three probes were installed in each of columns G-J.

probes consisted of five isolated iron grains, a platinum counter electrode, and an Ag/AgCl reference electrode. Three probes were installed in each column (at distances of 6.5, 140, and 369 mm from the inlet).

The second type of experiment utilized *ex situ* electrochemical probes. As detailed in Fig. 2.5, these systems consisted of a set of electrodes connected in series by short lengths of 1/8" diameter Delrin tubing (Upchurch Scientific; Oak Harbor, WA). Individual electrodes were connected to the tubing using 1/8" diameter PEEK® crosses (Upchurch Scientific; Oak Harbor, WA). Flow to these assemblies was supplied by a multichannel peristaltic pump (Ismatec IPC, Cole Parmer Instrument Co., Chicago, IL) that withdrew fluid from individual feedwater reservoirs.

For both electrochemistry setups the electrochemical response over time of each probe was monitored using multimeters (Keithley Instruments, Inc., Cleveland, OH) controlled by a Labview (National Instruments, Austin, TX) software code developed at JHU. Specific measurements included open circuit (corrosion) potential (OCP) and impedance. Each of these techniques is briefly described in the following sub-sections.

Open-Circuit (Corrosion) Potential

The open-circuit (or corrosion) potential is the voltage that is established when anodic and cathodic partial current densities are equal (no external current). In passive systems (such as the Master Builder iron with which we worked), these partial current densities are small and the corrosion potential is therefore not very well defined. As a result, small external perturbations can create large changes in potential. This represents an obvious limitation to the usefulness of open-circuit potential measurements alone. Nevertheless, in conjunction with the more sensitive

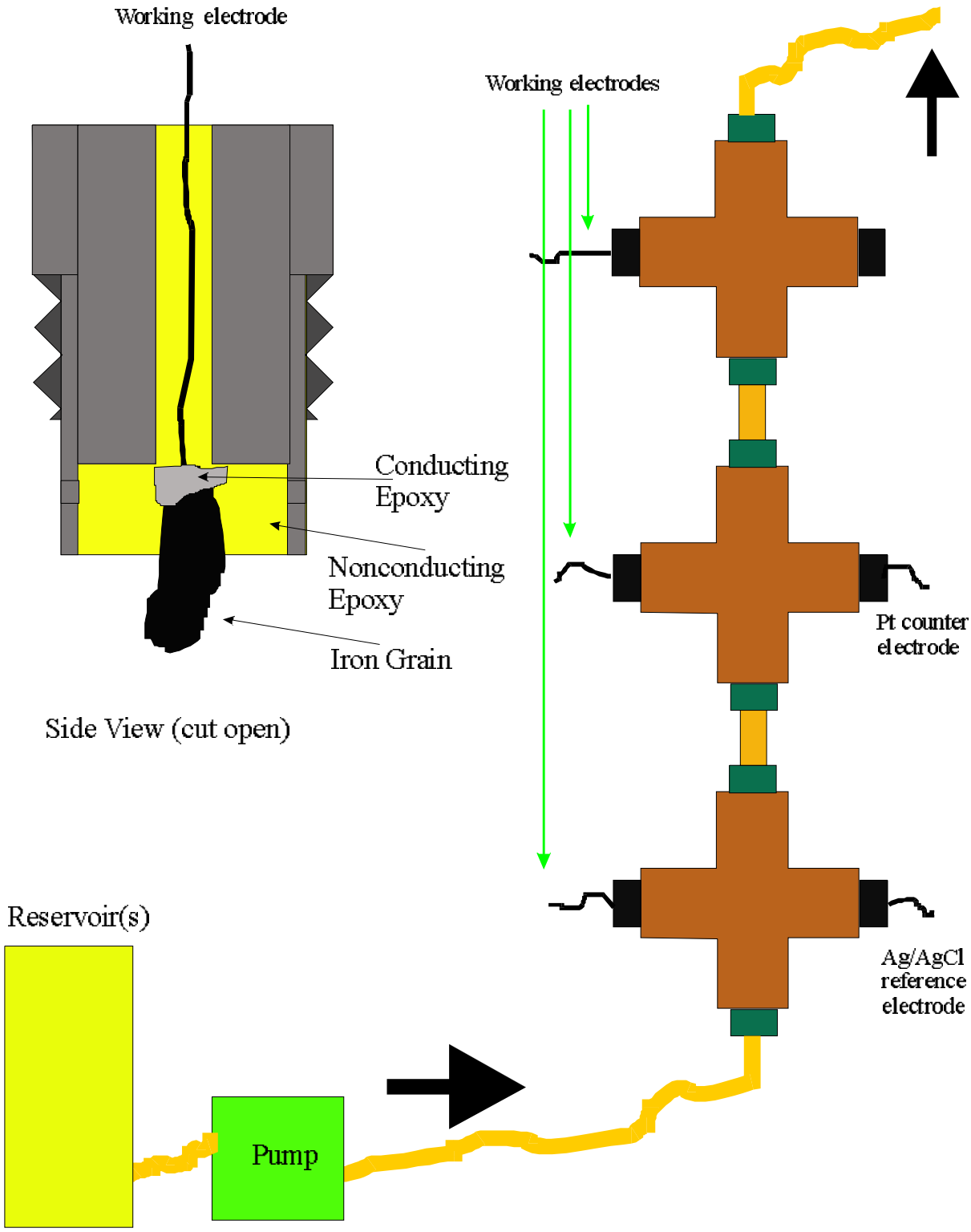

Figure 2.5 Schematic of *ex situ* electrochemical probe design. Flow is from bottom of figure to the top.

impedance measurements, the open-circuit measurements may provide a simple means of assessing overall changes in reactivity.

Impedance Spectroscopy

The second electrochemical tool applied in this work was impedance spectroscopy. Impedance spectra were obtained as a potential means to probe the electrical double-layer at the iron surface, to examine charge-transfer resistance at that double layer, and to help quantify mass-transfer limitations associated with transport through the double-layer (Hladky et al., 1980; MacDonald, 1991). During the course of the impedance spectroscopic measurements, the electrodes were excited using a small-amplitude AC perturbation of varying frequency. The current that results from these perturbations was then analyzed in terms of magnitude and phase shift. To conduct these experiments without polarizing the iron grains at a potential other than the open-circuit potential (OCP), we developed (in concert with the JHU chemistry department machine shop) a device that allowed the impedance experiments to be conducted at OCP.

SURFACE CHARACTERIZATION

Auger Electron Spectroscopy (AES)

Samples for surface characterization were taken from the new columns and examined using Auger Electron Spectroscopy (AES). AES is a technique that provides information about the composition of non-volatile surface species. In AES, a beam of excited electrons interacts with the sample surface and core level electrons are ejected and subsequently detected. AES has a very high spatial resolution (~ 75 nm), which can in turn provide information about localized

surface phenomena. AES was also used to probe the atomic composition deep into the grain. Specifically, an Ar^+ stream was used to remove surface layers, thereby allowing examination of particle composition as a function of precipitate depth.

The grains for AES analysis were obtained by first transferring an entire column to the anaerobic glovebox. Working within the glovebox, one of the solid sampling ports was opened to provide access to the iron grains within the column. The extracted iron grains were rinsed by quickly dipping them in and out of de-aerated water. The rinsed grains were attached to an AES platform, were transferred to a sealed container, were removed from the glovebox, and were then taken to the JHU Surface Analysis Laboratory. The samples were then introduced into a Perkin Elmer PHI 610 Scanning Auger Microscope through the use of a lock-load chamber maintained under nitrogen purge. Typically the total elapsed time between sample extraction from a given column and sample introduction into the surface analysis chamber was less than 20 minutes.

X-ray Diffraction

On the last day of column operation, the columns were taken into the anoxic glovebox. Three holes were drilled into columns B-E, adjacent to ports 1, 8 and 12. Holes had already previously been drilled into column F, and columns G-J had pre-drilled solid sampling ports. Grains were removed through the holes and were stored in two vials for each hole, filled with pore water from the nearest liquid sampling port. Enough grains were removed to fill both vials each to about a third. The vials were sealed and stored in the glovebox.

For analysis by XRD, several grains along with some liquid were removed from one of the vials. Grains were ground using a mortar and pestle until the liquid reached an inky color. The liquid was transferred onto a low background silicon (400) wafer and the sample was dried

for several hours in the glovebox, until all the water had evaporated and only a powder was left on the silicon wafer.

The samples were analyzed on a powder X-ray diffractometer model Philips XRG 3100, operated at 35 kV and 25 mA. The software package MDI Data Scan (Materials Data Inc., Livermore, CA 1995-1999) was used for data acquisition. Scans from $2\theta = 5$ to 80 degrees were obtained, where θ is the glancing angle between the beam and the sample. A Cu $K\alpha$ anode was used as the radiation ($\lambda = 1.54056$ Å) source. The scan rate was 0.05 degrees and 15 sec/step. The spectra were aligned to the background peak of the silicon wafer, which occurred at $2\theta = 69.13$ degrees. The analysis software package Jade 3.1 (Materials Data, Inc., Livermore, CA 1991-97) and the reference database Powder Diffraction File 1994 (PDF-2 Database Sets 1-44, Dataware Technologies, Inc., 1985-94) were used to identify the mineral phases.

Electron Microscopy

Microprobe

The second vial containing grain samples described above was used for scanning electron microscopy (SEM analysis). For the microprobe analysis, the grains were rinsed with deoxygenated DI water, dried and then removed from the glovebox. Between 3 and 5 grains from each sample were placed in a copper cylinder and embedded in epoxy. When the epoxy had hardened, the samples were polished using sandpaper of decreasing grid size until smooth cross-sections of the grains were obtained. Then the samples were carbon coated to ensure their conductivity under the electron beam.

The microprobe system used is a JEOL 8600, equipped for energy dispersive spectroscopy (EDS) as well as wavelength dispersive spectroscopy (WDS).

The samples were inspected by examining the SEM micrographs, and several Polaroid photographs were taken from the grains and regions of interest. The photographs were taken at an acceleration voltage of 15 keV. In addition, several EDS point analyses were performed on different spots on the samples to identify the regions of interest. Compositional maps of selected regions were obtained at a magnification of 750 or more, using EDS for the elements Si, Ca, Mn and Fe, and WDS for the elements O, S, Na and Cl.

Transmission Electron Microscopy

Two different sample preparation techniques were used for transmission electron microscopic (TEM) investigation. First, a small quantity of particle-laden fluid from the outlet of column D (sample D12) was extracted and mounted on a TEM grid containing a holey-carbon support film. The grains in suspension disperse onto the film and were examined in the Philips 420 TEM operating at 120 kV. This instrument has a point-to-point resolution of 0.35 nm and an analytical beam diameter of approximately 20 nm. Selected area electron diffraction (SAED) patterns were obtained from areas of 100 nm or greater. An Oxford light element X-ray detector was used to determine qualitative EDS analyses.

Another sample was generated by impregnating several altered grains from column J in a 1 in. diameter mold. The grain was ground and polished to expose the metallic core. The polished surface was then mounted on a glass slide with a temperature sensitive adhesive and the bulk of the sample was cut away with a trim saw. The remaining thin section was ground to a thickness of about 20 μm. The thinned sample was removed from the glass slide and glued onto a copper grid. The sample was then further thinned to electron transparency in a Gatan Duo ion

mill using a 6 kV beam, 1 μA current and 18˚ milling angle. A 5 nm thick carbon coating was applied to the sample to reduce charging of the oxides and silicates.

The milled sample was placed in an FEI CM300 FEG TEM operating at 297 kV. This TEM has an ultimate point-to-point resolution of 0.18 nm and a beam diameter of around 0.2 nm. The CM300 also has scanning transmission electron microscopy (STEM) capabilities, which collects transmitted beam and X-ray intensities generated by a rastered fine probe. X-rays were collected by an Oxford light element EDS detector and processed by an Emispec analyzer. In addition, electron energy loss (EEL) spectra were collected by a Gatan GIF spectrometer. Spectra were collected in imaging mode (diffraction coupled) with a large beam diameter (semi angle of collection = 100 mrad), 2 mm entrance aperture, and a dispersion of 0.2 eV. Spectra were processed by the Gatan EL/P program for thickness correction and zero-loss deconvolution. The resolution of the detector is 1-1.5 eV over several second acquisition times.

Raman Spectroscopy

In an anaerobic glovebox, sample grains for Raman spectroscopic characterization were extracted using solid sampling ports pre-drilled into the columns. At each sample port, eight to ten iron grains were removed and were immediately transferred into headspace-free vials containing porewater obtained from the nearest aqueous sampling port. Raman samples were prepared in an anaerobic glovebox by placing several grains into a Raman cell containing 1-2 mL of porewater. The cell was then sealed, removed from the glovebox, and multiple grains and multiple spots per grain were analyzed.

In-situ Raman spectroscopic measurements were obtained using a Renishaw 1000 Raman microscope system. This instrument consists of an Olympus microscope, a single spectrograph fitted with holographic notch filters, and a thermoelectric cooled charge coupled device (CCD)

detector. Sample excitation was achieved using the 632.8 nm line of a Melles Griot 35 mW HeNe laser. An objective lens with 50× magnification provided spatial resolution of 2 μm^2 and a focal depth of 26 μm.

CHAPTER 3 - EVALUATION OF TRANSPORT PROPERTY VARIABILITY

To address the long-term effects of precipitate and gas pocket formation on PRB efficacy, we undertook a column study aimed at decoupling changes in hydraulic residence time (HRT) from overall alterations in the chemical reactivity of the surface. Ten columns (A-F, G-J), filled with granular iron or a mix of granular iron and albite, were continually fed waters containing various inorganic (chloride, carbonate, silicate) and organic (trichloroethylene, 1,2,3-trichloropropane, 1,1-dichloroethane, 2-nitrotoluene, 4-nitroanisole, 4-nitroacetophenone) constituents for a period in excess of 475 days. Using ^3H_2O as an unreactive non-partitioning tracer, the overall hydraulic residence time distributions (HRTDs) of all ten columns were periodically measured. In addition, columns G-J were also subjected to separate measurements of the HRTD of specific portions of the columns. This chapter describes the results of these tracer experiments as well as of tracer experiments involving the volatile gas sulfur hexafluoride (SF_6).

TRITIATED WATER EXPERIMENTS

Data Analysis

Concentration-time histories (breakthrough curves) for tritiated water were first evaluated through moment analysis (Fogler, 1999; Young and Ball, 2000). More specifically, the zeroeth moment of the breakthrough curve was used to obtain an estimate of total collected radiolabeled activity ($\sum {}^3H_2O$; dpm/mL), and this was subsequently used to calculate the first temporal moment. The latter provided an estimate of the mean residence time (τ) for the tritiated water and hence, the mean linear pore water velocity (v). The results were further evaluated by

comparing experimental breakthrough curves with model simulations obtained by applying a dual-region solute transport model.

The dual-region solute transport model assumes that not all of the water in the column is mobile ("flowing") and that mobile water only slowly exchanges with the remaining water, which is assumed to reside in stagnant or "immobile" zones (van Genuchten and Wierenga, 1976; Brusseau et al., 1989; van Genuchten and Wagenet, 1989; Toride et al., 1993). As such, advection and hydrodynamic dispersion occur only within the mobile region. Accordingly, the mobile (θ_m) and immobile (θ_{im}) volumetric water contents are separately accounted for ($\theta_m + \theta_{im} = \theta_w$). Non-equality of solute concentration in the mobile and immobile fluids can occur at a given location in the column (local nonequilibrium) and is expected whenever mass transfer between the two zones is slow relative to the rate of convective solute transport. Immobile liquid regions are expected to comprise a negligibly small fraction of the total pore space in homogeneous and fully-saturated porous media, but they can be important for flow under unsaturated conditions and through domains of heterogeneous particle size and pore structure (van Genuchten and Wierenga, 1976). For the columns reported here, the volumes of the immobile regions were expected to increase over time owing to mineral precipitate and gas pocket formation.

To quantify transport in a dual-region system, we applied a model formulation in which mass transfer between the two zones is approximated as a first-order process (van Genuchten and Wierenga, 1976; Toride et al., 1995). With this formulation, the relationship between the "effective" first-order mass transfer rate coefficient and the actual diffusion coefficient will depend upon the specific experimental conditions as well as upon the actual size and geometry of the immobile regions (Young and Ball, 1997a). Although the latter are unknown for our

columns, the first-order model approximations provide reasonable simulations of experimental data and the model may be a useful heuristic means to assess results.

The dual-region model is represented by the following two equations, which describe transient accumulation of mass in the mobile and immobile phases:

$$\theta_m \frac{\partial c_m}{\partial t} = \theta_m D_m \frac{\partial^2 c_m}{\partial x^2} - \theta_m v_m \frac{\partial c_m}{\partial x} - k_{mt}(c_m - c_{im}) \tag{3.1}$$

$$\theta_{im} \frac{\partial c_{im}}{\partial t} = k_{mt}(c_m - c_{im}) \tag{3.2}$$

where v_m [cm/d] is the mobile phase linear pore water velocity (= $v\theta_w/\theta_m$) ; D_m [cm^2/d] is the effective dispersion coefficient for the mobile phase; c_m [dpm/mL] and c_{im} [dpm/mL] are the concentrations of solute in the mobile and immobile liquid phases, respectively; and k_{mt} [1/d] is a first-order mass transfer coefficient for ^3H_2O exchange between the mobile and immobile zones.

The analytical solution to the dual-region model has been incorporated into public domain software (CXTFIT 2.0) that applies a Marquardt-Levenberg least squares fitting algorithm to obtain "best-fit" values of selected model parameters (Toride et al., 1995). CXTFIT 2.0 was used to obtain estimates of D_m, θ_{im}, and k_{mt} for the dual region model by employing a third-type inlet boundary condition and an infinite outlet boundary condition (Parker and van Genuchten, 1984; van Genuchten and Parker, 1984). Concentrations were taken to represent "flux-averaged" values for the breakthrough curves where the samples were obtained from the column effluent (Parker and van Genuchten, 1984; van Genuchten and Parker, 1984). For those cases in columns G-J where the samples were taken from the intermediate sampling ports, the concentrations were assumed to represent "resident" values.

The input parameters to CXTFIT 2.0 for the end-of column simulations for columns A-F were the known values for: 1) observations of concentration (dpm ^3H_2O/mL) versus time, 2) total

collected tracer radioactivity ($\sum {}^{3}H_2O$), and 3) linear pore water velocity (v). For the evaluation of the breakthrough curves for columns G-J, the velocity values were not used as input parameters but rather were fit to the data. The rationale for this approach is described subsequently.

$\sum {}^{3}H_2O$ recovered was used in place of total radioactivity injected in order to minimize the impacts of data "truncation" on our results (i.e., to ensure that first moment estimates and subsequent parameter fits were not biased by the need of the model to account for unobserved ${}^{3}H_2O$ mass). Such unobserved mass presumably eluted at concentrations below the detection limit, and is unavoidable under conditions of extensive spreading. Analysis of simulated datasets has shown that data truncation can significantly affect parameter estimation (Young and Ball, 2000). To understand the possible extent of data truncation on our results, $\sum {}^{3}H_2O$ was compared to the total ${}^{3}H_2O$ mass injected. Excluding one set of six tracer injections, for which a bad injector seal prevented us from knowing the amount of ${}^{3}H_2O$ added to the columns, the average recovery of ${}^{3}H_2O$ activity in the remaining tracer tests was 94.6% ± 1.0% (at 95% confidence interval) with recovered values ranging between 84% and 113% of the injection estimate. Although it is possible for the ~ 6% (average) unaccounted mass to cause a slight underestimation of mean residence time under some conditions (Young and Ball, 2000), we believe that this level of recovery is adequate to provide a good qualitative indication of trends in our columns.

To simplify the analysis of the modeling results, the experimental and model data were expressed in terms of the following non-dimensional parameters:

$$C_m = c_m / c_0 \tag{3.3}$$

$$T = \frac{Qt}{\theta_{tot,initial} V_{column}} \tag{3.4}$$

$$\beta = \frac{\theta_m}{\theta_w} \tag{3.5}$$

$$\omega = \frac{k_{mt} L}{\theta_w v} \tag{3.6}$$

where C_m and T are non-dimensional concentration and time, respectively; β is a normalized mobile phase porosity, and ω is a normalized mass transfer coefficient. The normalizing concentration (c_0 [dpm/mL]) is as traditionally assumed for a Dirac pulse input (i.e., the concentration of the solute that would result if the whole mass were dissolved in one pore volume of the column (Young and Ball, 1997b)):

$$c_0 = \frac{\sum {}^3H_2O}{V_{column} \theta_w} \tag{3.7}$$

Because of this normalization scheme, normalized effluent concentrations greater than unity are expected.

Effluent Port Sampling of Columns A-F: HRTDs and Modeling Results

Over the course of column operation, changes in the color of the granular iron media were observed, with more pronounced changes observed earlier at the proximal ends of the columns, with a subsequent progression towards the distal end. Such changes were taken as evidence that precipitates were forming within the media. In addition, distinct gas bubbles were intermittently observed to emerge from the columns. As discussed in the subsequent chapter, the precipitates and gas pockets are believed to alter both the chemical reactivity and the pore-scale

accessibility of the surface. The data from the ^3H_2O tracer tests enable us to directly examine this possibility by providing direct measures of the HRTDs.

Only “full-column" tracer tests were conducted for columns A-F, with the ^3H_2O concentrations measured at the effluent end of each column. Obviously, such results reflect changes throughout the full column length. In fact, it is expected that changes in flow velocities and patterns will vary with longitudinal position, and that the most dramatic changes will be manifested near the column inlet. As discussed later in this chapter, these spatial variations do exist, however, their overall effect on solute transport and contaminant remediation is predicted to be minimal. In any case, the end of column results reported here provide a good indication of “column-averaged” media properties.

Over the course of the 1100-day study on columns A-F, nine tracer experiments were conducted on each column. To illustrate the results, three different breakthrough curves obtained for each column are depicted in Fig. 3.1. Qualitatively this figure shows that mean tracer retention time varied considerably and that tracer spreading generally increased over the course of operation. In general, not only does the spread of the residence time distribution increase over time, but the breakthrough curves also become increasingly asymmetric (i.e., they exhibit enhanced tailing). Previous work has suggested that asymmetric breakthrough curves indicate the existence of transport-related nonequilibrium due to intra-aggregate diffusion (Crittenden et al., 1986; Roberts et al., 1987; Brusseau et al., 1992) and unsaturated flow conditions (van Genuchten and Wierenga, 1976).

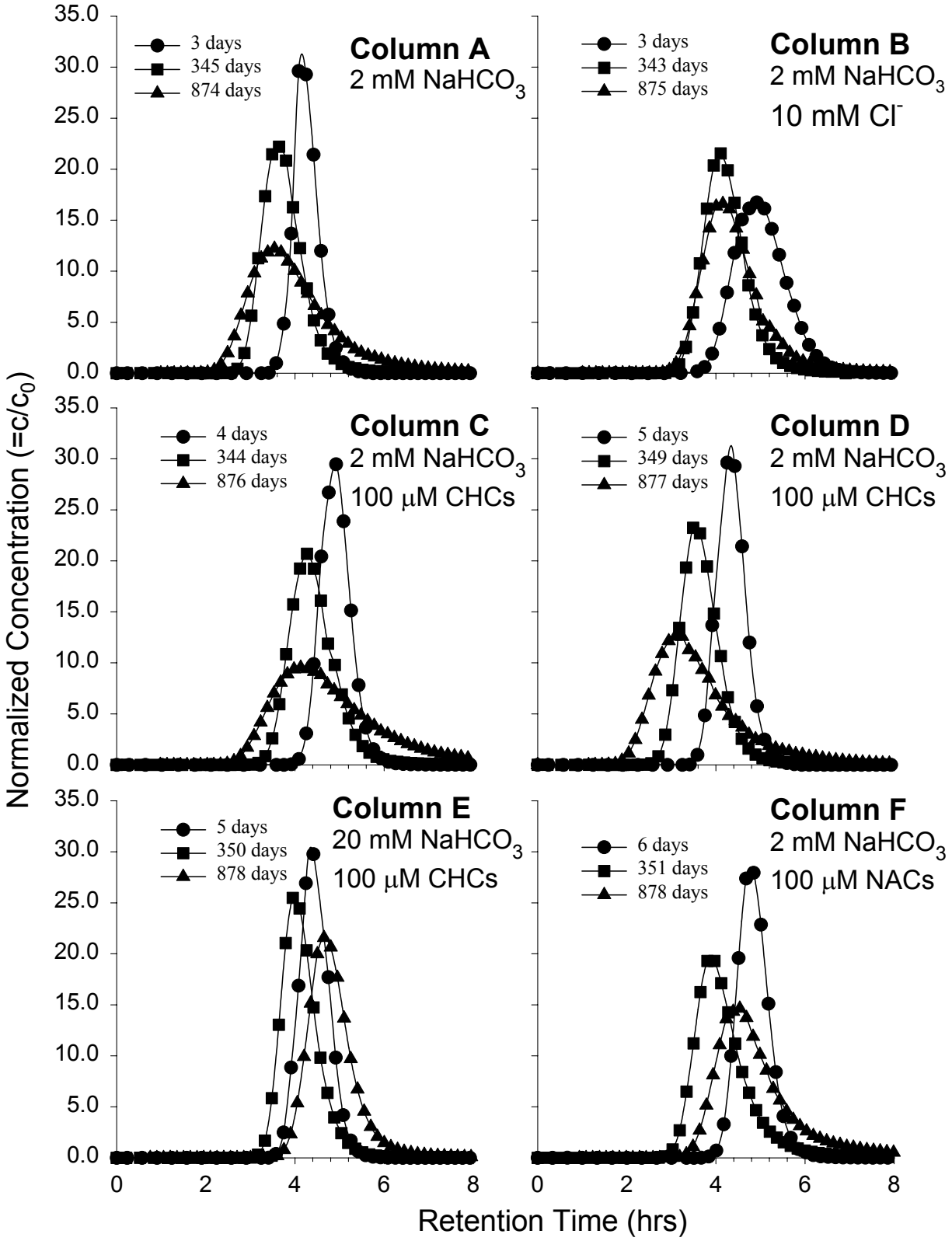

Figure 3.1 ^3H_2O breakthrough curves as a function of age for Columns A-F. Notice the variability in retention times as the columns age, as well as the enhanced spreading of the tracer pulses.

First Moments and Pore Water Velocity

First moment analyses of the effluent tritiated water breakthrough curves indicate that the hydraulic residence times (τ) of each column changed over time. Mean HRT is related to the volumetric water content (θ_w):

$$\tau = \frac{\theta_w \times V_{column}}{Q} \tag{3.8}$$

where $\theta_w = V_{H_2O}(t)/V_{column}$ and $V_{H_2O}(t)$ is the volume of water in the column at time t. These calculated values of τ were transformed to mean linear pore water velocities (v) using the following equation:

$$v = \frac{L}{\tau} \tag{3.9}$$

where L [cm] is bed length. The results of this calculation are tabulated in Table 3.1. The pore water velocities in most of the columns display modest increases over time, with the most dramatic changes evident by day 90. Initially, the pore water velocities in the six columns averaged 200 ± 10 cm/day; by day 900 they increased by 6 to 25% for columns A-D. For columns A, B, and D, the pore water velocities increased over the first three to six months and have remained reasonably stable ever since. In contrast to those three columns, the pore water velocities in columns C, E, and F increased initially, but have steadily decreased at later times. This latter effect could stem from gas dissolution, possibly resulting from a combination of both gradually increasing porewater pressures and, more importantly, occasional episodes of substantially higher pressure. For example, the effluent ends of columns C and E became temporarily clogged around day 200, and we hypothesize that gas dissolution occurred at this time. Other variables remaining constant, the associated decrease in intraparticle gas volume

Table 3.1 Parameters obtained from first moment analyses and CXTFIT dual region model. These tests were conducted using an ISCO high pressure syringe pump that precisely maintained a flow rate of 0.500 mL/min. Actual average flows in the columns over the full operation period were nominally at the same rate but exhibited some column to column and temporal fluctuation.

		1st Moment Model		CXTFIT Parameters			Derived Parameters	
	Operation Time [d]	v [cm/d]	$s_{tracer}(t)$ [-]	D_m [cm^2/d]	β [–]	ω [–]	% Immobile Water = 100× (1–β) [%]	k_{mt} [1/d]
Column A	3	192	0.959	15.1 ± 0.2	0.999 ± 0.001	64.3 ± 21.9	0.10 ± 0.54	174 ± 59.1
	90	217	0.849	52.5 ± 6.7	0.956 ± 0.008	0.117 ± 0.090	4.40 ± 0.80	0.32 ± 0.24
	152	244	0.755	48.2 ± 2.0	0.960 ± 0.002	0.075 ± 0.024	3.98 ± 0.21	0.20 ± 0.07
	230	245	0.752	54.9 ± 1.9	0.960 ± 0.002	0.076 ± 0.020	4.03 ± 0.18	0.20 ± 0.06
	345	245	0.752	59.6 ± 1.7	0.959 ± 0.002	0.065 ± 0.016	4.09 ± 0.15	0.17 ± 0.04
	454	243	0.758	77.1 ± 1.9	0.963 ± 0.002	0.062 ± 0.015	3.69 ± 0.16	0.17 ± 0.04
	533	240	0.768	108 ± 5.0	0.932 ± 0.006	0.328 ± 0.064	6.85 ± 0.56	0.89 ± 0.17
	764	240	0.768	109 ± 10	0.923 ± 0.013	0.573 ± 0.181	7.68 ± 1.31	1.55 ± 0.49
	874	231	0.797	139 ± 5.0	0.895 ± 0.005	0.502 ± 0.052	10.5 ± 0.52	1.36 ± 0.14
Column B	3	185	0.882	51.4 ± 0.9	0.997 ± 0.007	75.9 ± 24.7	0.30 ± 0.74	182 ± 59.0
	91	226	0.722	42.4 ± 1.2	0.970 ± 0.001	0.054 ± 0.017	2.98 ± 0.14	0.13 ± 0.04
	153	223	0.732	36.8 ± 1.0	0.972 ± 0.001	0.051 ± 0.015	2.76 ± 0.12	0.12 ± 0.04
	231	227	0.719	43.4 ± 1.5	0.974 ± 0.002	0.036 ± 0.019	2.63 ± 0.17	0.09 ± 0.05
	343	219	0.749	45.0 ± 1.0	0.970 ± 0.001	0.079 ± 0.015	3.00 ± 0.12	0.19 ± 0.04
	454	217	0.752	51.8 ± 1.6	0.964 ± 0.002	0.109 ± 0.024	3.60 ± 0.16	0.26 ± 0.06
	534	218	0.749	51.9 ± 7.4	0.912 ± 0.014	0.762 ± 0.244	8.85 ± 1.42	1.83 ± 0.58
	763	214	0.763	77.9 ± 2.1	0.966 ± 0.002	0.052 ± 0.017	3.40 ± 0.19	0.12 ± 0.04
	875	210	0.777	60.0 ± 2.7	0.943 ± 0.003	0.214 ± 0.041	5.70 ± 0.52	0.58 ± 0.11
Column C	4	189	0.920	15.6 ± 0.4	0.999 ± 0.011	52.75 ± 30.27	0.100 ± 1.1	134 ± 77.0
	92	227	0.766	54.9 ± 1.6	0.973 ± 0.002	0.029 ± 0.015	2.75 ± 0.16	0.07 ± 0.04
	154	228	0.762	45.7 ± 4.1	0.944 ± 0.006	0.313 ± 0.096	5.64 ± 0.62	0.80 ± 0.24
	232	228	0.762	55.9 ± 1.5	0.968 ± 0.002	0.054 ± 0.016	3.23 ± 0.15	0.14 ± 0.04
	344	210	0.828	43.9 ± 2.2	0.966 ± 0.003	0.093 ± 0.034	3.45 ± 0.28	0.24 ± 0.09
	448	213	0.816	47.7 ± 1.6	0.964 ± 0.002	0.101 ± 0.024	3.62 ± 0.20	0.26 ± 0.06
	537	206	0.844	43.7 ± 1.8	0.949 ± 0.003	0.218 ± 0.037	5.08 ± 0.26	0.55 ± 0.09
	762	201	0.865	53.6 ± 4.9	0.935 ± 0.008	0.416 ± 0.126	6.55 ± 0.84	1.06 ± 0.32
	876	194	0.896	111.9 ± 7.7	0.860 ± 0.010	0.811 ± 0.109	14.3 ± 1.01	2.19 ± 0.29

Table 3.1 (continued) CXTFIT Parameters for Columns D-F.

		1st Moment Model		CXTFIT Parameters			Derived Parameters	
	Operation Time [d]	v [cm/d]	$s_{tracer}(t)$ [-]	D_m [cm^2/d]	β [–]	ω [–]	% Immobile Water = 100×(1–β) [%]	k_{mt} [1/d]
Column D	5	210	0.873	18.6 ± 0.7	0.999 ± 0.022	51.0 ± 60.0	0.10 ± 2.2	137 ± 162
	92	255	0.719	43 ± 2.0	0.968 ± 0.002	0.064 ± 0.021	3.19 ± 0.16	0.17 ± 0.06
	155	249	0.737	38.2 ± 2.0	0.957 ± 0.002	0.114 ± 0.025	4.28 ± 0.23	0.31 ± 0.07
	232	247	0.743	49.0 ± 1.7	0.965 ± 0.002	0.063 ± 0.019	3.50 ± 0.16	0.17 ± 0.05
	349	248	0.740	58.5 ± 1.6	0.962 ± 0.002	0.061 ± 0.015	3.83 ± 0.15	0.17 ± 0.04
	452	244	0.752	71.7 ± 2.0	0.964 ± 0.002	0.097 ± 0.017	3.60 ± 0.19	0.26 ± 0.05
	537	231	0.794	65.2 ± 2.5	0.958 ± 0.002	0.123 ± 0.027	4.20 ± 0.20	0.33 ± 0.07
	762	243	0.755	95.5 ± 4.0	0.891 ± 0.004	0.411 ± 0.041	10.9 ± 0.40	1.11 ± 0.01
	877	252	0.728	177.2 ± 9.2	0.875 ± 0.007	0.447 ± 0.060	12.5 ± 0.69	1.21 ± 0.16
Column E	5	207	0.865	20.5 ± 0.8	0.999 ± 0.011	57.9 ± 34.9	0.10 ± 0.07	152 ± 92
	93	253	0.708	50.3 ± 1.1	0.963 ± 0.001	0.078 ± 0.013	3.71 ± 0.10	0.20 ± 0.03
	156	248	0.722	42.8 ± 1.8	0.962 ± 0.002	0.075 ± 0.025	3.77 ± 0.20	0.20 ± 0.07
	233	216	0.829	29.8 ± 3.4	0.945 ± 0.007	0.410 ± 0.132	5.53 ± 0.68	1.08 ± 0.35
	350	223	0.803	31.1 ± 1.9	0.962 ± 0.003	0.155 ± 0.047	3.73 ± 0.30	0.41 ± 0.12
	453	217	0.825	30.7 ± 0.9	0.971 ± 0.001	0.053 ± 0.017	2.88 ± 0.12	0.14 ± 0.04
	552	216	0.829	24.6 ± 0.8	0.974 ± 0.001	0.044 ± 0.017	2.62 ± 0.11	0.12 ± 0.04
	758	194	0.923	28.7 ± 1.5	0.918 ± 0.003	0.498 ± 0.051	8.16 ± 0.29	1.31 ± 0.13
	878	191	0.936	27.7 ± 0.88	0.962 ± 0.002	0.143 ± 0.024	3.77 ± 0.15	0.39 ± 0.06
Column F	6	194	0.883	17.3 ± 0.5	0.999 ± 0.010	57.6 ± 34.7	0.10 ± 1.0	145 ± 87
	93	218	0.786	49.6 ± 3.1	0.967 ± 0.003	0.000 ± 0.000	3.27 ± 0.33	0.00 ± 0.00
	157	217	0.79	43.2 ± 3.3	0.960 ± 0.004	0.155 ± 0.062	4.04 ± 0.44	0.39 ± 0.16
	234	208	0.824	65.0 ± 5.5	0.927 ± 0.007	0.315 ± 0.087	7.34 ± 0.71	0.79 ± 0.22
	351	221	0.775	44.8 ± 3.3	0.927 ± 0.005	0.368 ± 0.069	7.33 ± 0.46	0.93 ± 0.17
	453	227	0.755	62.9 ± 2.3	0.911 ± 0.002	0.305 ± 0.029	8.95 ± 0.24	0.77 ± 0.07
	554	228	0.752	111 ± 10	0.933 ± 0.005	0.160 ± 0.043	6.75 ± 0.49	0.40 ± 0.11
	757	191	0.897	39.1 ± 2.3	0.876 ± 0.004	0.700 ± 0.058	12.4 ± 0.40	1.76 ± 0.14
	878	187	0.914	44.2 ± 2.0	0.897 ± 0.003	0.466 ± 0.041	10.3 ± 0.30	1.26 ± 0.11

would be accompanied by an increase in the column's volumetric water content and a corresponding decrease in the mean pore water velocity. Such effects are discussed below in the context of time-varying estimates of "normalized water filled porosity" within the column.

Dual-region Model Parameter Estimates

The calculated mean porewater velocities (v) and the total collected tracer radioactivity ($\sum {}^3H_2O$) were used as inputs for simulation exercises designed to estimate the other parameters of the dual-region model (D_m, β, ω) by fitting model simulations to the tracer data. To reflect the possible influence of immobilized water on transport conditions, a dual-region model was used in place of the standard single-region advection-dispersion model (van Genuchten and Parker, 1984) under conditions where the fits obtained with the single-region model were poor (Fig. 3.2). Only for the first set of tracer tests (collected within the first week) were the single-region model fits satisfactory. For this set of tracer tests, both models fit the data equally well for all columns, reflecting the fact that few solutes had precipitated within the porous media and immobile water zones had yet to develop.

The model estimates of the mobile phase dispersion coefficient (D_m), mobile phase porosity (β), and the normalized first-order mass transfer coefficient (ω) are shown in Table 3.1. Estimates for the mobile zone dispersivities (α_m [cm]) of each of the columns were determined by dividing the dispersion coefficients obtained from the dual-region model by the calculated mobile phase porewater velocities (v_m; Bear, 1972). These α_m values are plotted as a function of column operation time in Fig. 3.3. For most columns the dispersivity values increased significantly over time, despite the fact that mass transfer-related sources of spreading were accounted for separately. If we assume that the hydrodynamic dispersivity of the mobile zone

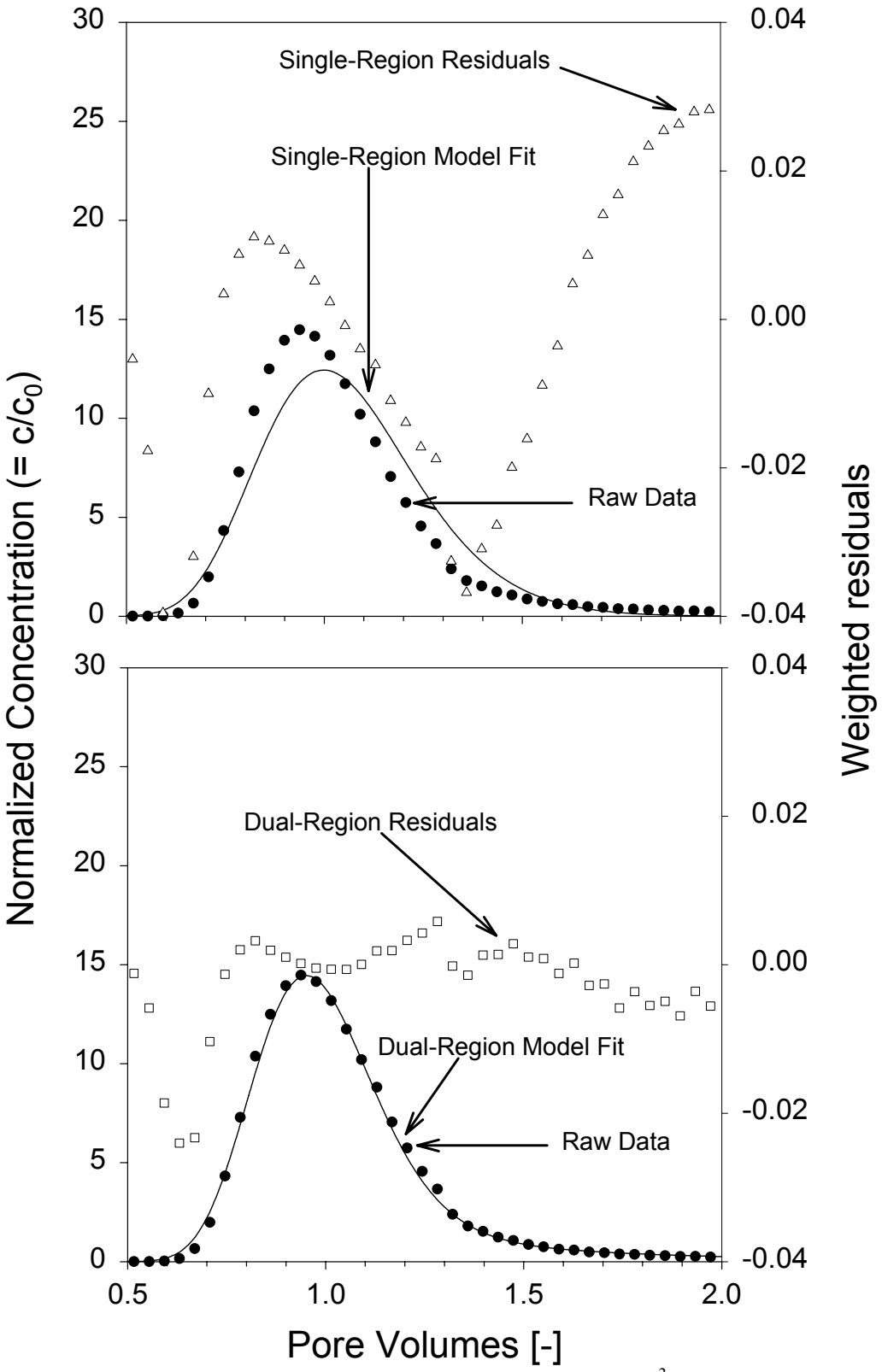

Figure 3.2 Comparison of single- and dual-region model fits for ^3H_2O test on Column F (day 554). Residuals from CXTFIT are weighted by the error associated with scintillation counting (weighted residual = $[(C_{observed} - C_{fitted})/\text{scintillation error}]$).

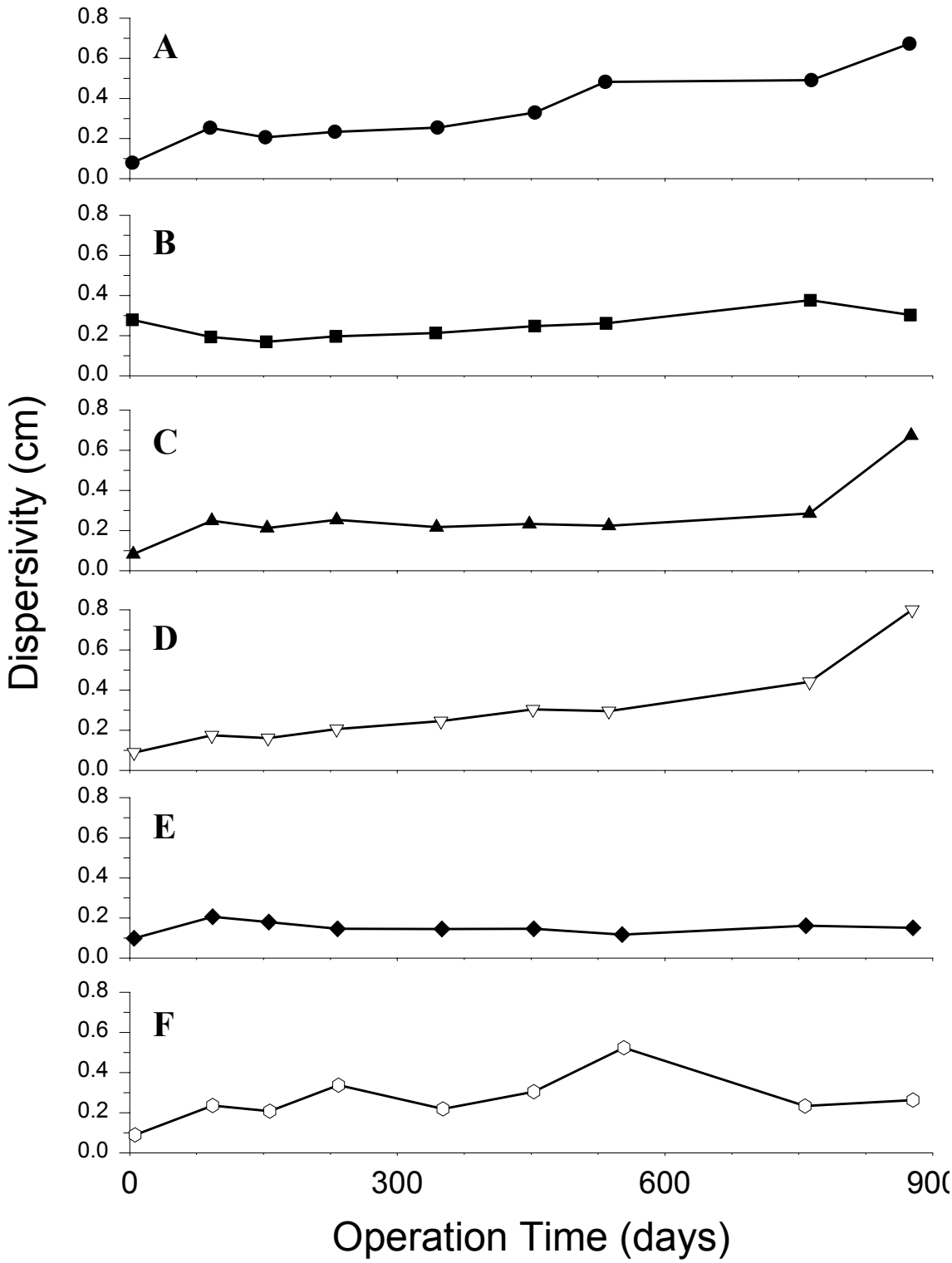

Figure 3.3 Calculated dispersivities (α_m) for columns A-F. Dispersivity = D_m/v_m.

reflects the geometry of the water-filled pore space (Bear, 1979), then such an increase may be indicative of changes in mobile-zone pore size distributions over the course of column operation. It is therefore an expected result of precipitation and gas pocket formation.

Columns A, C, and D exhibited the largest increases in dispersivity, going from an average of 0.083 ± 0.006 cm, to an average of 0.716 ± 0.086 cm. For columns B, E, and F the changes were more modest, and statistically insignificant, for these columns the average change in α_m was only 0.083 ± 0.090 cm. Interestingly, the columns with the largest changes in α_m (A, C, and D) also displayed the largest increases in immobile zone porosity, as discussed subsequently. These columns were fed primarily with a 2 mM $NaHCO_3$ solution that either continually or only periodically contained TCE. The columns with smaller changes in dispersivity were continually fed additional species (10 mM Cl^- for column B), were fed higher bicarbonate doses (20 mM $NaHCO_3$ for column E), or were fed NACs over substantial periods of operation (column F and column E at later time).

Table 3.1 provides the derived values for the immobile water content [%] of the column ($=100\times\theta_{im}/\theta_w = 100\times(1 - \beta)$, where $\theta_{im}=\theta_w-\theta_m$) and the first-order mass transfer coefficient for transport between the mobile and immobile regions ($k_{mt} = \omega\theta_w v/L$) . The model fits at the time of column startup indicate a statistically insignificant amount of immobile water. By approximately 90 days, however, model fits suggest an average of 3.4 ± 1.4% immobile water in columns A-F. After 90 days, with only a few exceptions, the immobile water content of each column continued to increase. Considering 54 comparisons among consecutive tracer tests in the columns (Table 3.1), there are only seven periods where θ_{im} did not demonstrate an increase. We believe that these periods may be associated with the previously described increases in column pressure and the possible dissolution of gas phases, which could conceivably improve

access to some previously immobile regions. Apart from these exceptions, the otherwise steady increases in immobile water content over time are consistent with the concept that increasing mineral precipitate mass and gas volume are leading to the creation of preferential flow paths and a corresponding larger volume of apparently immobile water.

For the initial set of tracer tests, the estimated ω values were all greater than 50. Values of ω larger than 10 indicate quasi-equilibrium conditions exist between the mobile and the immobile zones, such that single- and dual-region model predictions coincide (van Genuchten and Wierenga, 1976). In fact, these early time results have negligible sensitivity to ω (and therefore k_{mt}) and confirm that the dual-region model is unnecessary. These results were well fit by a single-region model with a virtually identical estimate for the dispersion coefficient (i.e., $D \approx D_{\mathrm{m}}$).

When nonequilibrium is significant (i.e., for the later tracer tests), the single- and dual-region model results no longer coincide, and dual-region modeling estimates of D_{m} are dramatically reduced relative to "effective" dispersion coefficients estimated using only a single-region model (data not shown). For these later time conditions, the use of the dual-region model is justified and our estimated values of β and ω are presumed to be indicative of mass transport to immobile regions. Estimates for k_{mt} suggest that mass transfer rates were within an order of magnitude in all columns, with somewhat more consistent values obtained when the immobile water fraction was above 6%. Values of ω for these cases tended to range between 0.3 and 0.8, corresponding to k_{mt} values between 0.7 and 1.8 day^{-1}. Aside from the very first tracer studies, higher fractions of mobile water ($\beta > 0.95$) tend to be associated with lower values of k_{mt}, most often under 0.3 day^{-1}.

Effluent Port Sampling of Columns A-F: Estimates of Water Volume and Precipitate Mass

Calculation of Column Normalized Water-Filled Porosity

In this study, we directly estimated τ using tracer studies with tritiated water. Because such studies disrupt column operation and are labor intensive, we also assessed the utility of a simpler technique to estimate τ from equation (3.8) by inferring θ_w from periodic measurements of column mass. This is a useful approach if alterations in θ_w primarily stem from accumulation of gas pockets but is inaccurate when a significant change in column mass occurs through precipitation or dissolution of solids within the porous media. In this latter case, the gravimetric measurements provide supplementary information regarding combined weight changes due to both gas and solid volume changes. A comparison of data obtained from gravimetric measurements to water volume estimates computed from tritiated water tracer tests can therefore be used to obtain additional information pertaining to the processes responsible for variations in θ_w.

For the purposes of our discussion, we define a normalized water-filled porosity (*s(t)* [-]) as the ratio of the volumetric water content (θ_w [-]) to the total *initial* porosity of a column at startup ($\theta_{tot,initial}$ [-]):

$$s(t) \equiv \frac{\theta_w}{\theta_{tot,initial}} \equiv \frac{V_{H_2O}(t)/V_{column}}{V_{V,initial}/V_{column}} \tag{3.10}$$

s(t) is defined with respect to $\theta_{tot,initial}$ to avoid complications that result from fluctuations in the total pore volume over time, owing to solid precipitation within the porous media. Using this definition, the only parameter required to calculate *s(t)* is the volume of water present within the column at any point in time.

The volume of water within the columns, $V_{H_2O}(t)$, was estimated via two methods. First, we utilized the value of τ obtained from the first moment analyses:

$$V_{H_2O}(t) = Q \times \tau \tag{3.11}$$

Normalized water-filled porosity values obtained using equations (3.10) and (3.11) are referred to hereafter as $s_{tracer}(t)$. Estimated values for the six columns are tabulated in Table 3.1 and are depicted by the open triangles in Fig. 3.4.

An alternative method to calculate $V_{H_2O}(t)$ is based on the mass of water in the column ($m_{H_2O}(t)$ [g]):

$$V_{H_2O}(t) \equiv \frac{m_{H_2O}(t)}{\rho_{H_2O}} \tag{3.12}$$

where ρ_{H_2O} [g/mL] is the density of water. For a given column, $m_{H_2O}(t)$ is related to the gravimetric measurement of the total column mass ($m_{total}(t)$ [g]):

$$m_{H_2O}(t) = m_{total}(t) - \left[m_{Fe}(t) + m_{precip-solutes}(t) + m_{gas}(t) + m_{column} \right] \tag{3.13}$$

The mass of gas ($m_{gas}(t)$ [g]) in the columns was negligibly small, and the mass of column material (m_{column} [g]) was known and remained constant. The term $m_{Fe}(t)$ [g] can also be assumed constant (and equal to the initial mass of granular iron) if oxidized iron species reprecipitate within the column. For the present column studies, the soluble iron content of the column effluent was consistently below the detection limit of the Ferrozine technique (0.286 μM; Vikesland, 1998). If soluble iron occurred consistently at this level, then a maximum of 0.010 g, or < 0.002% of the initial iron mass, could have been lost by day 900 without detection. The term $m_{precip\text{-}solutes}(t)$ [g] represents the mass of precipitated material within the column that is attributable to elements other than iron. If this value is negligible relative to the other variables, the interpretation of the gravimetric column measurements is straightforward:

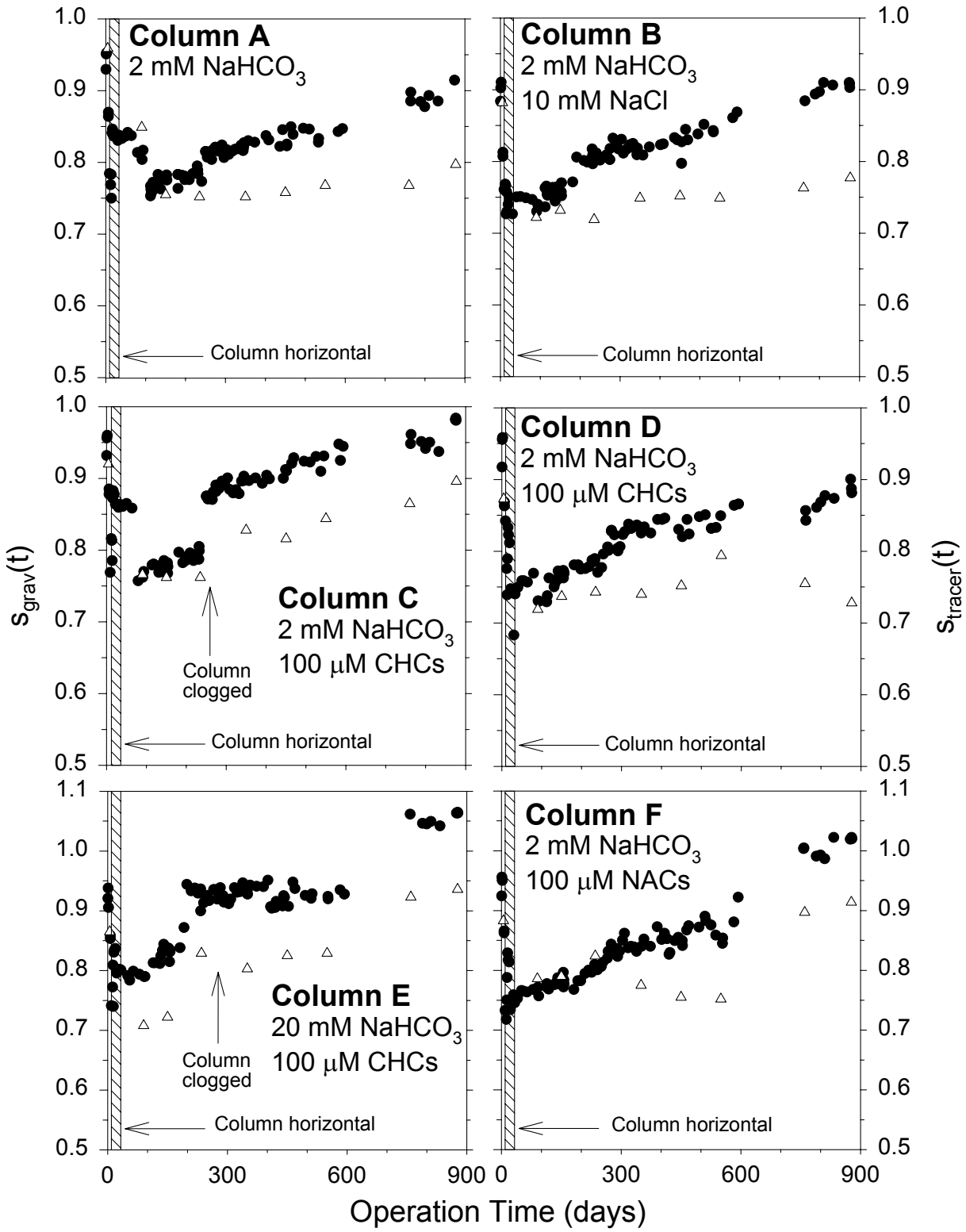

Figure 3.4 Comparison of normalized water filled porosity estimates for Columns A-F using gravimetric data ($s_{grav}(t)$) to those determined using the ^3H_2O tracer data ($s_{tracer}(t)$). △ = $s_{tracer}(t)$ and • = $s_{grav}(t)$. Note that $s_{grav}(t)$ estimates assume no change of solid mass within the column. See equations (3.13) and (3.14).

$$m_{H_2O,grav}(t) = m_{total}(t) - \left[m_{Fe}(t=0) + m_{column} \right] \tag{3.14}$$

If significant precipitate formation occurs, however, the value of $m_{H_2O}(t)$ estimated by equation (3.14) will differ from the true value. Estimates of normalized water-filled porosity obtained using equations (3.10), (3.12), and (3.14) are subsequently referred to as $s_{grav}(t)$. Calculated values for the various columns are depicted as solid circles in Fig. 3.4.

Values of $s_{grav}(t)$ dramatically decreased during the first 10 days of column operation, presumably due to a combination of H_2 gas production and the potential accumulation of N_2 gas (which may have evolved from the N_2-purged synthetic groundwater). Following this initial sharp decline, the $s_{grav}(t)$ values progressively increased under uninterrupted flow conditions. The slow increase in $s_{grav}(t)$ could be a result of two simultaneous processes: 1) increasing volumetric water content (θ_w) over time owing to decreased gas volume in the columns; and 2) an increasing mass of solids in the column as the result of solute precipitation. To independently assess the role of these two factors, the $s_{grav}(t)$ values were compared to the $s_{tracer}(t)$ values obtained from the tracer studies. Because the $s_{tracer}(t)$ values are based on the mean τ, they should accurately reflect the water volume in the column, irrespective of precipitate mass.

With the exception of column E, the $s_{tracer}(t)$ and the $s_{grav}(t)$ values agreed fairly well for approximately the first 100-200 days of column operation (Fig. 3.4). For column E, the normalized water filled porosity estimates agreed only for the first tracer test. After the initial period of agreement, the two estimates diverge for all columns, with the $s_{tracer}(t)$ values being consistently lower than the $s_{grav}(t)$ values. The differences in the two estimates for the later tracer tests suggest that solutes have precipitated within the porous media, and that the $m_{H_2O,grav}(t)$ value calculated using equation (3.14) differs from $m_{H_2O}(t)$ because of its neglect of $m_{precip\text{-}solutes}(t)$. Accordingly, the more rapid deviation for column E likely reflects an earlier buildup of solids in

this column. This seems reasonable in light of the ten-fold higher bicarbonate concentration in the feed to column E (Table 2.4).

Although precipitate formation is hypothesized to dominate the observed changes in $s_{grav}(t)$, changes in $s_{tracer}(t)$ reveal that gas-related changes in θ_w also occurred. Both $s_{tracer}(t)$ and $s_{grav}(t)$ increased when the outlet to columns C and E clogged around day 200 (Fig. 3.4). As discussed previously, increases in θ_w could result from gas absorption by the water in the column during periods of enhanced pore water pressure that accompany effluent line clogging. Despite simultaneous increases of $s_{grav}(t)$ and $s_{tracer}(t)$ during these periods, the two values generally diverge as the columns age. We interpret the increasing difference as evidence of precipitate formation within the columns. Aside from the effects of precipitates, both measures are estimates of total water-filled porosity, so long as any immobilized water is diffusively accessible by solutes. An additional source of difference may occur, however, if some pore water is either completely occluded from solute diffusion, or is accessed too slowly to be detected in breakthrough curves.

Comparison of the $s_{tracer}(t)$ and $s_{grav}(t)$ values allows us to make several conclusions regarding the relative merits of these two estimates. Theoretical considerations suggest that the tracer experiments should provide a more accurate means of assessing $s_{tracer}(t)$ and thereby θ_w under all conditions. The initial similarity of the $s_{tracer}(t)$ and $s_{grav}(t)$ values indicates that the gravimetric determinations provide a useful estimate of water-filled pore volume during the early stages of column operation (i.e., before significant accumulation of precipitates). In fact for these early stages, the gravimetric measures are indispensable since they allow for the collection of considerably more data than is possible using the time-consuming tracer technique alone. Without the gravimetric data it would have been difficult to discern the rapid declines in water

filled porosity that were observed. For the later stages of column operation, however, gravimetric estimates of *s(t)* are highly inaccurate. Because the simultaneous processes of gas evolution, gas absorption, and solute precipitation all occur within the granular iron media, tracer tests are needed to obtain direct estimates of τ. Nevertheless, the gravimetric estimates of *s(t)* provide a useful means to assess changes in precipitated solid mass.

Estimation of Precipitate Mass and Volume

An independent measurement of $m_{H_2O}(t)$ can be obtained by dividing the $V_{H_2O}(t)$ value determined from the tracer studies by ρ_{H_2O}. The term $m_{\text{precip-solutes}}(t)$ can then be computed by substituting $m_{H_2O}(t)$ into equation (3.13) and rearranging:

$$m_{precip-solutes}(t) = m_{total}(t) - m_{H_2O}(t) - \left[m_{Fe}(t) + m_{gas}(t) + m_{column} \right] \tag{3.15}$$

The results of such calculations for our columns A-F are depicted in Fig. 3.5.

In general, the total precipitated solute mass continually increased over time for all six columns. Given the column averaged nature of the results and the scatter in the data it is difficult to detect any trends that might have resulted from the differences in the feedwater composition. There is a tendency for precipitated solids to initially accumulate more rapidly in column E (fed high bicarbonate), but by day 500, solids are accumulating at close to the same rate in all columns. Although the exact nature of the precipitated solutes is presently unknown, we hypothesize (based on our known feed-water composition) that they should consist primarily of carbonate and hydroxide mineral phases such as siderite and $Fe(OH)_2$ (s).

If we know the chemical composition and density of the precipitated solids, we can use the estimated mass of precipitated solutes to calculate the total solid mass and volume as a function of time in each column. Based upon equilibrium phase diagrams for each of these

species and our given aqueous conditions, siderite should be the dominant precipitate; we note, however, that results from XRD and spectroscopic analyses conducted to date (as discussed in Chapter 5) have failed to confirm the presence of this mineral phase. Nonetheless, for present purposes we proceed under an assumption of 100% siderite when converting solute mass to solid mass and volume, with the understanding that solids of different chemical composition and density might have correspondingly different volumetric implications.

The results shown in Fig. 3.5 suggest that on average 25 g of previously dissolved material was retained within each of the columns by day 900. If we assume that all of the "lost" solutes were carbonate (i.e., assuming no hydr(oxide) precipitates, no significant sodium or calcium precipitation, and recognizing that any precipitated iron must be derived from other locations within the column), this estimate would correspond to roughly 3.2% (column E) or 32% (other columns) of the total amount of carbonate fed during this period. If we further assume 100% siderite for the solid phase (see prior discussion), these 25 g would correspond to roughly 48 g of new solids which, at the solid density of siderite (3.96 g/mL), would occupy 12.2 mL of pore volume.

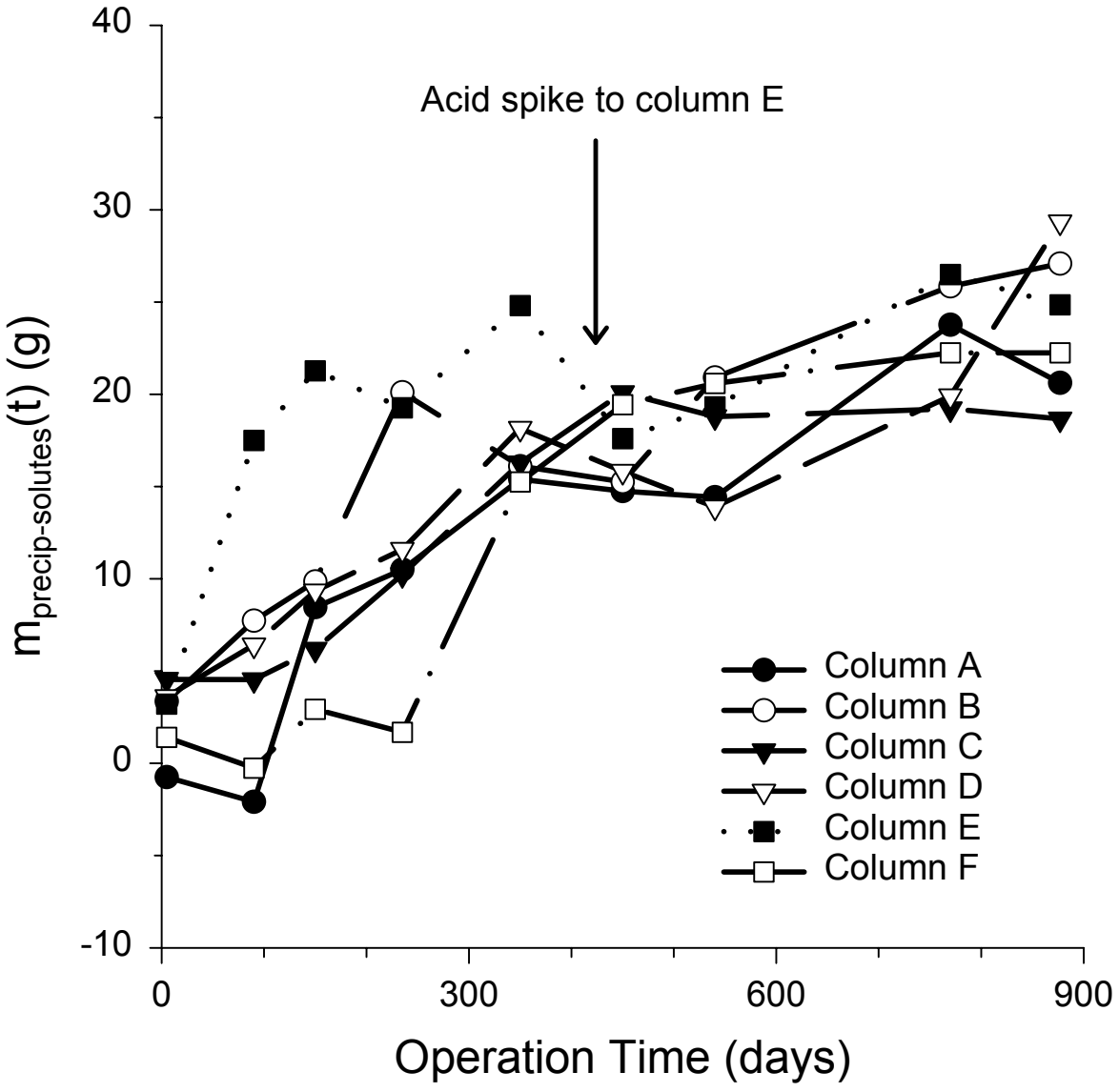

Figure 3.5 Calculated mass of precipitated solute materials as a function of column age. As noted, 5 mL of concentrated HCl was added to column E on day 400. This led to the dissolution of some of the material within this column.

After correcting for the volume associated with the 23 g of iron lost from the granular iron particles ($\rho_{granular\ iron}$ = 7.00 g/mL), the total decrease in the pore volume of the column should be 8.9 mL. This amounts to approximately 6% of the initial pore volume ($V_{V,initial}$) for each of the six columns by day 900. This loss of pore volume should increase the pore water velocity by ~ 6%, a value that is at the low end of the experimentally observed increases of 6-25% (Table 3.1). The disparity between the two values suggests that gas accumulation within the columns may play a significant role in altering the pore water velocity. However, because we were unable to directly measure changes in the gas volume within our columns and because we do not have evidence that definitively shows siderite is the predominant precipitate in our columns, this conclusion should be viewed as preliminary. Additional studies are needed to fully account for the relative importance of gas accumulation versus precipitate formation.

Port Sampling of Columns G-J

The ^3H_2O breakthrough curves obtained from effluent samples reflect changes to the porous media that occur throughout the entire column length. As such, they do not provide any information about spatial changes in the HRTD that may result from preferential solute deposition or gas accumulation near the column inlet. To assess whether such variability exists, an extensive study of the transport properties of columns G-J was conducted. In this study, breakthrough curves were obtained for multiple points along the column length. By spatially distributing these sampling points over the length of the columns, it was possible to examine how the HRTDs developed with distance. In addition, by making such evaluations at different times (spread over the 475 day column operating period) it was also possible to obtain temporal information about HRTD variability at a given sampling port. As noted in Table 3.2, four sampling periods were employed for each column.

Representative sets of breakthrough curves obtained for each column are depicted in Figs. 3.6-3.9. A qualitative examination of these curves indicates that each ^3H_2O pulse broadened as it traveled through the column. This was an anticipated result, in that pulse broadening with distance is a well known phenomena, even under conditions of uniform dispersivity (Fogler, 1999). Thus, quantitative interpretations are needed for a better understanding of spatial variations. From a strictly qualitative perspective, however, we do note some significant differences between the nature of the curves obtained for the four columns. In particular, the samples obtained from port 1 on columns G and J exhibited extremely sharp breakthrough curves. In contrast, for columns H and I the breakthrough curves at the same port were considerably broader. As discussed shortly, these differences are believed to be the result of differences in the proximal end precipitate mass, owing to differences in the geochemistry of the feedwater of the four columns.

To more carefully examine these and other spatial effects and to examine how they vary over time, the collected breakthrough curves were evaluated using the dual-region solute transport model. More specifically, we used data fitting algorithms to obtain values for the following parameters: v, D_m, β, and ω. In contrast to the previously described studies on columns A-F, where the pore water velocity was determined by moment analysis, the velocities for the port studies on columns G-J were determined as part of the CXTFIT fitting exercise. This step was taken in order to better quantify the error associated with each velocity value. The v, D_m, β, and ω values obtained from CXTFIT were then used to calculate the dispersivity (α_m), immobile

Table 3.2 Parameters obtained from CXTFIT dual region model for columns G-J. These tests were conducted using an ISCO high pressure syringe pump that precisely maintained a flow rate of 0.500 mL/min. Actual average flows in the columns over the full operation period were nominally at the same rate but exhibited some column to column and temporal fluctuation.

Column G		**CXTFIT Parameters**				**Derived Parameters**	
Operation Time [d]	Sample Port [#]	v [cm/d]	D_m [cm^2/d]	β [–]	ω [–]	% Immobile Water = 100× (1–β) [%]	k_{mt} [1/d]
54	1	378 ± 64.6	47.2 ± 15.5	0.714 ± 0.082	0.351 ± 0.320	28.6 ± 8.21	0.752 ± 0.685
55	5	211 ± 24	57.6 ± 6.95	0.991 ± 0.107	0.006 ± 0.032	0.90 ± 10.7	0.013 ± 0.070
55	7	191 ± 3.7	46.8 ± 14.2	0.998 ± 0.032	0.107 ± 21.3	0.18 ± 3.20	0.230 ± 45.7
56	10	194 ± 3.3	39.8 ± 4.31	0.999 ± 0.006	0.002 ± 0.069	0.10 ± 0.60	0.004 ± 0.145
29	13	166 ± 1.3	71.1 ± 8.76	0.999 ± 0.009	0.027 ± 1.72	0.10 ± 0.89	0.059 ± 3.692
134	1	326 ± 9.5	14.9 ± 1.77	0.658 ± 0.019	0.679 ± 0.073	34.3 ± 1.92	1.45 ± 0.161
134	5	254 ± 10	126 ± 7.7	0.999 ± 0.026	1.58 ± 22.2	0.10 ± 2.55	3.38 ± 47.6
136	7	208 ± 2.4	94.9 ± 2.71	0.999 ± 0.004	0.000 ± 0.012	0.10 ± 0.38	0.000 ± 0.026
130	10	196 ± 0.6	42.3 ± 2.72	0.956 ± 0.009	0.363 ± 0.153	4.42 ± 0.92	0.777 ± 0.328
129	13	167 ± 0.6	54.4 ± 2.26	0.999 ± 0.003	0.001 ± 0.024	0.10 ± 0.32	0.002 ± 0.050
305	1	804 ± 1.8	12.3 ± 0.66	0.899 ± 0.004	0.254 ± 0.028	10.1 ± 0.41	0.543 ± 0.060
301	5	186 ± 2.8	61.9 ± 4.55	0.943 ± 0.011	0.000 ± 0.031	5.70 ± 1.13	0.000 ± 0.066
302	7	186 ± 0.8	58.6 ± 3.49	0.933 ± 0.014	0.341 ± 0.139	6.70 ± 1.42	0.731 ± 0.298
246	10	196 ± 1.4	67.0 ± 14.8	0.930 ± 0.046	0.613 ± 0.688	7.00 ± 4.62	1.31 ± 1.472
250	13	162 ± 0.4	47.4 ± 1.01	0.988 ± 0.003	0.059 ± 0.028	1.20 ± 0.32	0.126 ± 0.060
461	1	738 ± 24.2	22.4 ± 2.24	0.894 ± 0.020	0.177 ± 0.075	10.6 ± 1.98	0.379 ± 0.161
428	5	167 ± 2.9	38.5 ± 1.46	0.848 ± 0.013	0.226 ± 0.034	15.2 ± 1.31	0.485 ± 0.072
462	7	152 ± 1.4	41.1 ± 2.41	0.959 ± 0.011	0.137 ± 0.093	4.08 ± 1.10	0.294 ± 0.200
429	10	153 ± 3.7	82.2 ± 6.67	0.996 ± 0.008	0.000 ± 0.034	0.42 ± 0.84	0.000 ± 0.073
413	13	154 ± 0.8	78.9 ± 4.14	0.999 ± 0.046	19.7 ± 27.4	0.10 ± 4.58	42.2 ± 58.6

Table 3.2 Continued.

Column H		CXTFIT Parameters				Derived Parameters	
Operation Time [d]	Sample Port [#]	v [cm/d]	D_m [cm^2/d]	β [–]	ω [–]	% Immobile Water = 100× (1–β) [%]	k_{mt} [1/d]
69	1	257 ± 11.1	17.0 ± 2.66	0.730 ± 0.038	0.466 ± 0.147	27.0 ± 3.77	0.999 ± 0.315
70	5	203 ± 6.3	21.2 ± 9.64	0.655 ± 0.057	1.61 ± 0.500	34.5 ± 5.74	3.46 ± 1.07
71	7	184 ± 0.6	14.8 ± 2.8	0.747 ± 0.017	2.41 ± 0.272	25.3 ± 1.73	5.17 ± 0.583
72	10	202 ± 0.8	26.6 ± 7.26	0.863 ± 0.031	1.81 ± 0.644	13.8 ± 3.06	3.87 ± 1.38
69	13	178 ± 0.3	29.4 ± 7.15	0.872 ± 0.031	2.24 ± 0.812	12.8 ± 3.13	4.79 ± 1.74
	1	Improper injection; extremely low ^3H_2O recovery					
145	5	178 ± 4.6	71.8 ± 13.0	0.948 ± 0.030	0.000 ± 0.078	5.19 ± 3.03	0.000 ± 0.168
146	7	183 ± 5.5	49.6 ± 2.36	0.999 ± 0.005	0.000 ± 0.022	0.11 ± 0.47	0.000 ± 0.047
145	10	168 ± 21.1	53.6 ± 3.37	0.999 ± 0.032	1.95 ± 18.9	0.10 ± 3.21	4.18 ± 40.4
147	13	169 ± 1.6	56.4 ± 14.3	0.977 ± 0.090	0.437 ± 2.97	2.30 ± 8.96	0.936 ± 6.36
303	1	157 ± 8	15.6 ± 6.13	0.410 ± 0.173	6.37 ± 3.18	59.0 ± 17.3	13.6 ± 6.81
300	5	165 ± 2.4	9.96 ± 5.47	0.765 ± 0.112	2.92 ± 2.03	23.5 ± 11.2	6.27 ± 4.34
246	7	140 ± 8	111 ± 31.0	0.958 ± 0.043	0.000 ± 0.119	4.21 ± 4.25	0.000 ± 0.254
280	10	180 ± 6.8	38.7 ± 5.17	0.999 ± 0.043	0.005 ± 0.126	0.10 ± 4.25	0.011 ± 0.270
287	13	170 ± 0.2	34.5 ± 3.12	0.931 ± 0.014	1.10 ± 0.358	6.91 ± 1.42	2.35 ± 0.767
460	1	146 ± 3.7	11.9 ± 2.56	0.582 ± 0.04	1.13 ± 0.217	41.8 ± 4.30	2.42 ± 0.465
427	5	153 ± 0.2	13.9 ± 0.38	0.949 ± 0.01	0.297 ± 0.061	5.14 ± 0.54	0.637 ± 0.131
449	7	142 ± 1.6	40.5 ± 1.64	0.999 ± 0.00	0.000 ± 0.018	0.11 ± 0.41	0.000 ± 0.038
443	10	160 ± 17.2	95.4 ± 9.43	0.997 ± 0.01	0.000 ± 0.041	0.26 ± 1.12	0.000 ± 0.088
412	13	166 ± 2.1	62.6 ± 7.77	0.998 ± 0.04	31.8 ± 75.0	0.24 ± 4.02	68.1 ± 161

Table 3.2 Continued.

Column I		CXTFIT Parameters				Derived Parameters	
Operation Time [d]	Sample Port [#]	v [cm/d]	D_m [cm^2/d]	β [–]	ω [–]	% Immobile Water = 100× (1–β) [%]	k_{mt} [1/d]
75	1	234 ± 3.5	6.10 ± 0.557	0.675 ± 0.013	1.01 ± 0.093	32.5 ± 1.30	2.14 ± 0.197
76	5	218 ± 6.5	31.1 ± 14.2	0.781 ± 0.091	1.08 ± 0.835	21.9 ± 9.11	2.29 ± 1.77
76	7	197 ± 0.9	30.1 ± 1.45	0.919 ± 0.006	0.397 ± 0.074	8.08 ± 0.64	0.84 ± 0.157
	10	Not sampled					
75	13	172 ± 0.6	47.5 ± 2.44	0.999 ± 0.036	2.04 ± 24.6	0.10 ± 3.57	4.33 ± 52.2
187	1	171 ± 2	17.2 ± 1.03	0.579 ± 0.012	0.808 ± 0.053	42.1 ± 1.18	1.72 ± 0.113
164	5	227 ± 1.6	31.5 ± 2.65	0.828 ± 0.016	0.740 ± 0.137	17.3 ± 1.59	1.57 ± 0.291
186	7	184 ± 0.8	26.5 ± 2.18	0.830 ± 0.010	1.09 ± 0.133	17.0 ± 1.04	2.32 ± 0.283
177	10	194 ± 0.8	23.4 ± 5.6	0.859 ± 0.024	1.79 ± 0.519	14.1 ± 2.43	3.79 ± 1.10
164	13	162 ± 0.3	41.5 ± 1.51	0.962 ± 0.005	0.320 ± 0.080	3.82 ± 0.47	0.68 ± 0.169
304	1	132 ± 3.8	16.6 ± 1.89	0.421 ± 0.017	1.03 ± 0.075	58.0 ± 1.74	2.19 ± 0.160
302	5	196 ± 5.9	49.5 ± 14.3	0.958 ± 0.119	0.209 ± 1.11	4.24 ± 11.9	0.44 ± 2.35
305	7	173 ± 0.5	26.1 ± 2.37	0.863 ± 0.015	1.08 ± 0.203	13.7 ± 1.46	2.29 ± 0.432
247	10	191 ± 0.7	30.9 ± 5.97	0.882 ± 0.026	1.46 ± 0.526	11.8 ± 2.59	3.10 ± 1.12
249	13	163 ± 0.2	24.6 ± 3.44	0.875 ± 0.017	2.15 ± 0.430	12.5 ± 1.65	4.57 ± 0.913
446	1	124 ± 2.3	3.40 ± 0.228	0.380 ± 0.007	1.34 ± 0.037	62.0 ± 0.73	2.85 ± 0.079
426	5	203 ± 1.3	30.5 ± 0.77	0.871 ± 0.005	0.315 ± 0.030	12.9 ± 0.54	0.67 ± 0.063
447	7	152 ± 0.9	15.1 ± 3.41	0.805 ± 0.027	1.84 ± 0.424	19.5 ± 2.68	3.91 ± 0.900
446	10	143 ± 0.8	17.6 ± 2.31	0.841 ± 0.012	1.25 ± 0.191	15.9 ± 1.18	2.65 ± 0.405
409	13	161 ± 0.4	29.3 ± 2.44	0.863 ± 0.008	1.42 ± 0.150	13.7 ± 0.78	3.02 ± 0.318

Table 3.2 Continued.

Column J		CXTFIT Parameters				Derived Parameters	
Operation Time [d]	Sample Port [#]	v [cm/d]	D_m [cm^2/d]	β [–]	ω [–]	% Immobile Water = 100× (1–β) [%]	k_{mt} [1/d]
113	1	121 ± 5.2	22.1 ± 7.58	0.634 ± 0.109	1.17 ± 0.429	36.6 ± 10.9	2.53 ± 0.930
114	5	210 ± 3.0	17.2 ± 11.9	0.559 ± 0.079	3.24 ± 0.726	44.1 ± 7.88	7.03 ± 1.57
113	7	202 ± 1.6	26.5 ± 2.90	0.854 ± 0.012	0.810 ± 0.153	14.6 ± 1.24	1.76 ± 0.33
115	10	198 ± 0.8	16.4 ± 8.72	0.869 ± 0.053	2.46 ± 1.50	13.2 ± 5.31	5.34 ± 3.24
116	13	159 ± 3.5	82.9 ± 3.72	0.999 ± 0.004	0.000 ± 0.019	0.100 ± 0.390	0.00 ± 0.042
195	1	466 ± 44.7	9.30 ± 1.80	0.775 ± 0.065	0.196 ± 0.033	22.5 ± 6.46	0.425 ± 0.072
194	5	299 ± 4.8	116 ± 12.4	0.707 ± 0.025	0.867 ± 0.149	29.3 ± 2.53	1.88 ± 0.323
194	7	226 ± 2.6	42.8 ± 4.35	0.770 ± 0.012	0.904 ± 0.107	23.0 ± 1.17	1.96 ± 0.232
193	10	214 ± 1.5	54.2 ± 4.45	0.920 ± 0.010	0.468 ± 0.129	7.96 ± 1.00	1.01 ± 0.280
188	13	155 ± 3.3	80.6 ± 3.45	0.999 ± 0.051	2.79 ± 14.6	0.100 ± 5.12	6.04 ± 31.6
304	1	659 ± 6.4	31.3 ± 0.94	0.910 ± 0.006	0.113 ± 0.019	8.96 ± 0.570	0.245 ± 0.041
301	5	228 ± 7.2	78.7 ± 22.9	0.674 ± 0.074	1.24 ± 0.481	32.6 ± 7.44	2.70 ± 1.04
303	7	205 ± 3.2	84.3 ± 9.45	0.732 ± 0.018	0.818 ± 0.125	26.8 ± 1.80	1.77 ± 0.270
282	10	197 ± 1.4	45.4 ± 14.2	0.803 ± 0.047	2.09 ± 0.796	19.7 ± 4.72	4.53 ± 1.73
305	13	159 ± 0.3	91.3 ± 3.60	0.999 ± 0.043	15.5 ± 15.1	0.100 ± 4.34	33.67 ± 32.7
449	1	678 ± 9.2	9.47 ± 1.57	0.848 ± 0.020	0.973 ± 0.217	15.2 ± 1.95	2.11 ± 0.471
420	5	253 ± 7.1	350 ± 43.4	0.600 ± 0.053	2.56 ± 0.419	40.0 ± 5.28	5.54 ± 0.908
447	7	217 ± 6.3	88.8 ± 6.37	0.687 ± 0.018	0.469 ± 0.041	31.3 ± 1.83	1.02 ± 0.089
449	10	203 ± 1.3	66.5 ± 3.32	0.847 ± 0.006	0.586 ± 0.054	15.3 ± 0.59	1.27 ± 0.118
405	13	162 ± 0.6	78.1 ± 5.50	0.929 ± 0.013	0.487 ± 0.169	7.08 ± 1.26	1.06 ± 0.366

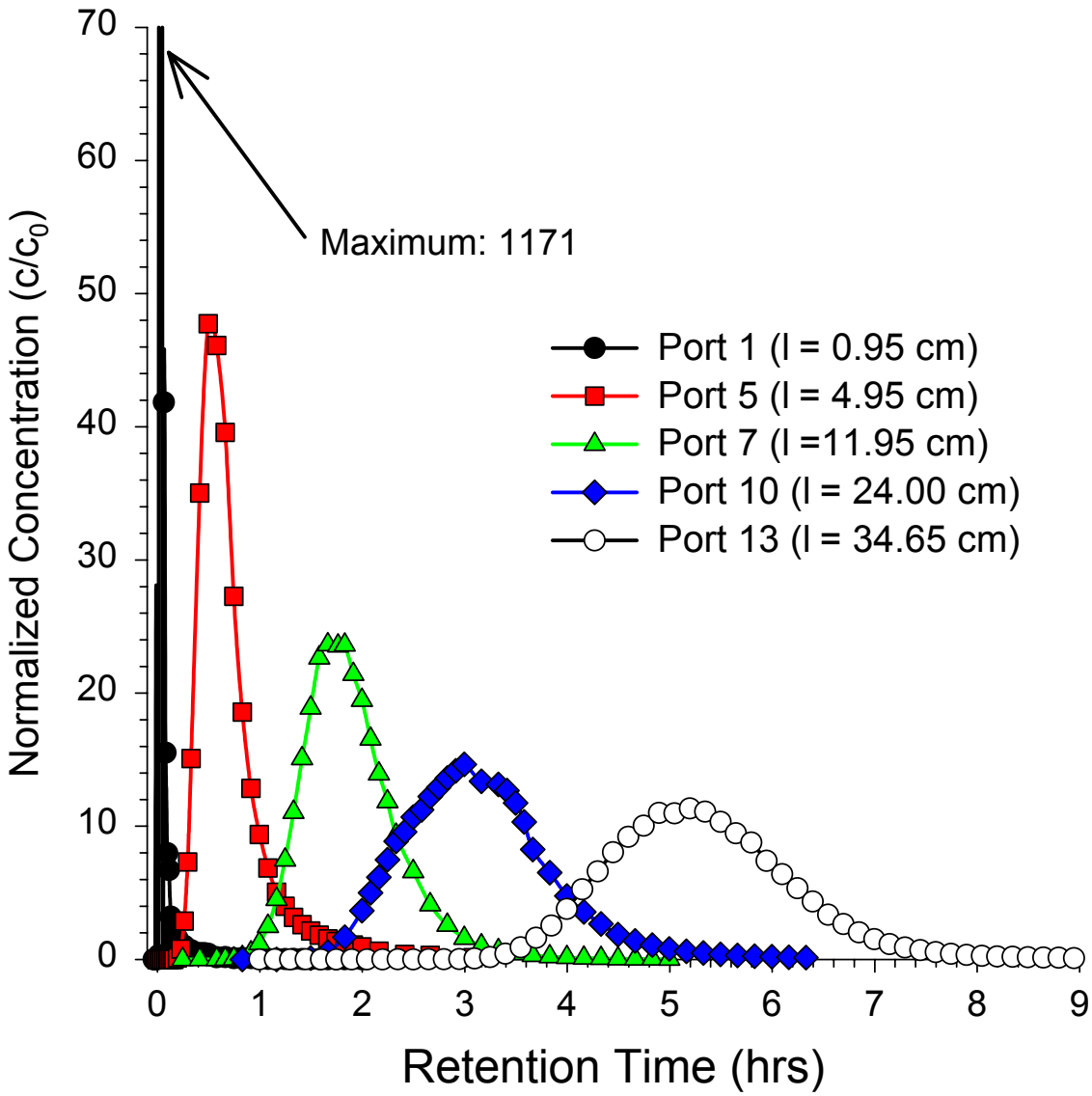

Figure 3.6 ^3H_2O breakthrough curves obtained by sampling from five different ports along the length of column G. The feed to this column was a saturated $CaCO_3$ solution buffered at pH 7.5 $\pm$ 1.0 that contained ~ 100 μM CHCs. Qualitatively it can be observed that the breakthrough curves obtained from the ports nearest the proximal end (1, 5, and 7) exhibit significantly more tailing (i.e., are non-symmetric) than the curves obtained within the distal portion. Average ^3H_2O recovery = 95.2 ± 9.48% (at 95% confidence interval). Samples were obtained between days 413 and 462.

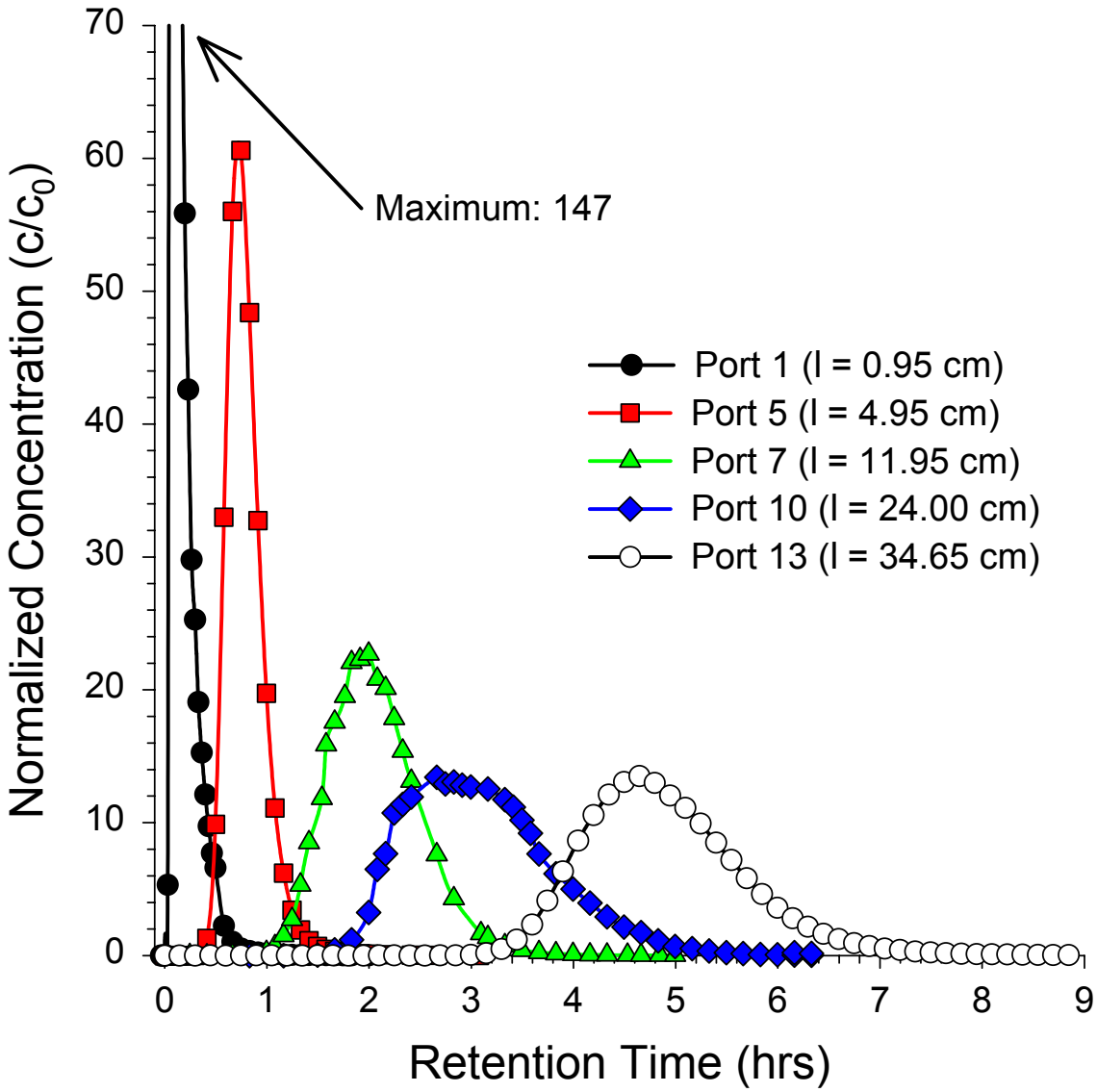

Figure 3.7 ^3H_2O breakthrough curves obtained by sampling from five different ports along the length of column H. The feed to this column was a 3.1 mM $NaHCO_3$ solution buffered at pH 7.5 $\pm$ 1.0 that contained ~ 100 µM CHCs. Qualitatively it can be observed that the breakthrough curves obtained from the ports nearest the distal end (7, 10, 13) exhibit significantly more tailing (i.e., are non-symmetric) than the curves obtained within the proximal portion. Average ^3H_2O recovery = 99.3 $\pm$ 5.98% (at 95% confidence interval). Samples were obtained between days 412 and 460.

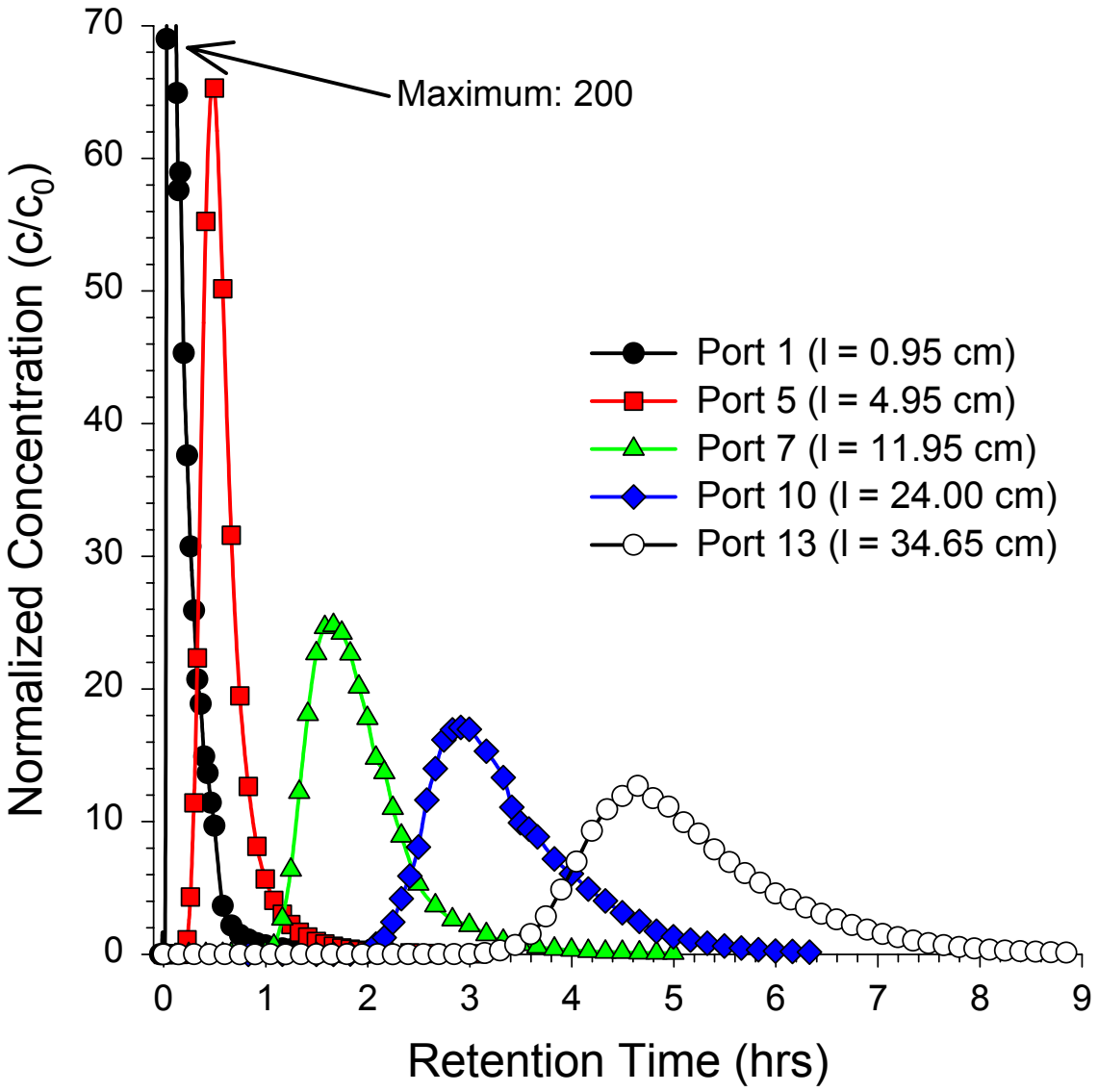

Figure 3.8 ^3H_2O breakthrough curves obtained by sampling from five different ports along the length of column I. The feed to this column was a 3.1 mM $NaHCO_3$ solution buffered at pH 7.5 $\pm$ 1.0 that contained ~ 100 μM CHCs. Qualitatively it can be observed that all of the breakthrough curves exhibited significant tailing (i.e., are non-symmetric). Average ^3H_2O recovery = 91.7 ± 7.43% (at 95% confidence interval). Samples were obtained between days 409 and 447.

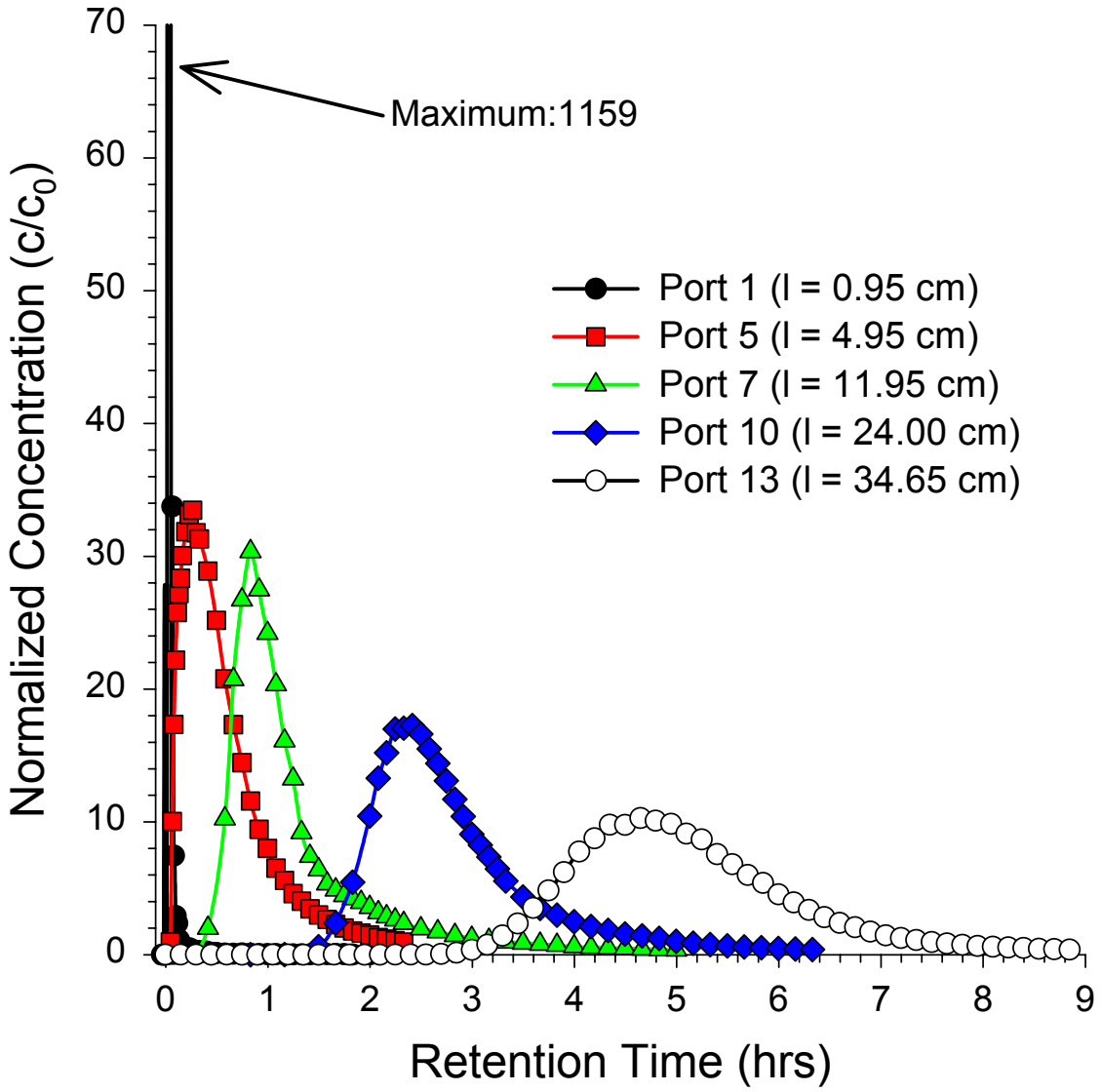

Figure 3.9 ^3H_2O breakthrough curves obtained by sampling from five different ports along the length of column J. The feed to this column was a 3.1 mM $NaHCO_3$ solution buffered at pH 9.3 ± 0.5 that contained ~ 100 μM CHCs. Qualitatively it can be observed that all of the breakthrough curves exhibited significant tailing (i.e., are non-symmetric). Average ^3H_2O recovery = 97.6 ± 6.23% (at 95% confidence interval). Samples were obtained between days 405 and 449.

water content (%), and the coefficient for mass transfer between the mobile and immobile regions (k_{mt}). The results of this fitting exercise are tabulated in Table 3.2.

Pore Water Velocity Variability

In the transport studies conducted on columns A-F it was generally observed that the pore water velocity measured at the column outlet increased with operation time. This increase was attributed to solute deposition within the porous medium of each column. In columns G-J, however, the pore water velocities measured at the column outlet (port 13) were found to be relatively time-invariant (Figs. 3.10-3.13). This somewhat surprising result suggests that solute deposition did not exert the same effect in columns G-J as in columns A-F. Although it is known that solute deposition did occur within columns G-J (evidenced by the changes in porewater geochemistry, as discussed in Chapter 4), the deposited solute quantities were not large enough to exert a noticeable effect on the effluent pore water velocity. There could be many reasons for this disparity, however, the higher initial porosity of columns G-J could be at least partially responsible. The average initial porosity of columns A-F was 0.576, whereas for columns G-J it was 0.612. Therefore, columns G-J had a larger volume of pore space that could be occupied by precipitates; accordingly, the effects of precipitation would be damped relative to columns A-F.

Although the pore water velocity measured at the column outlet did not change appreciably during this set of experiments, there was considerable variability in the pore water velocities measured at the other sampling ports. As would be expected, this variability was greatest for port one. In columns G and J, the pore water velocity at port one increased dramatically between column start-up and the final sampling period. For column G, the velocity increased from ~ 350 cm/d to ~ 770 cm/d and for column J it increased from ~ 120 cm/d to ~ 680 cm/d. In contrast, for columns H and I, the measured pore water velocities at port one actually

decreased over time. For column H, the velocity decreased from ~ 260 cm/d to ~ 150 cm/d and in column I it decreased from ~ 230 cm/d to ~ 120 cm/d.

The increased pore water velocities at port one for columns G and J are most likely due to precipitate formation near the inlet of each column. Enhanced precipitation near the inlet of column J, relative to columns H and I which were fed inlet solutions with similar $NaHCO_3$ concentrations, is not surprising since the influent pH for column J was set to 9.3 whereas for columns H and I it was set to 7.5. At the higher pH value, the solubility of carbonate bearing precipitates, such as siderite, is lower and one would therefore expect solute deposition onto the iron to occur more readily. It is also likely that solute precipitation near the inlet to column G is responsible for the observed high velocities within that region. Although column G, like columns H and I, was fed an influent solution with an approximate pH of 7.5, the feed was buffered by $CaCO_3$ instead of $NaHCO_3$. The presence of calcium provided a second possible cation (in addition to ferrous iron) for the precipitation of carbonate mineral species. Because no calcium was present in the feed to either columns H, I or J, carbonate precipitated only as siderite and thus the formation of Fe(II) was required, a process that is dictated by the iron corrosion rate. The presence of calcium presumably removed this limitation and enabled the formation of carbonate-bearing precipitates (e.g., aragonite), thus forming greater quantities of precipitates (relative to columns H and I) near the inlet.

The observed declines in the pore water velocities measured at port one in columns H and I suggest that precipitation was initially slow at pH 7.5 and also that some pore space previously occupied by the porous media or by distinct gas pockets may have become available over time. For column H, the admixed albite readily dissolved (as discussed in Chapter 4) and this dissolution may have increased the water filled volume, which would result in a decreased pore

water velocity. It is also possible that the granular iron media itself may have dissolved. It is well established that metal corrosion and dissolution occur more readily at circumneutral pH values than at slightly alkaline ones (Wranglén, 1985). A final possibility is that gas pockets initially present near the inlets to these columns may have either dissolved or been mobilized.

Upon examining the spatial distribution of pore water velocities within the four columns it is apparent that there were consistent velocity gradients within both columns G and J. For each of those columns the pore water velocities nearest the inlet (at ports 1, 5, and 7) were almost always larger than those measured for the distal portion of the column (ports 10 and 13). As previously noted, the biggest velocity gradient within both columns was between the first two sampled ports (1 and 5). Nevertheless, over the full 475 day monitoring period there was a 13-87 cm/day gradient in the porewater velocities between ports 5 and 13 for column G and a 51-144 cm/day gradient between those same ports for column J. These differences (significant at the 95% confidence level) confirm that preferential solute deposition and gas accumulation within the proximal portions of columns G and J occurred. This effect, however, was not observed for the lower pH sodium bicarbonate columns H and I. Within each of those columns, no consistent trends in velocity were observed.

Dispersivity Variability

In general, no systematic trends in the mobile zone dispersivity were detected (Figs. 3.10-3.13). Dispersivities for Ports 5, 7, 10, and 13 typically ranged from 0.25-0.5 cm for column G, 0.1-0.6 cm for column H, 0.15-0.30 cm for column I, and from 0.05-2.3 cm for column J. For

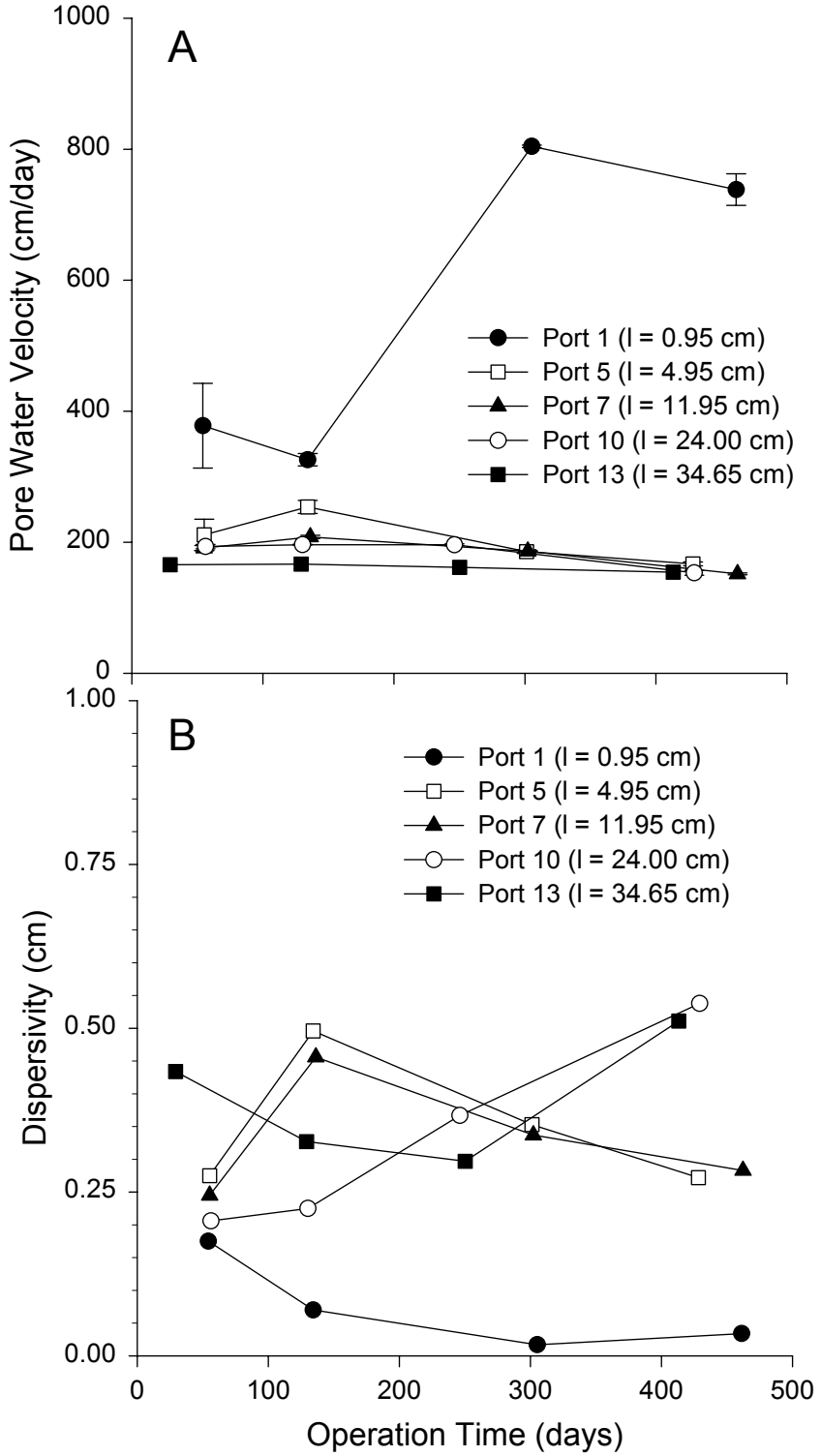

Figure 3.10 Variation in A) Pore water velocity, B) Dispersivity, C) Dispersion coefficient, and D) Immobile water content for ports 1, 5, 7, 10, and 13 of Column G. The feed to this column was a saturated $CaCO_3$ solution buffered at pH 7.5 $\pm$ 1.0 that contained ~ 100 μM CHCs. Average ^3H_2O recovery = 95.1 ± 5.12% (at 95% confidence interval).

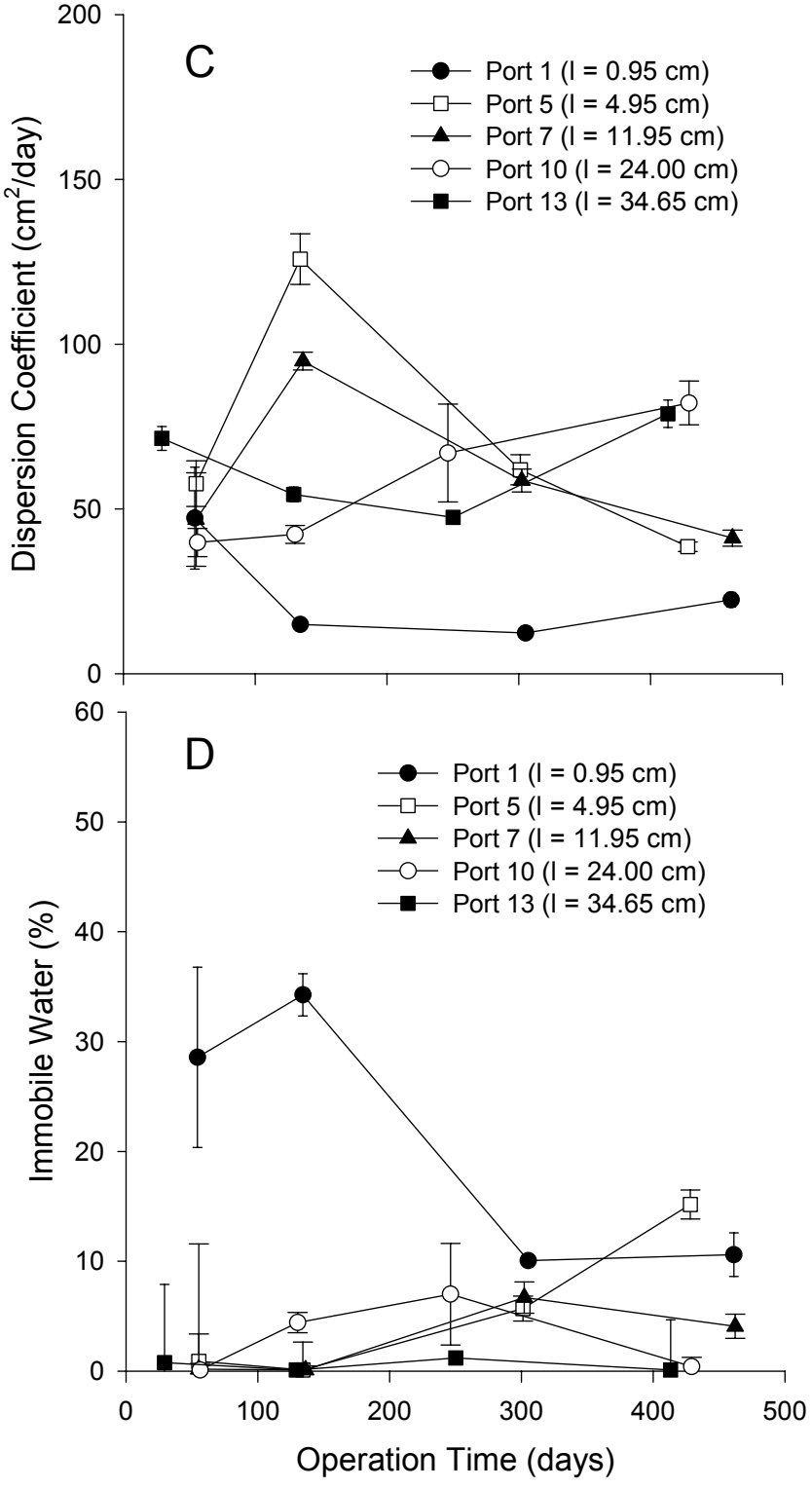

Figure 3.10 continued.

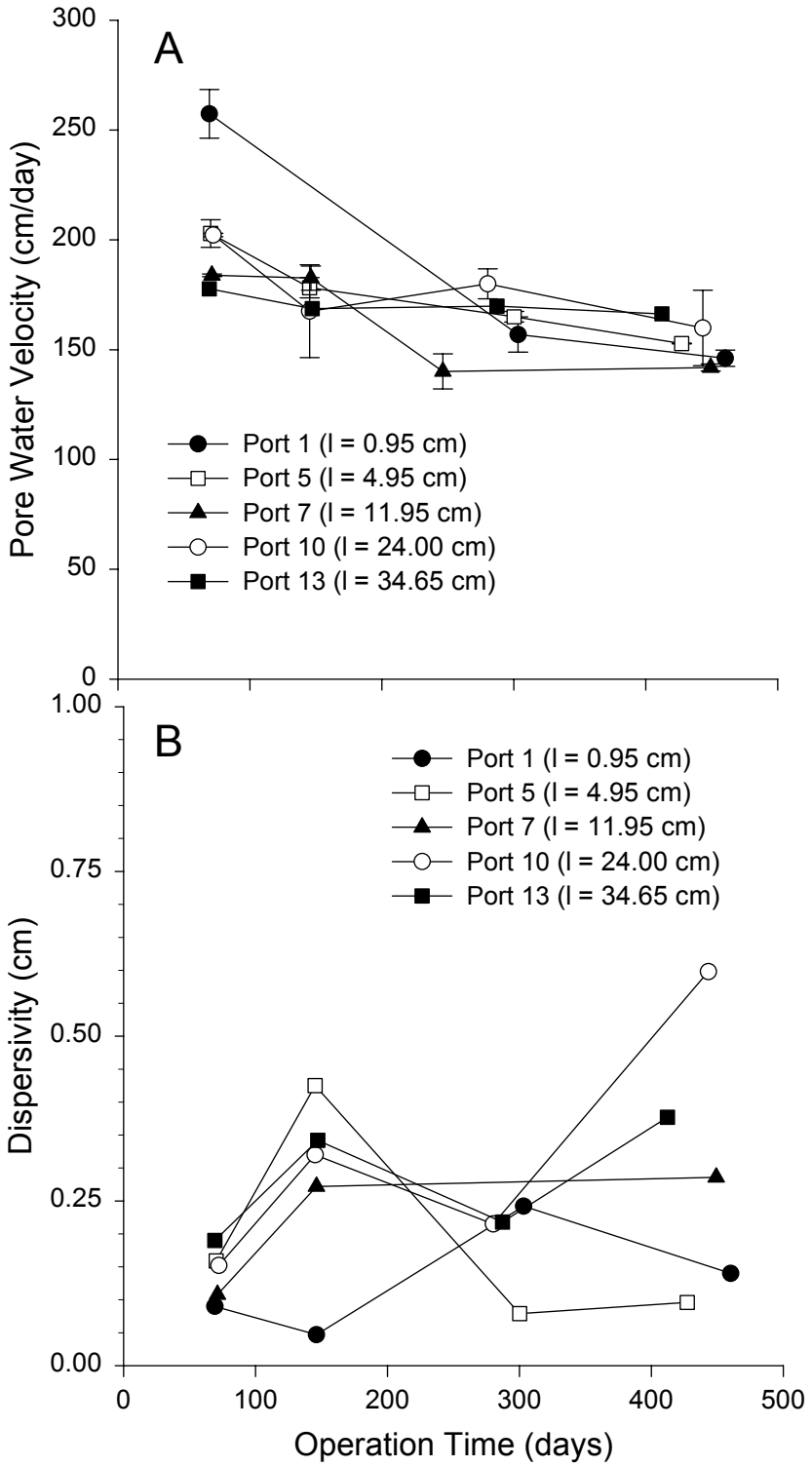

Figure 3.11 Variation in A) Pore water velocity, B) Dispersivity, C) Dispersion coefficient, and D) Immobile water content for ports 1, 5, 7, 10, and 13 of Column H. The feed to this column was a 3.1 mM $NaHCO_3$ solution buffered at pH 7.5 $\pm$ 1.0 that contained ~ 100 μM CHCs. Average ^3H_2O recovery = 92.4 ± 6.01% (at 95% confidence interval).

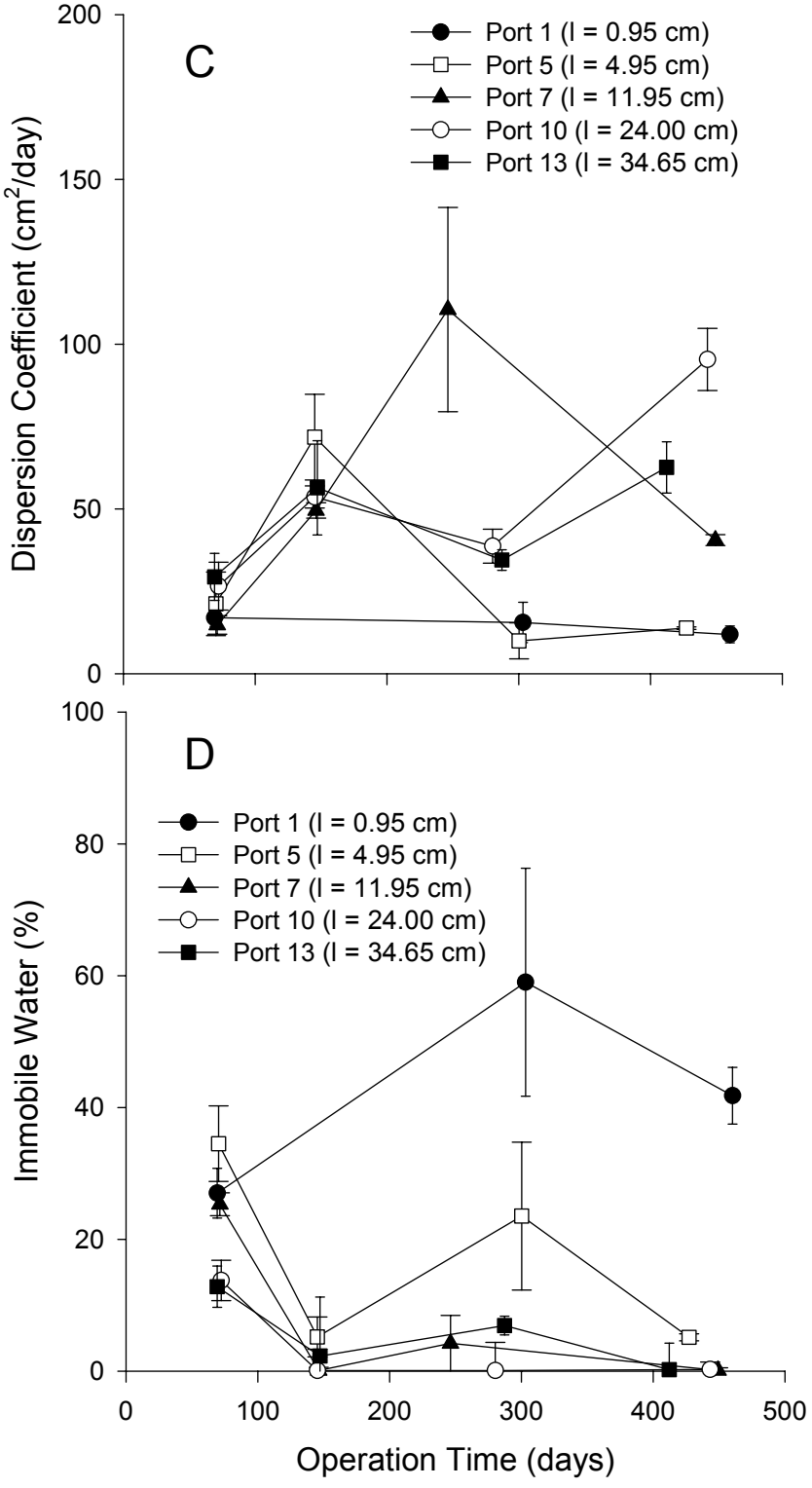

Figure 3.11 continued.

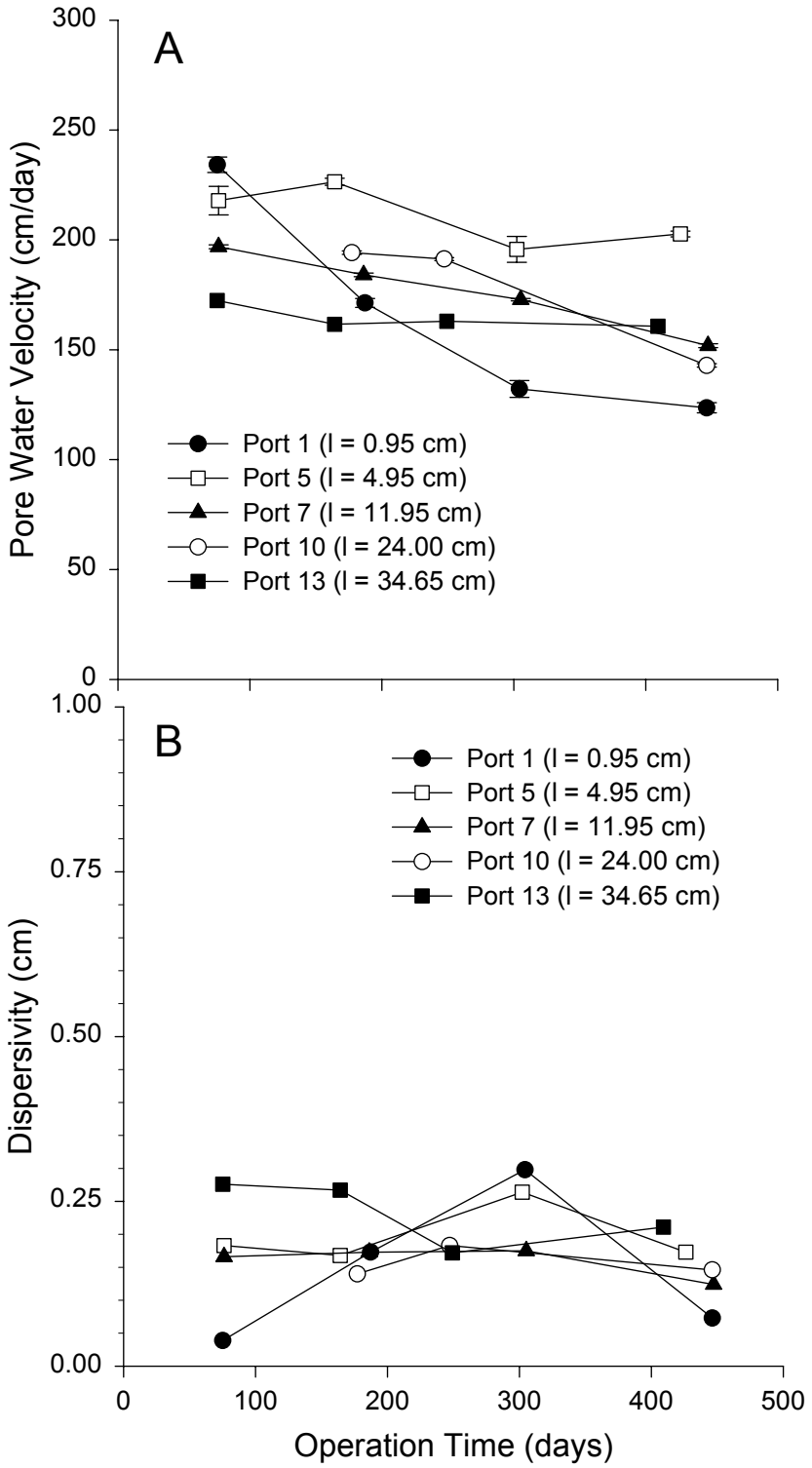

Figure 3.12 Variation in A) Pore water velocity, B) Dispersivity, C) Dispersion coefficient, and D) Immobile water content for ports 1, 5, 7, 10, and 13 of Column I. The feed to this column was a 3.1 mM $NaHCO_3$ solution buffered at pH 7.5 $\pm$ 1.0 that contained ~ 100 μM CHCs. Average ^3H_2O recovery = 94.6 ± 2.96% (at 95% confidence interval).

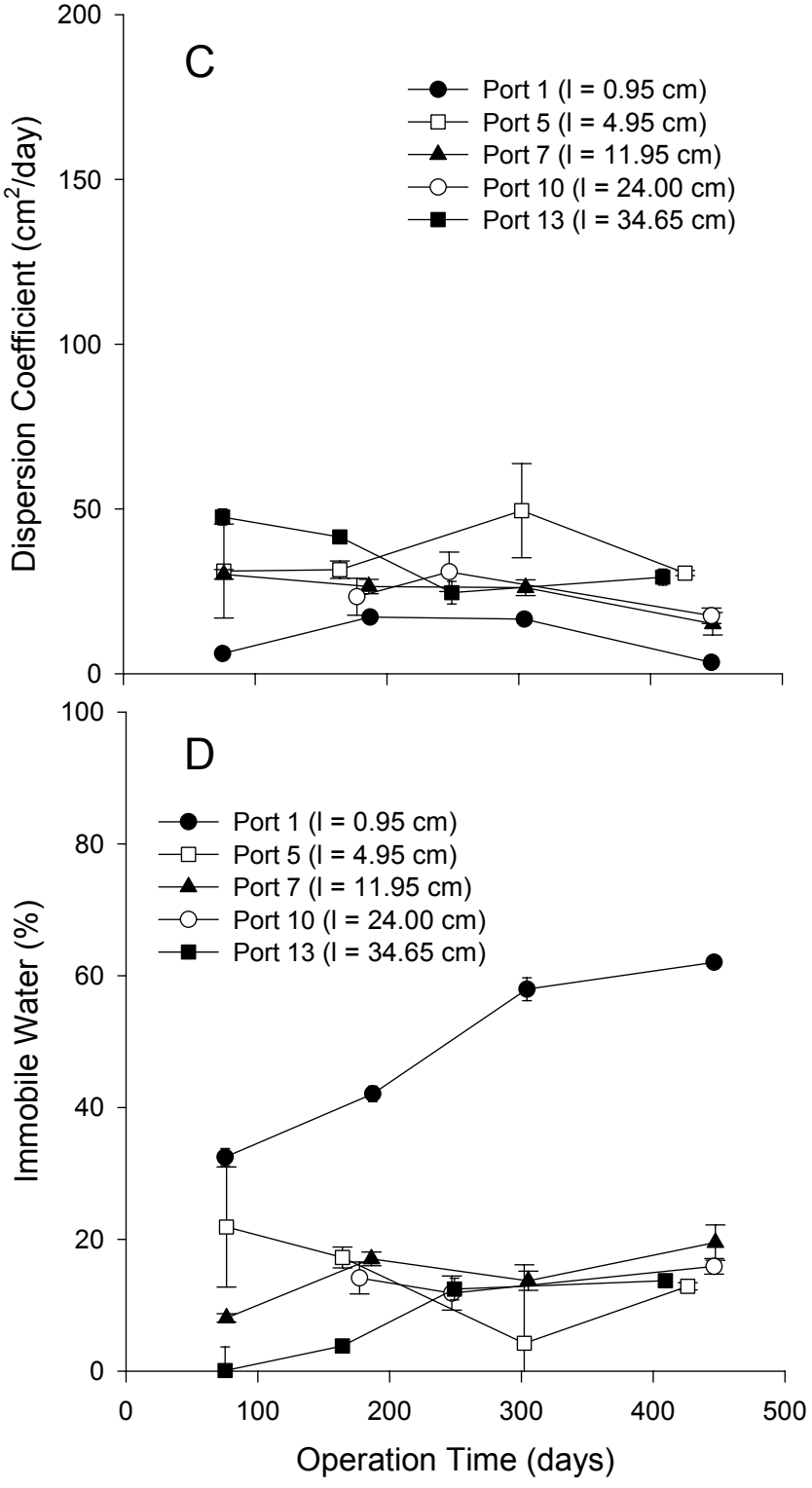

Figure 3.12 continued.

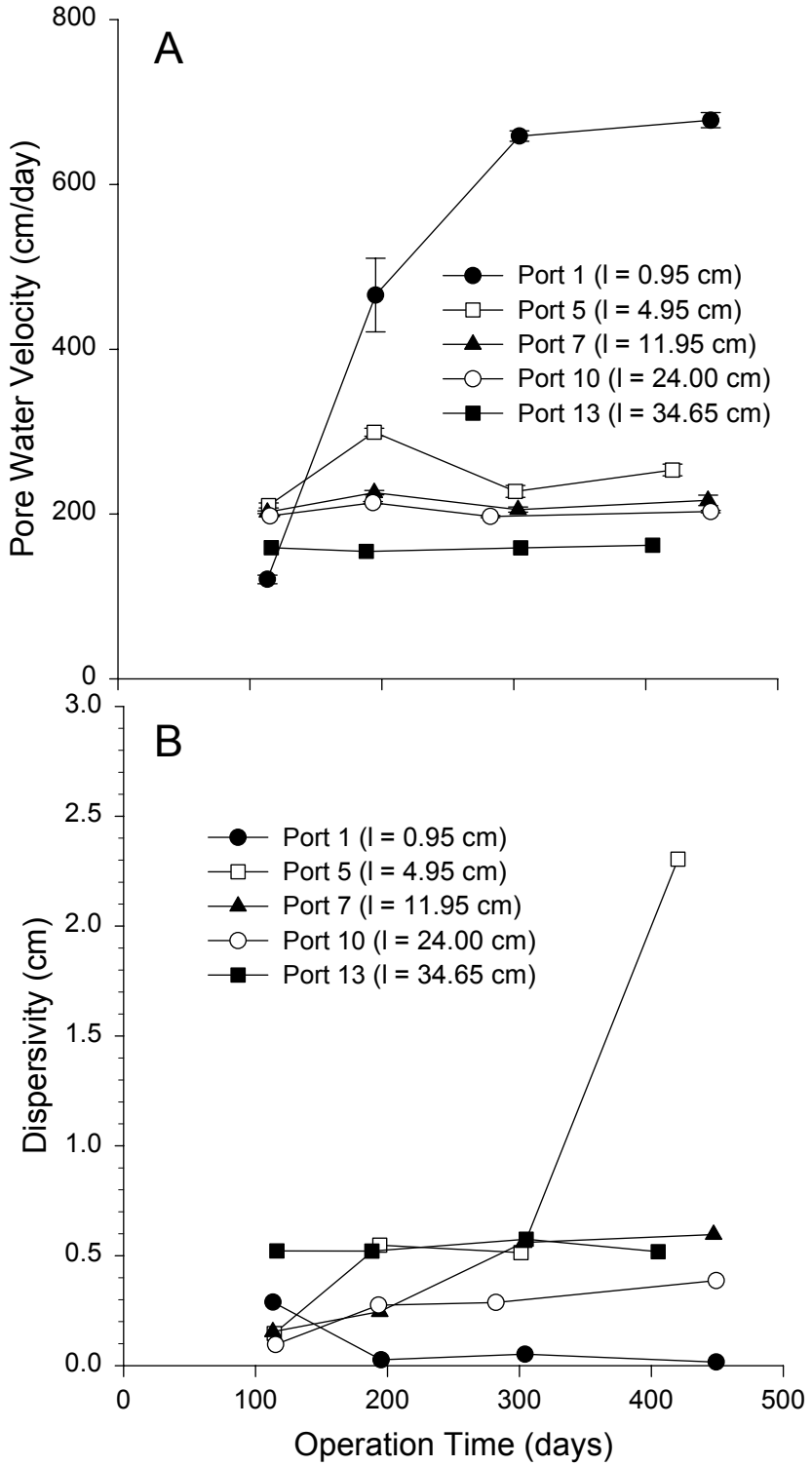

Figure 3.13 Variation in A) Pore water velocity, B) Dispersivity, C) Dispersion coefficient, and D) Immobile water content for ports 1, 5, 7, 10, and 13 of Column J. The feed to this column was a 3.1 mM $NaHCO_3$ solution buffered at pH 9.3 $\pm$ 0.5 that contained ~ 100 μM CHCs. Average ^3H_2O recovery = 94.0 ± 4.52% (at 95% confidence interval).

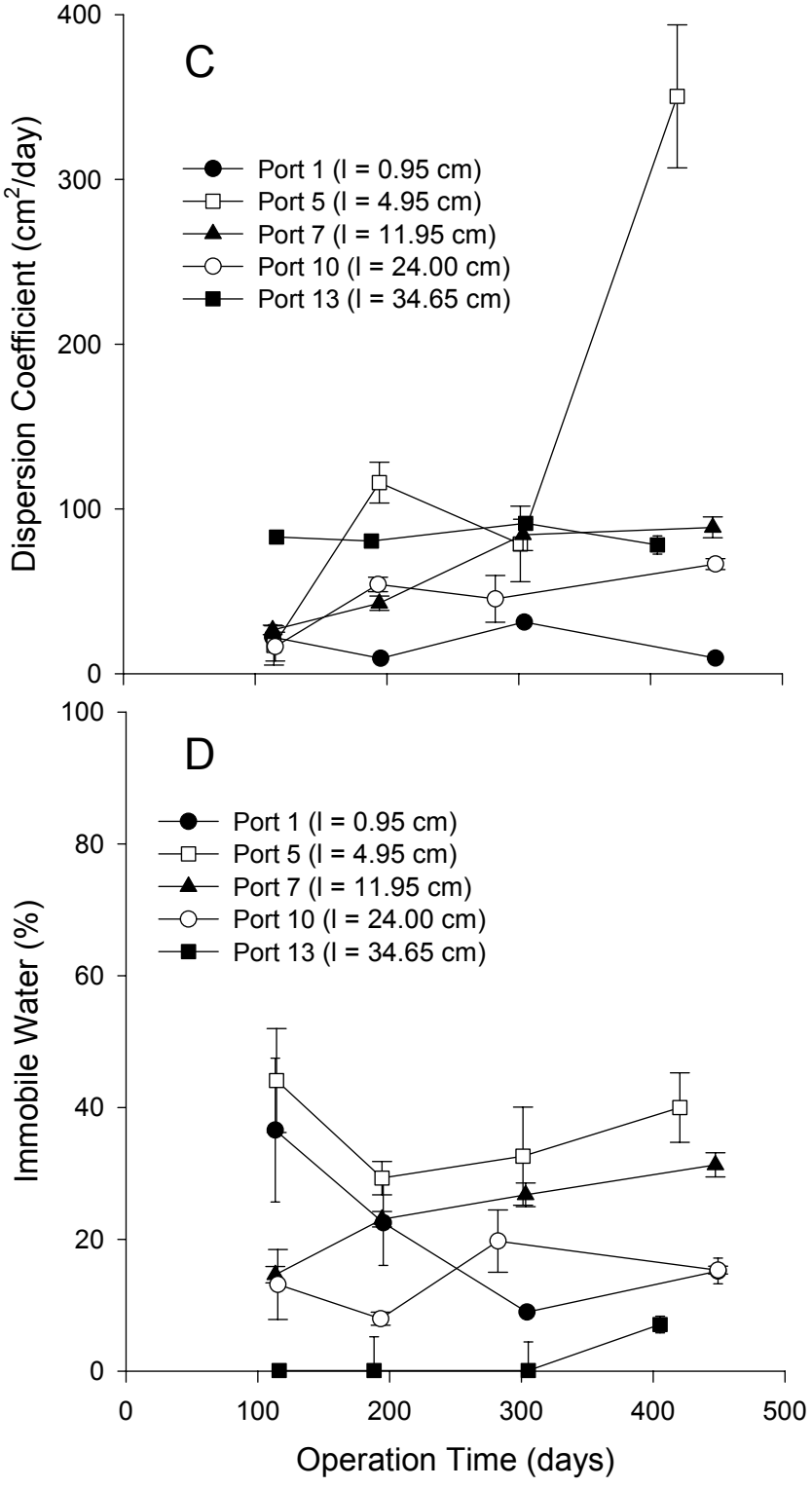

Figure 3.13 continued.

port 1, the D_m values were typically lower than those observed further within the column: 0.03-0.18 for column G, 0.08-0.25 for column H, 0.04-0.29 for column I, and 0.05-0.3 for column J.

Immobile Water Variability

The immobile water content of each of the columns was observed to vary with both time and position. Within each of the columns it was generally observed that the immobile water content was higher near the inlet (port 1) than at the outlet (port 13). This would be consistent with the notion of greater solute deposition and gas accumulation near the inlet, given that such precipitation is also a likely cause for the formation of zones of immobile water. Based on the extreme variability in the immobile water content, however, it is apparent that the majority of these zones are transient in nature.

TRACER TESTS WITH SULFUR HEXAFLUORIDE

In theory, a comparison of the retardation of a gas-partitioning tracer relative to the non-partitioning tracer ^3H_2O can be used to calculate the volume of the pore space occupied by a distinct gas phase. To assess this possibility, tracer studies with SF_6 were conducted on several of the experimental columns.

Column Studies

Figs. 3.14 and 3.15 show the breakthrough curves for SF_6 in both the liquid and gas phase in columns C and D. In these figures the measured concentration of SF_6 in the gas phase (C_G) is expressed not as a gas-phase concentration, but rather as the liquid concentration that would be in equilibrium with this gas phase (i.e., $C_L^* = C_G/H_c$). This form of display permits an

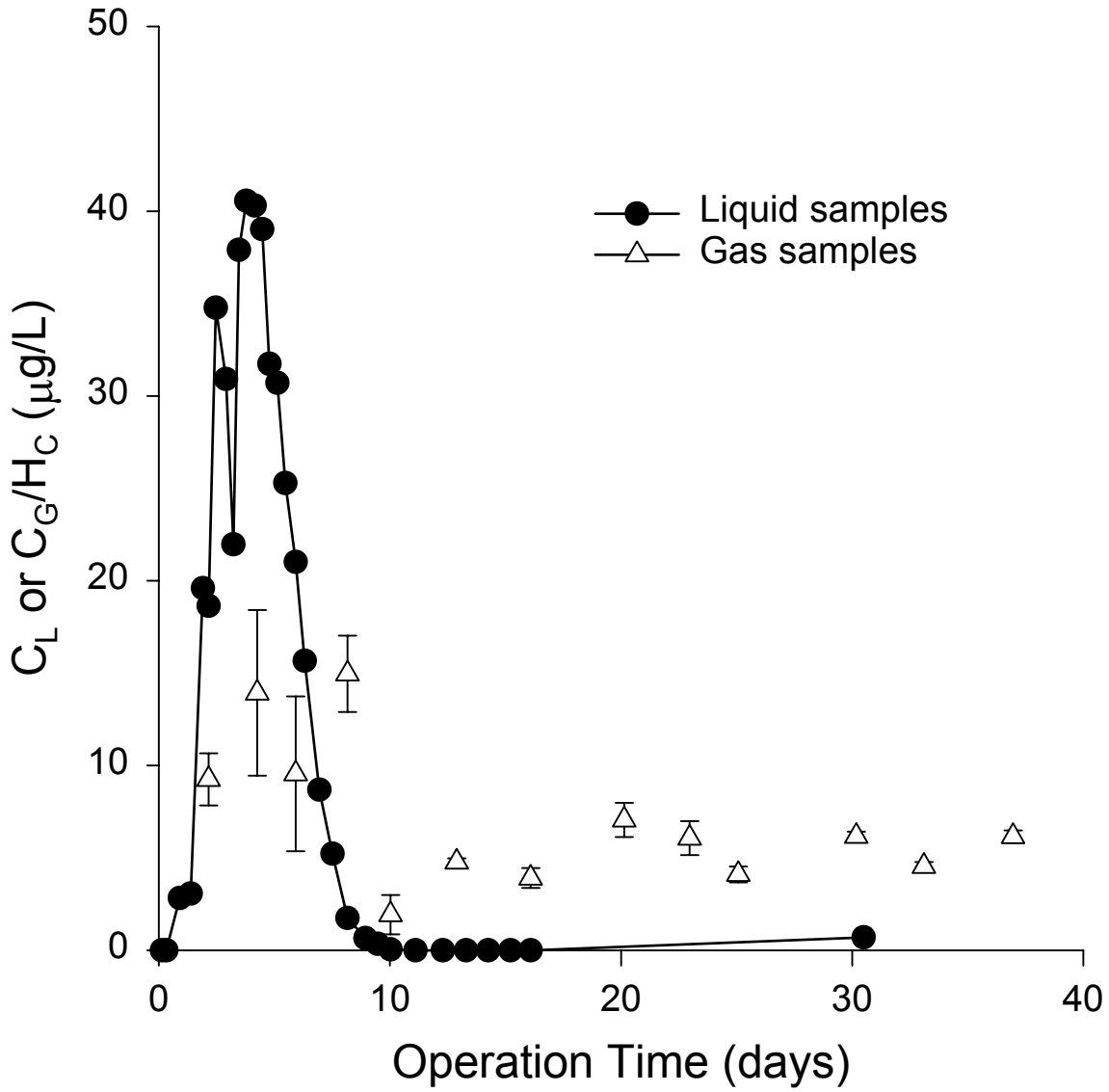

Figure 3.14 Column C - SF_6-tracer test (pulse input) - experimental data

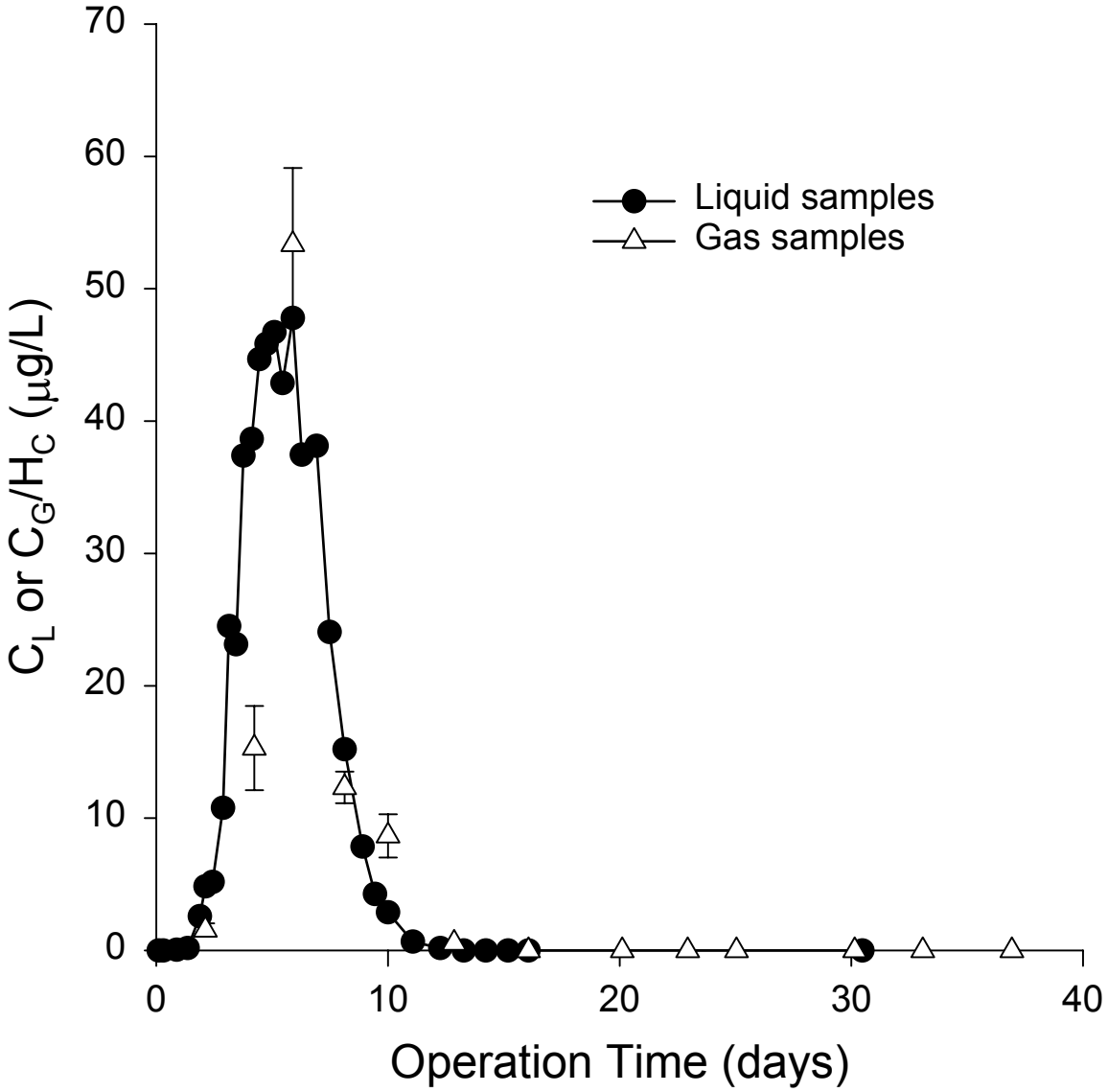

Figure 3.15 Column D - SF_6-tracer test (pulse input) - experimental data

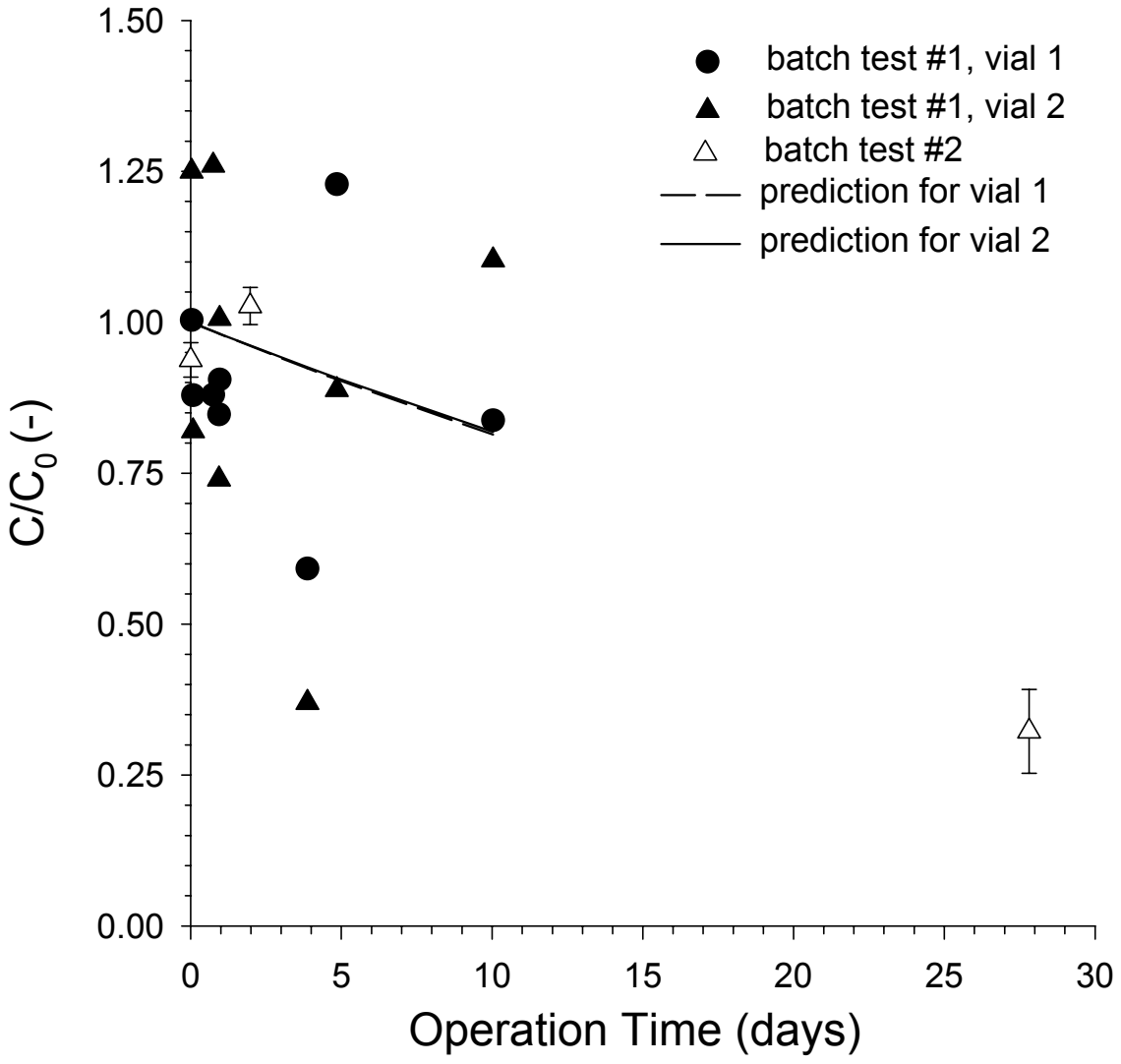

Figure 3.16 SF_6 batch set #1 with predictions for vial 1 and 2 based on batch set #2. The different liquid phase to mass of Fe(0) ratios have been taken into account.

easy visual assessment of whether the measured liquid- and gas-phase concentrations of SF_6 reflect a local equilibrium at the end of the column.

It is apparent from Fig. 3.14 that the SF_6 concentrations measured in the liquid and gas phases of column C are not in equilibrium. On the other hand, deviations for column D (Fig. 3.15) are not so severe, and agreement is quite good at the peak and in the tail. In an effort to better understand these observations, a series of batch experiments were conducted to assess the possibility of SF_6 sorption or transformation by the granular iron media.

Batch Studies

Fig. 3.16 shows the SF_6 measurements made for two different batch tests. Although the data from the first test were ambiguous (presumably due to experimental uncertainty associated with the injection technique used for this test), the second set (batch test #2) clearly shows that the SF_6 concentration is not stable in the presence of granular iron. The observed instability of the SF_6 concentration indicates that SF_6 either reacted with the granular iron (or with impurities in the iron grains) or that it sorbed to the iron particle surface. Insufficient evidence exists to discern which of these pathways is dominant; however, ion chromatography results suggest that some level of reaction occurs, as evidenced by the appearance of sulfate and fluoride in aqueous solution.

Assuming that a first-order process removes SF_6 in the presence of granular iron (whether this is via reaction or via sorption is immaterial), the data from batch test #2 were used to obtain an effective rate coefficient ($k_{eff,batch}$ $[T^{-1}]$). Note that although the results from batch test #1 were deemed unreliable for direct analysis, they appear to be generally consistent with expectations that could be made on the basis of the rate coefficient predicted using batch set #2. This comparison is shown in Fig. 3.16.

Using the relationship developed in Chapter 2, estimated first-order rate coefficients for columns C and D were calculated based on the $k_{eff,batch}$ value from batch set #2. The resulting estimates are listed in Table 3.3. Extrapolation of the batch results to column performance in this manner is reasonable because both experiments utilized the same buffer (2 mM $NaHCO_3$) and both had similar volumetric ratios of liquid to granular iron (1.8 : 1 for batch set #2 and 1.2 : 1 for the columns at an estimated normalized water-filled porosity, *s(t)*, of 0.7). Table 3.4 summarizes the mass of SF_6 that would be expected to be lost in the tracer tests for columns C and D, if we use the effective reaction/sorption rate coefficients estimated from the batch data (as shown in Table 3.4). The SF_6 residence time in the column (first moment) is also used for this calculation, and was calculated based on the evolution of total SF_6 mass. The results predict that 81% of mass will be lost in column C and 38 % of mass in column D due to reaction/sorption. Also shown, for purposes of comparison, are our best estimates of total SF_6 mass recovery from the experimental columns. Note that the comparison is reasonably good for Column D, but that we have an unexplained mass balance problem in the experimental data for Column C (where high "tailing" concentrations of SF_6 were observed in the gas phase).

Considering the mass recovery difficulties, the evidence for nonequilibrium between the eluting gas and eluting liquid, and the suspected reactivity and/or sorption of SF_6 with granular iron, we concluded that SF_6 was not an appropriate choice for use in the columns. Not only does the reactivity of SF_6 hinder the evaluation of the SF_6 residence time distribution but it could also affect the reactivity of the granular iron with respect to contaminant degradation.

Table 3.3 Results from batch test #2

	$k_{eff,,batch}$ [d^{-1}]	$R_{d,batch}$ [-]	$m_{Fe(0),batch}$ [g]	$V_{L,batch}$ [mL]	$R_{d,column}$ [-]	$m_{Fe(0),column}$ [g]	$V_{L,column}$ [mL]	$k_{eff,column}$ [d^{-1}]
Batch Set #2	0.0406	111	117.6	26.9				
Column C					56.7	839	131	0.116
Column D					81.0	790	111	0.0906

Table 3.4 Measured and calculated loss of SF_6 mass during the column tracer tests.

	$k_{eff,column}$ [d^{-1}]	first moment [d]	Calculated* M/M_0 [-]	Measured M/M_0 [-]
Column C	0.116	14.4	0.189	0.837
Column D	0.0906	5.36	0.615	0.589

* based on estimated rate coefficient and tracer-study estimate of mean SF_6 residence time

CHAPTER 4 – CHANGES IN COLUMN REACTIVITY

To gain insight into the longevity of granular iron, we undertook long-term studies in which alterations in the reactivity of the interfacial region were carefully decoupled from changes in the hydraulic residence time (HRT) that result from mineral precipitate and H_2 gas pocket formation within the porous medium. Three sets of columns, filled with granular iron and continually fed solutions containing various organic and inorganic solutes, were operated concurrently. As noted previously, two sets were housed at Johns Hopkins (columns A-F, run for 1100 days; columns G-J, run for 475 days), and the third was maintained at the Air Force Research Laboratory (K-O, run for 407 days). At a flow velocity of 1.2 – 1.8 m/d, these operation times correspond to ~ 4500 pore volumes (columns A-F), ~ 1600 pore volumes (columns G-J), and ~ 1800 pore volumes (columns K-O).

Thirteen of the fifteen columns were continuously exposed to mixtures of contaminant species, and contaminant concentrations were determined by sampling the columns at periodic intervals. Rate coefficients were obtained by fitting an exponential decay model to the resulting contaminant profiles. Target mixtures included three CHCs: trichloroethylene (TCE), 1,2,3-trichloropropane (1,2,3-TCP), and 1,1-dichloroethane (1,2-DCA); and three NACs: 2-nitrotoluene (2-NT), 4-nitroacetophenone (4-NAP), and 4-nitroanisole (4-NA). Although the reactivities of many of these species with iron have previously been examined, long-term effects of solute composition on granular iron reactivity towards mixtures of these compounds have not been investigated. The principal experimental variables included the type and concentration of co-solutes (calcium carbonate/sodium bicarbonate, chloride, silica, and NOM). Two columns were only periodically exposed to trichloroethylene so as to test the effect of co-solutes and water (as opposed to trichloroethylene) on iron passivation. For the ten columns operated at JHU,

periodic tracer tests were conducted with tritiated water (^3H_2O); these studies enabled delineation of the effects of altered HRT from changes in the reactivity of the interfacial region on overall system performance. The observed changes in hydraulic residence time distributions were discussed within the previous chapter; this chapter emphasizes the effects of solute composition on reactivity toward CHCs and NACs.

DATA ANALYSIS

Calculation of Rate Coefficients

Spatially averaged rate coefficients for contaminant degradation in each column were determined by fitting a pseudo-first-order expression to the concentration profiles (C vs. residence time, $\tau_x(t)$):

$$\frac{d[C]}{dt} = -k_{obs}[C] \tag{4.1}$$

where k_{obs} (h^{-1}) is a pseudo first-order kinetic coefficient and C refers to a given contaminant (i.e., TCE, 2-NT, 4-NAP, 4-NA). Values of local residence time $\tau_x(t)$ for each sample port (at distance x along a column of length L) were calculated using the mean hydraulic residence time, $\tau(t)$, for the entire column:

$$\tau_x(t) = \tau(t) \times \frac{x}{L} \tag{4.2}$$

The $\tau(t)$ values for columns A-F and G-J were calculated using $\tau_{tracer}(t)$ values interpolated from tracer tests periodically conducted using a near-Dirac pulse of ^3H_2O and a flow rate of 0.500 mL/min established with an Isco syringe pump. To correct for variations in the flow provided by the peristaltic pump normally used with the columns, the interpolated $\tau_{tracer}(t)$ values were

adjusted according to the actual volumetric flow rate measured for any given day. Details concerning the determination of $\tau_{tracer}(t)$ and its variation over time are found in Chapter 3. The $\tau(t)$ values for columns K-O were calculated on the basis of periodic volumetric flow measurements only.

The pseudo first-order model was adopted as a means of quantifying reactivity trends after first exploring a Langmuir-Hinshelwood-Hougen-Watson (LHHW) approach similar to that previously used in our laboratory (Arnold and Roberts, 2000a and b) and elsewhere (Johnson et al., 1998; Scherer et al., 1998; Wüst et al., 1999; Devlin et al., 2000). It was found that the LHHW model did not provide any significantly improved fit to the contaminant profiles relative to a simpler pseudo-first-order expression. The use of a pseudo-first-order expression is consistent with previous studies of iron-mediated reduction of CHCs and NACs (Agrawal and Tratnyek, 1996; Johnson et al., 1996; Devlin et al., 1998; Klausen et al., 2001).

Mass Transfer Considerations

Proper evaluation of reaction rate coefficients for surface-mediated processes requires knowledge of the mass transfer coefficient that describes the rate at which a reactant is transported to the surface (Arnold et al., 1999; Arnold and Roberts, 2000a). For this purpose the simplified Gnielinski correlation (Roberts et al., 1985)

$$Sh = (2 + 0.644\,\mathrm{Re}^{1/2}\,Sc^{1/3})[1 + 1.5(1-\varepsilon)] \tag{4.3}$$

was used to estimate external mass transfer coefficients (k_{mt} = D × ψ × Sh/d) for the flow conditions and particle sizes in our columns. Independent estimates were made for the Reynolds number (Re = d × v/ν = 0.024), the diffusion coefficient (D = 8.8 × 10^{-10} m^2s^{-1}), the pore-water velocity (v = 2.43 × 10^{-5} ms^{-1}), the kinematic viscosity of water (ν = 1 × 10^{-6} m^2s^{-1}), the Schmidt

number ($Sc = \nu/D = 1000$), the porosity ($\varepsilon = 0.576$), the shape correction factor (assumed to be $\psi = 2$), and the mean particle diameter (d = 0.001 m). Using a calculated area-to-volume ratio (λ) of 3839 m^{-1}, the corresponding pseudo first-order rate coefficient ($k_{max} = k_{mt} \times \lambda$) can be calculated as 119 h^{-1}. This represents the maximum first-order rate coefficient that could reflect limitations imposed by processes other than external mass transfer (i.e., that is limited by intrinsic reaction rates). The k_{obs} values determined for TCE reduction as part of this work were considerably below k_{max} and can thus be interpreted to reflect intrinsic surface reaction limitations. Rate coefficients for NAC reduction, in contrast, were within an order of magnitude of the k_{max} value; we therefore cannot rule out the possibility that the k_{obs} values for the NACs could be partially mass transfer controlled.

RESULTS

Variations in Geochemical Parameters of Columns G-J

Fe(II) Profiles

Samples for ferrous iron quantification were taken from ports over the entire column length. Measurable levels of ferrous iron were primarily detected near the proximal end of the three columns fed an influent solution at pH 7.5 (columns G-I); in contrast, no ferrous iron was detected in column J, which had an influent pH of 9.3 (Fig. 4.1). Of the three columns where ferrous iron was detected, the concentrations were significantly higher in the column buffered with calcium carbonate (G) than in those buffered with sodium bicarbonate (H and I). Presumably, the increased ferrous iron concentration results from competition by calcium for CO_3^{2-} or for sorption sites on the granular iron surface.

Carbonate Profiles

Measurements of the porewater inorganic carbon concentrations of columns G-J indicate, as was previously hypothesized in Chapter 3, that carbonate was retained within the columns (Fig. 4.2). Additionally, as the columns aged, the effluent carbon concentration increased, thereby suggesting that the saturation of sorptive sites within the column was occurring.

Variation in Porewater pH Values

In PRBs employed in the field, it is typically observed that the pH of the groundwater increases with travel distance into the PRB (O'Hannesin and Gillham, 1998). These pH changes presumably affect not only the geochemistry of the porous medium, but also the contaminant reduction rate. To better understand the reactivity of the granular iron it was therefore important to account for any pH variations within the columns. Taking pH measurements from specific sampling ports along the column length allowed us to assess the variability in the porewater pH of columns G-J.

As shown in Fig. 4.3, the pH throughout column J remained fairly stable at its influent value (~ 9.3 $\pm$ 0.5). This result agrees with the stable pH observed for columns A-F and K-O that were also fed solutions that had a pH ~ 9.3. This pH is representative of values typically observed within the 'interior' of a PRB. For columns G, H, and I, the influent pH was set to ~ 7.5, a value more representative of calcium carbonate-buffered groundwater. Within these columns, the pH increased with travel distance, rising from the influent value of ~ 7.5 ($\pm$ 1.0) to values ranging between 8.5 and 9.5. In both columns H (92% iron/8% albite) and I (100% iron),

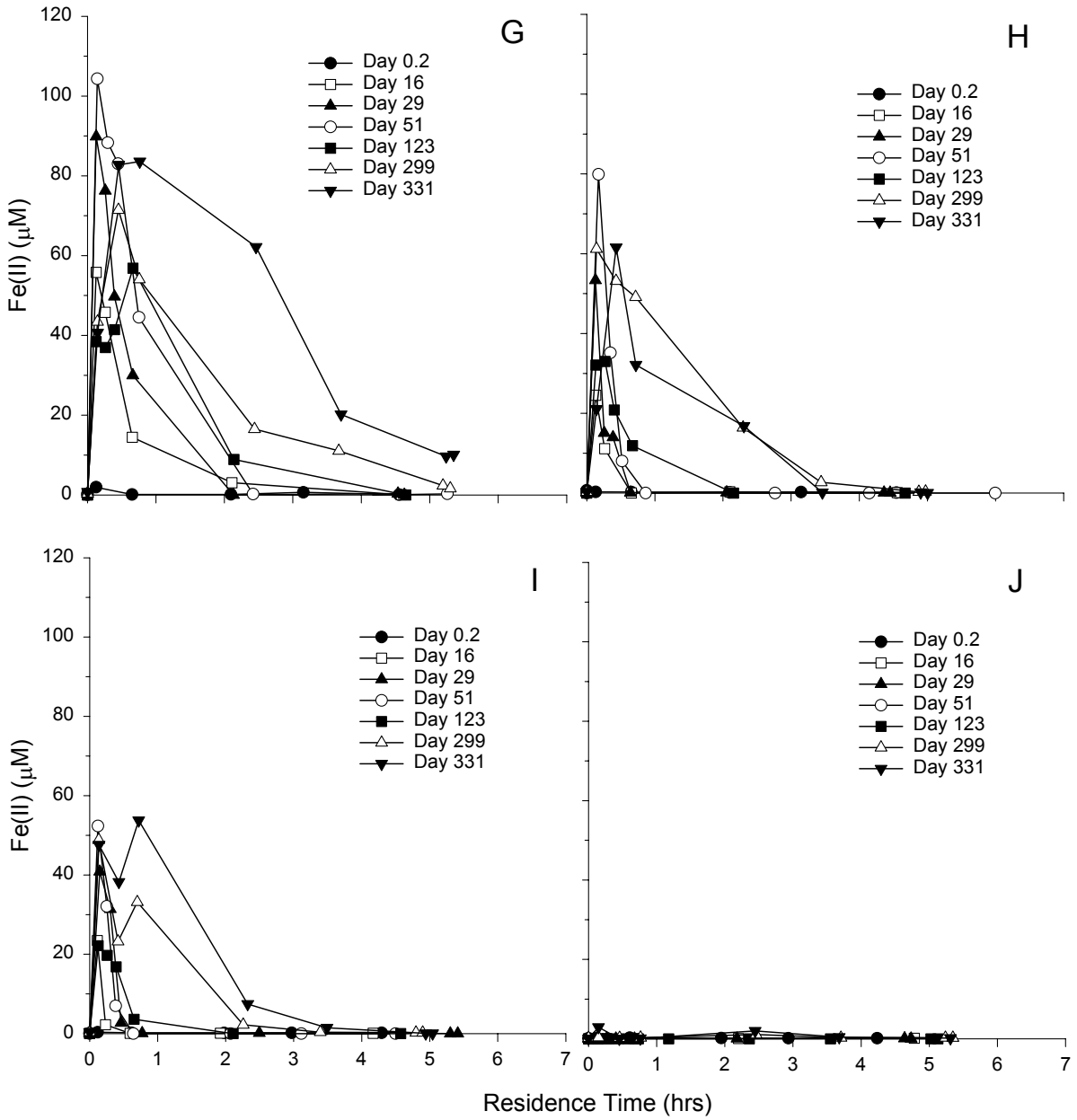

Figure 4.1 Fe(II) profiles for columns G-J. The porous medium in columns G, I, and J was 100% Master Builder iron and in column H it was 92% Master Builder iron/8% albite (w/w).

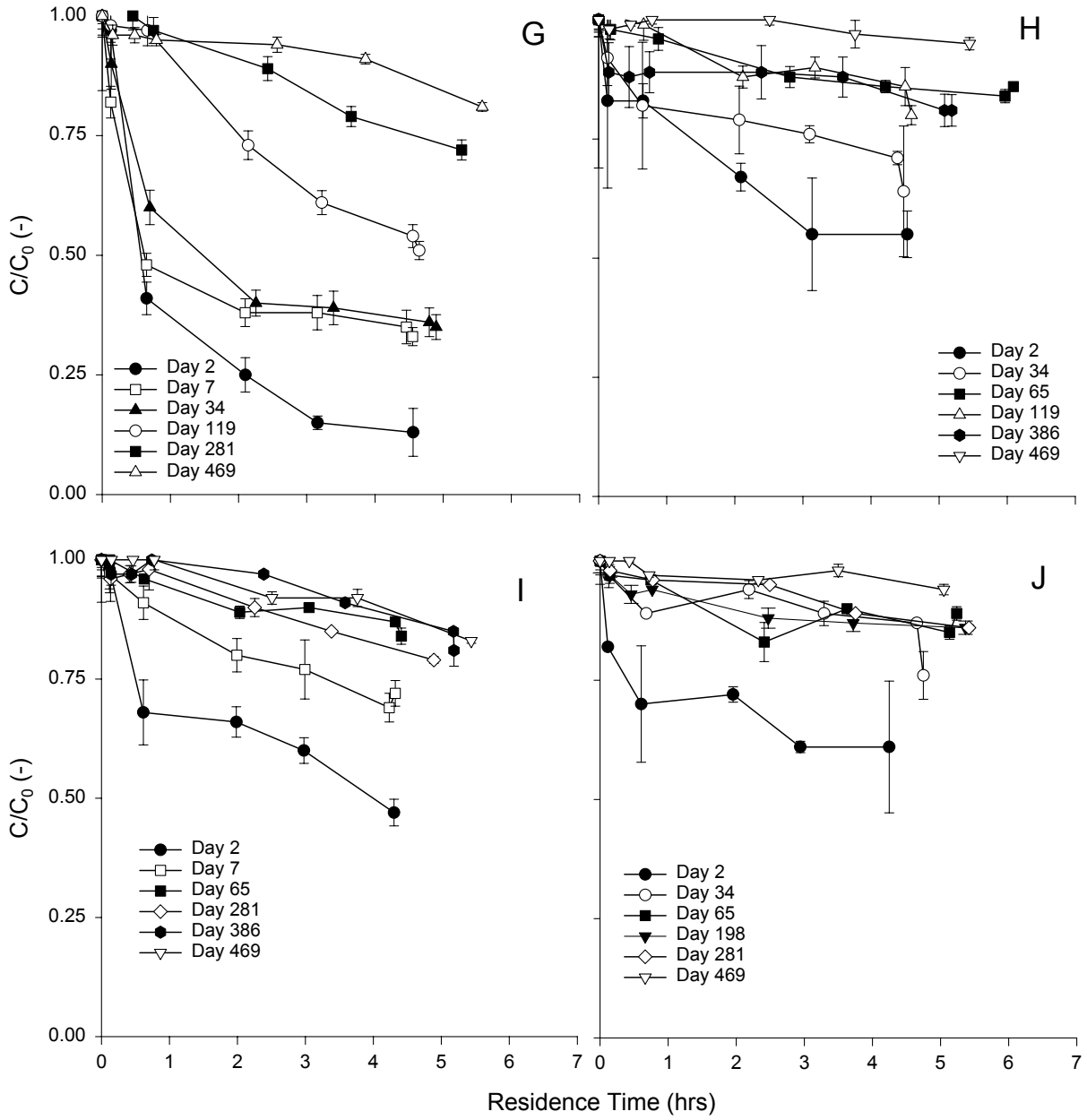

Figure 4.2 Inorganic carbon profiles for columns G-J. The porous medium in columns G, I, and J was 100% Master Builder iron and in column H it was 92% Master Builder iron/8% albite (w/w).

the pH increased through the first half of the column and then stabilized at the effluent pH value of ~ 9.5.

Column G also had an influent pH of ~ 7.5, however, the porewater pH values in this column were typically lower than those in columns H and I. Apparently, the calcium carbonate influent solution provided a more effective buffer against pH changes than the sodium bicarbonate buffer employed in columns H and I. This enhanced buffering cannot be due to changes in the total buffering capacity of the influent since the total carbonate concentration of the sodium bicarbonate columns (H and I) was larger than that of the calcium carbonate column (C_{T,CO_3} = 3.1 mM for columns H and I versus C_{T,CO_3} = 2.4 mM for column G). Contrary to what was observed by other researchers, the albite in column H had no pH buffering effect (Powell and Puls, 1997).

The pH buffering exhibited by the calcium carbonate could potentially be due to the retention of calcium within the porous medium of column G. As shown in Fig. 4.4, the calcium concentration decreased between the column inlet and the column outlet, thereby indicating that calcium was retained within the column. Presumably the calcium either precipitated on the iron surface as a distinct mineral phase (such as calcite; $CaCO_3$) or it formed iron-calcium surface complexes (Dzombak and Morel, 1990). Either process could explain the observed pH buffering effect. The precipitation of calcite is described as:

$$Ca^{2+} + HCO_3^- \Leftrightarrow CaCO_3(s) + H^+ \tag{4.4}$$

Similarly, were calcium to form a surface complex at the iron-water interface, protons will also be released:

$$>FeOH + Ca^{2+} \Leftrightarrow >FeOCa^+ + H^+ \tag{4.5}$$

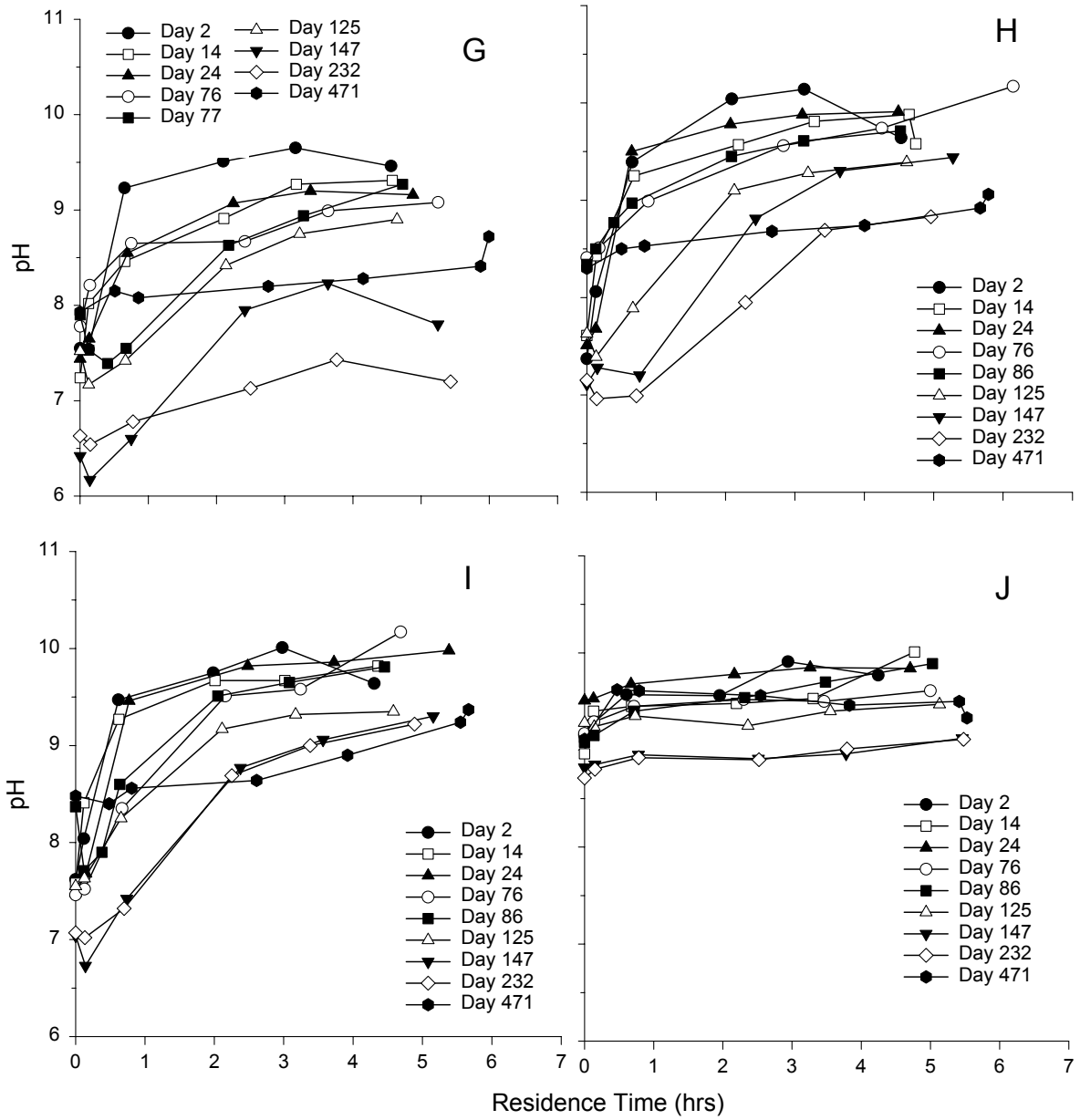

Figure 4.3 Variation in porewater pH values for columns G-J. The influent pH to columns G, H, and I was set to 7.5 ± 1.0 and for column J it was 9.3 ± 0.5. The porous medium in columns G, I, and J was 100% Master Builder iron and in column H it was 92% Master Builder iron/8% albite (w/w). **Must note avg. influent pH and effluent pH w/ std. deviations…

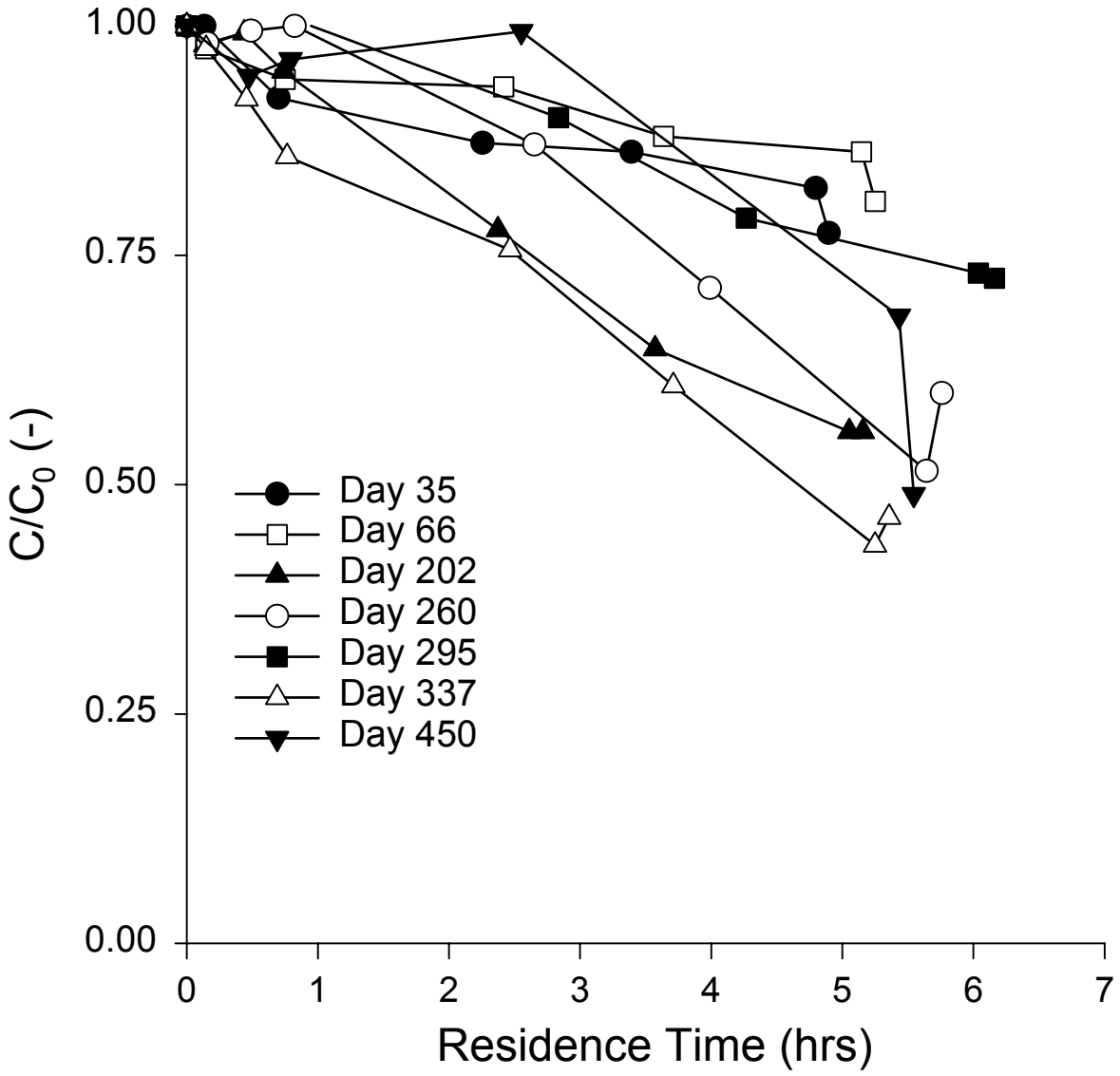

Figure 4.4 Calcium retention within Column G. The influent pH was set to 7.5 $\pm$ 1.0 and the porous medium was 100% Master Builder iron.

Such proton release acts to counteract the proton consumption reactions involved in the corrosion of the iron.

$$Fe^0 + 2H^+ \rightarrow Fe^{2+} + H_2 \quad (4.6)$$

Irrespective of the mechanism for calcium retention, calcium removal from solution affected the solution pH. Nevertheless, as discussed shortly, calcium retention did not alter granular iron reactivity.

Reduction of Chlorinated Alkanes

1,2,3-TCP (Fig. 4.5) and 1,1-DCA (data not shown) were considerably less reactive than TCE. Because 1,1-DCA was only minimally transformed, it was removed from the feed to columns C-E after 197 days (and was never introduced to columns G-J or columns K-O). Interestingly, 1,2,3-TCP and 1,1-DCA degraded only within the initial 10% (~ 4.0 cm) of the column, remaining at essentially constant concentrations thereafter. This pattern persisted for 1,2,3-TCP throughout this study, and was apparent even as the total amount of 1,2,3-TCP degraded decreased from ~ 20% at day 103 to ~ 10% by day 1013. Other column studies (Focht, 1994) have shown that the dechlorination of 1,2,3-TCP is a relatively slow process; nevertheless, we are unaware of previous work that demonstrates removal only within the proximal end of a column. To examine whether TCE or one of its degradation products was inhibiting 1,2,3-TCP reduction, the TCE feed to columns C-E was halted on day 1085, with no discernable effect on the 1,2,3-TCP profiles within the final 15 days of column operation. This suggests that 1,2,3-TCP reduction was not affected by competition for reactive sites from either TCE or its reduction products.

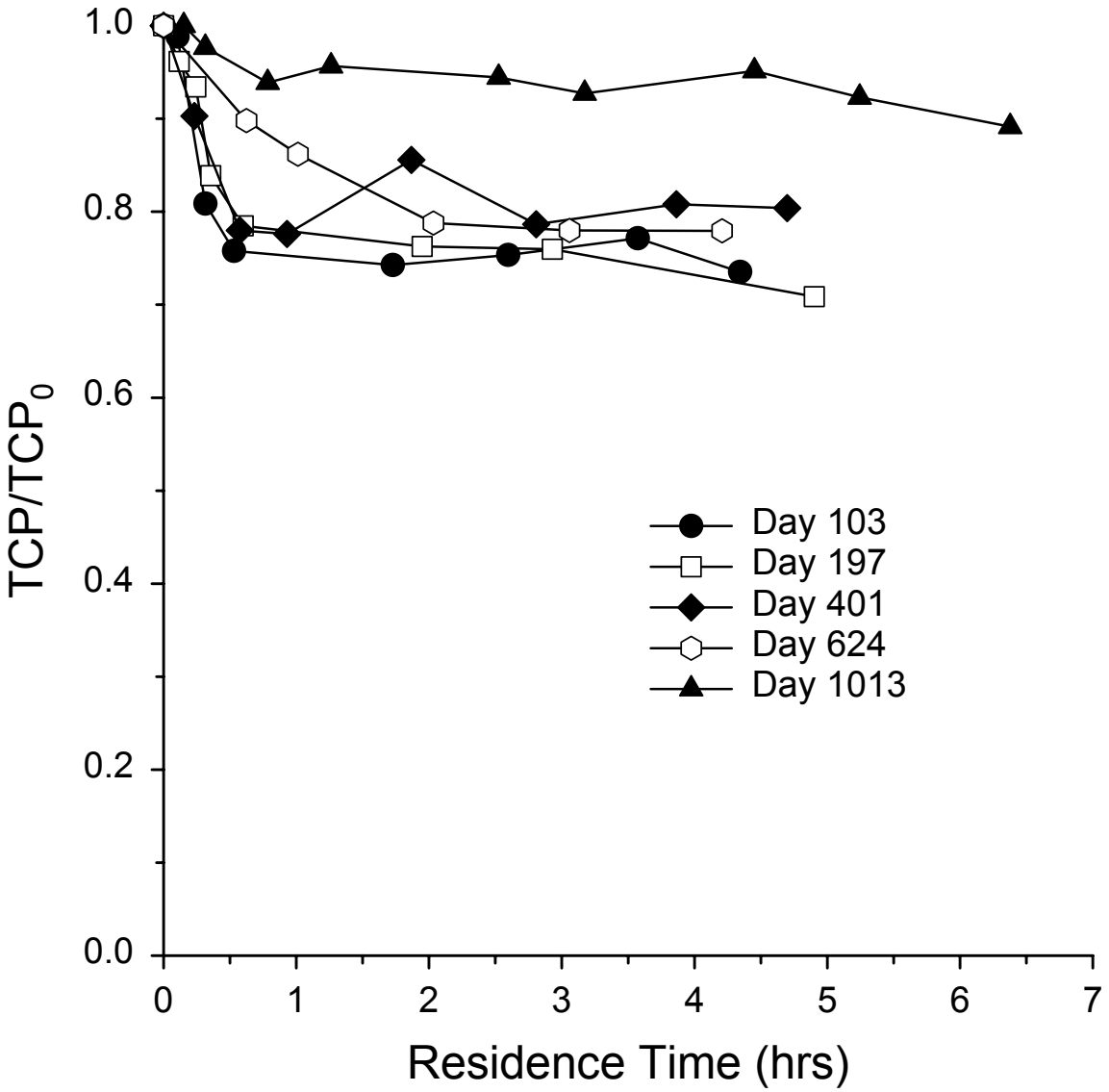

Figure 4.5 1,2,3-TCP profiles for column C. Similar results were obtained with all other columns continually fed 1,2,3-TCP. TCP_0 refers to the measured initial 1,2,3-TCP concentrations. The influent pH for column C was 9.3 ($\pm$ 0.5) and the porous medium was 100% Master Builder iron.

Reduction of TCE

Examples of concentration profiles obtained for TCE in columns C, E, and N are shown in Fig. 4.6. Similar results were obtained for other columns to which these contaminants were introduced on a continuous basis. TCE was efficiently reduced at early times, although degradation rates decreased markedly as the columns aged. This decrease in reactivity occurred as a result of gradual passivation of the iron surface over time. At the proximal end of the columns, which had experienced considerably larger contaminant and co-solute fluxes than the distal end, an apparently unreactive zone grew over time. The rate at which this zone developed appears to depend on solution composition, with the waters containing 20 mM $NaHCO_3$ (column E) and NOM (columns L-O) exhibiting the most pronounced effects. In fact, by day 1013 the unreactive zone for column E occupied ~ 40% of the column.

Overall kinetic coefficients (k_{obs}) for TCE disappearance were determined via eq. 4.1 for each TCE profile; example model fits are provided in Fig. 4.6. Figs. 4.7, 4.8, and 4.9 show the results for columns C-E, G-J, and K-O when TCE was present in a mixture of CHCs, and Fig. 4.10 shows the results for columns A-F under conditions for which TCE was the only organic oxidant. The vertical error bars in these figures reflect the 95% confidence intervals for each k_{obs} value (or in the case of Fig. 4.10, for averaged sets of k_{obs} values) and reflect the extent to which the profiles adhered to pseudo-first-order decay. For the TCE profiles that exhibited a lack of reactivity within the proximal region, the data obtained within the inactive zone (defined as $C/C_0 > 0.9$ for three or more consecutive samples) were neglected in order to obtain reasonable k_{obs} values.

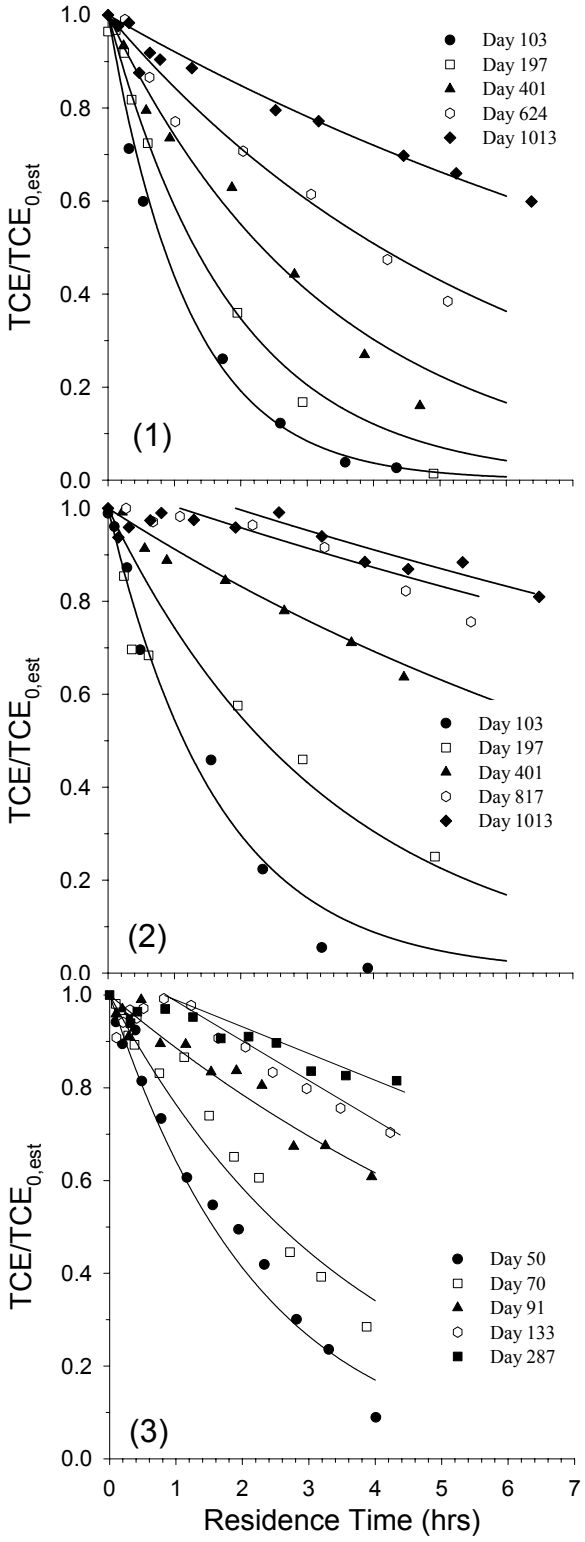

Figure 4.6 TCE profiles for 1) column C, 2) column E, and 3) column N. Curves represent fits to a first-order model. For column E and column N, the later time model fits only applied to data downgradient from the unreactive zone (see text for details). $TCE_{0,est}$ was determined as part of the first-order fitting exercise. The influent pH was ~ 9.3 ($\pm$ 0.5) and the porous medium was 100% Master Builder iron.

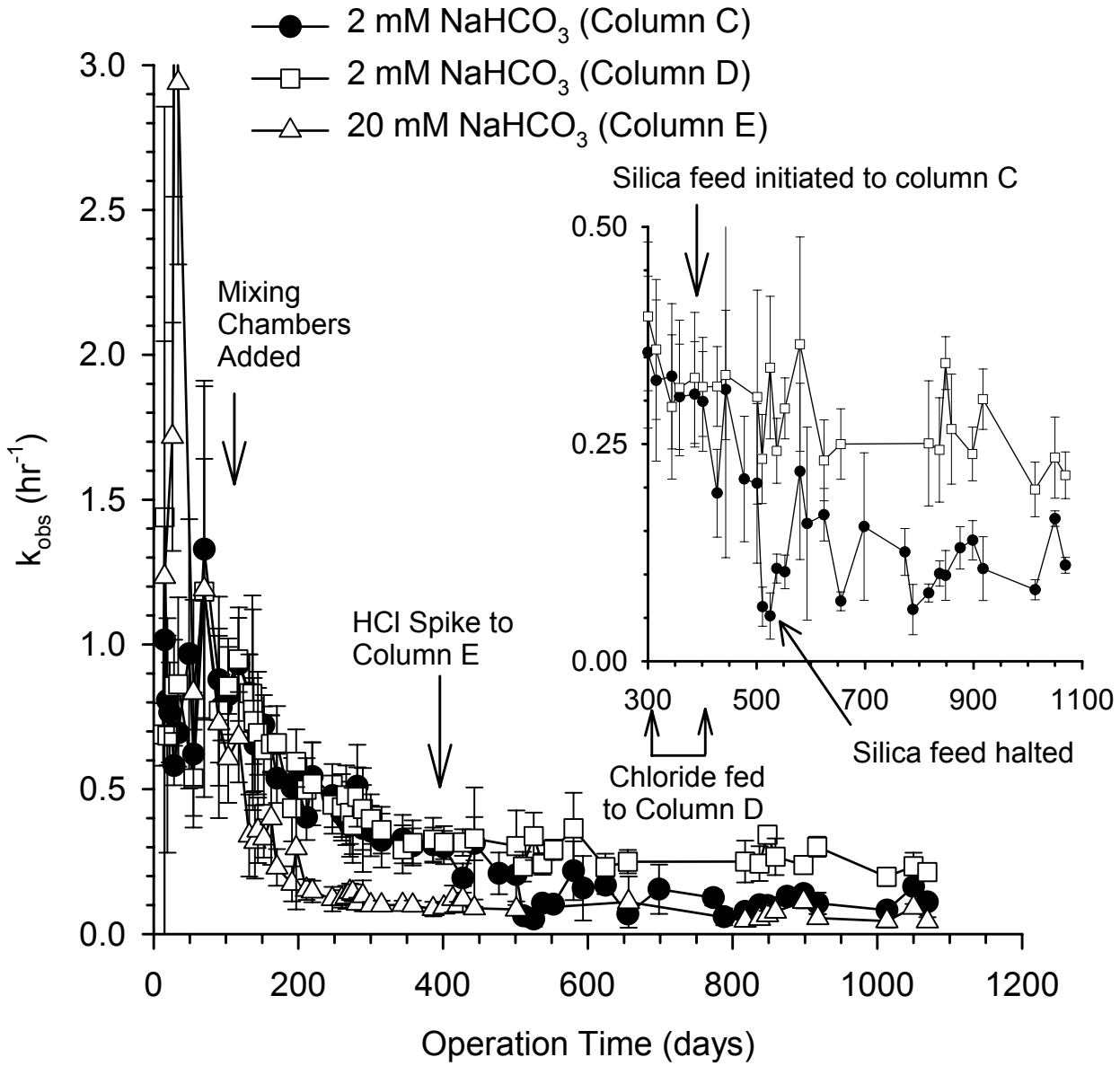

Figure 4.7 Pseudo first-order kinetic coefficients for TCE reduction in columns C-E. The inset depicts the effect of silica on TCE degradation in column C. These columns were continually exposed to a mixture of CHCs for 1100 days. The influent pH to all columns was 9.3 ± 0.5 and the porous medium was 100% Master Builder iron.

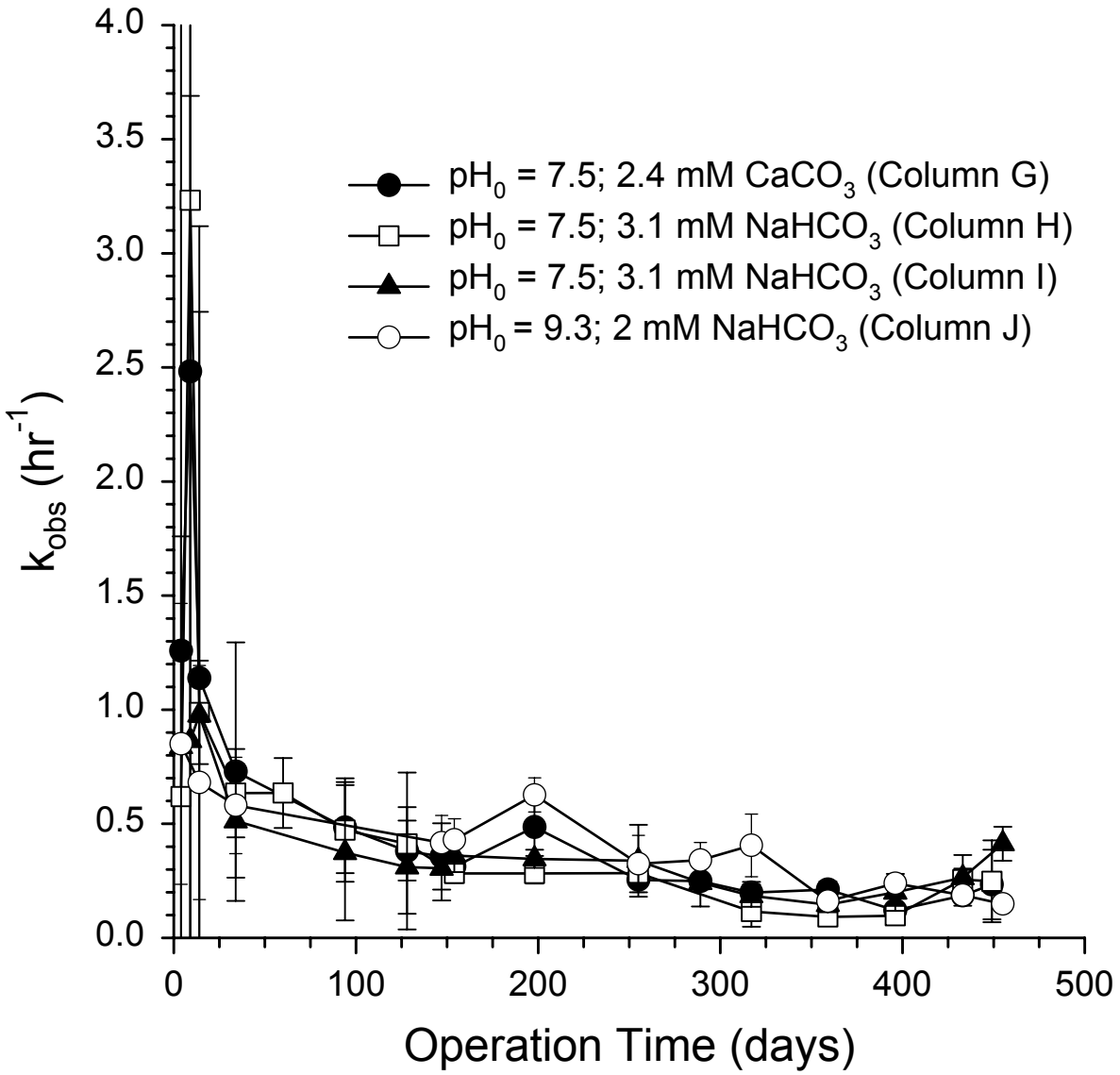

Figure 4.8 Pseudo first-order kinetic coefficients for TCE reduction in columns G-J. These columns were continually exposed to a mixture of CHCs for 475 days. The influent pH to columns G, H, and I was set to 7.5 $\pm$ 1.0 and for column J it was 9.3 $\pm$ 0.5. The porous medium in columns G, I, and J was 100% Master Builder iron and in column H the medium was 92% Master Builder iron/8% albite (w/w).

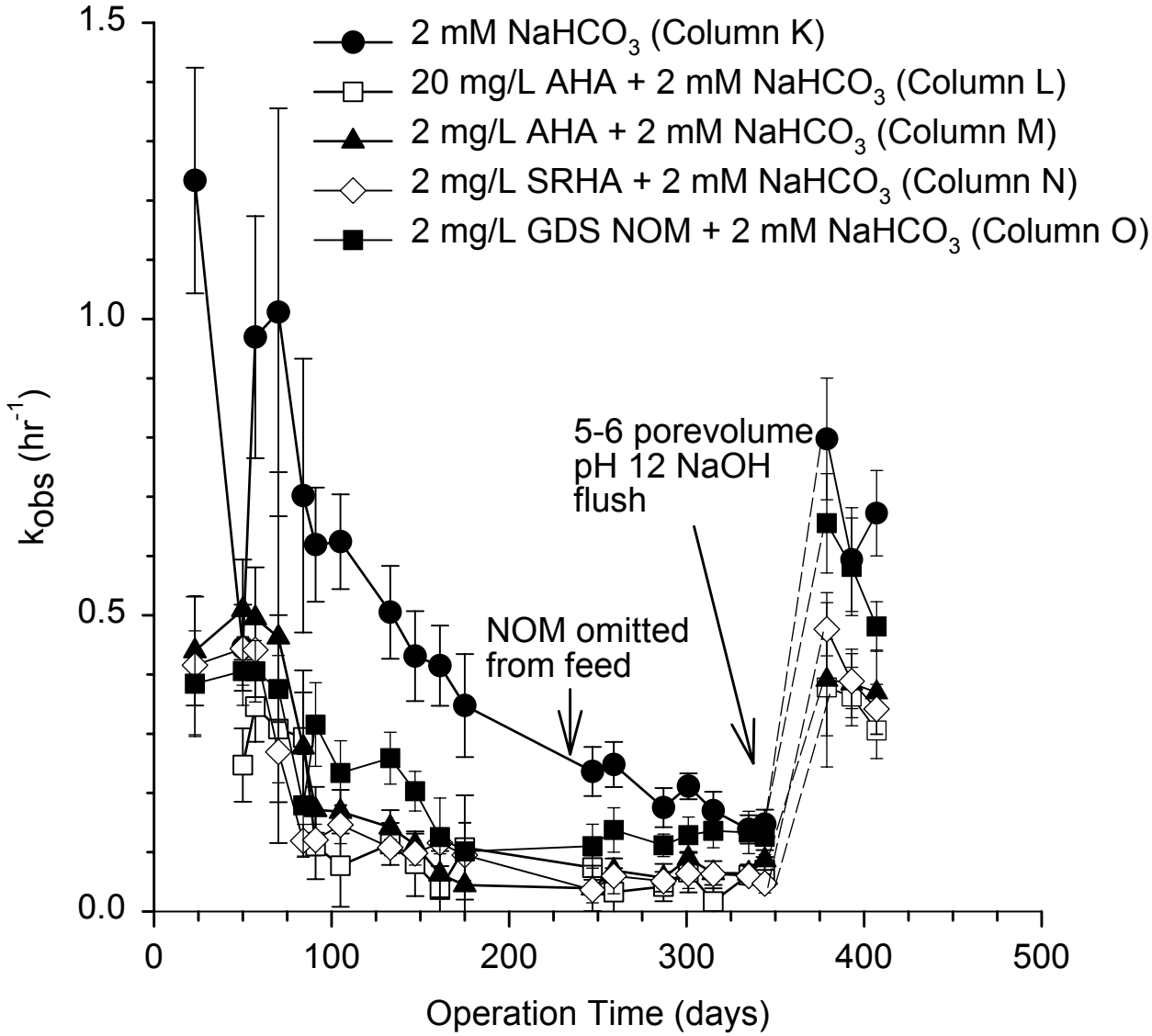

Figure 4.9 Pseudo first-order kinetic coefficients for TCE reduction in columns K-O continually exposed to a mixture of CHCs. Varying concentrations of NOM were fed to the columns as Aldrich Humic Acid (AHA), Suwannee River Humic Acid (SRHA) or Great Dismal Swamp Natural Organic Matter (GDS NOM) for 240 days. On day 240 the NOM was omitted from the feed to columns L-O, on day 290 the 2 mM bicarbonate buffer was omitted (not shown), and on day 345 a 5-6 pore volume alkaline (pH 12) flush was initiated. The influent pH to all columns was 9.3 $\pm$ 0.5 and the porous medium was 100% Master Builder iron.

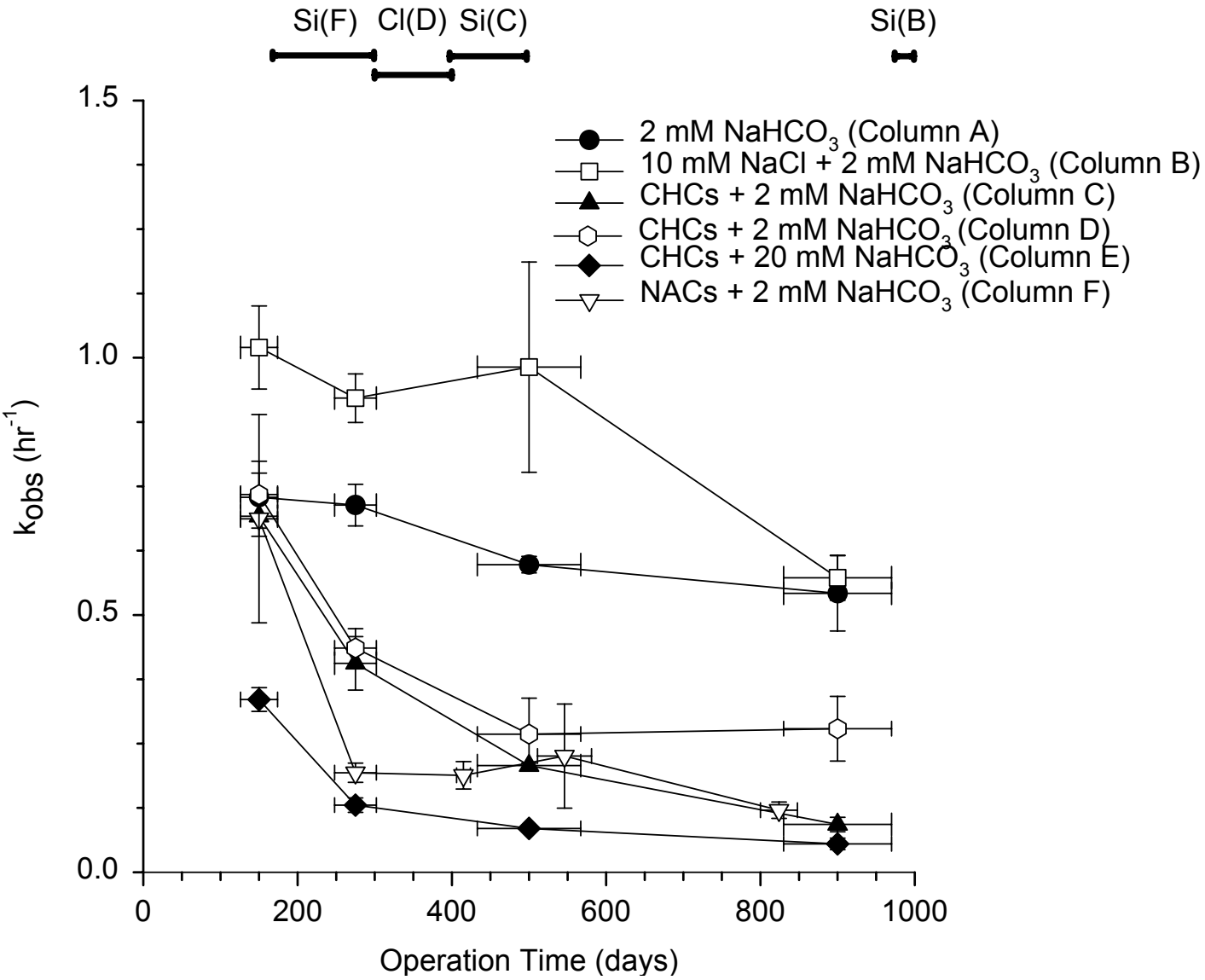

Figure 4.10 Pseudo first-order kinetic coefficients obtained during the 'TCE probe' tests for columns A-F. Each point reflects the average coefficient obtained from 2-4 individual profiles (with the exception of column E during the period of 425-575 days, for which only one profile is shown). As discussed within the text, these averaged coefficients only consider the k_{obs} values acquired under quasi-steady-state conditions. Vertical error bars reflect the 95% confidence interval for kinetic coefficients averaged over the operation period indicated by the width of the horizontal error bars. The legend refers to the normal feed to each column. The bars at the top of the figure indicate periods when the normal feed to each column was augmented with either silica (in column F for days 183-300; in column C for days 409-538; and in column B for days 875-1100) or with chloride (in column D for days 313-409). Not shown within the figure is the 5 mL concentrated HCl spike introduced to column E on day 400. The influent pH to all columns was 9.3 $\pm$ 0.5 and the porous medium was 100% Master Builder iron.

Products of CHC Degradation

Ethane and ethylene were the primary products of TCE degradation, with acetylene appearing as a transient intermediate. Small quantities of 1,1-DCE, *cis*-DCE, and C_4 coupling products (i.e., 1-butene, *cis*-butene, *trans*-butene, *n*-butane) were also typically observed. Trace quantities (< 0.25 μM) of *trans*-DCE and vinyl chloride were only occasionally detected. The TCE products are consistent with β-elimination (Roberts et al., 1996) as the predominant reduction pathway, and corroborate product distributions previously reported for TCE reduction by Master Builder iron (Farrell et al., 2000). Propane, propylene, and trace amounts of allyl chloride were the only identified 1,2,3-TCP reduction products.

Reduction of Nitroaromatic Compounds

Fig. 4.11 shows typical concentration profiles for 2-NT, 4-NA, 4-NAP, and their reduction products in column F. Although iron reactivity towards each of the nitroaromatic compounds decreased over the full duration of this study, the statistical significance of this decrease (at the 95% confidence interval) is difficult to assess (Fig. 4.12). The earliest profiles (< day 30) taken for 2-NT and 4-NA indicated that these species disappeared too quickly to be detectable at the first sampling port (~ 1 cm from column inlet). Nevertheless, the stoichiometric formation of 2-aminotoluene (2-AT) and 4-aminoanisole (4-AA) indicated that 2-NT and 4-NA were reduced by contact with the granular iron with essentially 100% efficiency. Once quasi-steady-state conditions were attained after 49 days, the concentrations of 2-AT and 4-AA remained constant throughout the rest of the column. Prior to that time, significant declines in the concentrations of these products were observed towards the distal end of the column. These

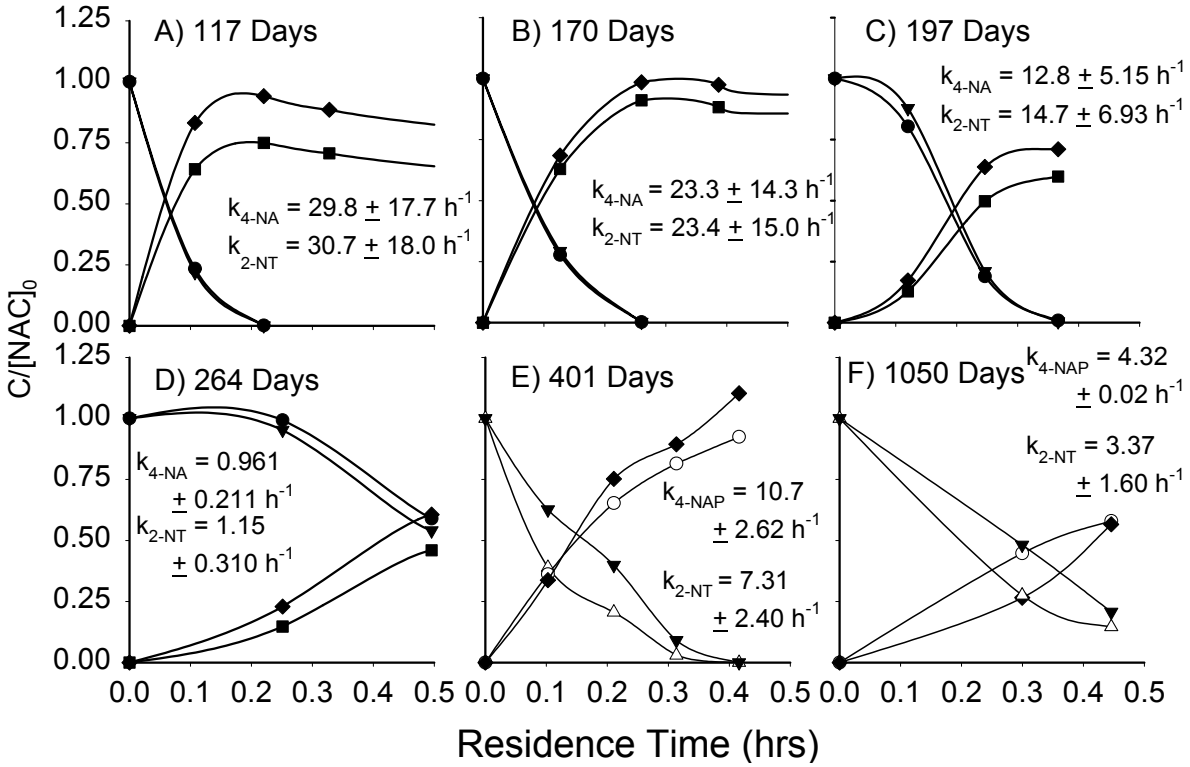

Figure 4.11 Nitroaromatic compound (NAC) profiles for column F for A) 117, B) 170, C) 197, D) 264, E) 401, and F) 1050 days. Concentrations of individual NACs (2-NT, ▼; 4-NA, ●; 4-NAP, △) and their corresponding reduction products (2-AT, ◆;4-AA,■ ; 4-AAP, ○) are normalized to the initial NAC concentrations. Silica was fed to the column during the period 183-300 days and the effect of this feed on NAC reduction is shown in panels C and D). Curves are depicted to show trends and are not representative of model fits. Kinetic coefficients for parent compound reduction were determined using eq. 4.1. The influent pH to the column was 9.3 ± 0.5 and the porous medium was 100% Master Builder iron.

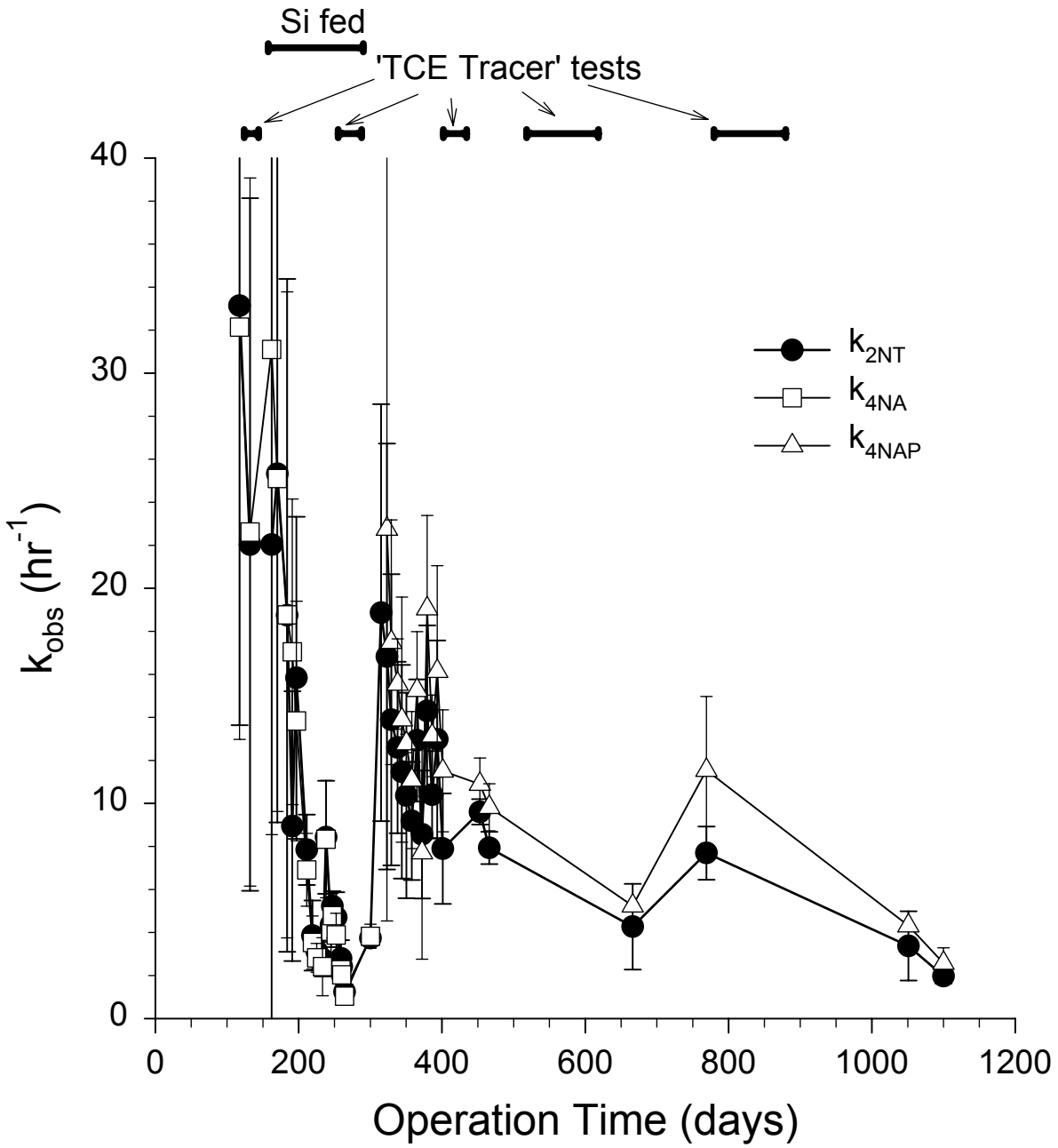

Figure 4.12 Pseudo first-order rate coefficients for reduction of nitroaromatic compounds. Shown for reference are the periods where silica was included in the influent (days 183-300) and also the periods where 'TCE probe' experiments were conducted (days 134-158, 264-291, 401-446, 509-623, 789-848). After day 305 a slight decreasing trend is evident in the observed rate coefficients, although this trend is not significant at the 95% confidence interval and may be the result of errors associated with the calculation of rate coefficients on the basis of a limited number (3-4) of data points. For all of these profiles, the NACs were fully reduced to their respective anilines by the fourth sample port. The influent pH to the column was 9.3 $\pm$ 0.5 and the porous medium was 100% Master Builder iron.

declines were interpreted to reflect sorption of the anilines to the granular iron medium (Banerjee and Malhotra, 1992; Devlin et al., 2000).

By day 117, reactivity towards 2-NT and 4-NA had decreased slightly such that both compounds were detected at the second port (~ 2 cm from inlet). This level of reactivity remained relatively constant until 500 μM silica was introduced to the column influent on day 183. As discussed subsequently, silica addition depressed reactivity for both 2-NT and 4-NA (Fig. 4.11). On day 300, the silica feed was halted, and the 4-NA was replaced with 4-NAP. Following these changes, reactivity towards 2-NT rebounded to the levels observed prior to silica addition. Because the 4-NAP was readily reduced to 4-aminoacetophenone (4-AAP) it can be concluded that the removal of silica from the influent was responsible for the recovered reactivity of the column towards 2-NT. Were 4-NAP not reduced, the rebound in reactivity towards 2-NT could have potentially been due to decreased competition for 2-NT reduction within the column.

DISCUSSION

Comparison of Results Obtained at JHU and AFRL

Columns D and J at JHU and column K at AFRL were run under identical conditions with a constant 2 mM sodium bicarbonate feed and continuous TCE introduction to each throughout their operation. The average variability in the k_{obs} values obtained between these three columns was around 15-25% (Fig. 4.13), with the greatest differences observed between the AFRL column and the JHU columns. This level of variability is not surprising given that the $\tau_x(t)$ value for column K (as well as the other columns at AFRL) was inferred from periodic flow measurements only and was not computed by the more sensitive ^3H_2O tracer approach employed

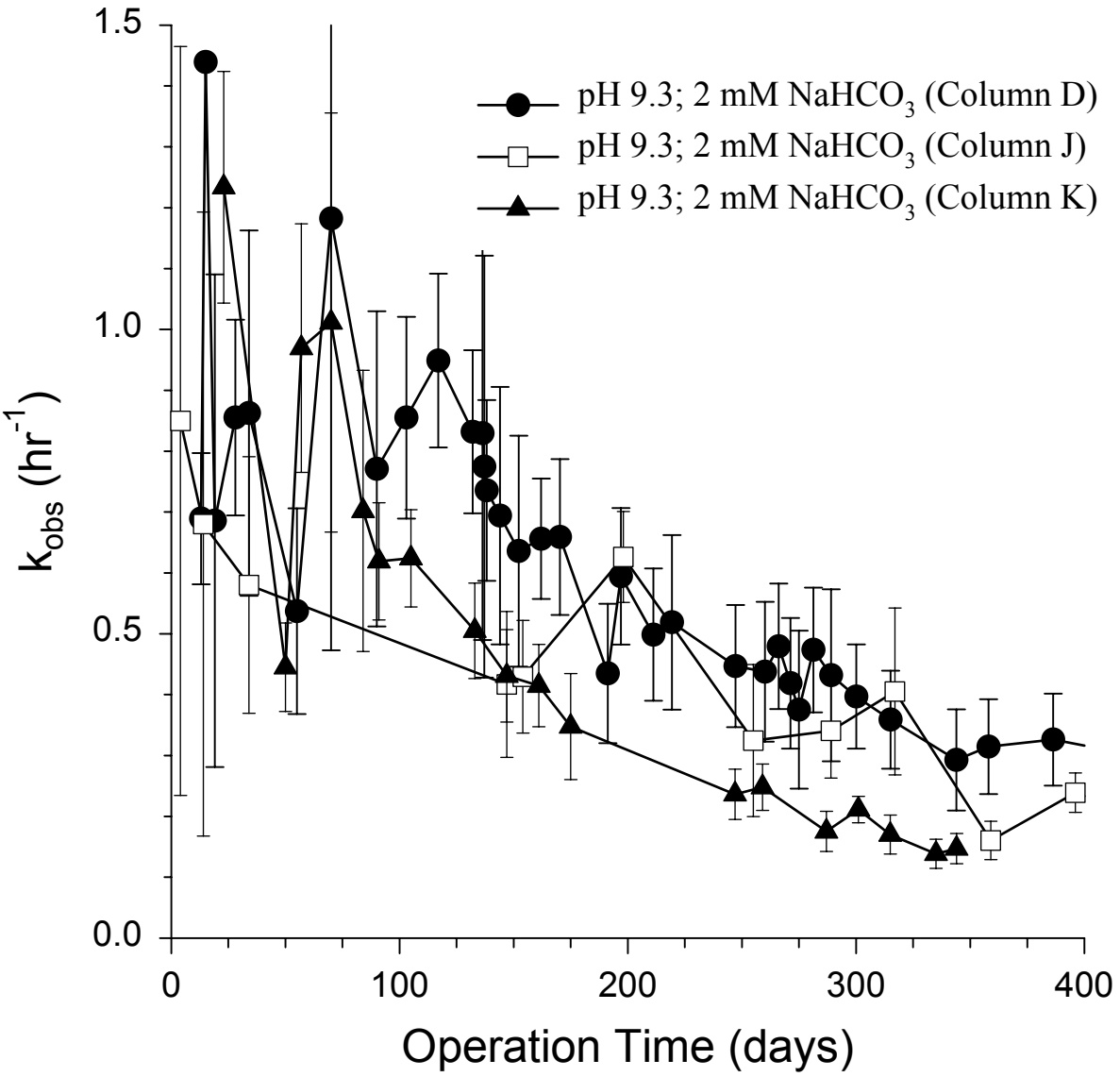

Figure 4.13 Comparison of pseudo first-order rate coefficients obtained with columns D, J (operated at JHU) and K (operated at AFRL). The overall average variability between columns was approximately 15-25%. As noted, the influent pH to the columns was 9.3 $\pm$ 0.5 and the porous medium was 100% Master Builder iron.

for columns A-F and G-J. This comparison therefore suggests that any observed deviations between k_{obs} values for any two columns that are greater than 15-25% are significant, and reflect effects other than the normal experimental error associated with replicate columns.

Effect of Influent pH on Reactivity

Prior work has suggested that a decrease in solution pH may enhance granular iron reactivity towards organohalides (Matheson and Tratnyek, 1994). As such, the lower influent pH for columns G, H, and I would be expected to enhance reactivity within the proximal portion of the column (i.e., the region where the porewater pH is below the quasi-stable effluent value). Nevertheless, a comparison (Fig. 4.8) of the rate coefficients calculated for columns I (influent pH ~ 7.5; 2 mM $NaHCO_3$) and J (influent pH ~ 9.3; 2 mM $NaHCO_3$) indicates that pH appeared to have little if any effect on overall column reactivity. Throughout their operation lifetimes, both columns exhibited similar levels of reactivity. Nor were significant differences evident in the activity of the iron present within the proximal region of column I relative to its distal portion (i.e., a single exponential term readily fit all of the data from a given profile). These results suggest that if any pH effects exist, their role in altering iron reactivity over the long term is quite small.

Effect of Continuous vs. Intermittent TCE Exposure on Granular Iron Reactivity

The quasi-steady-state k_{obs} values obtained in columns C-E during the 'TCE-probe' experiments (i.e., the periods during which TCE alone was fed; Fig. 4.10) were very similar to those obtained either immediately before or after such an experiment in the presence of a mixture of organohalides (Fig. 4.7). This indicates that TCE reactivity was not influenced by the presence

of the other CHCs in the feed. In other words, no competitive effect of 1,2,3-TCP or 1,1-DCA on TCE reduction was evident.

Interestingly, the initial k_{obs} values acquired during a 'TCE-probe' experiment, but prior to the attainment of quasi-steady-state conditions (k_{obs} varying by less than 15% for replicate profiles) were consistently larger than those obtained once steady state was reached (Fig. 4.14). Because the influent TCE concentration did not change appreciably when switching from the mixed CHC feed to the 'TCE-probe' feed, this short-lived apparent enhancement may reflect losses incurred by TCE sorption to unreactive sites previously occupied by 1,2,3-TCP, rather than to reaction. Once unreactive sites were fully occupied by TCE, the TCE rate coefficient returned to that obtained prior to the onset of a 'TCE probe' test. These transient sorptive losses illustrate the previously described (Burris et al., 1998) need to attain quasi-steady-state conditions when evaluating contaminant remediation by granular iron materials that contain significant quantities of unreactive yet sorptive sites.

Rate coefficients obtained during the TCE probe tests for column A were considerably (up to 6-fold) larger than those obtained for columns C and D during the same intervals (Fig. 4.10). The principal difference between these columns was that CHCs were typically absent from the feed to column A; it therefore appears that the additional deterioration in the performance of columns C and D can be attributed at least in part to continuous exposure to CHCs. This suggests that the concentration of contaminants undergoing treatment may introduce additional passivation (beyond that resulting from reactions involving the iron, water, and co-solutes) that significantly reduces granular iron longevity.

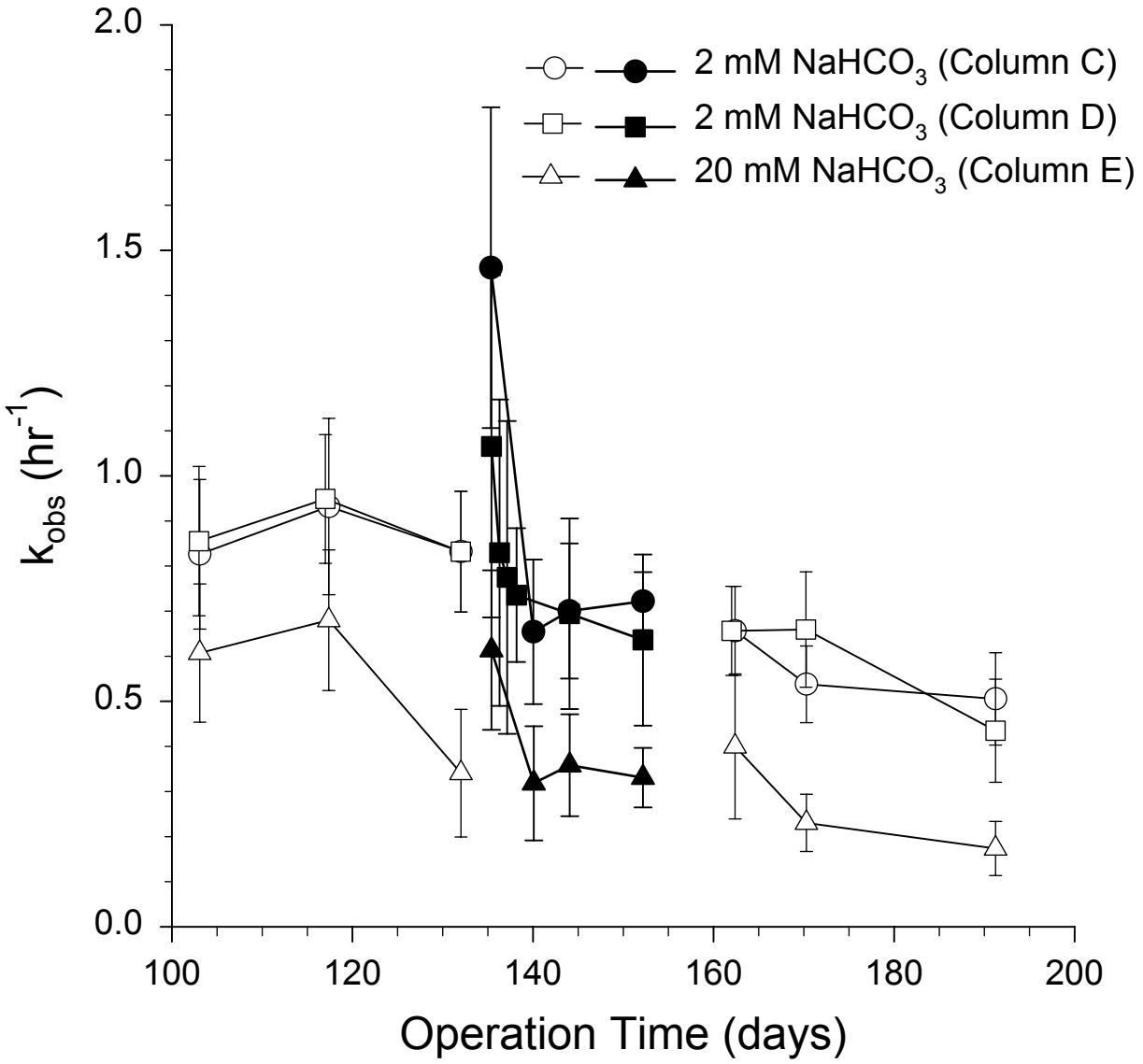

Figure 4.14 Example illustrating the initial variability of k_{obs} values obtained during a typical 'TCE-probe' experiment. Open symbols represent rate coefficients determined while TCE was fed in a mixture of CHCs and closed symbols represent rate coefficients determined during a 'TCE-probe' experiment in which TCE was the only organohalide present. For all three columns, k_{obs} declined significantly between the first and second profiles. As described within the text, these transient declines are consistent with the sorption of TCE to non-reactive sites previously occupied by 1,2,3-TCP. The influent pH to the columns was 9.3 $\pm$ 0.5 and the porous medium was 100% Master Builder iron.

Effect of Co-Solutes on Granular Iron Reactivity

Influence of Sodium Bicarbonate Concentration

Column E, which was exposed to 20 mM bicarbonate, exhibited slightly greater reactivity during the first 90 days of operation than either columns C or D, which were exposed to only 2 mM bicarbonate (Fig. 4.7); nevertheless, this higher level of reactivity was not sustained indefinitely. Rate coefficients for column E declined rapidly to the point where after three months, it was substantially less reactive than either column C or D. The initial reactivity enhancement observed for Column E is consistent with the corrosion promoting ability of carbonate (Gui and Devine, 1995; Reardon, 1995; Agrawal and Tratnyek, 1996; Gu et al., 1999). It has been suggested that carbonate complexes the Fe(II) generated during iron corrosion to form the aqueous species $FeHCO_3^+$ and $Fe(HCO_3)_2^0$ (Castro et al., 1991); the stability of these species has been hypothesized to enhance the corrosion process.

The longer-term declines in reactivity observed for columns C-E can be attributed to the combined effects of surface passivation resulting from contaminant and water reduction and the gradual formation of carbonate-bearing precipitates on the granular iron surface. Occlusion of reactive sites by precipitation of siderite and other carbonate-containing phases has previously been hypothesized (Agrawal and Tratnyek, 1996) to reduce reactivity, and could explain the more rapid deterioration in the performance of column E, which had a higher influent bicarbonate concentration. More extensive precipitation of carbonate phases in column E is supported by experimentally-derived estimates of precipitate mass (as discussed in Chapter 3) and by the more rapid changes in the color of column E. Over time, all columns evinced a change in color from an initial dark gray/black to a lighter gray, consistent with the precipitation

of carbonate bearing precipitates (Sivavec et al., 1995). These color changes were not instantaneous, but instead progressed slowly from the column inlet toward the distal end.

Influence of Calcium Carbonate vs. Sodium Carbonate

Of the fifteen columns used in this study, fourteen were fed an influent solution containing sodium bicarbonate and one, column G, was fed 2.4 mM $CaCO_3$. This column was operated with a $CaCO_3$ buffer to test the hypothesis that calcium carbonate buffered waters might exhibit a different level of reactivity than sodium bicarbonate buffered waters. As discussed previously, calcium ion was retained within this column; nevertheless, as shown in Fig. 4.8 this retention did not appear to affect column reactivity. This result suggests that although calcium retention does occur, its effect on granular iron reactivity is minimal.

Influence of a Hydrochloric Acid Pulse

To evaluate whether dissolution of an iron (hydr)oxide/iron carbonate passive film would restore reactivity, a 5-mL pulse of concentrated hydrochloric acid was applied to column E on day 407. This pulse resulted in vigorous gas evolution, the release of ~ 1.7 g of soluble iron, and a drop in effluent pH from 9.3 to 4.8 within the first seven hours. This pH drop was short-lived and the effluent pH rebounded to 9.3 within 32 hours. The release of soluble iron is consistent with the acid-catalyzed dissolution of iron (hydr)oxides (Stumm, 1992) and iron carbonates (Wang and Reardon, 2001), thereby providing evidence that the passive film on the granular iron surface was at least partially dissolved, although we note that acid addition could also have led to the dissolution of the granular iron itself. The value of k_{obs} increased slightly immediately following acid addition, but the acid pulse did not result in any long-term rate enhancement.

Presumably the pulse was unable to dissolve enough of the passive film to exert any lasting benefit.

Influence of Chloride

The influence of chloride on TCE degradation was evaluated by conducting two separate experiments. In the first, 10 mM chloride was continually fed to column B, whose reactivity was periodically examined via intermittent 'TCE-probe' experiments. The results indicate that up through the third probe test, the presence of chloride enhanced the reactivity of column B (relative to column A) towards TCE (Fig. 4.10) by as much as 75%. By the fourth probe test (days 789-848, immediately prior to introduction of silica to column B), however, the reactivities of columns A and B were statistically indistinguishable (at the 95% confidence level). These longer-term results suggest that the corrosion-promoting ability of chloride decreased over time, similar to our prior observations with 2-nitrotoluene (Klausen et al., 2001).

The second experiment pertaining to the role of chloride involved adding 10 mM NaCl to the normal 2 mM sodium bicarbonate feed to column D for days 313-409, while maintaining the feed to column C at 2 mM sodium bicarbonate (Fig. 4.7). Despite the activating effect of chloride on column B, a comparison of the k_{obs} values obtained for columns C and D during this period reveals that chloride addition had little if any effect on the TCE reduction rate.

The disparity between the results for columns B and D could stem from differences in the composition of the passive films that formed on the iron surfaces within each column. If chloride is present while the passivating film is being formed (as was the case with column B), the film may have a composition that differs from that formed in the presence of the low chloride concentrations (< 300 μM) that result from CHC degradation (i.e., for column D). Previous studies have suggested that the passive film formed in chloride-containing bicarbonate solutions

more readily undergoes localized attack by chloride than the passive film formed in bicarbonate solution alone (MacDougall and Graham, 1995; Simard et al., 1998). The implication of these observations is that the induction time required for corrosion pit formation can be extremely long for passive films formed in the absence of chloride. It is therefore possible that the chloride amendment to column D was of insufficient duration to produce any discernable outcome.

Influence of Silica

Two types of experiments were conducted to examine the effect of silica on granular iron reactivity. In the first, the normal feeds to columns F (days 183-300), C (days 409-538), and B (days 925-1100) were augmented with 500 μM sodium metasilicate (Na_2SiO_3). This test was conducted to determine how the continuous input of relatively high concentrations of silica would affect granular iron reactivity. In the second test, the aluminosilicate mineral albite ($Na(Si_3Al)O_8$) was admixed with the granular iron medium (at a 92% Master Builder iron/8% albite mass ratio). This test was conducted to ascertain whether sufficient quantities of silica could leach from the albite so as to adversely effect reactivity. Previous studies (Powell and Puls, 1997) have suggested that the admixing of aluminosilicate minerals such as albite could enhance granular iron reactivity, and we wanted to test that hypothesis.

Silica was found to be retained by the granular iron in each column to which it was added, as evidenced by its slow breakthrough, as well as by observations of decreasing silica porewater concentrations between the influent and effluent ends of a column (Fig. 4.15). For the column with admixed albite, the porewater silica concentrations increased between the proximal and distal ends of the column (Fig. 4.16). This is consistent with the *in-situ* dissolution of albite (Blum and Stillings, 1995):

$$2\ NaAlSi_3O_8 + 2\ H^+ + 9\ H_2O \Leftrightarrow Al_2Si_2O_5(OH)_4 + 4\ H_4SiO_4\ (aq) + 2\ Na^+ \qquad (4.7)$$

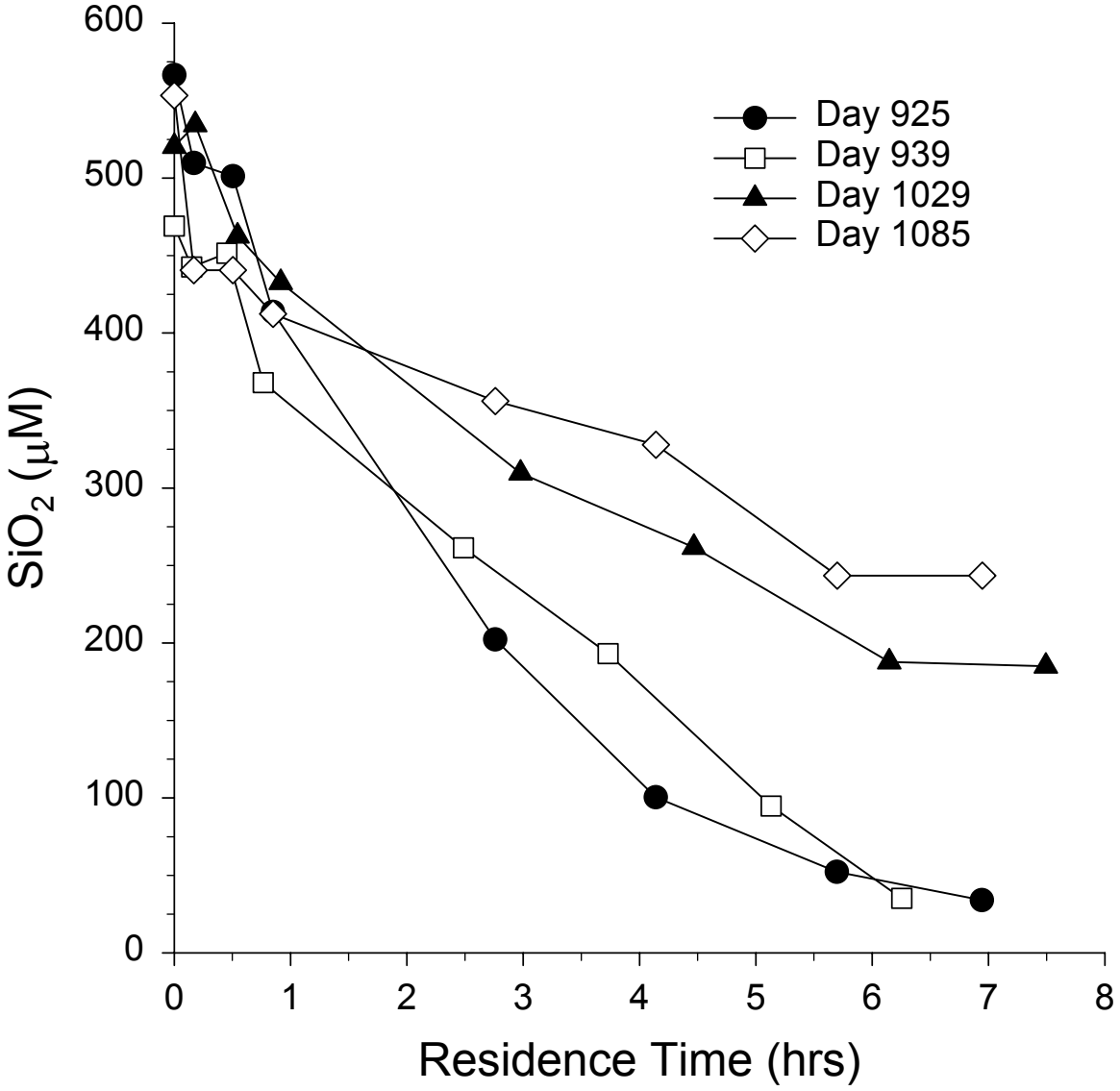

Figure 4.15 Dissolved silica profiles for column B. Silica was introduced to the feed of this column on Day 925 until termination of experiments on Day 1100. As illustrated, the silica pore-water concentration declined significantly from the influent to the effluent end of the column. The steady increase in the effluent silica concentration from day 925 to day 1085 is indicative of the slow saturation of sorptive sites within the porous medium. The influent pH to the column was 9.3 $\pm$ 0.5 and the porous medium was 100% Master Builder iron.

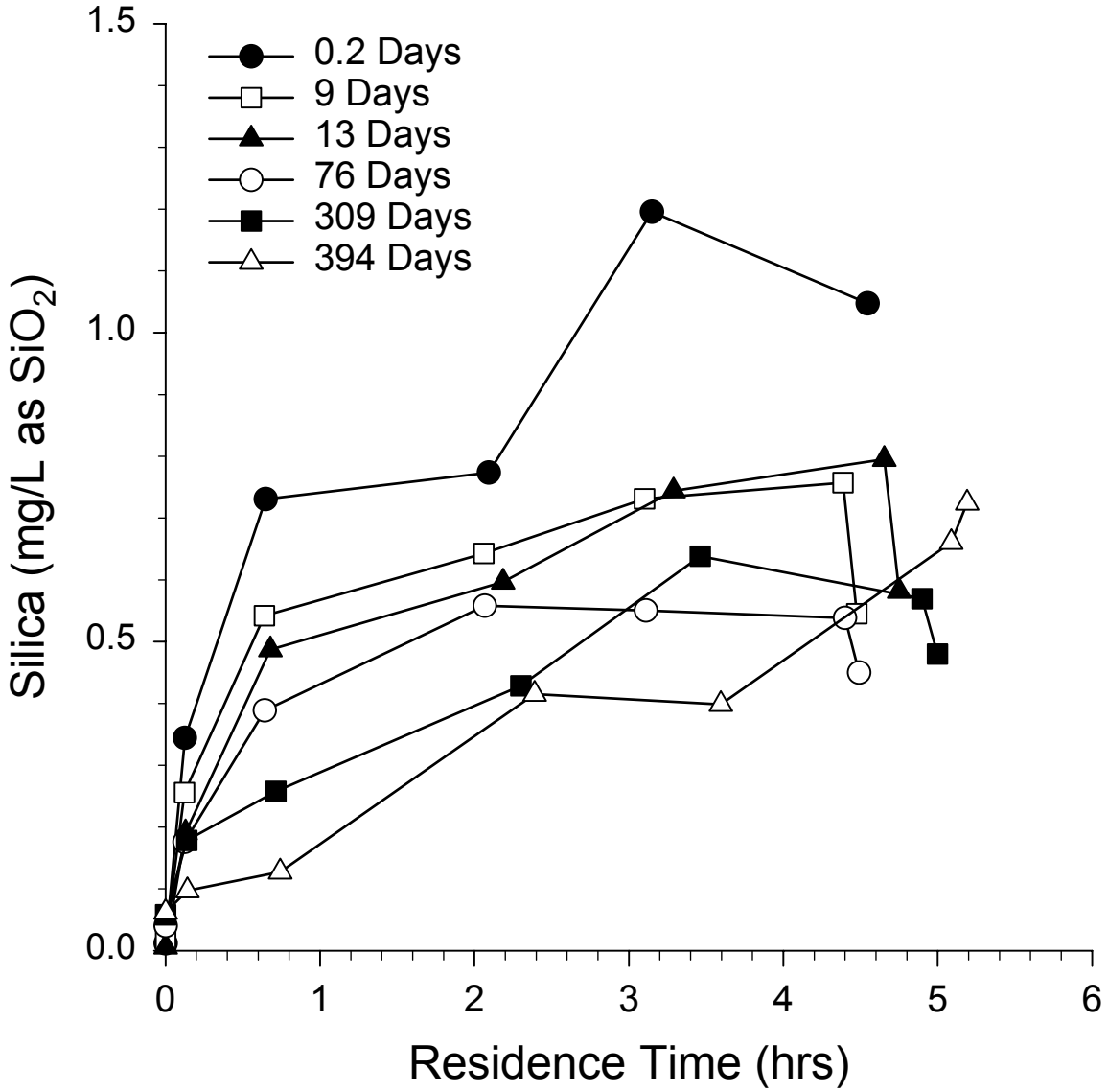

Figure 4.16 Silica porewater concentrations within column H as a function of time. The influent pH to the column was 7.5 ± 1.0 and the porous medium was 92% Master Builder iron/8% albite (w/w).

Interestingly, it appears over the long term that the albite dissolution rate has slowed, as evidenced by the observed decrease in porewater silica concentrations with time. Were silica dissolution occurring at a constant rate, one would expect that the porewater silica concentrations would either stay constant or would increase over time.

The addition of silica to the influent of columns F and C resulted in a pronounced loss of reactivity towards the NACs (Fig. 4.11) and to a lesser extent towards TCE (Figs. 4.3 and 4.6). Reactivity losses were most pronounced near the influent end, where silica retention predominately occurred, but were nonetheless manifested throughout each column. Upon discontinuing silica from the feed to column F, dissolved silica concentrations measured at the column outlet decreased slowly and the reactivity towards the NACs recovered (Fig. 4.11). For column C, the discontinuation of the silica feed led to an initial rebound in reactivity (Fig. 4.7), although it never recovered to the level displayed by the otherwise identical column D. For column B, addition of silica to the feed also led to significant deterioration (up to three-fold) in reactivity (Fig. 4.17). In contrast to the silica effects observed in columns B, C, and F, the dissolution of albite did not significantly alter granular iron reactivity (Fig. 4.8). Apparently not enough silica leached from the albite and subsequently adsorbed to the iron surface to have a discernable passivating effect. While porewater silica concentrations are not a true measure of the amount of silica present at the iron surface, for the albite system the porewater silica concentrations were roughly an order of magnitude less than those measured in the columns where silica was present in the feedwater.

Within the columns fed 500 μM sodium metasilicate, we hypothesize that silica precipitates or adsorbs to the interfacial region in sufficiently high concentrations so as to passivate reactive sites. Silica most likely initially forms monomeric surface complexes

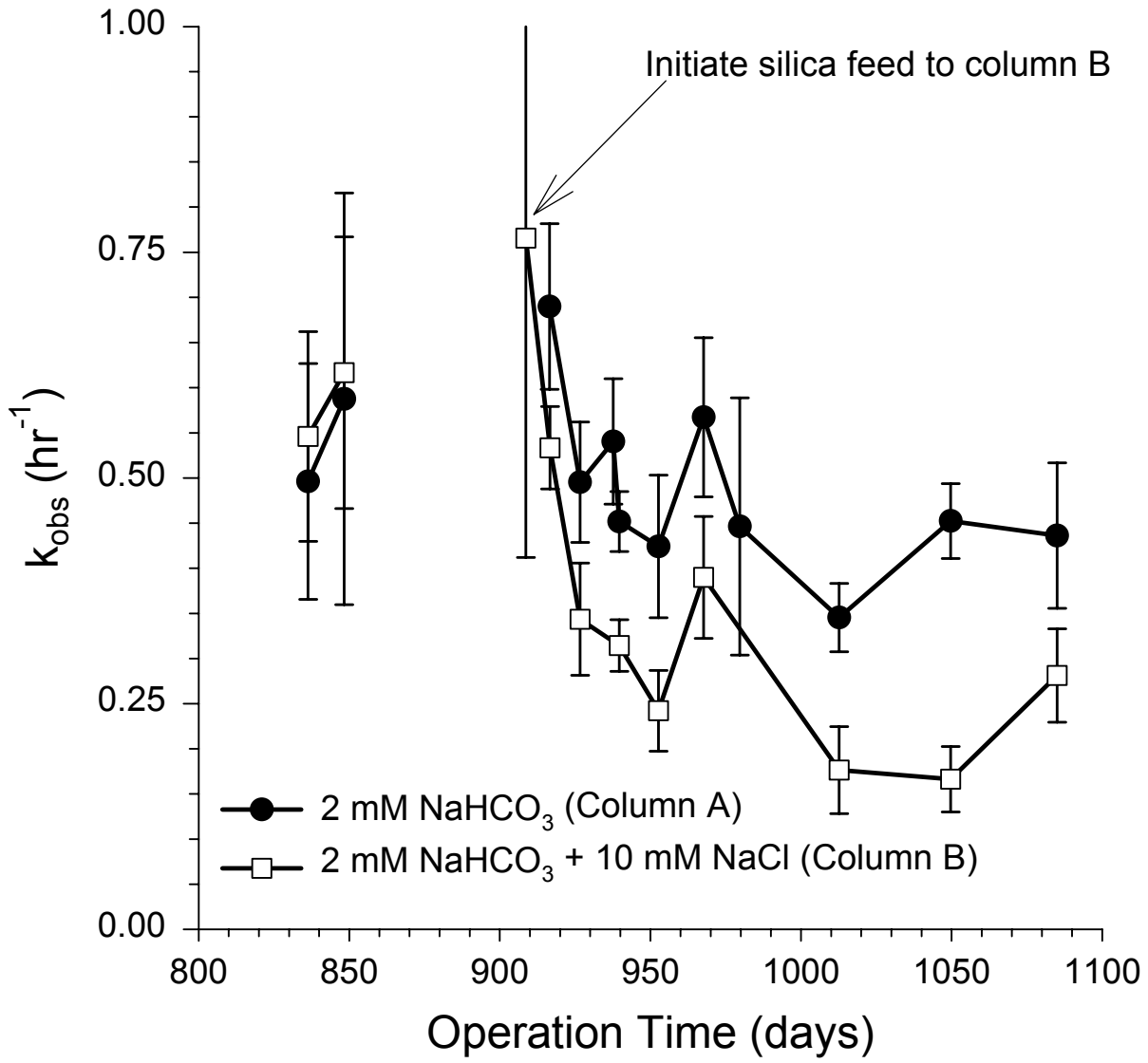

Figure 4.17 Comparison of the reactivity of column B (fed silica) to column A (not fed silica). This test was conducted to verify that silica addition did lead to a significant (at the 95% confidence interval) decline in iron reactivity towards TCE. TCE was fed to columns A and B from day 789-848 and then again from day 918-1100. The influent pH to the column was 9.3 $\pm$ 0.5 and the porous medium was 100% Master Builder iron.

($>FeH_3SiO_4$, $>FeH_2SiO_4^-$, and $>FeHSiO_4^{2-}$) (Sigg and Stumm, 1981; Hansen et al., 1994; Swedlund and Webster, 1999; Marmier and Fromage, 2000) that polymerize over time (Swedlund and Webster, 1999). The net effect of these processes is the development of a silica film or gel on the iron surface that physically hinders contaminant access to active sites and that may also alter the electronic environment of reactive sites (Becker et al., 2001). In the column containing admixed albite, the amount of silica produced as a result of base-catalyzed dissolution is presumably too small to lead to a discernable passivation effect. At albite to iron ratios higher than that employed here it is possible, however, that albite dissolution could inhibit iron reactivity. Additional detailed studies of silica effects on reactivity and selectivity in reactions of organohalides with granular iron are currently under way in our laboratory.

Influence of NOM

The presence of NOM adversely affected reactivity towards TCE (Fig. 4.6, Fig. 4.9). For a given operation time, the reactivity in each column fed NOM was substantially less than that in the "NOM-free" columns. In fact, by day 100 the k_{obs} values in the presence of NOM were roughly half those for comparable columns not fed NOM (columns C, D, and K). Although the performance of all columns deteriorated over time, rate coefficients for TCE reached low levels (~ 0.1 hr^{-1}) at early times (~ 150 days) in columns fed NOM, whereas they reached that level only after ~ 400 days in columns C, D, J, and K.

NOM is known to readily sorb to iron (hydr)oxides (Tipping, 1981; Davis, 1982) and many (hydr)oxide phases are typically present on the granular iron surface (Odziemkowski and Gillham, 1997). NOM sorption to iron surfaces is dictated by nonspecific surface interactions, free energy changes associated with NOM solvation, electrostatic interactions between the oxide surface and the NOM molecule, and the specific interactions that occur between functional

groups in the NOM molecules and the oxide surface (Davis, 1982; Gu et al., 1994; Hering, 1995; Avena and Koopal, 1998). Under the alkaline pH range typically observed in PRBs, it is anticipated that specific interactions will dominate NOM sorption since both the NOM molecules and the iron hydr(oxides)/carbonates present in the interfacial region are predominantly negatively charged. The net result of NOM sorption is that species such as TCE that are expected to form weakly bonded surface complexes (Johnson et al., 1998; Arnold and Roberts, 2000b) may be competitively excluded from the surface as a result of the stronger NOM-iron interactions. Observed declines (Johnson et al., 1998) in the rate of CCl_4 reduction in the presence of simple organic ligands (e.g., catechol, ascorbate, EDTA, acetate) that form complexes on the zero-valent iron surface support this hypothesis. Another possibility is that NOM sorption may inhibit surface complexation of the Fe(II) produced by the corrosion process (Colon et al., 1997; Colon et al., 1998), thereby lowering the reductive capacity of the columns.

Of the three types of NOM studied in this work, GDS NOM exhibited the least inhibitory effect on TCE degradation. After 100 days, with the exception of two data points, reaction rates determined for this column were consistently higher than those obtained in columns fed with either AHA or SRHA. This may reflect the differences in the character of the NOM. Whereas AHA and SRHA are both humic acids, GDS NOM is predominantly composed of fulvic acids (Dempsey, 1983). It is well established that humic acids sorb to iron (hydr)oxide surfaces more strongly than do fulvic acids (Murphy et al., 1990); this enhanced sorption may have led to the earlier declines in reactivity observed for AHA and SRHA relative to GDS NOM.

NOM was omitted from the influent to columns L-O on day 240; nevertheless, reactivity towards TCE did not rebound (Fig. 4.8), suggesting that the inhibitory effect of NOM did not stem from reversible competition between NOM and TCE for reactive sites. Once NOM sorbs to

an iron (hydr)oxide surface, it is known to be very difficult to remove unless the pH is increased (Gu et al., 1994; Avena and Koopal, 1998). In an attempt to restore column reactivity, an alkaline flush of 5-6 pore volumes of a pH 12 NaOH solution was introduced on day 345 to columns K-O. (During this period, the CHC feed was eliminated.) As a result of this alkaline flush, adsorbed organic carbon was mobilized and significant quantities of dissolved NOM were measured in the column effluent (Table 4.1). For columns L-O, the mass of organic carbon eluted as a result of the alkaline flush (28-134 mg; Table 4.1) was significantly greater than that eluted from column K (3 mg). The organic carbon extracted from column K, the nominally "NOM-free" control, apparently reflects the sorption of trace quantities of NOM present in the influent water. For columns L-O, the recovered masses range from 3.6% to 18% of the total organic carbon fed to each column. Following the pH 12 flush, it was observed that reactivity rebounded substantially for all columns. Interestingly, column K (the "NOM-free" control) rebounded the most, followed by the columns to which NOM had been added. The reason for the strong rebound of the control column is not clear at this time.

Table 4.1 Organic carbon extracted using 5-6 pore volumes of pH 12 NaOH

Column	Description	Mass Organic Carbon Recovered (mg)[a]	% of Organic Carbon Added (minus control)
K	2 mM $NaHCO_3$	3	n/a
L	2 mM $NaHCO_3$ + 20 mg/L AHA	134	3.6%
M	2 mM $NaHCO_3$ + 2 mg/L AHA	28	6.9%
N	2 mM $NaHCO_3$ + 2 mg/L SRHA	44	11%
O	2 mM $NaHCO_3$ + 2 mg/L GDSW NOM	69	18%

[a] Corrected for extractable background organic carbon present within Master Builder iron (4 mg).

NAC Reduction

Despite significant differences in their one-electron reduction potentials ($E_h^{1'}$; 2-NT = -0.590 V, Schwarzenbach et al., 1990; 4-NAP = -0.360 V, Schwarzenbach et al., 1990 or half-wave potential ($E_{½}$; 4-NA = -0.53 V, Meites et al., 1982), k_{obs} values for each of the NACs were virtually indistinguishable. Previous studies (Agrawal and Tratnyek, 1996; Devlin et al., 1998) suggested that such a lack of correlation between $E_h^{1'}$ (or $E_{½}$) and the kinetics of NAC reduction indicates that electron transfer is not the rate-determining process. These investigators have hypothesized that other potential rate-controlling steps (e.g., precursor complex formation, successor complex breakdown, mass transport limitations) govern observed reaction rates. Scherer et al. (2001) have recently demonstrated using a rotating disk electrode that nitroaromatic compounds can be subject to mixed mass transfer and surface kinetic control. Their conclusions, however, may not be applicable to granular iron materials, such as Master Builder ion, in which the iron core is covered by a thick oxide coating. The k_{obs} values for the NACs obtained herein were within an order of magnitude of calculated k_{max} values for external mass transfer limitations, and we hence cannot rule out the possibility that external mass transfer effects influenced at least initial reaction rates. That rates of NAC reduction did decrease during the first months of operation does, however, suggest that reactions were under at least partial reaction control rather than exclusively external mass transfer control, by day ~ 183 if not earlier.

Comparison of the Reactivity of CHCs to NACs

Of the six organic contaminants examined in this study, the three NACs were significantly more reactive than the three CHCs. For 2-NT, 4-NA, and 4-NAP, the reactivity of the iron was so high that, in the absence of silica, each was completely reduced to the respective

aniline within the first 1-4 cm of the column. In contrast, the reactivity of the CHCs was considerably lower, with 1,1-DCA and 1,2,3-TCP degraded only within the front ~ 4.0 cm of the column, and with TCE degraded throughout the column but at a significantly slower rate than the NACs.

Our results suggest that TCE, 1,2,3-TCP, and the NAC pairs (either 2-NT/4-NA or 2-NT/4-NAP) all react at different sites on the iron surface. This conclusion is supported by several lines of evidence: 1) Silica introduction to columns B, C, and F resulted in significant losses in reactivity towards TCE and the NACs. When the silica was removed from the influent to columns C and F, the reactivity towards the NACs rebounded (Fig. 4.11), whereas that towards TCE remained low (inset Fig. 4.7). A sustained reduction in reactivity towards TCE was also observed in column F, as shown by the 'TCE-probe' test conducted from days 401-446 (i.e., after the period where silica was fed to the column; Fig. 4.10). Although passivation of the iron by the NACs could contribute to the declining k_{obs} observed for TCE in column F, this is not likely to be the sole effect since even with silica present, the NACs were fully reduced to their respective nitroanilines within the first 8 cm (20% of the length) of the column. Diminished reactivity towards TCE was observed throughout the entire column, suggesting that silica retention within the distal portion of the column, rather than passivation by NACs, was at least partially responsible for the deactivation. 2) Although its reactivity towards TCE had diminished substantially, column E readily degraded the NACs fed to it from day 509-623 (data not shown). In fact, throughout this period, all of the NACs were reduced to their respective anilines by the second port of column E (~ 2 cm from the inlet). 3) Only the proximal ends of the columns C-E and G-O displayed any reactivity towards 1,2,3-TCP, even under conditions where TCE evinced only slight reactivity within the same region. Others (Hofstetter, 1999; Schwarzenbach et al.,

2000) have previously suggested that nitroaromatic compounds and chlorinated hydrocarbons degrade at different types of sites; our results would appear to corroborate this.

Reactivity Losses at the Proximal End

The concentration profiles observed in this study exhibited a progressive loss in reactivity over time. This is the anticipated result of a gradual loss of reactive sites within the porous medium. Losses in reactivity were particularly pronounced at the influent end of the some of the columns, to the point that an essentially unreactive zone was evident in some columns. Larger contaminant and co-solute fluxes were encountered near the influent and this may have preferentially deactivated the proximal region, giving rise to a passivation front. It is, however, also possible that this deactivated zone could indirectly result from mineral precipitation. As the porosity decreases under constant discharge conditions, local flow velocities will increase. This effect could be particularly pronounced if minerals preferentially precipitate near the influent end of the columns. As discussed in Chapter 3, although spatial variations in porewater velocity did exist for two of the four columns investigated (columns G and J), these variations were primarily significant within the first 5% of the column and as such could be ignored without introducing significant error.

CHAPTER 5 – SURFACE SPECTROSCOPIC RESULTS

The previous chapter discussed the observed spatial and temporal variations in column reactivity. In that chapter, we hypothesized that changes in the surface composition of the iron could have occurred as the columns aged and that these changes may have been responsible for the observed alterations in reactivity. To assess whether or not this was the case, we evaluated the interfacial composition of the iron both as a function of time and as a function of distance within a given column. Furthermore, comparisons between columns enabled us to assess how different groundwater compositions affected interfacial speciation.

Four different surface spectroscopic techniques were employed: Auger spectroscopy, X-ray diffraction, electron microscopy, and micro-Raman spectroscopy. These techniques were employed because they provided complimentary information to one another and thus their combined usage facilitated an improved overall understanding of the iron-water interface. Auger was used to elicit information about the atomic composition of the iron-water interface. Auger provided high spatial (75 nm) resolution and thus enabled an evaluation of the heterogeneity of the iron surface as a function of both position within a given column as well as of operation time. As discussed shortly, Ar^+ depth profiling was used in conjunction with Auger spectroscopy in an effort to assess both the depth and the composition of the precipitate material formed on the iron surface. In collaboration with the JHU Earth and Planetary Science department, we utilized X-ray diffraction (XRD) and electron microscopy to further characterize the surface and the oxide layer. XRD is not surface sensitive, but can identify the phases present throughout the entire oxide layer. A Philips XRG 3100 powder X-ray diffractometer was used for these studies. Electron microscopy was used to examine the interfacial area at high resolution. Both a JEOL 8600 electron microprobe with SEM/EDS/WDS capabilities and a Philips CM300FEG high

resolution TEM were employed. In addition to these *in vacuo* surface techniques, in-situ Raman spectroscopy was also employed. Raman provided information about the presence and absence of specific surface phases. Raman measurements were obtained using a Renishaw 1000 Raman microscope system. Sample excitation was achieved using the 632.8 nm line of a Melles Griot 35 mW HeNe laser.

AUGER ELECTRON SPECTROSCOPY

Auger electron spectroscopy (AES) provides information about the composition of non-volatile surface species. In AES, a beam of excited electrons interacts with the sample surface and core level electrons are ejected. The subsequent relaxation process that fills the core level vacancy results in the ejection of another electron. The measured kinetic energy of these Auger electrons is related to the atomic composition of the interfacial area and it is therefore possible to obtain information about the types of species present at the interface. AES exhibits a very high spatial resolution, thereby providing information about localized surface phenomena.

Characterization of Raw Master Builder Iron

AES was used to analyze the surface of the raw Master Builder iron used in the column studies at JHU and AFRL. An AES spectrum from the analysis of these particles is shown in Fig. 5.1. The surface of the raw particle had the following elemental composition: 17.0% iron, 28.0% oxygen, 0.4% chlorine, 0.7% sulfur, and 54.0% carbon. Elemental mapping of the particle surface indicated that the iron and oxygen were highly associated with one another (Fig. 5.2), implying that these species co-exist on the surface as an iron (hydr)oxide. Conversely, carbon, sulfur, and chlorine (not shown) were not associated with either iron or oxygen, but instead existed as separate randomly spaced components on the particle surface.

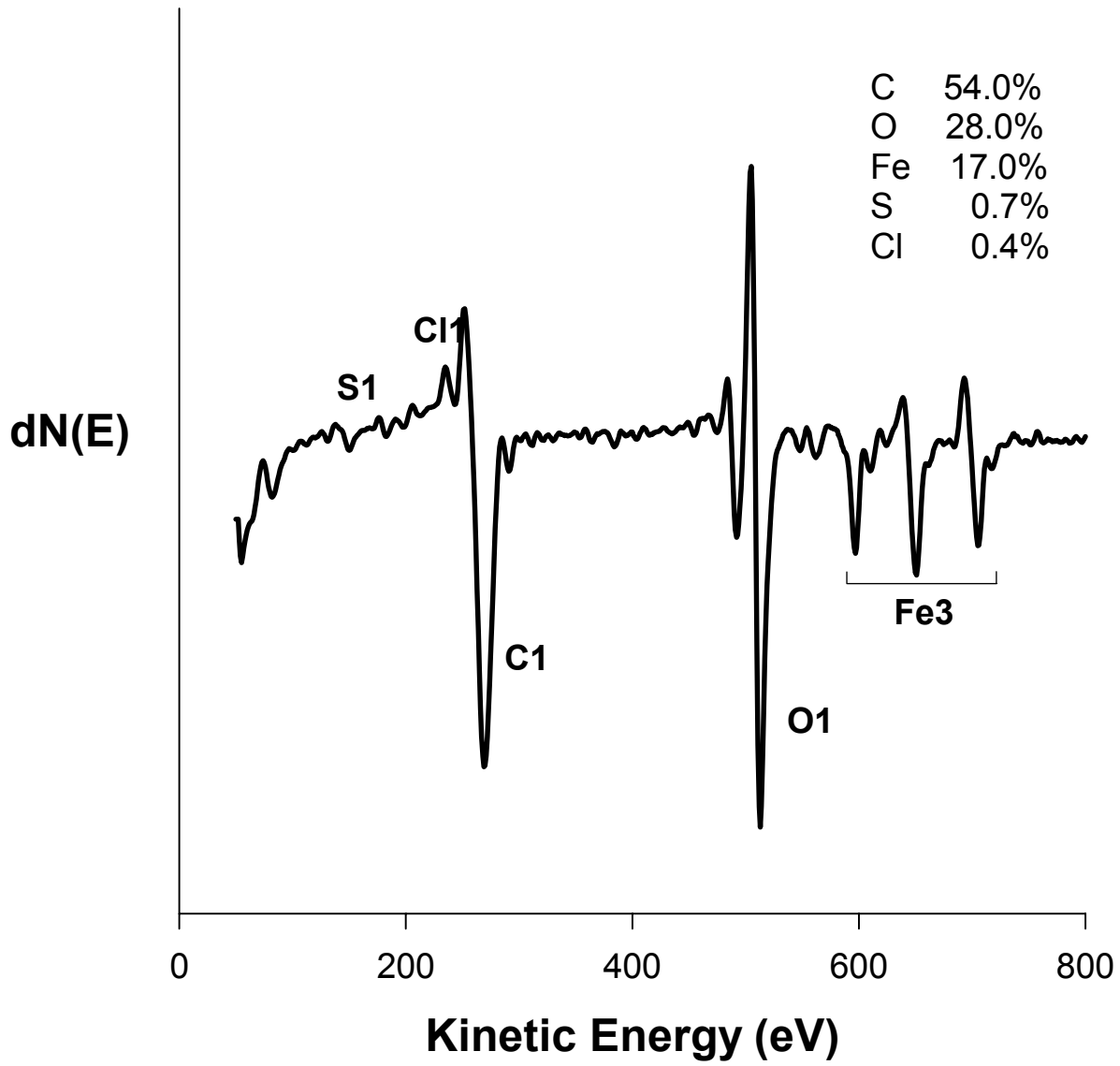

Figure 5.1 AES analysis of raw Master Builder iron indicates that the granular iron surface is coated by an iron oxide layer (17.0 % iron, 28.0 % oxygen). The surface also contains chlorine (0.4 %), sulfur (0.7 %), and carbon (54.0 %) impurities. The carbon impurity is due to deposition of hydrocarbons on the granular iron surface during heat treatment.

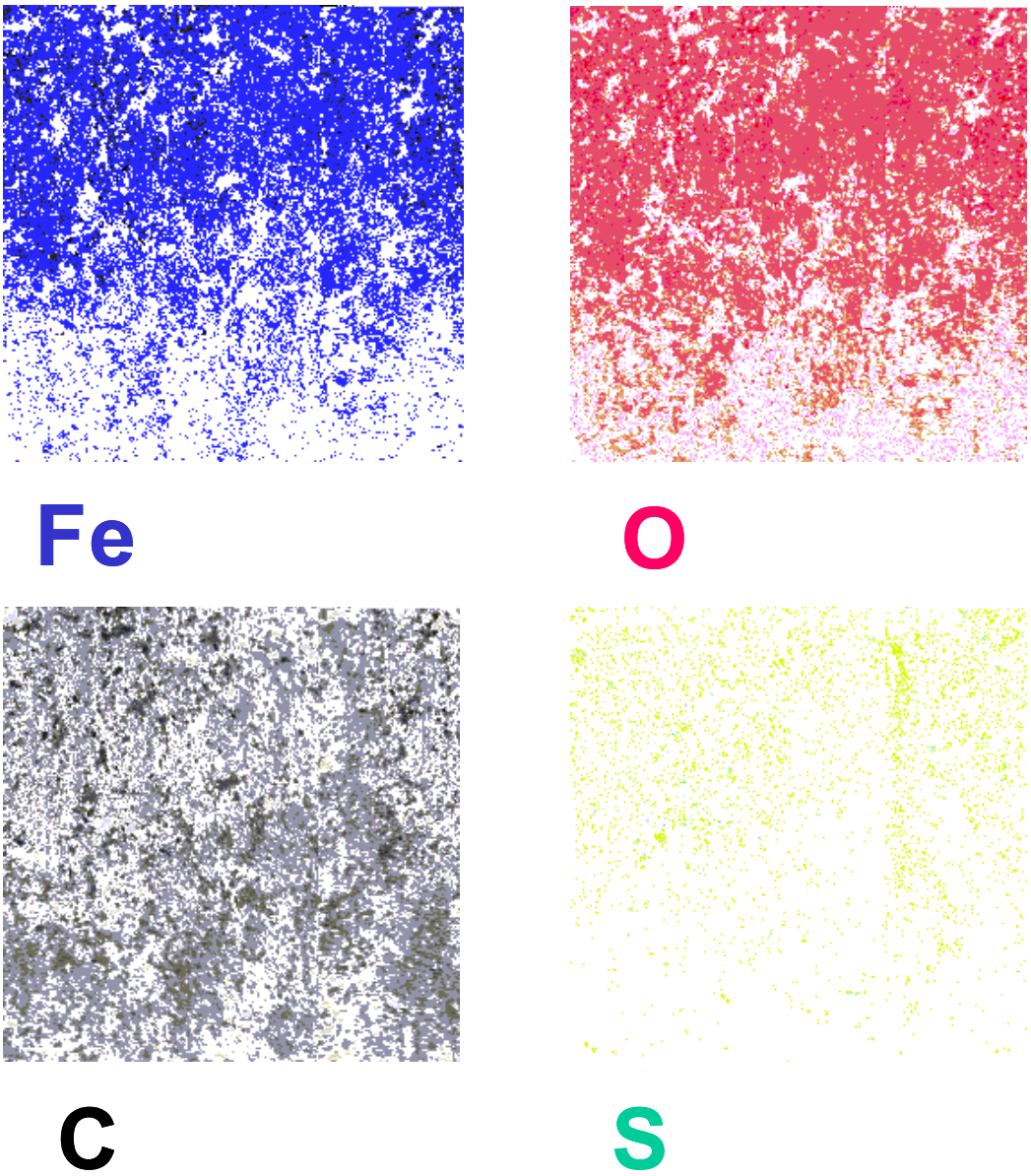

Figure 5.2 AES maps for raw Master Builder iron. Spot intensity (darkness) reflects the composition at a particular spot, with darker spots indicating the predominance of a particular element. Upon comparing the four elemental maps it is apparent that iron and oxygen are associated whereas carbon and sulfur appear as distinct patches amongst the iron-oxygen areas.

In addition to obtaining information about the surficial coating of the granular iron particles, AES, in conjunction with an Ar^+ beam, was used to obtain depth profiles. The Ar^+ beam strips away the surface coating a few molecular layers at a time, thereby enabling the measurement of material composition as a function of depth. This technique was applied to a raw Master Builder iron particle and the resultant depth profile is shown in Fig. 5.3. From this analysis it appears that the carbon associated with the iron particle surface has a depth of only 100-300 nm, suggesting the carbon is predominantly a surface contaminant. Deeper into the particle, the iron to oxygen (Fe/O) ratio increased until it eventually stabilized at ~ 3000 nm. This point presumably occurs at the interface between the surface (hydr)oxide and the bulk granular iron material.

Characterization of Contaminant-Exposed Iron Grains

AES was utilized to examine the interfacial atomic composition of iron grains extracted from port 1 of columns G-J at three different points in time (July 2000, February 2001, August 2001). Typically, 3-5 spots per grain were studied and the measured atomic compositions were averaged. As shown in Fig. 5.4, no distinct temporal trends in interfacial atomic composition were observed.

As had been done with the raw Master Builder iron grains, depth profiles were also taken of the exposed iron grains, however, these depth profiles were inconclusive (Fig. 5.5). It appears that the thickness of the precipitate layer was such that it was impossible to completely break through the layer and get to the unreacted iron core and thus the iron to oxygen ratio never stabilized.

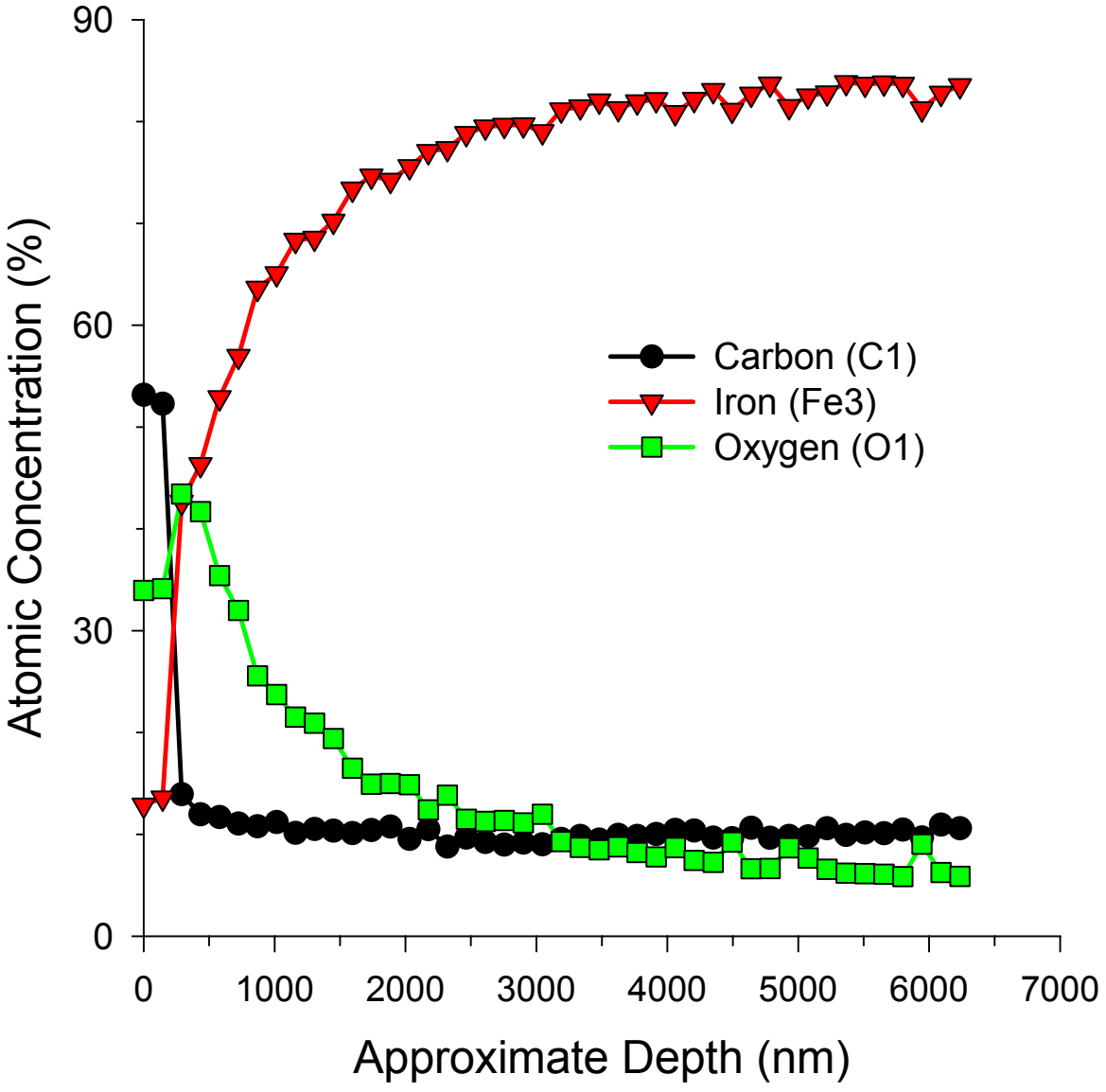

Figure 5.3 Depth profile of Master Builder iron particle. Sputtering: Ar at 4kV, 6.3 mA/mm^2, 45º, AugerScan: 5kV, 200 x 200 µm^2, 30º.

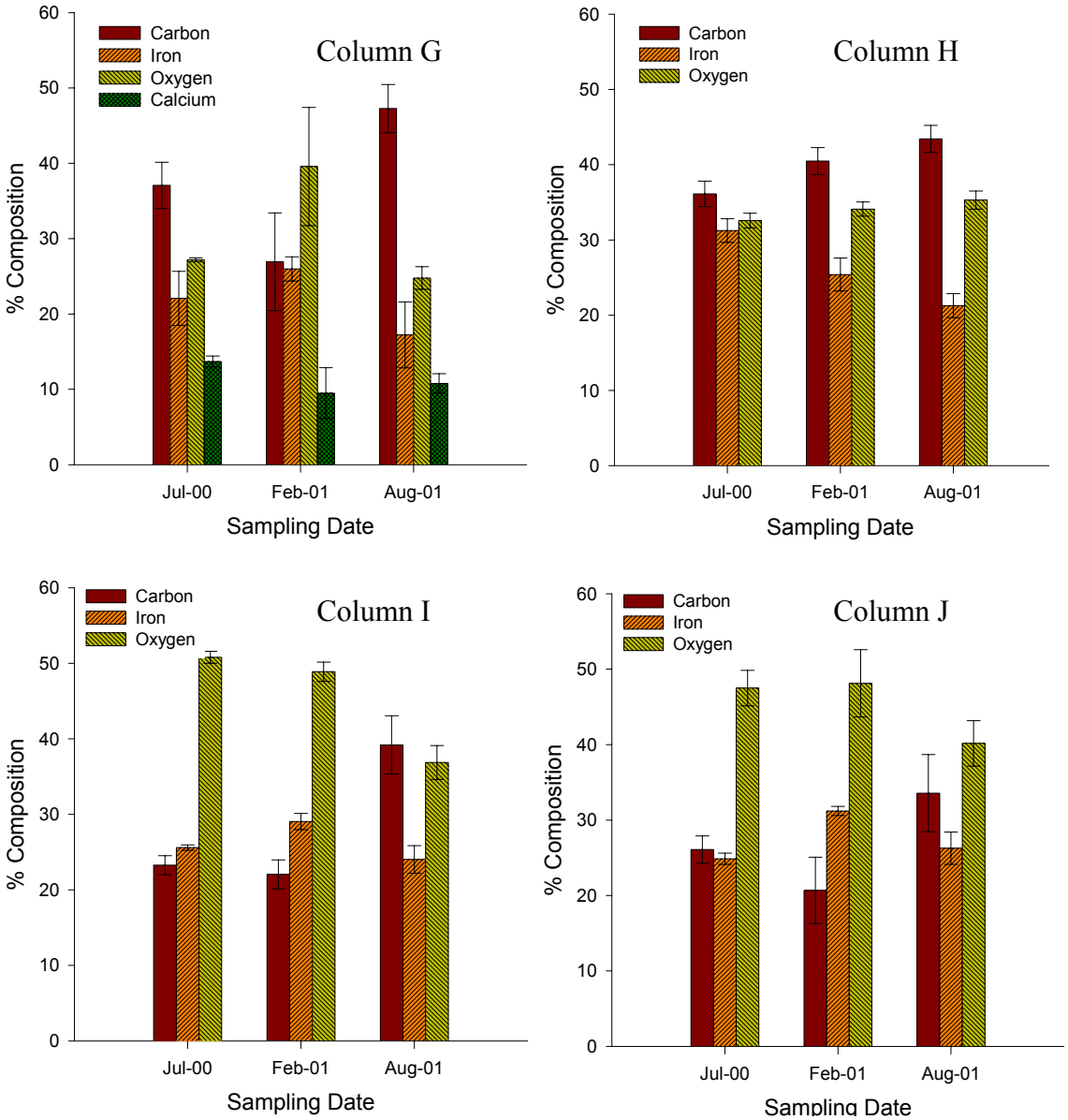

Figure 5.4 Average atomic compositions of grains extracted from port 1 for columns G-J in July 2000, February 2001, and August 2001. Error bars reflect the standard deviation of replicate measurements.

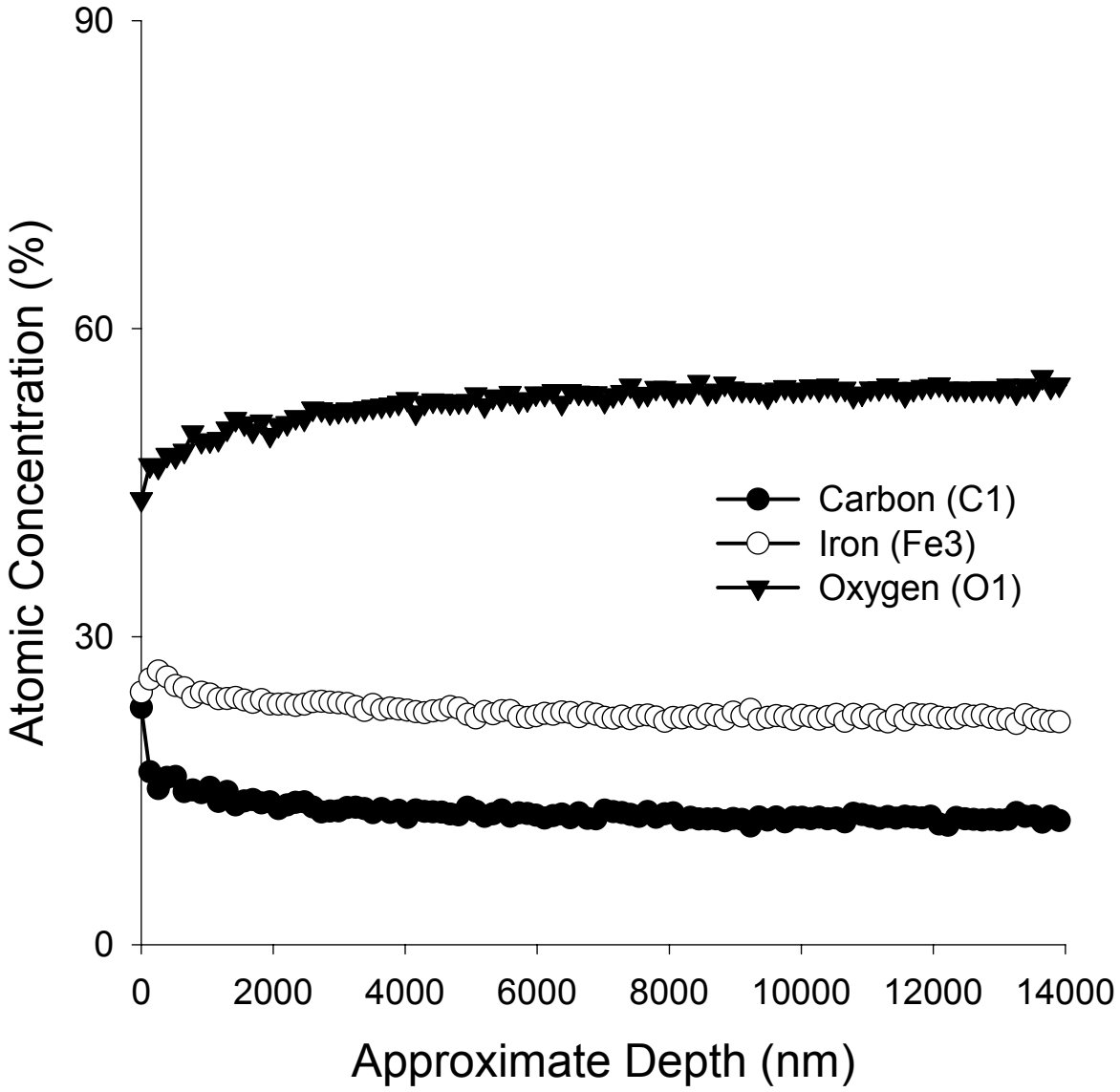

Figure 5.5 Attempted depth profile on a grain from column G

X-RAY DIFFRACTION

X-ray diffraction (XRD) is the technique of choice for the characterization of the mineral phases present in a powder. The technique is fairly well established and therefore large reference databases are available for comparison with experimental samples. In XRD, the sample is irradiated by X-rays, which are reflected by several atomic layers of the sample. Variation of the angle between sample and X-ray beam leads to positive or negative interference of the reflected X-rays. The resulting intensity pattern of the reflected X-rays is related to the periodic array of the minerals and gives characteristic fingerprints for every phase.

In this study, XRD was used to determine the nature of the iron oxides and other minerals present throughout the oxide phase of the grains. The findings were used to further identify the structures observed by electron microscopy. While electron microscopy gives a spatially resolved picture of grain cross-sections and Raman spectroscopy identifies the interfacial composition, XRD gives a bulk signal of all the mineral phases, as long as these could be easily removed from the iron grains. In addition to augmenting the electron microscopy data, the XRD results were used to investigate differences between columns of different age and operating conditions.

Sample Preparation and Analysis

XRD measurements were obtained for samples of columns B-J, as well as for untreated Master Builder iron grains. Samples were extracted on the last day of column operation and were prepared as described in Chapter 2. Between sample extraction and analysis, the solid samples were kept in porewater from the nearest liquid sampling port and were stored in the anoxic glovebox to avoid oxidation.

All the analyzed samples were taken from the port nearest the influent end of the column, as we expected this region to have reacted to the greatest extent. One scan on the XRD took 6.25 hours, during which time the dried samples were exposed to air. Therefore some mineral phases may have oxidized during the scan. Nevertheless no visible change in the sample color or structure was observed. Typically, one or two samples were analyzed for each column, at a range of 2θ from 5 to 80 degrees. The relevant peak positions are listed in Table 5.1.

Characterization of Raw Master Builder Iron

XRD was used to identify the initial mineral phases present in the bulk oxide layer of raw Master Builder iron. The XRD spectrum is shown in Fig. 5.6. The dominant iron oxide phases are wüstite (FeO) and magnetite (Fe_3O_4). These two phases are frequently found to be the dominant phases in oxide scales, with wüstite forming as the major phase at temperatures above 700 ºC (Burke and Higginson, 2000; Jenko et al., 2000). Also apparent is metallic iron that has been stripped off the grains in the grinding process. In addition, a large graphite peak and small amounts of fayalite (Fe_2SiO_4) can be seen. Graphite and fayalite are commonly found in steel scales. Fayalite forms from silicon slags during the heating process, if the temperature is around 1170 ºC or higher (Burke and Higginson, 2000; Jenko et al., 2000; Taniguchi et al., 2001). The slags are rich in silicon and contain little to no iron. Graphite is also produced during the heating process, forming from organic residues such as oil or other contaminants on the iron filings.

Table 5.1 High intensity XRD peaks of selected species for a CuKα1 anode. Data is taken from the reference database Powder Diffraction File 1994, Dataware Technologies, Inc., 1985-94.

	d(Å)	*I/I₀*	*h*	*k*	*l*	*2θ*		*d(Å)*	*I/I₀*	*h*	*k*	*l*	*2θ*		*d(Å)*	*I/I₀*	*h*	*k*	*l*	*2θ*
iron	2.03	100	1	1	0	44.67	hematite	2.70	100	1	0	4	33.15	fayalite	3.56	55	1	1	1	25.02
	1.43	20	2	0	0	65.02		2.52	70	1	1	0	35.61		2.83	86	0	3	1	31.60
								1.84	40	0	2	4	49.48		2.57	45	1	3	1	34.95
magnetite	2.97	30	2	2	0	30.10		1.69	45	1	1	6	54.09		2.50	100	2	1	1	35.89
	2.53	100	3	1	1	35.42		1.49	30	2	1	4	62.45		1.78	79	2	2	2	51.34
	2.10	20	4	0	0	43.05		1.45	30	3	0	0	63.99		1.77	65	0	4	2	51.49
	1.62	30	5	1	1	56.94														
	1.48	40	4	4	0	62.52	goethite	4.18	100	1	1	0	21.22	silicon	1.36	6	4	0	0	69.13
								2.69	35	1	3	0	33.24							
maghemite	2.95	30	2	0	6	30.27		2.45	50	1	1	1	36.65	siderite	2.80	100	1	0	4	32.00
	2.51	100	1	1	9	35.68		1.72	20	2	2	1	53.24		2.35	20	1	1	0	38.34
	2.09	15	0	0	12	43.34									2.13	20	1	1	3	42.32
	1.60	20	1	1	15	57.40	akaganeite	7.47	40	1	1	0	11.84		1.97	20	2	0	2	46.16
	1.47	40	4	0	12	63.01		5.28	30	2	0	0	16.79		1.74	30	0	1	8	52.61
								3.33	100	3	1	0	26.73		1.73	35	1	1	6	52.83
wüstite	2.49	80	1	1	1	36.04		2.30	35	3	0	1	39.22							
	2.15	100	2	0	0	41.93		1.64	35	5	2	1	55.90	aragonite	3.40	100	1	1	1	26.21
	1.52	60	2	2	0	60.76									3.27	50	0	2	1	27.22
	1.30	25	3	1	1	72.74	green rust[a]	7.52	100	0	0	3	11.76		2.70	60	0	1	2	33.13
								3.78		0	0	6	23.52		2.37	45	1	1	2	37.88
lepidocrocite	6.26	61	2	0	0	14.14		2.47		1	0	4	36.34		1.98	55	2	2	1	45.85
	3.29	100	2	1	0	27.05		2.35		0	1	5	38.27							
	2.47	76	3	0	1	36.30								calcite	3.04	100	1	0	4	29.41
	1.94	53	5	0	1	46.78	graphite	3.38	100	0	0	2	26.38		2.29	18	1	1	3	39.40
	1.94	72	0	2	0	46.88		2.04	6	1	0	1	44.39		2.10	18	2	0	2	43.15
															1.91	17	0	1	8	47.49

[a] Data adapted from Williams and Scherer, 2001

d = interplanar spacing, I/I_0 = relative peak intensity, hlk = Miller indices, θ = glancing angle

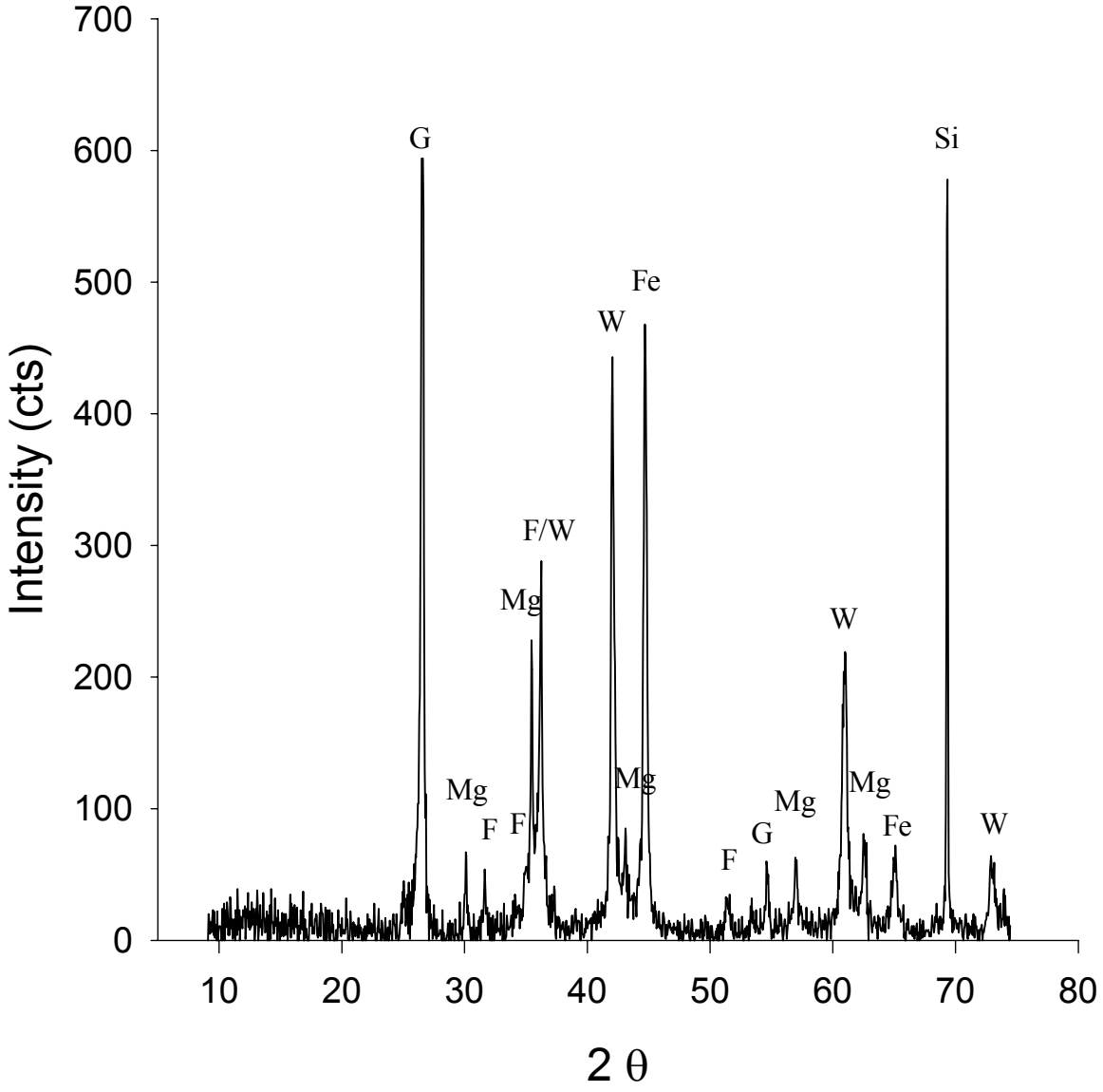

Figure 5.6 XRD pattern of the oxide layer of raw Master Builder iron. F = Fayalite, Fe = iron, G = graphite, Mg = magnetite, Si = silicon, W = wüstite.

Characterization of Exposed Grains

The bulk oxide phase of the exposed grains significantly differs from the raw Master Builder iron grains. Fig. 5.7 shows the spectra obtained from grains from the port nearest the influent from columns B-J.

The dominant features in the XRD spectra are similar for all columns, as can be seen in Fig. B. Subtle differences as a function of solution and matrix composition can be seen, though, as will be discussed later. Fig. 5.8 shows a labeled XRD pattern for the sample from column D. This sample is representative of all reacted samples. As was the case for the raw Master Builder iron, graphite and metallic iron are still present. However, the relative amount of graphite seems to have decreased. The wüstite and fayalite peaks have almost disappeared. This is either due to the transformation of wüstite to a different mineral phase, or to the insufficient sensitivity of the instrument to detect small amounts of wüstite and fayalite among more prevalent mineral phases. One of the dominant mineral phases is now magnetite (main peak at $2\theta = 35.42$ degrees). Magnetite and maghemite have very similar diffraction patterns (see Table 5.1). Magnetite matches the diffraction pattern better than maghemite, but it cannot be ruled out that maghemite is present as well.

The other dominant feature on all the spectra from the reacted grains are the first three peaks at $2\theta = 14.5$, 17.4 and 23.8 degrees. At the current time we have been unable to identify these peaks. Since they always appear together and are always in a very similar ratio to one another we currently assume that they are caused by one mineral phase. This phase is hypothesized to be green rust, with either carbonate or chloride as interlayer anions. As will be discussed later, Raman spectroscopic and TEM studies have shown the presence of green rust in

our samples. Furthermore, several other researchers have found this mineral phase to be present in field and column studies (Gu et al., 1999; Roh et al., 2000). The XRD pattern found for our samples is not coherent with diffraction patterns found for green rust in the literature (Drissi et al., 1995; Abdelmoula et al., 1996; Genin et al., 1996; Hansen et al., 1996; Refait et al., 1997; Refait et al., 1998a; Benali et al., 2001; Genin et al., 2001; Legrand et al., 2001a; Williams and Scherer, 2001). Green rust usually exhibits characteristic peaks at very low regions of 2θ, with the most intensive peak occurring around 2θ = 12 degrees (see Table 5.1). However, green rust is difficult to analyze by XRD, since it is easily oxidized. The green rust in our samples could have been altered during the sample acquisition in air, or even while drying in the glovebox, which may contain trace amounts of oxygen. This would result in a drastic change of the XRD pattern (Abdelmoula et al., 1996).

There are also alternative explanations for the three initial peaks. The first peak at 14.5 degrees could stem from lepidocrocite. However, the match is not exact, and several other major lepidocrocite peaks don't appear in the spectra. The second peak could be a poor match for one of the maghemite peaks or akaganéite (β-FeOOH), and the third peak could be interpreted as akaganéite, hematite, maghemite or magnetite. As was the case for for lepidocrocite, other major hematite or akaganéite peaks are missing, making their matches rather unlikely. In the cases of magnetite and maghemite, the peaks would be out of proportion compared to the rest of the pattern. From the poor matches with other well-defined oxide phases, from the position of the peaks at the low end of the pattern, and from the evidence provided by Raman spectroscopy and TEM we postulate that the three initial peaks can be attributed to green rust.

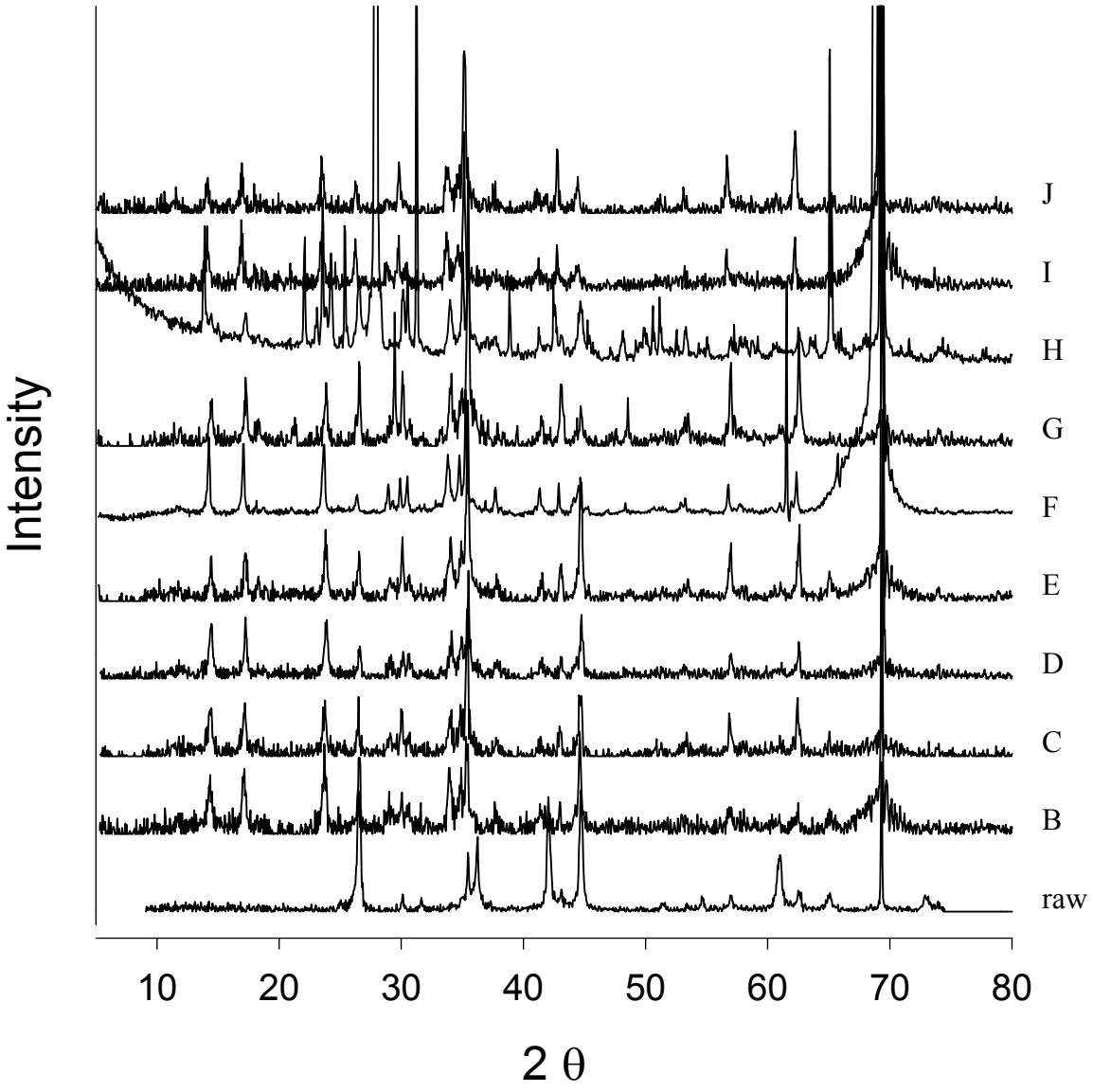

Figure 5.7 XRD patterns of the oxide layer of raw Master Builder iron and of grains from the influent end of columns B-J.

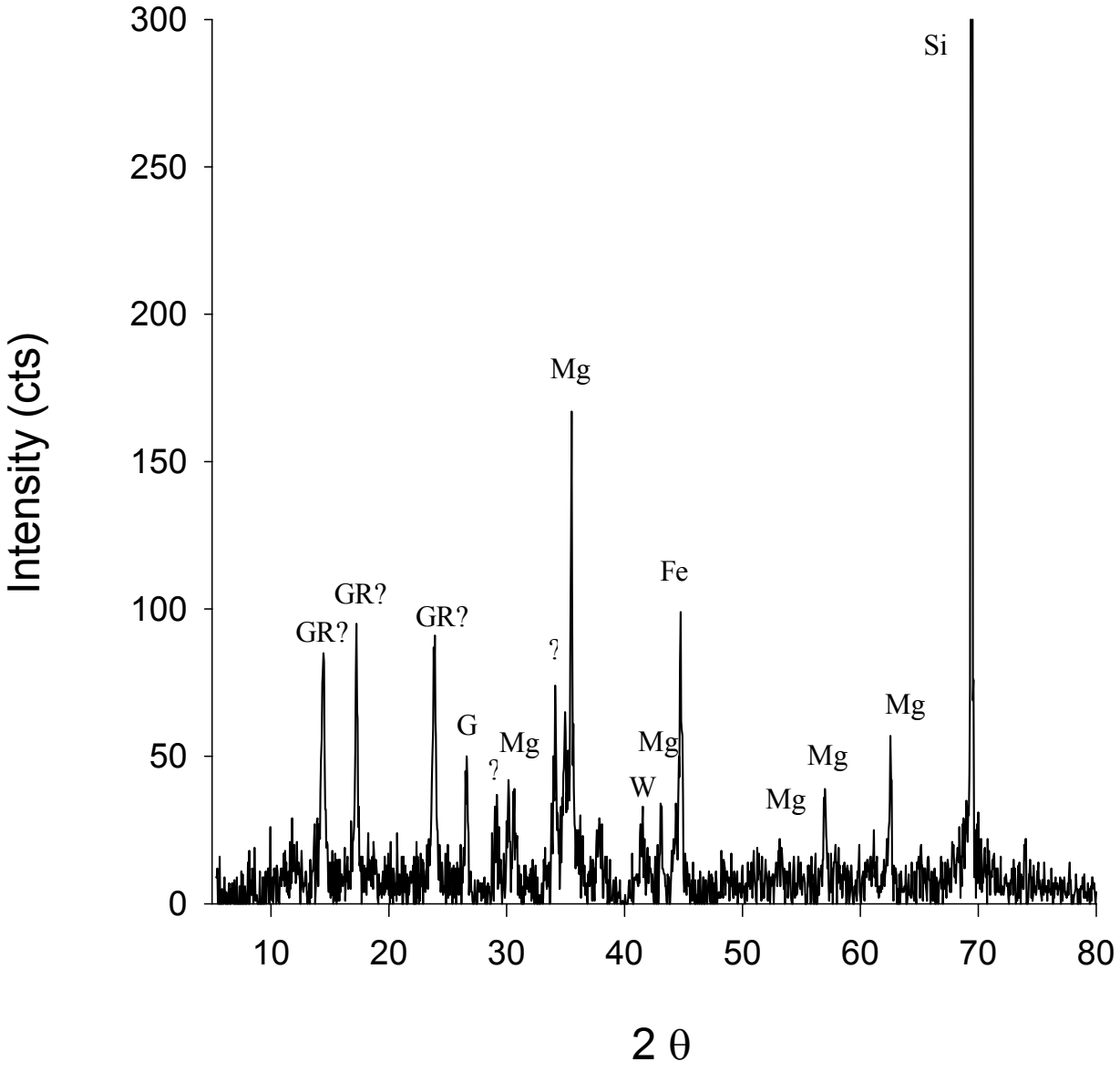

Figure 5.8 XRD pattern of the oxide layer in column D. Fe = iron, G = graphite, GR = green rust, Mg = magnetite, Si = silicon, W = wustite, ? = unidentified peak.

Column E – 100% Master Builder iron, influent pH 9.2, buffered with 20 mM $NaHCO_3$

In spite of the high carbonate content, no siderite was detected in column E, contrary to what other researchers have reported for column and field experiments (Gu et al., 1999; Roh et al., 2000). We assume that most of the carbonate that remained in the column formed carbonate green rust, since green rust was previously determined to be the dominant iron carbonate species in our pH and concentration range (Legrand et al., 2000).

Column G – 100% Master Builder iron, influent pH 7.5, buffered with $CaCO_3/CO_2$

In addition to the mineral phases described in the previous section, calcite can be identified in the spectrum of the grain obtained from column G. The main calcite peak occurs at 29.41 degrees, accompanied by several smaller peaks, some of which coincide with the magnetite pattern. The identity of the $CaCO_3$ precipitates seems to vary from system to system. Some researchers have reported aragonite in field studies (Phillips et al., 2000), aragonite in column studies and calcite in the field (Bruce Sass, Batelle, personal communication), or both phases in the same system (Roh et al., 2000). In our samples calcite is the predominant Ca – containing phase, but aragonite may still be present in our samples. The peak around $2\theta = 38$ degrees and $2\theta = 48$ degrees may stem from aragonite. As will be discussed later in this chapter, aragonite was detected on the very surface of our samples using Raman spectroscopy. However, since XRD gives a bulk signal of the oxide phase, the aragonite peaks in our sample are generally too small for us to conclude with certainty that this phase is present.

Column H – 92% Master Builder iron/8% albite, influent pH 7.5, buffered with $NaHCO_3/CO_2$

The spectrum of column H is largely dominated by big albite peaks. These peaks can be attributed to grains of albite from the matrix that were crushed along with the iron grains. Possibly some of the albite also stems from precipitation of albite onto the iron surface. Since the XRD spectrum is a spectrum of the bulk, however, it is not possible to make this distinction.

Characterization as a Function of Column Age

To describe the influence of age on the mineral phases in the bulk surface, columns D and J are compared. These columns were run under identical conditions, but column D was run 625 days longer than column J. The XRD patterns of these two columns show no significant differences. The oxide phases in both columns, as in all the other columns, are hypothesized to be mainly green rust and magnetite. It has to be noted, though, that differences between these columns may still exist. XRD as employed in this study is not a quantitative tool, therefore no statement about the amount of iron oxides, the thickness of the oxide layer, or the surface coverage can be made.

ELECTRON MICROSCOPY

Electron microscopy techniques are *in vacuo* techniques. They are based on the irradiation of the sample with a focussed beam of accelerated electrons. The use of electrons rather than photons allows for much higher resolution than can be obtained with conventional light microscopes.

In scanning electron microscopy (SEM) the sample is scanned with the electron beam and secondary electrons are emitted from the sample. These electrons are collected and

transformed into an image. The information obtained is either topographical (secondary electron imaging) or related to the density of the sample (backscattered electron imaging). The resolution of the microprobe system employed for this study was on the order of 20 nm. In addition to its SEM capabilities, the JEOL 8600 microprobe has capabilities for energy dispersive spectroscopy (EDS) as well as wavelength dispersive spectroscopy (WDS). These additional functions allow compositional analysis and compositional mapping of the sample.

In transmission electron microscopy (TEM), electrons pass through the sample and an image is collected on film or a CCD camera. In order for the electrons to pass through the sample, it has to be very thin. The electrons are accelerated to reach a higher energy than in the microprobe and therefore allow for even higher resolution. The Philips CM300FEG TEM system employed has a resolution of approximately 0.2 nm. In addition, the system is equipped to perform chemical analysis by electron energy loss spectroscopy (EELS) and selected area electron diffraction (SAED). The TEM analyses confirm the basic interface structure determined by SEM observations and add detail.

In order to assess the effects of column age, position in the column and feed composition on precipitate formation, electron microscopy was employed to look at cross-sections of the iron grains.

Because of the very high resolution of the TEM and the difficulties associated with sample preparation, only very small sections of a sample can be analyzed using this technique. Therefore, the samples were initially studied on the microprobe to identify regions of interest. Those samples were then further investigated by TEM. TEM enables the analysis and identification of the major oxides present. Furthermore, TEM allows for the identification of

many oxides that are only present in small amounts, and that cannot be distinguished as a separate phase by SEM or XRD (Hochella et al., 1999).

Sample Extraction and Analysis

Iron grains were extracted from the solid sampling ports as described in Chapter 2. The samples were extracted on the last day of column operation. Between extraction and analysis, the grains were stored in the glovebox, in vials containing anoxic porewater obtained from the nearest liquid sampling port. Samples from the influent ends of columns B, D, E, G, H, and J, as well as samples from the effluent end of columns D and J were analyzed on the microprobe. This enabled us to distinguish between columns with different matrices and feed solutions (B with silica, E with high bicarbonate, G with $CaCO_3$, H with albite matrix), different column age (J is a younger replicate of D), and different positions along the columns (influent versus effluent ends of D and J).

All the grains of one sample were inspected by examining the SEM micrographs. Several photographs were taken of every sample, and EDS point analyses were performed at regions of interest. In addition, compositional maps of selected regions were obtained for samples from all the investigated columns.

Regions of interest were identified on the effluent sample of column D (sample D12) and on the influent sample of column J (sample J2). These samples were further thinned as described in Chapter 2 and investigated on the TEM. Diffraction patterns were obtained and pictures were taken of selected areas, in order to identify the oxide phases present.

Characterization of Raw Master Builder Iron

A total of five raw Master Builder iron grains were examined by SEM. Fig. 5.9a shows one of the raw grains. The grains are very porous and are covered by a thin, compact oxide layer, which appears as the gray, less dense material on the image. As can be seen in Fig. 5.9 the thickness of the oxide layer surrounding the grain varies strongly. This is partly due to the heterogeneous surface of the grain, but also to experimental artifacts. The oxide layer may be partly damaged during handling and preparation of the grains. Therefore we focused on the iron oxides present in more confined pores rather than on the surface. These oxides were more protected and only exposed when the sample was polished to obtain the cross sections.

Fig. 5.9b shows a pore leading from the surface of a large grain to the interior. The pore is covered with a thin oxide layer, which most likely consists of wüstite, magnetite, and fayalite, as determined by XRD and discussed in the previous section. An elemental map of this same section, shown in Fig. 5.10, revealed that the pore boundaries are indeed marked by increased amounts of silicon compared to the core, an indication of the fayalite present in the scale.

Most of the oxide layers examined on the raw grains had well-defined boundaries like the one shown in Figs. 5.9 and 5.10. We therefore define the fayalite/wüstite/magnetite scale as the border of raw grains as they were originally present in the columns before contact with the feed solution. Any oxide found beyond the fayalite-containing boundary thus results from oxide formation during column operation.

a

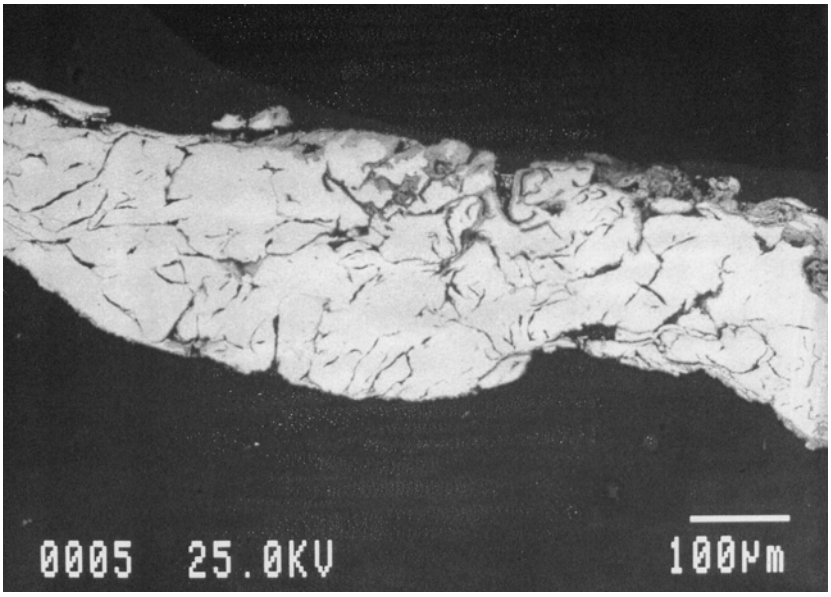

b

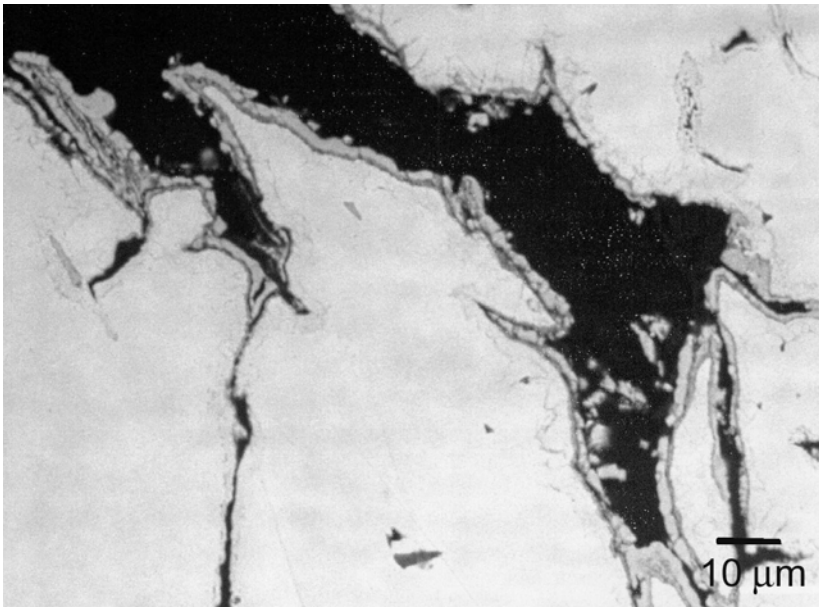

Figure 5.9 (a) Cross section of a raw Master Builder iron grain. (b) Close-up on a pore.

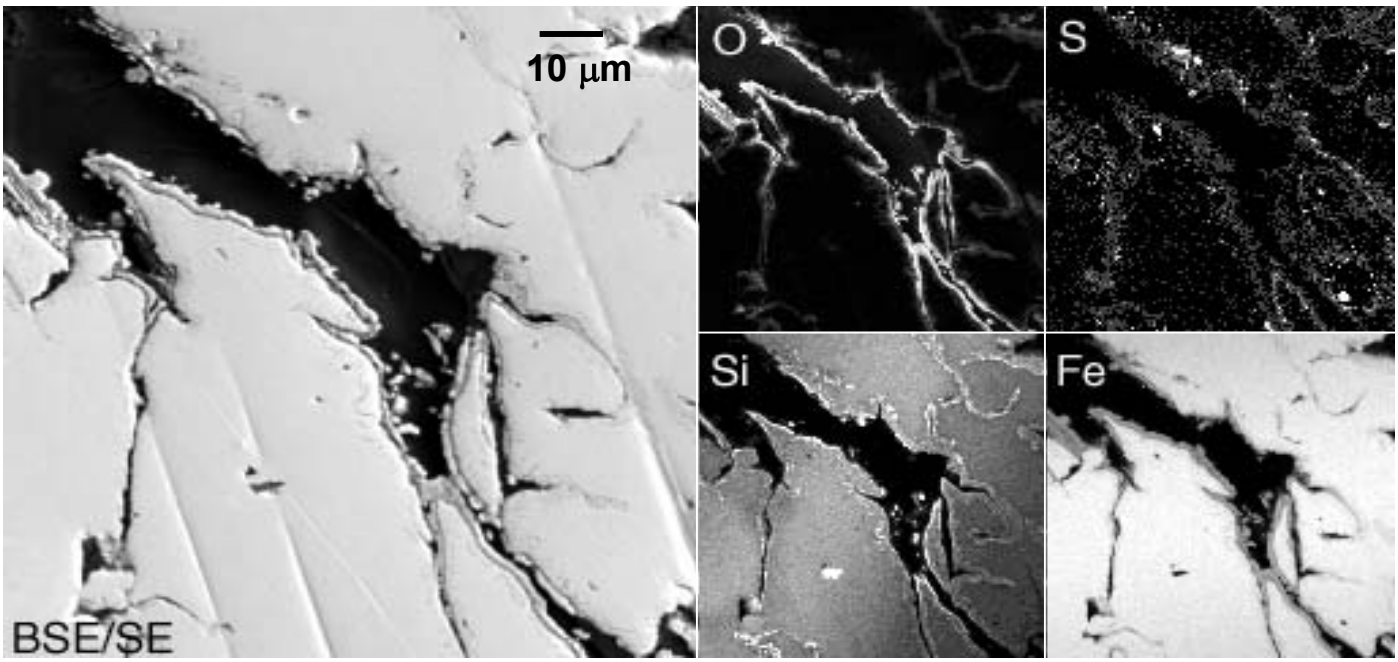

Figure 5.10 Elemental map of oxygen, sulfur, silicon and iron of a pore of in raw Master Builder iron grain. BSE/SE = mixture of backscattered and secondary electrons.

Characterization of Exposed Grains

The pores of the exposed grains generally contain more iron oxides than the raw grains, as can be seen in Fig. 5.11. These images show two grains from column D with large pores, partially filled with oxides. Unlike the raw grains, where the oxide phase consists of mainly one dense phase, the oxides present on the exposed grains could be divided into at least three different types: the previously described, dense fayalite-containing scale; a compact, "blocky" oxide, and a very fragile-looking oxide phase consisting of "needles" or thin plates. Other researchers have identified a very similar thin plate or needle structure to be carbonate green rust (Gu et al., 1999; Roh et al., 2000; Legrand et al., 2001a).

TEM images of these needles show that the majority are an iron hydroxide with hexagonal plate habit (Fig. 5.12). Energy dispersive analysis (EDS) shows that there is oxygen and iron present (Fig 5.13). It was not possible to analyze for H or C, and there was little indication of Cl present. The O *K* and Fe $L_{2,3}$ absorption edges were collected by electron energy loss spectroscopy (EELS) analysis. EELS is sensitive to the concentration, valence state and bonding environment of atoms. Van Aken et al. (1999) have developed methods for determining the proportion of $Fe^{3+}/\Sigma Fe$. This method was employed on spectra from the platelets. Analysis of the EEL spectra estimated the $Fe^{3+}/\Sigma Fe$ at 0.33 (Fig 5.14). This is consistent with green rust. Selected area electron diffraction (SAED) patterns of the platelets do not discriminate between different sheet structures, but can distinguish between hematite and magnetite/maghemite. The SAED patterns were not consistent with hematite or magnetite/maghemite.

During the course of analysis, it became apparent that the platelets were damaged under the electron beam. EELS analysis of spectra before damage and after damage revealed that the

platelets oxidized to $Fe^{3+}/\Sigma Fe = 0.75$ (Fig 5.14). The selected area diffraction patterns of the damaged platelets are consistent with either maghemite or magnetite. The shape of the O *K* edge is also similar to either maghemite or magnetite. However, the amount of Fe^{3+} is greater than magnetite. We assume that damage of the platelets produces a partially oxidized maghemite structure.

Also identified in the grain mount of column D were the "blocky" structures seen on the microprobe, which appear as small grains of magnetite or maghemite on the TEM image (Fig 5.15). SAED patterns cannot distinguish between these structures. Based on the XRD results we assume that these structures are mainly magnetite.

As discussed in the previous section, magnetite and green rust were also the two major oxide phases found by XRD. Other researchers using similar techniques have also found amorphous iron (hydr)oxides, goethite, lepidocrocite and other hydrated forms of ferric oxides on samples from actual barriers and sediments (Hochella et al., 1999; Roh et al., 2000). In our samples, the sequence of phases can be described as metallic iron to fayalite/wüstite/magnetite to magnetite and finally to green rust. The transition from the relatively smooth, raw grain to the structurally varied reacted grain has also been observed in other studies (Mackenzie et al., 1999), where the formation of precipitates was correlated with porosity loss observed in column studies.

a

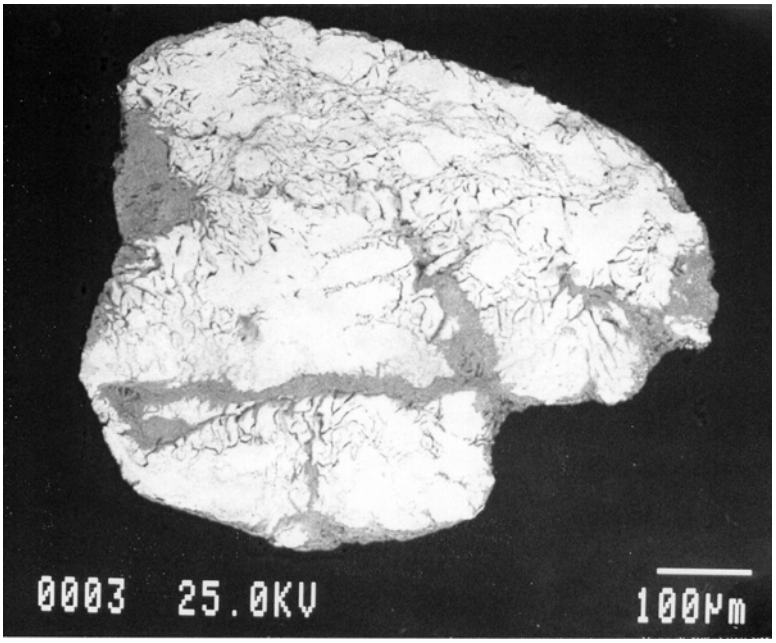

b

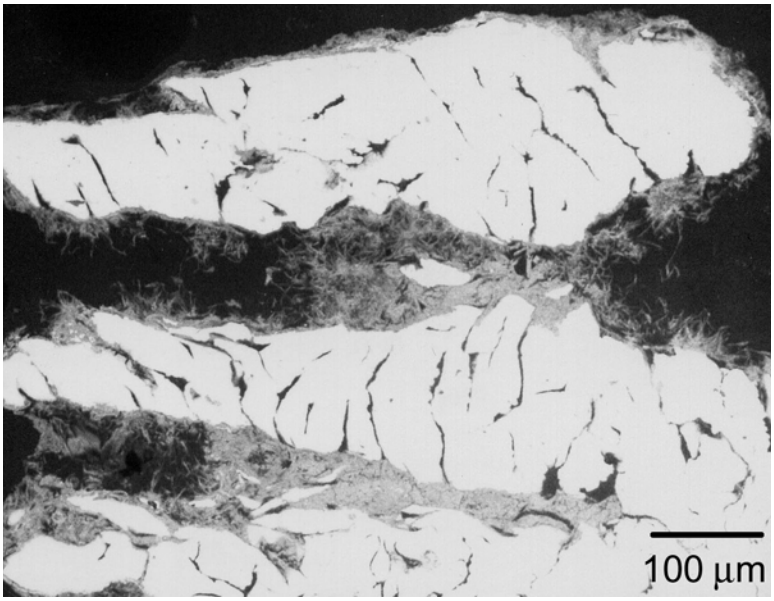

Figure 5.11 (a) Cross section of a grain from the effluent end of column D. (b) Second grain from column D at higher magnification, showing wide pores partially filled with intact oxides.

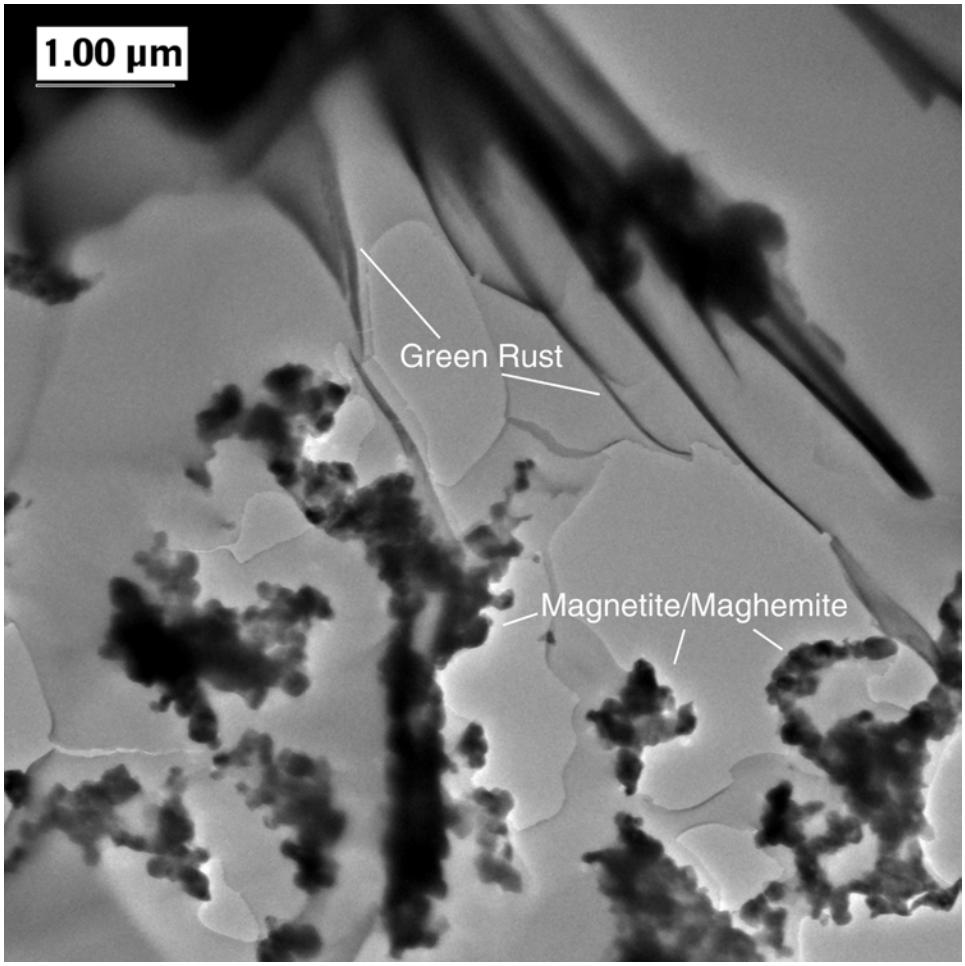

Figure 5.12 TEM image of ion milled sample J12. Platelets of green rust are seen on edge. Both green rust and iron oxide particles have been imbedded in epoxy and ion milled.

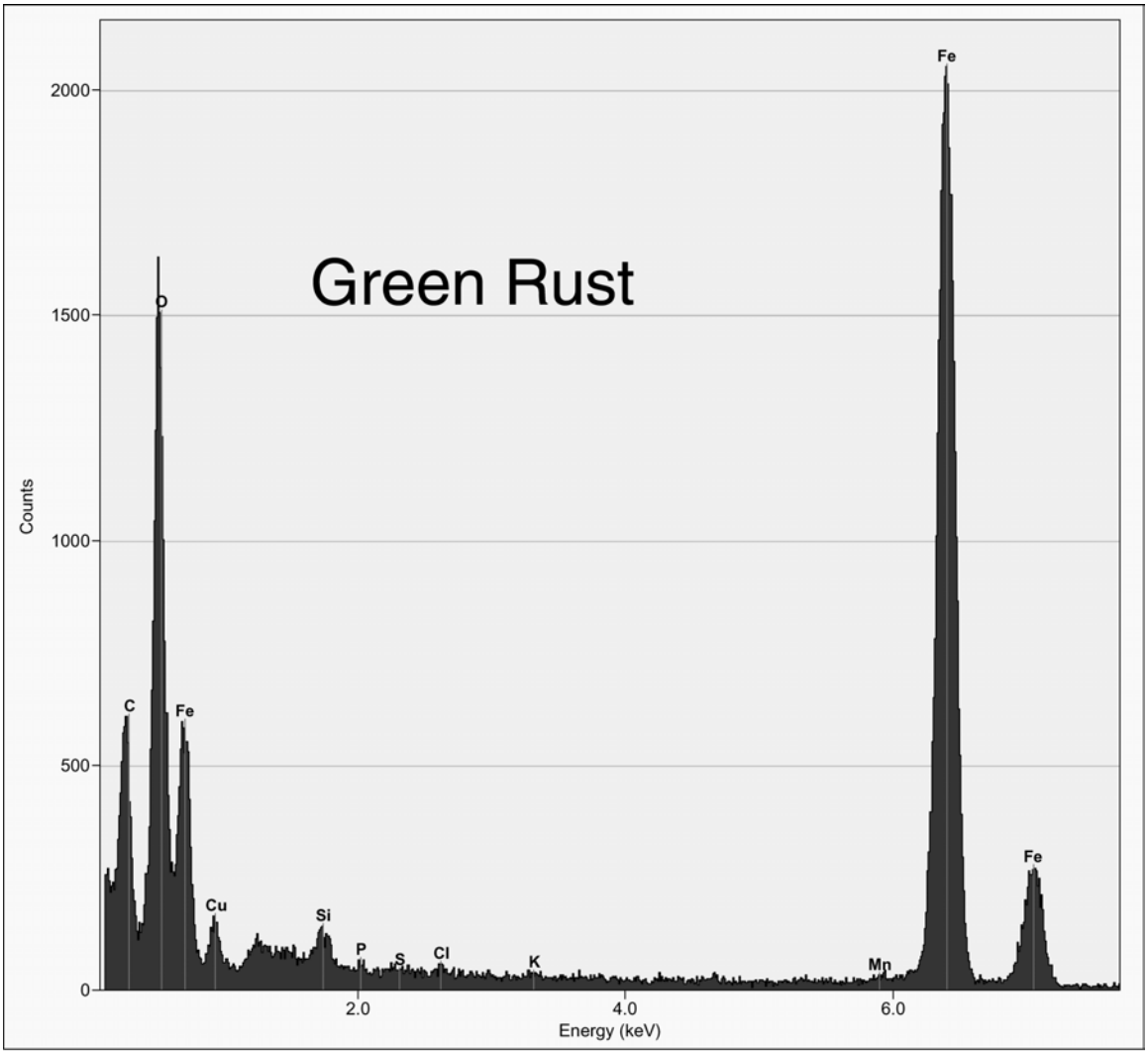

Figure 5.13 EDS analysis of green rust platelet.

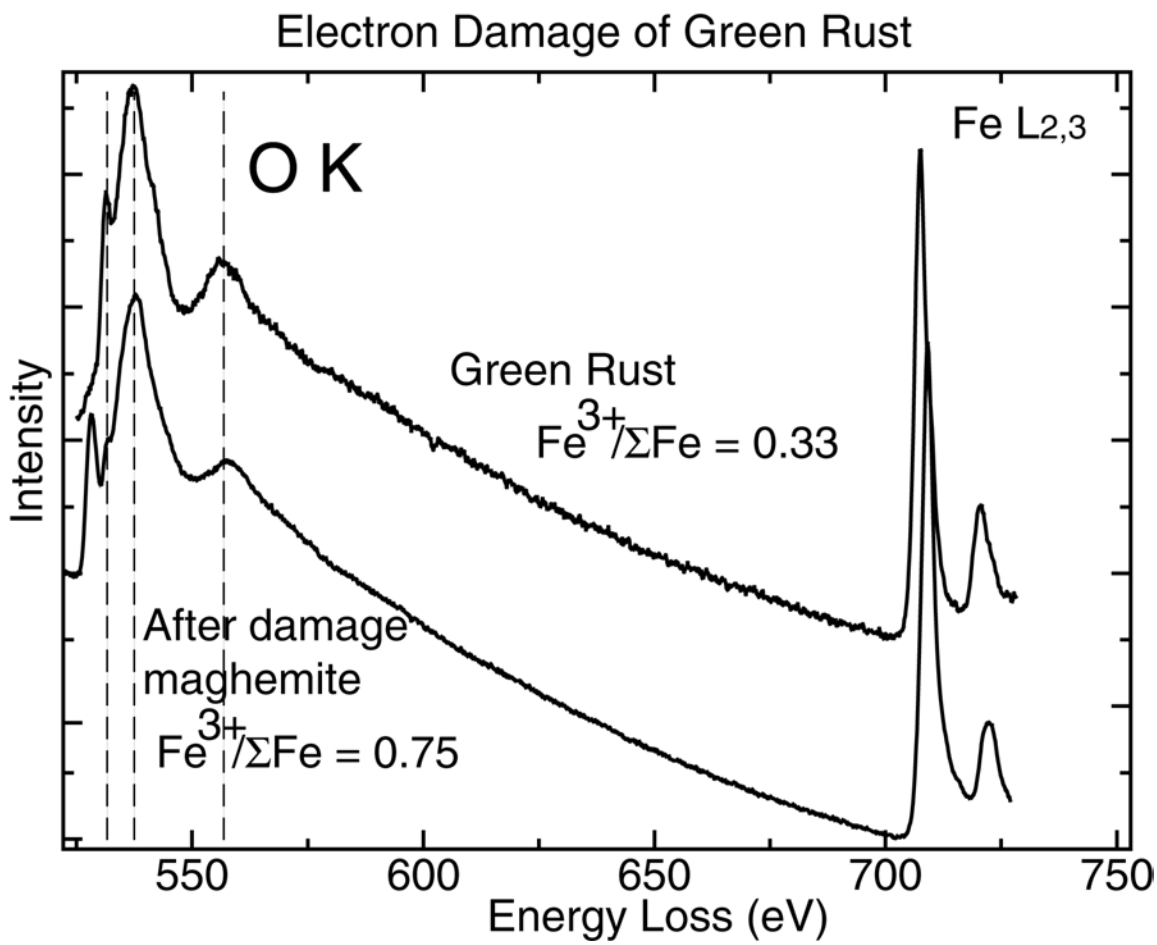

Figure 5.14 EELS spectra of green rust showing the chemical shift due to differences of iron valence state before and after damage from the electron beam.

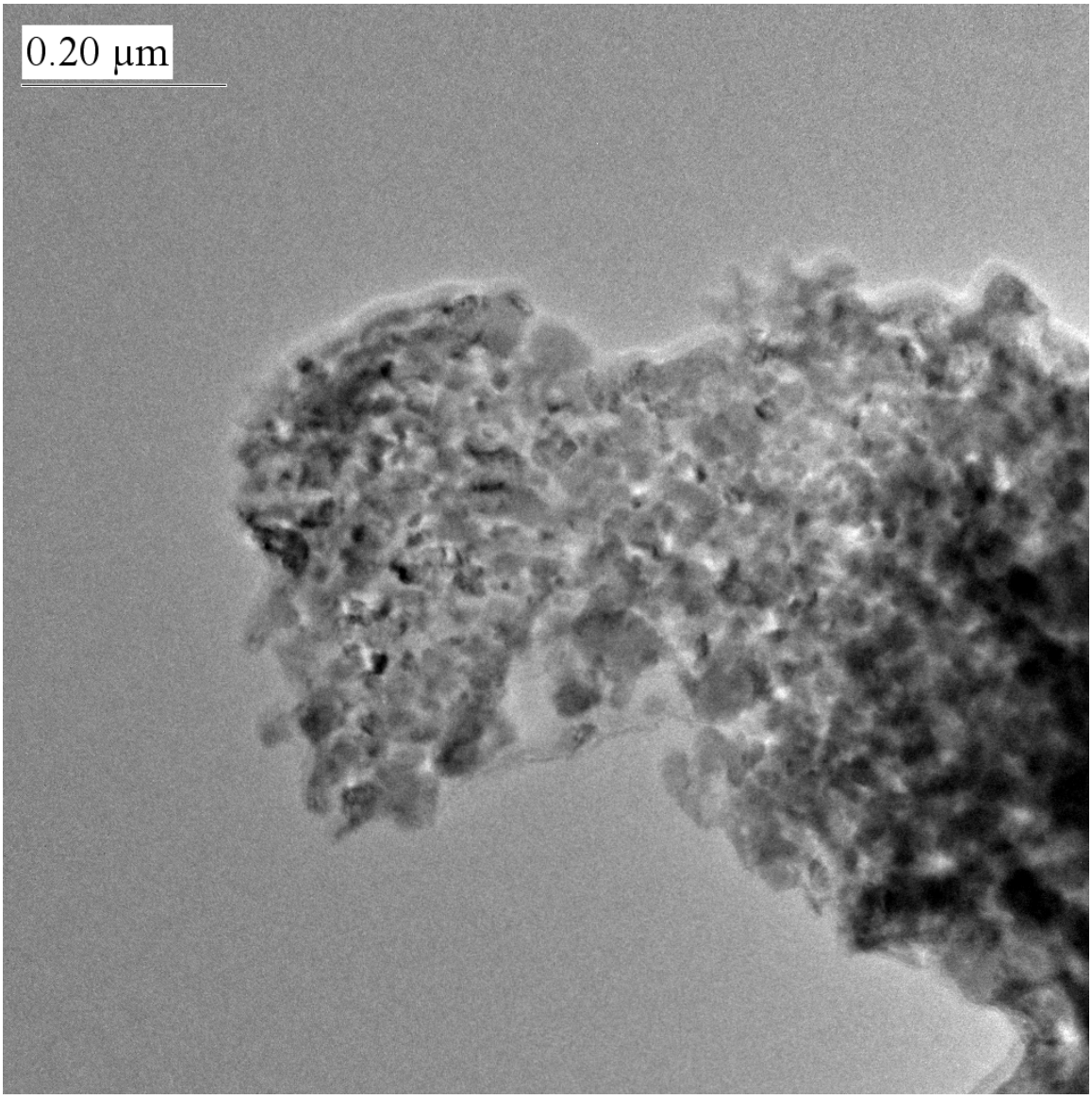

Figure 5.15 TEM image of fine-grained iron oxides in sample D2.

The three types of oxide can be easily recognized in Fig. 5.16, a close-up on the grain shown in Fig. 5.11. From the elemental map of the same region, shown in Fig. 5.17, the original grain boundary can be identified by the presence of the fayalite-rich scale. The newly formed oxides contain little or no silicon.

The oxide layer on the reacted grains is generally very thick, sometimes ranging to over 100 μm, compared to less than 5 μm on the raw grain. The entire grain is covered by oxide, with the iron core never being exposed. This finding contradicts the suggestions of other researchers who suggest that exposed bare iron could be partly responsible for the reaction with the contaminants (Scherer et al., 1999).

The new oxide phases are probably formed by a combination of deposition from solution on top of the original oxide layer, and from degradation of the original oxide layer. Even though evidence of the original scale is still visible on most grains, regions of degradation of the scale could be identified, as is shown in Fig.5.16b. It can be seen how the original oxide layer is being degraded to form the "blocky" oxide.

Besides iron, EDS analysis and elemental maps revealed the presence of MnS and silicon slags on all grains, as can be seen in Fig. 5.17b. The slags appear as darker spots on the backscattered image, and as holes in the iron map, and they show up as light spots on the sulfur or silicon maps. Since the MnS slags seem to remain intact during exposure, and only little Mn or S is found in the oxide phase, we assume that neither element is strongly involved in the reactions occurring with the chlorinated contaminants. However, a slight concentration of sulfur was observed at the interface between the iron core and the oxide, as can be seen in Figs. 5.10 and 5.17.

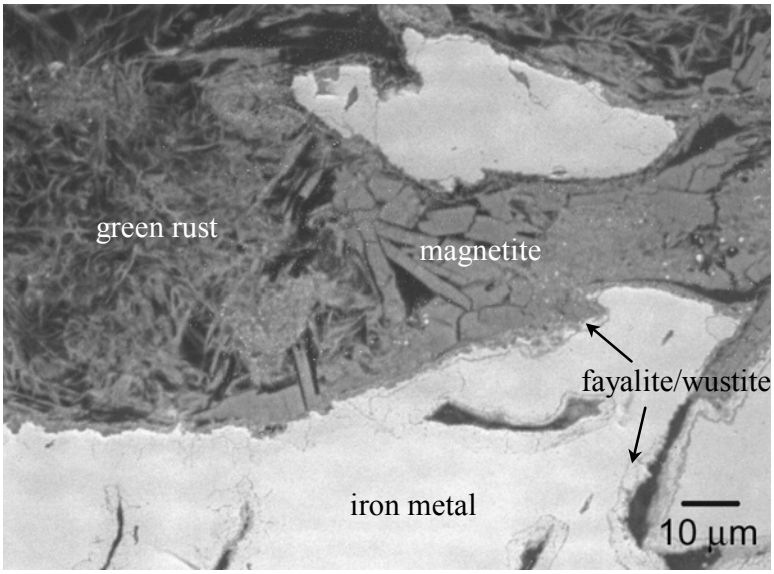

a

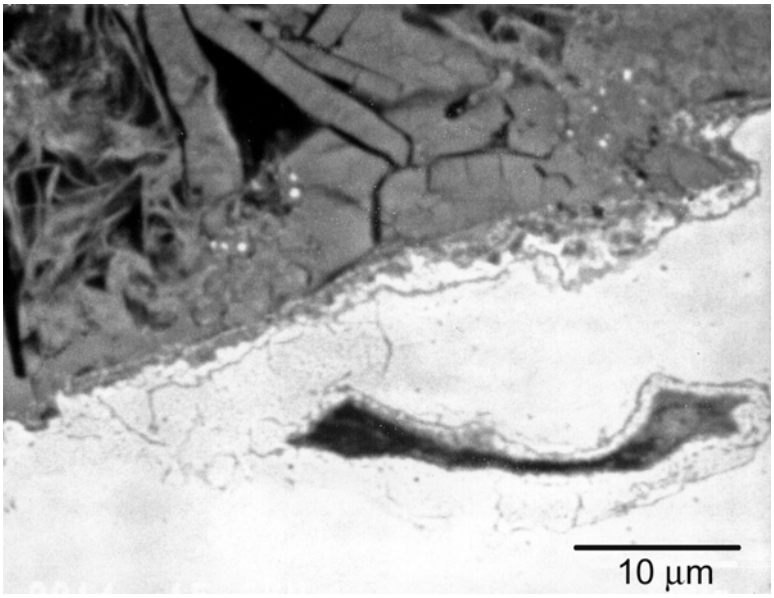

b

Figure 5.16 (a) Close-up on the metal/oxide interface of a grain from column D. (b) Close-up on the metal/oxide interface of picture (a). The fayalite/wüstite scale is being penetrated by the newly forming oxide.

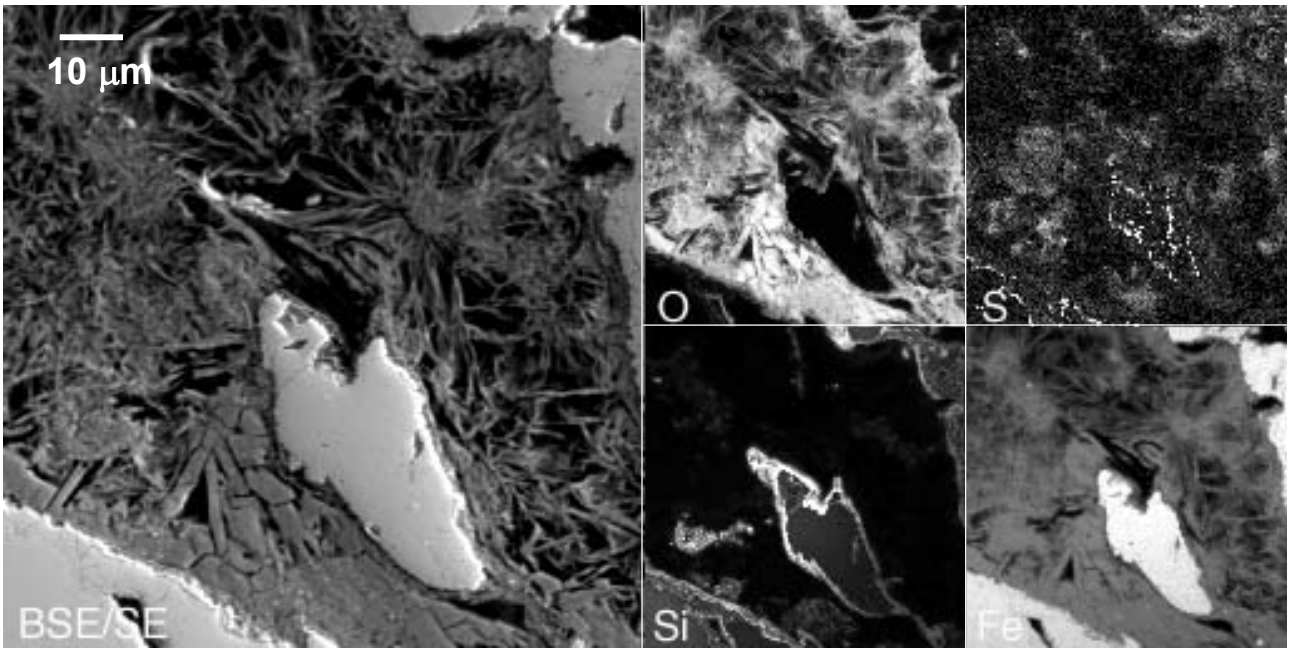

a

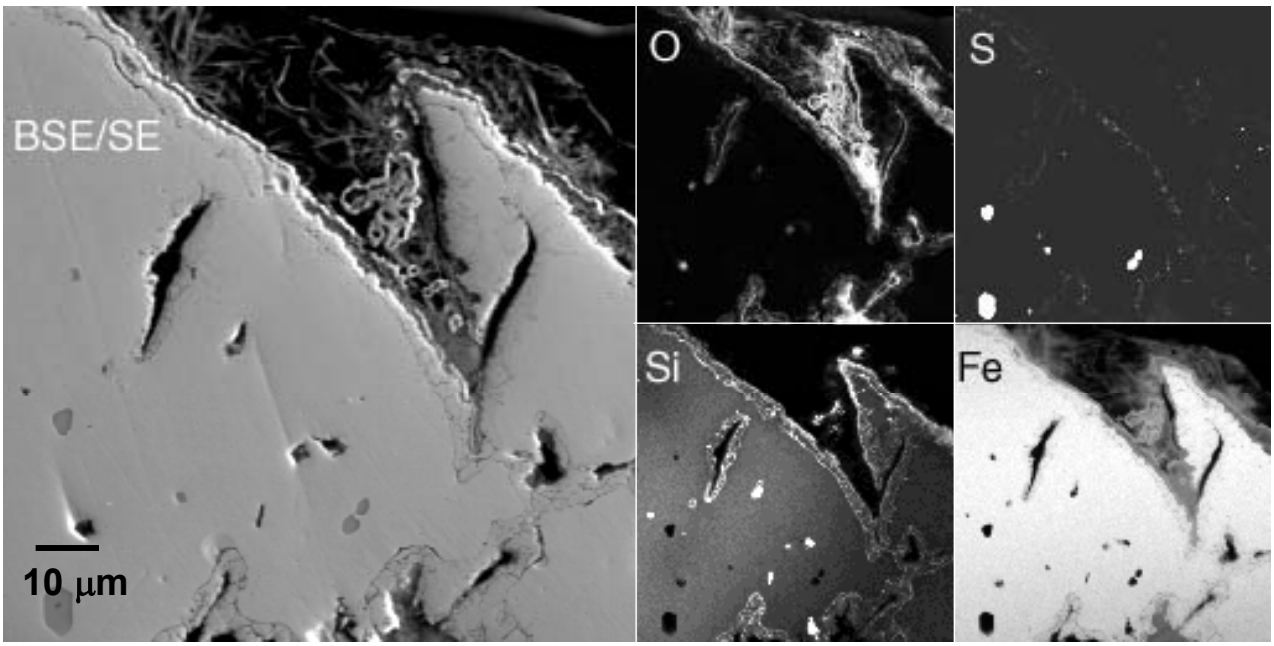

b

Figure 5.17 (a) Compositional map of the region shown in figure D (a). (b) Compositional map of a second region on the same grain, showing MnS and silicon slabs. BSE/SE = mixture of backscattered and secondary electrons.

Some of the iron grains used in the newer columns (G-J) appear to stem from a different batch of iron. These grains have enclosed bubbles that appear as round holes on the SEM images, as is shown in Fig. 5.18. The presence of these bubbles does not seem to have affected the reactivity of the grains, since the reactivity of the new columns compares very well with the first column set (see discussion in Chapter 4).

The sample from column J was ion milled along the oxide/metal interface. The interface was analyzed by conventional TEM imaging and by scanning transmission electron microscopy (STEM) collecting EDS X-ray maps. The nanometer scale texture of the metal/oxide interface consisted of several layers (Fig. 5.19). The iron metal at the interface contained many defects indicative of a shearing process used to produce the metal shards. In intimate contact with the metal was a very thin layer of fine-grained iron oxides identified as magnetite or maghemite (Fig. 5.20). After this oxide layer, there is a gap in the layers filled with carbonaceous material which could be part of the alteration structure or due to epoxy pore filling. The next layer contained a mixture of fayalite and magnetite/maghemite, with fayalite forming crystals (~200 nm) elongated roughly parallel to the interface (Fig. 5.21). The magnetite crystals are fine-grained (~ 50 nm) and mix with green rust platelets further from the interface.

EDS analyses of the fine-grained iron oxides show that there was a minor amount of Si present in the sample. This could be due to either solid solution of Si into the spinel structure or amorphous silica mixed in between the small crystals. The analyses of the green rust contained minor amounts of Si, S, and Cl as well as substantial Na and K. The alkali elements probably originate from salt crystals that precipitated during sample drying. The S and Cl may be consituents of the green rust interlayer. The Si is problematic in that green rust has no tetrahedral site to include Si. It may indicate that amorphous silica was present.

a

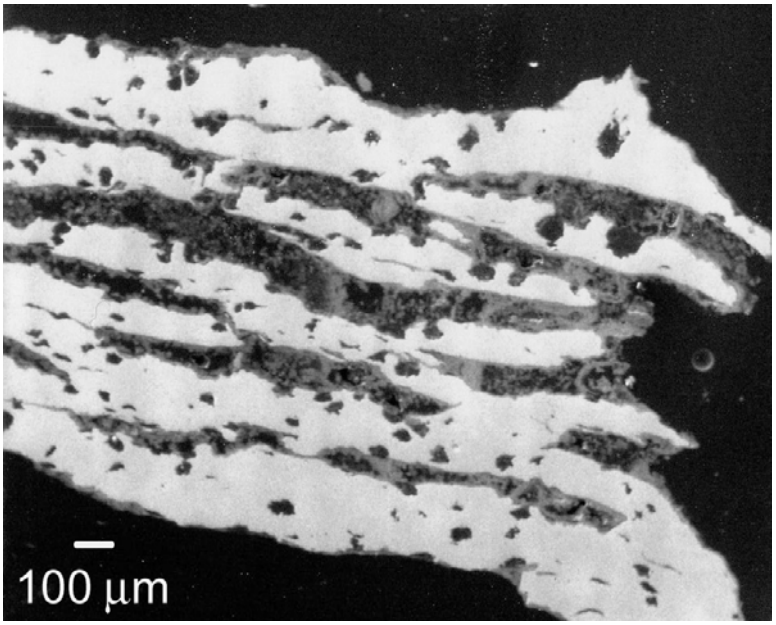

b

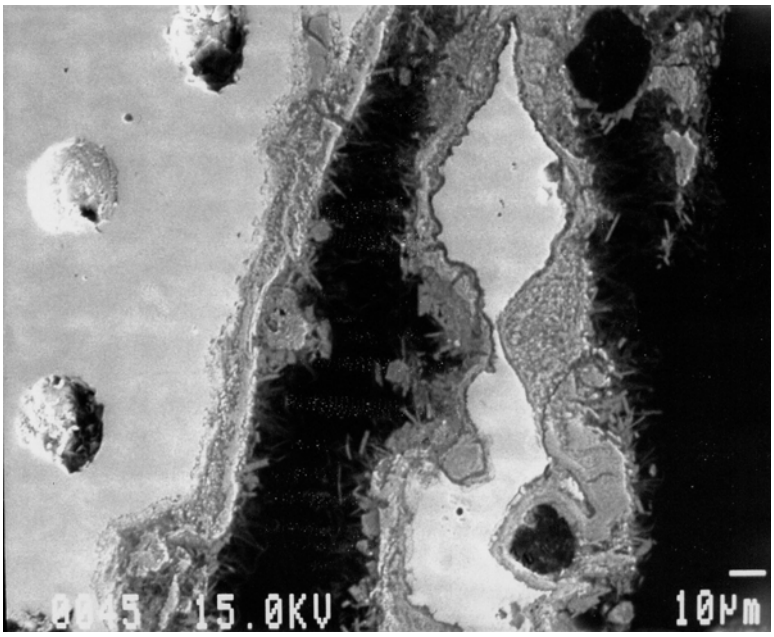

Figure 5.18 (a) Cross section of a grain from the influent end of column J. (b) Close-up on the holes in the grain of figure (a).

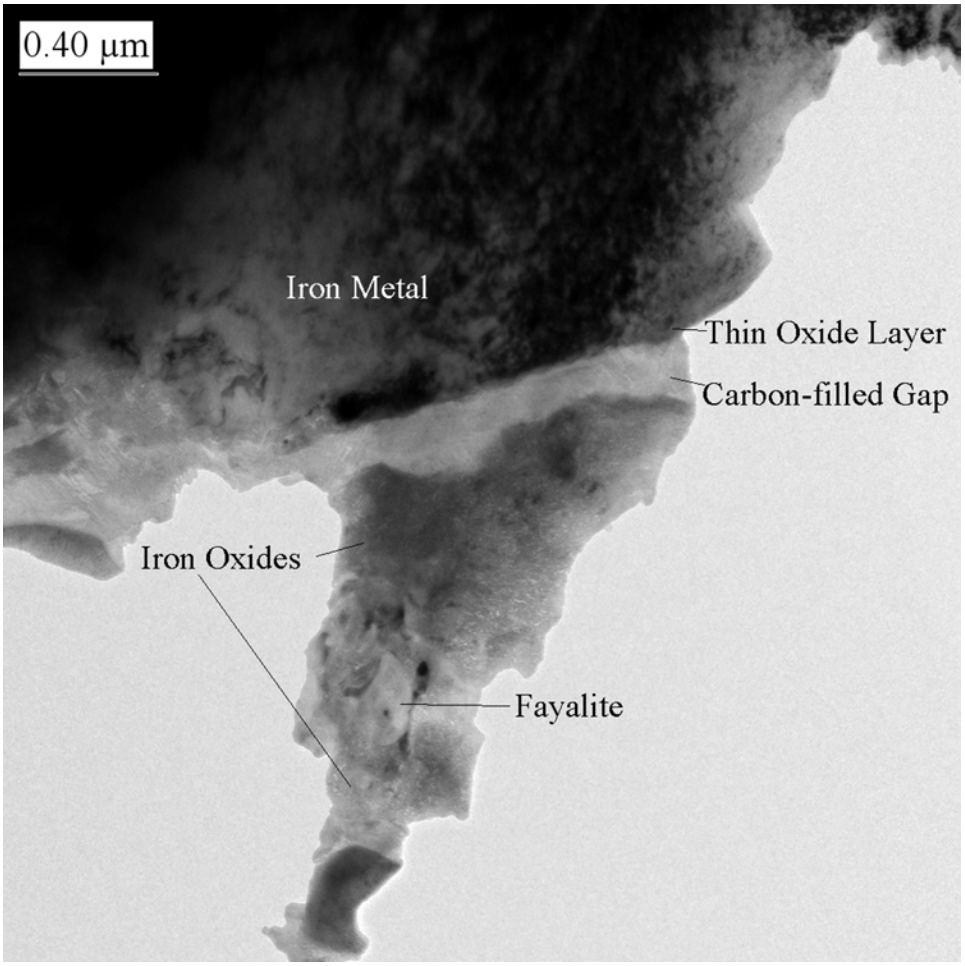

Figure 5.19 TEM image of the metal/oxide interface in sample J12

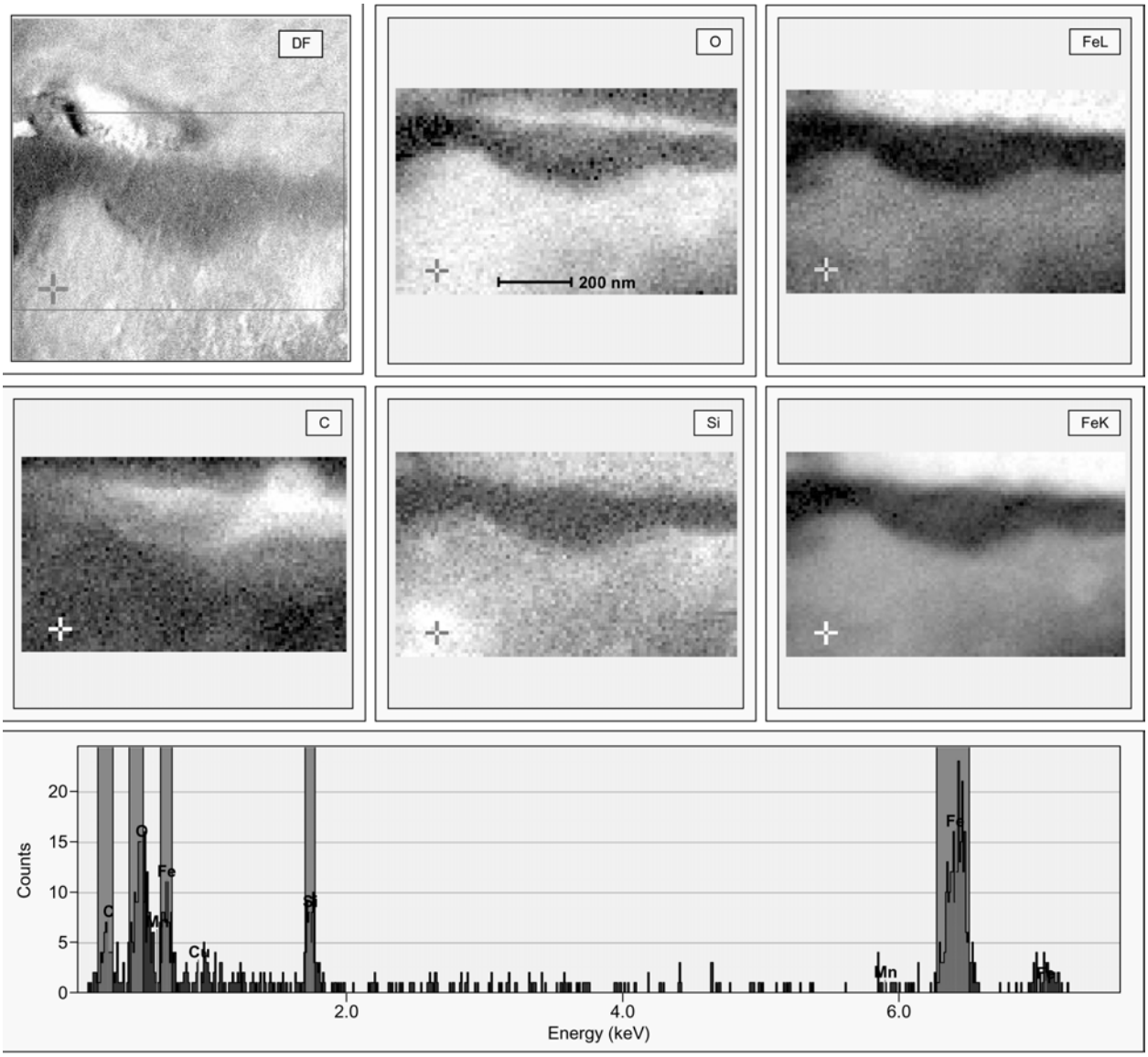

Figure 5.20 STEM images of sample J12. DF = dark field image. Other images are X-ray maps generated from the area delineated by the rectangle in the DF image. FeK and FeL are the $K\alpha$ and $L\alpha$ X-ray lines of iron, respectively. At bottom is an EDS spectrum of the sample at the location of the cross in other images.

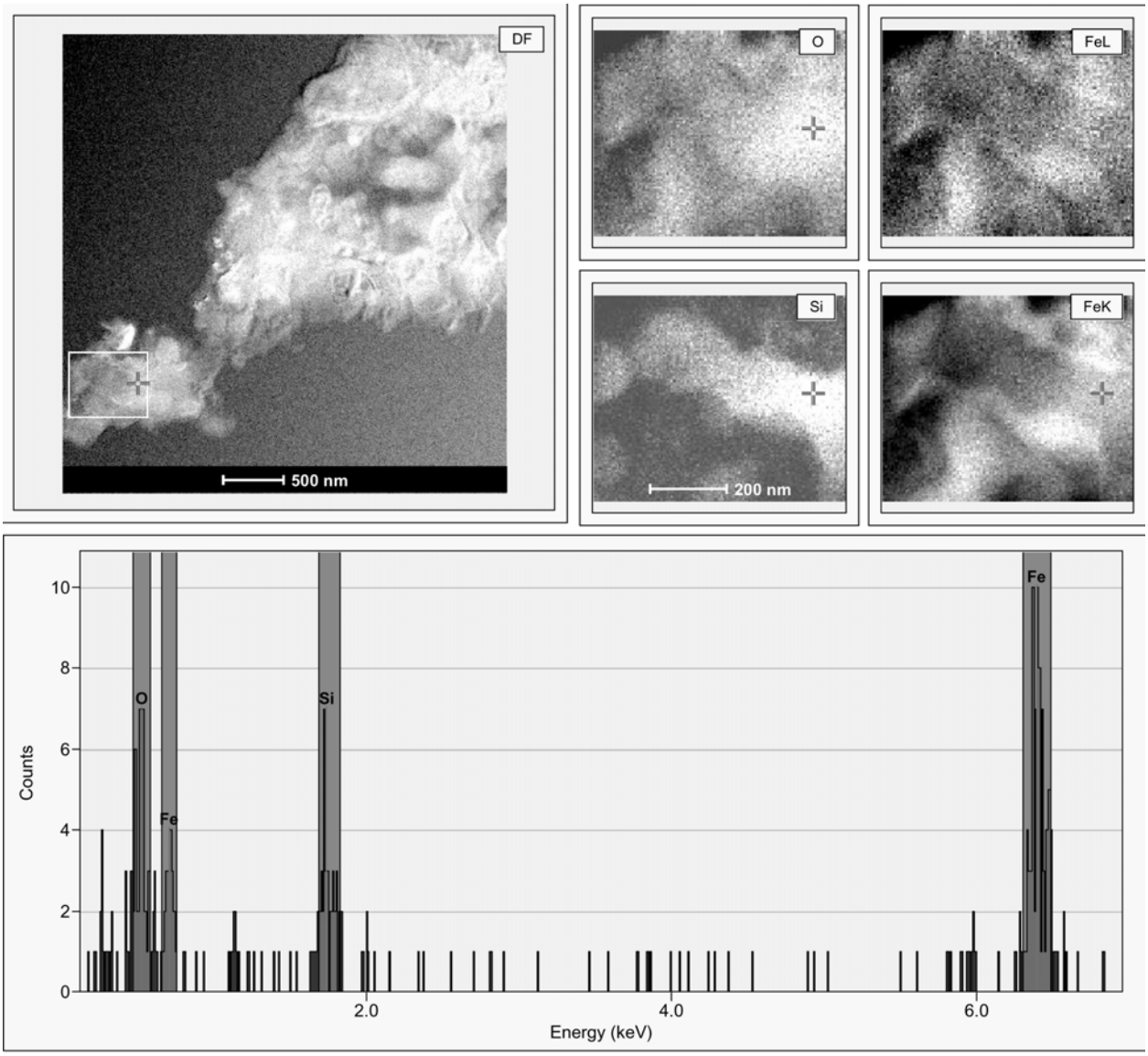

Figure 5.21 STEM image of Si-rich fayalite near the metal/oxide interface. Labels are as in Fig. 5.20

Column B – 100% Master Builder iron, $NaHCO_3$, pH 9.2, 0.5 mM SiO_2 added to the feed during the last 225 days

An elemental map of a grain segment from column B revealed the presence of substantial amounts of silicon not only in the original scale, but also in the subsequent oxide phase. This is shown in Fig. 5.22. Silicon was not present at all in the structurally similar oxide phases of column D (see Fig. 5.17), and very little silicon was found in the oxides of columns G and H (compare Figs. 5.23 and 5.24). For all examined columns, the Si:Fe ratio as determined by ratioing the peak heights of the EDS peaks, was in the range of 0.13 to 0.15 for the core, and 0.33 for the original scale of the grains. In column D, this ratio decreased from the scale to the outside of the grain, and in column E it stayed in the range of the core throughout the newly formed oxide layer on the grain. In column B, however, the ratio increased from 0.13 in the core to 0.33 in the original scale, to 0.45 in the crystalline green rust structures and then to 0.6 in the subsequent fine-grained structure. A silicon inclusion within the fine grained structure even had a Si : Fe ratio of 1:1.

As discussed in Chapter 4, the addition of silica to the feed of column B led to a decrease in reactivity. Since the original scale layer of all grains had a Fe:Si of 0.33, we assume that the ratio of 0.45 or above, as found in the green rust layer in column B, results in lesser reactivity toward chlorinated contaminants.

The green rust found in column B is structurally very similar to the green rust found in all the other columns. The close association of silica with green rust thus does not seem to change its physical properties. Silica may be adsorbed or incorporated into green rust as well as the fine-grained structures with the even higher Si:Fe ratio.

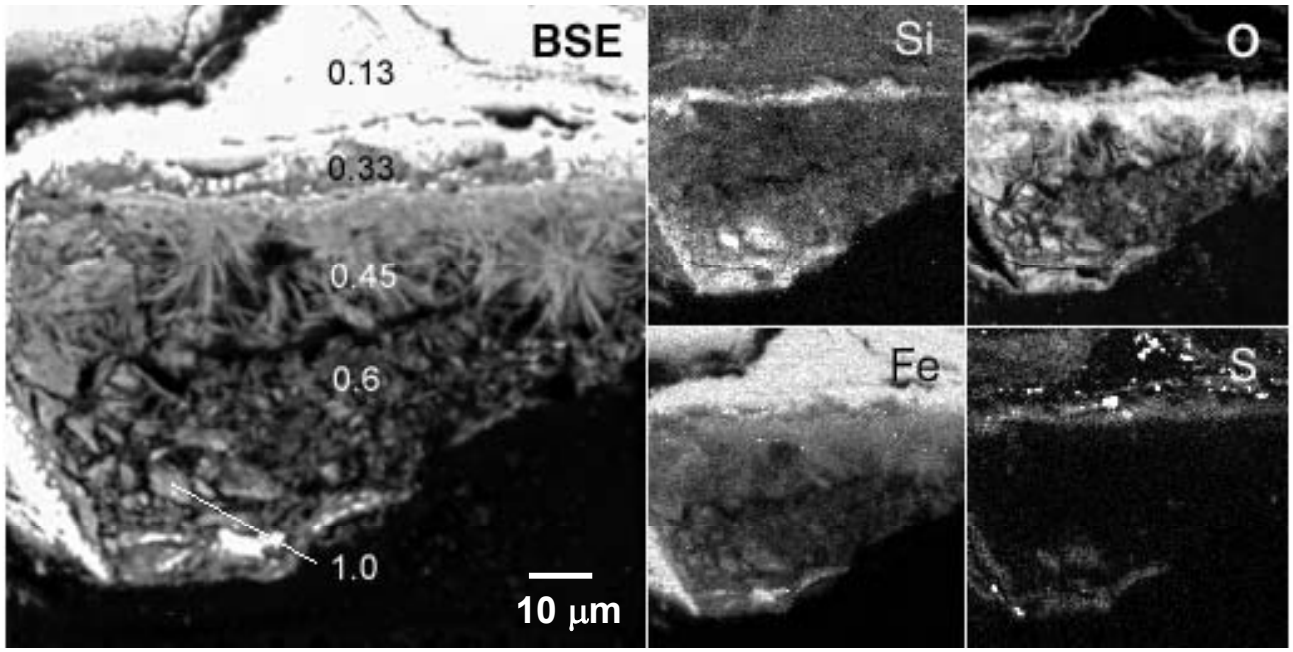

Figure 5.22 Compositional map of the oxide layer of a grain from column B. The numbers indicate the ratio of Si / Fe determined by peak height of the EDS spectrum. BSE = back-scattered electrons.

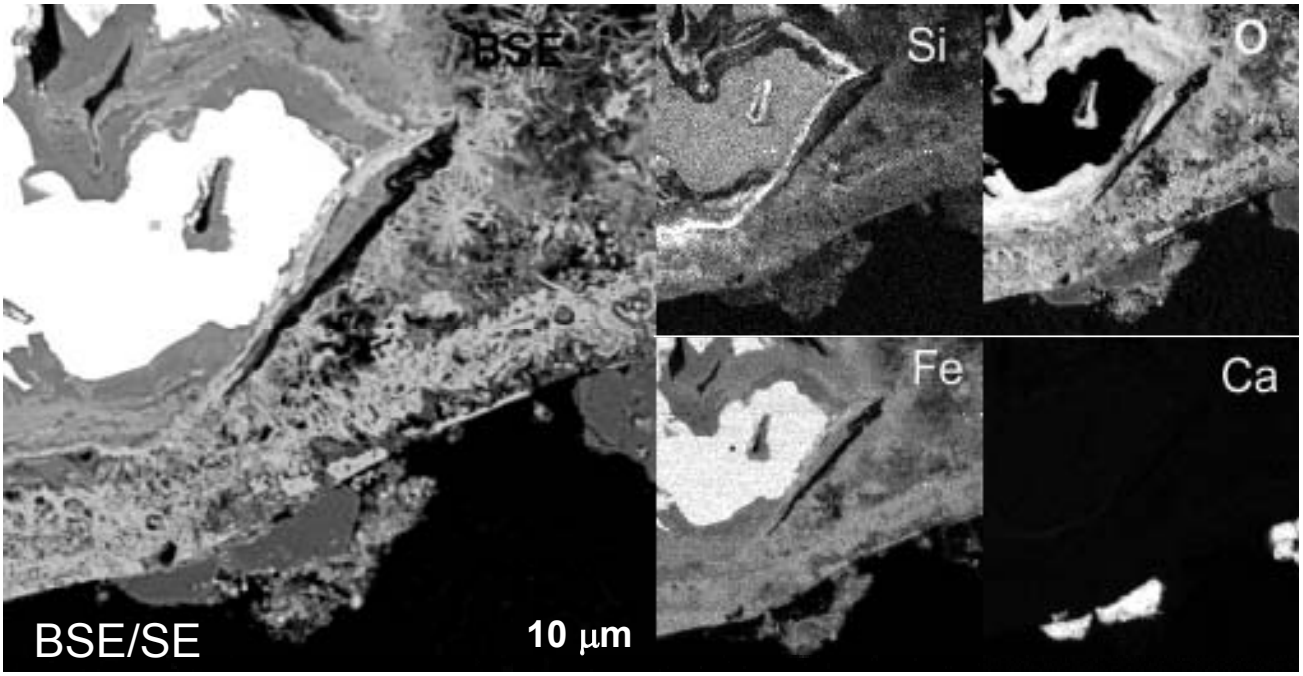

Figure 5.23 Compositional map of a grain from the influent end of column G. BSE/SE = mixture of backscattered and secondary electrons.

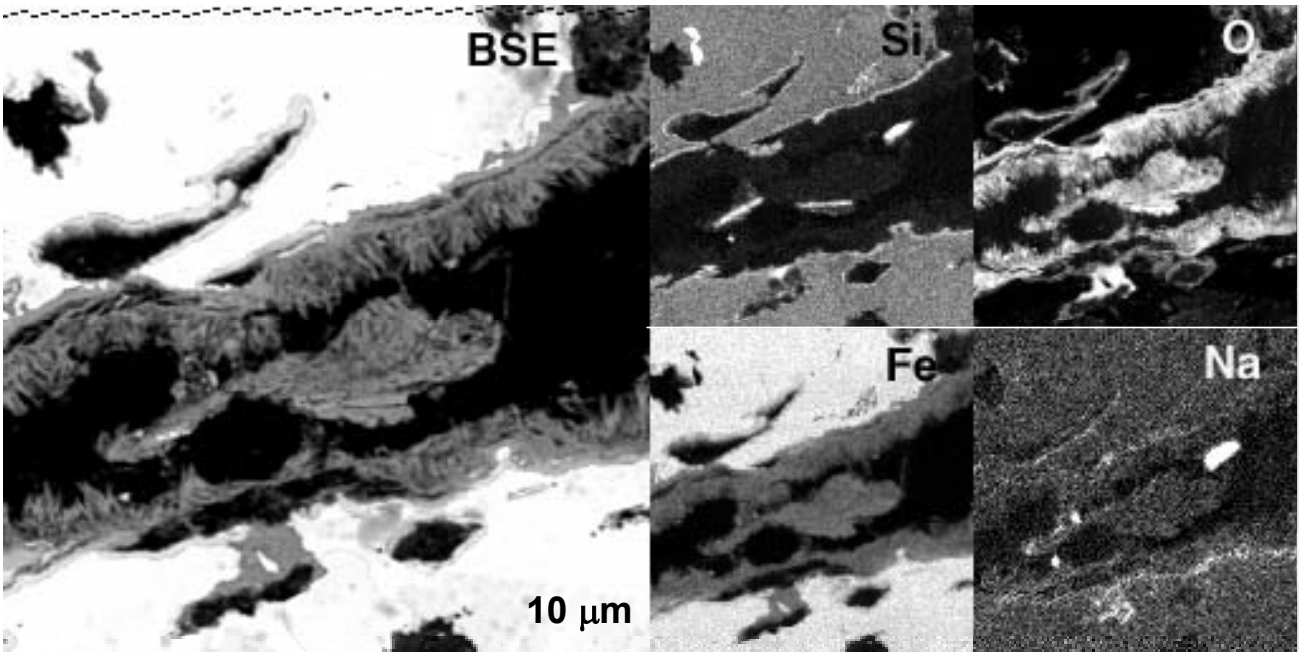

Figure 5.24 Compositional map of a pore in a grain from column H. BSE/SE = mixture of backscattered and secondary electrons.

Column E – 100% Master Builder iron, influent pH 9.2, buffered with 20 mM $NaHCO_3$

The heterogeneity between the grains from column E was greater than in any other column. Generally, the grains from column E were more heavily reacted than the other grains, but the degree of weathering varied greatly between grains from this column. Shown in Fig. 5.25 is one of the more heavily reacted grains extracted from column E. It can be seen that the pores are almost entirely filled with oxide. A close-up on the middle pore of this grain revealed that the oxides have also filled the smaller side pores of the grain. As can be seen in Fig. 5.25b the oxide layer is over 100 μm thick in some places.

Even though the oxide phase looks compact, magnification of the area revealed that it actually consists of closely packed, fine needles or plates. We are thus potentially seeing a very thick layer of green rust. It should be pointed out that no siderite was found by XRD in column E or in the other columns. We therefore assume green rust to be the major sink for carbonate. The formation of green rust appears to have been enhanced by the presence of larger amounts of carbonate.

As discussed in Chapter 4, the reactivity of column E decreased more rapidly than in any other column. One possible explanation for the reactivity loss is the thickness of the oxide layer. The oxide layer could either create a diffusion barrier for the contaminants, or it could result in too thick of a barrier between the contaminant and the electron-donating iron core.

a

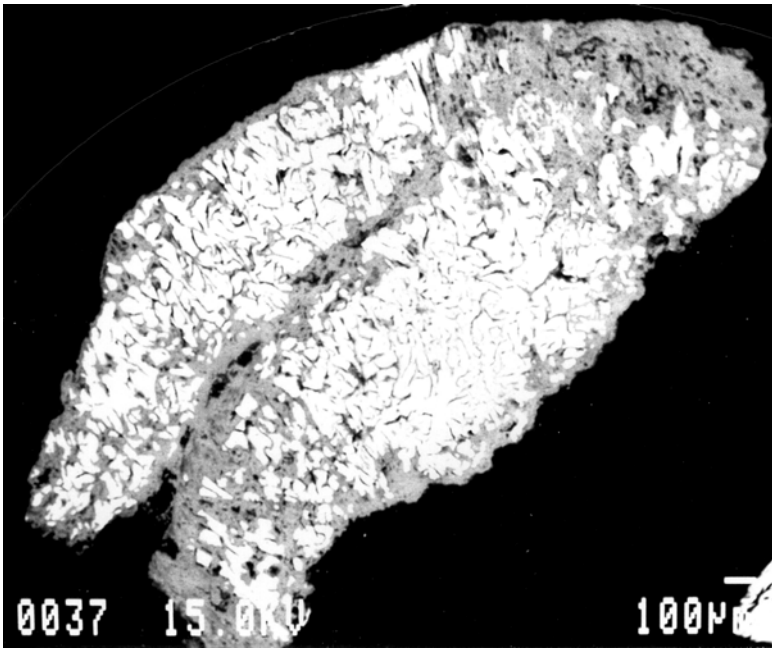

b

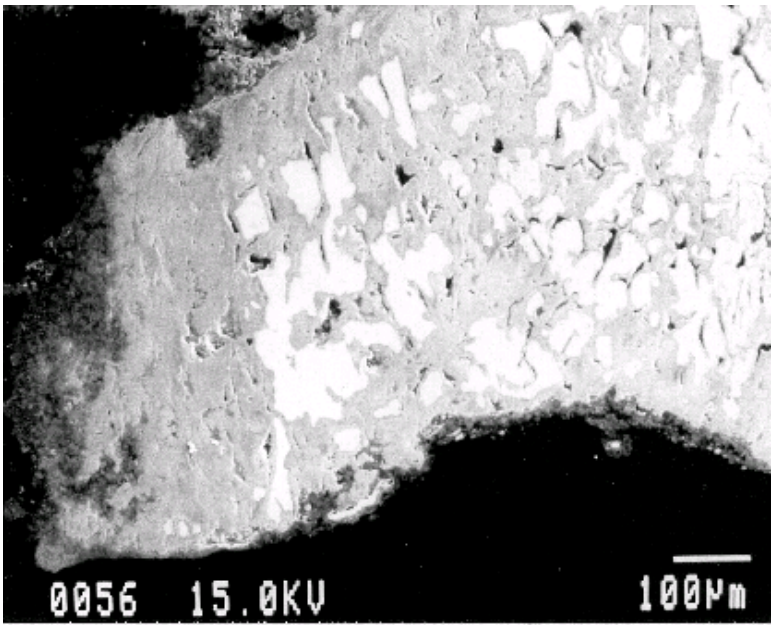

Figure 5.25 (a) Cross section of a heavily reacted grain from the influent end of column E. (b) Close-up on the lower left part of the grain shown in (a).

Column G – 100% Master Builder iron, influent pH 7.5, buffered with $CaCO_3/CO_2$

The oxide layer of the grains of column G contains dense, smooth chunks identified by XRD as calcite. The compositional map of this grain shows that no calcium is present in any other part of the oxide layer (Fig. 5.23). Curiously, the calcite plates are always on the outermost part of the oxide layer, even though the oxide seems to have grown on top of the original scale rather than as a result of iron degradation. Furthermore, the calcite plates are only rarely covered by iron oxides. It appears that the calcite is continuously being pushed out to the surface. This could be due to the lower density of calcite (specific gravity = 2.72) compared with magnetite (specific gravity = 5.18) (Klein and Hurlblut, 1985).

Another noteworthy point is that calcite is not uniformly distributed, but only appears in big chunks in a few spots. As discussed in Chapter 4, the presence of calcium carbonate in the feed solution did not have an effect on reactivity of the iron. Calcite thus does not seem to be an inhibitor for the reaction of chlorinated hydrocarbons with iron.

Column H – 92% Master Builder iron/8% albite, influent pH 7.5, buffered with $NaHCO_3/CO_2$

The compositional map of a grain from column H shows the presence of small regions of high silicon concentrations in conjunction with sodium (Fig. 5.24). These are presumably small pieces of albite or its dissolution products that have found their way into the pores of the iron grain. The Na map in Fig. 5.24 was generated with a WDS spectrometer that was not background corrected. The apparent minor amount of Na in the metal is due to the increase of background intensity from the metal.

Other than the pieces of albite, the oxide layer in column H is not more enhanced in silicon than any other grain. However, several silicon inclusions were found in the oxide layer of grains from this column. They appear as the dark spots in the oxide layers in Fig. 5.26. It has to be pointed out that these inclusions were also found on grains from different columns, but less frequently than in column H. A close-up on the silicon slag shows, that they are intertwined with small branches of iron oxide. However, the reactivity of column H was similar to all other columns, as discussed in Chapter 4. The small number of these slags does not seem to negatively affect reactivity in column H.

Characterization as a Function of Position in the Column and Column Age

Grains from the influent and effluent end of column D were analyzed. Both sets of grains seem to be equally reacted. Even though certain differences were found by Raman spectroscopy, as described later in this report, no visual differences could be seen on the microprobe. Both samples contained magnetite and green rust. It needs to be pointed out again, that the thickness of oxide layer on the grain surface may vary from influent to effluent. These oxide layers may have washed away while rinsing the grains.

In column J, slight differences between the influent and the effluent ends could be seen. Whereas the grains from the influent end of column J were just as weathered as to the grains from the influent end of column D, the grains from the effluent end were cleaner and contained mainly magnetite and little green rust. This can be seen from a comparison of Figs. 5.18 and 5.27. Green rust thus seems to form gradually with time, from influent to effluent. This corroborates with the observation, that the grains in all columns slowly obtained a white coating. This coating, which we assume to be associated with green rust formation, climbed up the column from the influent to the effluent end, over a time-period of several months.

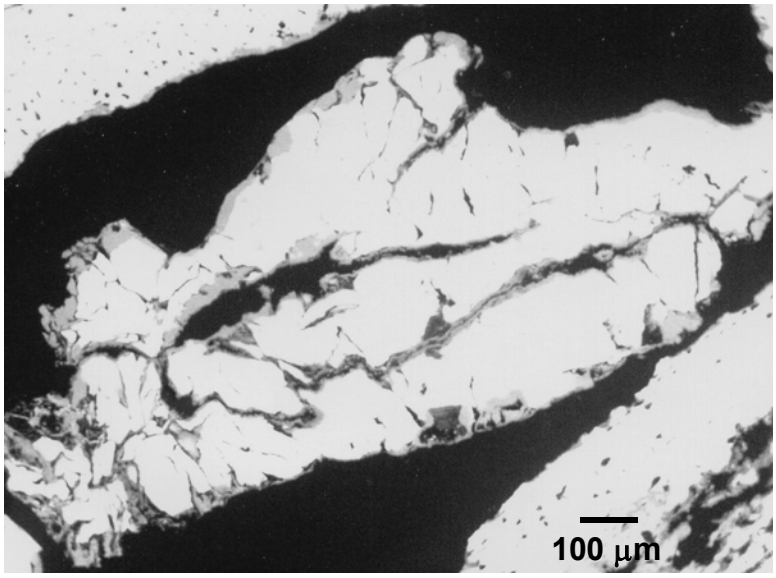

a

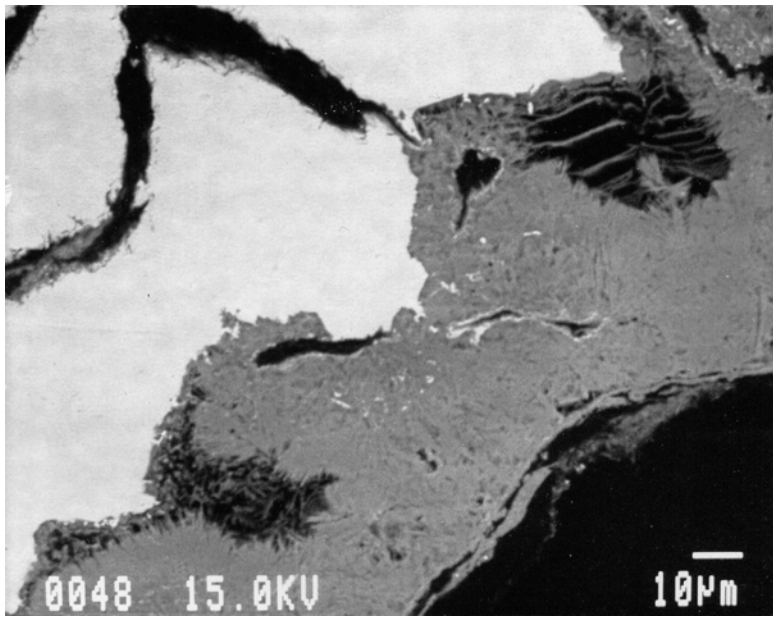

b

Figure 5.26 (a) Cross section of a grain from the influent end of column H. The dark inclusions in the oxide layer are a silicon slags. (b) Close-up on the oxide layer and the slags in figure (a).

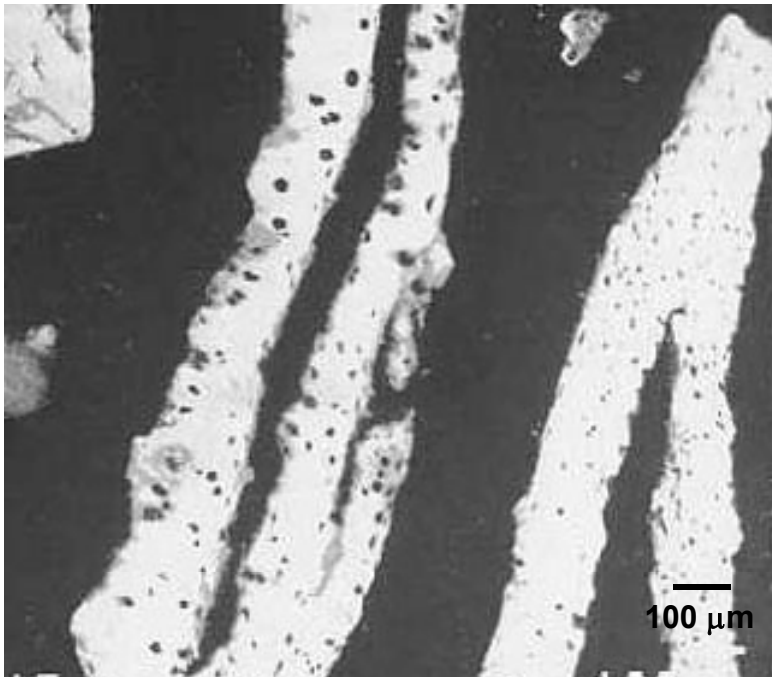

Figure 5.27 Two grains from the effluent end of column J.

MICRO-RAMAN SPECTROSCOPY

Micro-Raman spectroscopy is a powerful vibrational spectroscopic technique that can be used for the *in-situ* analysis of environmental surfaces. Water exhibits low Raman activity, therefore there is little solvent interference associated with Raman measurements obtained in its presence. As such, it was possible to obtain Raman spectra of redox sensitive species such as green rusts (Boucherit et al., 1991; Boucherit and Hugot-Le Goff, 1992; Trolard et al., 1997; Simard et al., 1998; Bonin et al., 2000b) and $Fe(OH)_2$ (Gui and Devine, 1995; Simpson and Melendres, 1996). Due to their sensitivity to air, these species are difficult to observe using *in-vacuo* surface spectroscopic techniques such as Auger spectroscopy or electron microscopy.

Sample Extraction and Analysis

Iron grains for Raman spectral analysis were obtained from columns F and G-J. The samples from column F were extracted from points located ~ 5 and ~ 30 mm from the column inlet on days 308 and 921. On day 288, iron grains were removed from columns G-J using the solid sampling ports described in Chapter 2 (port 1 at ~ 5 mm (from inlet), port 2 at ~ 30 mm, port 3 at ~ 80 mm, port 4 at ~ 200 mm, and port 5 at ~ 340 mm). The extracted grains were taken from the columns and placed into sample vials filled with column porewater obtained from the nearest aqueous sampling port. The sealed vials were then transported from JHU to the University of Waterloo for Raman analysis. In all cases, the time between sample extraction and analysis was less than four weeks.

By coupling a Raman spectrometer to a microscope and utilizing charge couple device (CCD) detection it was possible to study spot sizes of ~ 2 μm^2 (with a focal depth of ~ 26 μm in nonconfocal mode). This relatively small spot size coupled with a rapid analysis time (< 30

minutes per spot) enabled the acquisition of 10-14 spectra for each sample (typically 3-6 spots per iron grain for 2-3 grains). Two types of Raman scans were obtained for each sample. The first type was a static scan from 180-800 cm^{-1} and the second was a continuous grating scan (using a single grating) from 180-2000 cm^{-1}. Typically, 10-20 scans were averaged to obtain the resultant spectra for both types of scans. The collected spectra were analyzed using Grams/386 (ThermoGalactic Inc.; Salem, NH) spectral analysis software.

Data Analysis – Spectral Deconvolution and Raman Band Identification

Raman band locations reflect the types of precipitates present at the surface of the iron grain. A tabulation of the major Raman bands for a number of iron (hydr)oxides, carbonates, and silicates is found in Table 5.2. In addition, this table also lists the Raman bands for a number of the aqueous species present in our system. To illustrate how Raman spectra are analyzed, we first discuss how bands from a typical Raman spectrum are assigned and then examine how different band patterns can be used to identify specific oxide phases.

An example of a typical Raman spectrum (180-800 cm^{-1}) obtained from a spot on one of the grains extracted from column G (port 1) is shown in Fig. 5.28. A qualitative examination of this spectrum suggests that it contains one main Raman band centered at ~ 680 cm^{-1} and some smaller bands at 294, 319, 415, 453, and 553 cm^{-1}. As noted in Table 5.2, a number of iron phases (magnetite, maghemite, and feroxyhyte) give rise to strong Raman bands in the 650-700 cm^{-1} range (Boucherit et al., 1991; de Faria et al., 1997). Of these phases, wüstite (FeO) and feroxyhyte (δ-FeOOH) cannot be responsible for the band at ~ 680 cm^{-1}. Wüstite is discounted because the main band for wüstite actually occurs at ~ 652 cm^{-1} (de Faria et al., 1997) and is considerably broader than the peak observed here. Feroxyhyte can be discounted because

Table 5.2 High intensity Raman bands of selected species in the 200-2000 cm^{-1} region.

Iron Oxides and Hydroxides		Raman Bands (cm^{-1})									References
hematite	α-Fe_2O_3	225	245	295	415	500	615	1320			Ohtsuka et al., 1986
goethite	α-FeOOH	225	244	299	390	420	480	550	1003		Thierry et al., 1991
lepidocrocite	γ-FeOOH	252	380	526	650	1307					Gui and Devine, 1995
akagénite	β-FeOOH	400	725								Boucherit et al., 1991
feroxyhyte	δ-FeOOH	400	655								Boucherit et al., 1991
maghemite	γ-Fe_2O_3	245	300	345	395	515	645	670	715	1440	Ohtsuka et al., 1986
magnetite	Fe_3O_4	294	319	415	540	669					Odziemkowski et al., 1994
	$Fe(OH)_2$	460	550								Gui and Devine, 1995
Green rusts											
Fe^{2+}-OH stretch of GR		433									Bonin et al., 2000b
Fe^{3+}-OH stretch of GR		509									Bonin et al., 2000b
Interlayer CO_3^{2-} in GR		1053									Bonin et al., 2000b
Interlayer Cl^-		221									Simard et al., 2001
Carbonates											
siderite	$FeCO_3$	289	732	1090	1731						this work
calcite	$CaCO_3$	281	712	1088	1436						Simpson, 1998
aragonite	$CaCO_3$	205	704	1085							Herman et al., 1987
Silicates											
albite	$NaAlSi_3O_8$	209	251	270	291	479	510	765	1100		this work
fayalite	Fe_2SiO_4	289	369	505	562	814	835				Chopelas, 1991
am. silica	SiO_2	450	1050								Gout et al., 1997
Aqueous Species											
carbonate	CO_3^{2-}	1065									Bonin et al., 2000a
bicarbonate	HCO_3^-	1015									Bonin et al., 2000a
Fe^{3+}-OH_2 in $[Fe(H_2O)_6]^{3+}$ (A_{1g})		496									Bonin et al., 2000a
Fe^{3+}-OH_2 in $[Fe(H_2O)_6]^{3+}$ (E_g)		456									Bonin et al., 2000a
Fe^{2+}-OH_2/Fe^{2+}-OH in $[Fe(H_2O)_6]^{2+}$ (E_g)		430									Bonin et al., 2000a

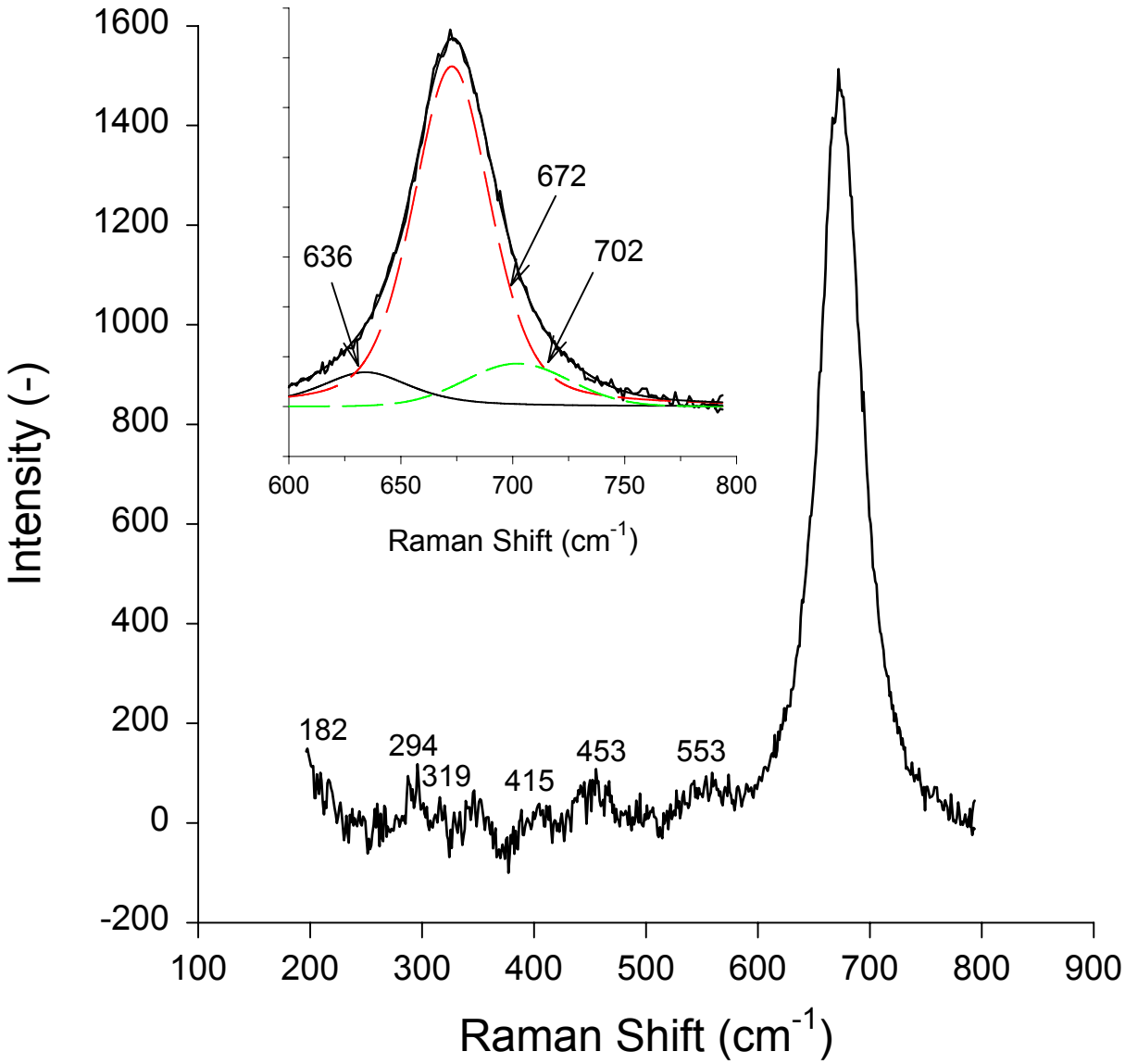

Figure 5.28 Example Raman spectra for the 180-800 cm^{-1} region. The iron grain was extracted from port 1 on column G. Inset: spectral bandfits for high intensity peak at ~ 670 cm^{-1}.

the broad band observed at 400 cm^{-1} for authentic feroxyhyte samples (Boucherit et al., 1991; de Faria et al., 1997) was not found here.

Attempting to distinguish between magnetite (Fe_3O_4) and maghemite (γ-Fe_2O_3) is a relatively complex process. The strongest band for each of these oxides occurs at ~ 670 cm^{-1} and it is therefore difficult to discern between the two species based solely on the location of this peak (Bonin et al., 1998). The presence of the small bands at 294, 319, 415, and 553 cm^{-1} does suggest, however, that magnetite was present. The simultaneous occurrence of intense bands at ~ 550 and ~ 670 cm^{-1}, the T_{2g} and A_{1g} modes of magnetite further indicate that magnetite was present. Upon first glance, the absence of peaks at ~ 645 and ~ 715 cm^{-1} suggests that maghemite was absent. Upon closer examination, however, it was apparent that the band at 680 cm^{-1} was actually a composite of three smaller bands. Spectral de-convolution of the peak indicated a high intensity band at 672 cm^{-1} and two side bands at 636 and 702 cm^{-1} (The χ^2 value for the fit was equal to 1.27, alternate fits obtained using either one or two bands were less successful in replicating the peak shape). De-convolution was necessary because the measured full width at half maximum (FWHM) of 44 cm^{-1} was slightly larger than the reported range of FWHM values for magnetite (35-42 cm^{-1}; Odziemkowski et al., 1994). The presence of the side bands at 636 and 702 cm^{-1} indicates that along with magnetite that some maghemite (γ-Fe_2O_3) was also present (Odziemkowski et al., 1994). Maghemite forms topotactically when magnetite is oxidized and is thus often detected in the presence of magnetite (Cornell and Schwertmann, 1996). As discussed within the electron microscopy section, it is possible that a solid solution of magnetite/maghemite exists, and because of the difficulties associated with discerning between these two species, we attribute the peak at ~ 670 cm^{-1} to a mixture of the two.

Upon a cursory examination of Table 5.2, it is apparent that there is significant overlap between many of the Raman bands. This overlap can make it difficult to identify all of the species present at the iron surface. In many cases, however, a given phase will exhibit multiple bands and by a careful examination of the band patterns (i.e., locations and relative intensities) it is often possible to unambiguously identify the surface (and solution) species responsible for a given band. To illustrate how these band patterns are analyzed, we discuss some exemplary Raman spectra obtained from spots located on the iron grains. These spectra illustrate some of the distinct mineral phases that could be detected at the iron surface. We note, however, that because each of the collected spectra (with the exception of albite, whose spectrum was obtained from a pure albite grain) was obtained for precipitates that had formed on the iron grain surface, the spectra are not representative of **pure** mineral phases but of a mixture of all the phases present at a particular spot. As such, each spectrum contains a significant peak resulting from magnetite/maghemite at ~ 670 cm^{-1}.

As noted in Table 5.2 and as depicted in Fig. 5.29, goethite (α-FeOOH) exhibits two high intensity bands (at 299 and 390 cm^{-1}) and a number of less intense bands (225, 244, 420, and 480 cm^{-1}). Of the high intensity bands, the one at 390 cm^{-1} is roughly one and a half times more intense than the band at 299 cm^{-1}. This ratio agrees fairly well with that observed in pure goethite samples (de Faria et al., 1997) and thus should exist for all of the column samples. Similar to goethite, hematite (α-Fe_2O_3) exhibits a high intensity band at ~ 300 cm^{-1}, however, in this case the band at ~ 390 cm^{-1} is no longer observed but a band at 225 cm^{-1} appears instead. Lepidocrocite exhibits bands at ~ 250 cm^{-1} and ~ 380 cm^{-1}. Finally, green rust exhibits two characteristic bands: one at 433 cm^{-1} that corresponds to the Fe^{II}-OH stretch and another at 509 cm^{-1} that corresponds to the Fe^{III}-OH stretch. Two non-iron bearing species observed within our

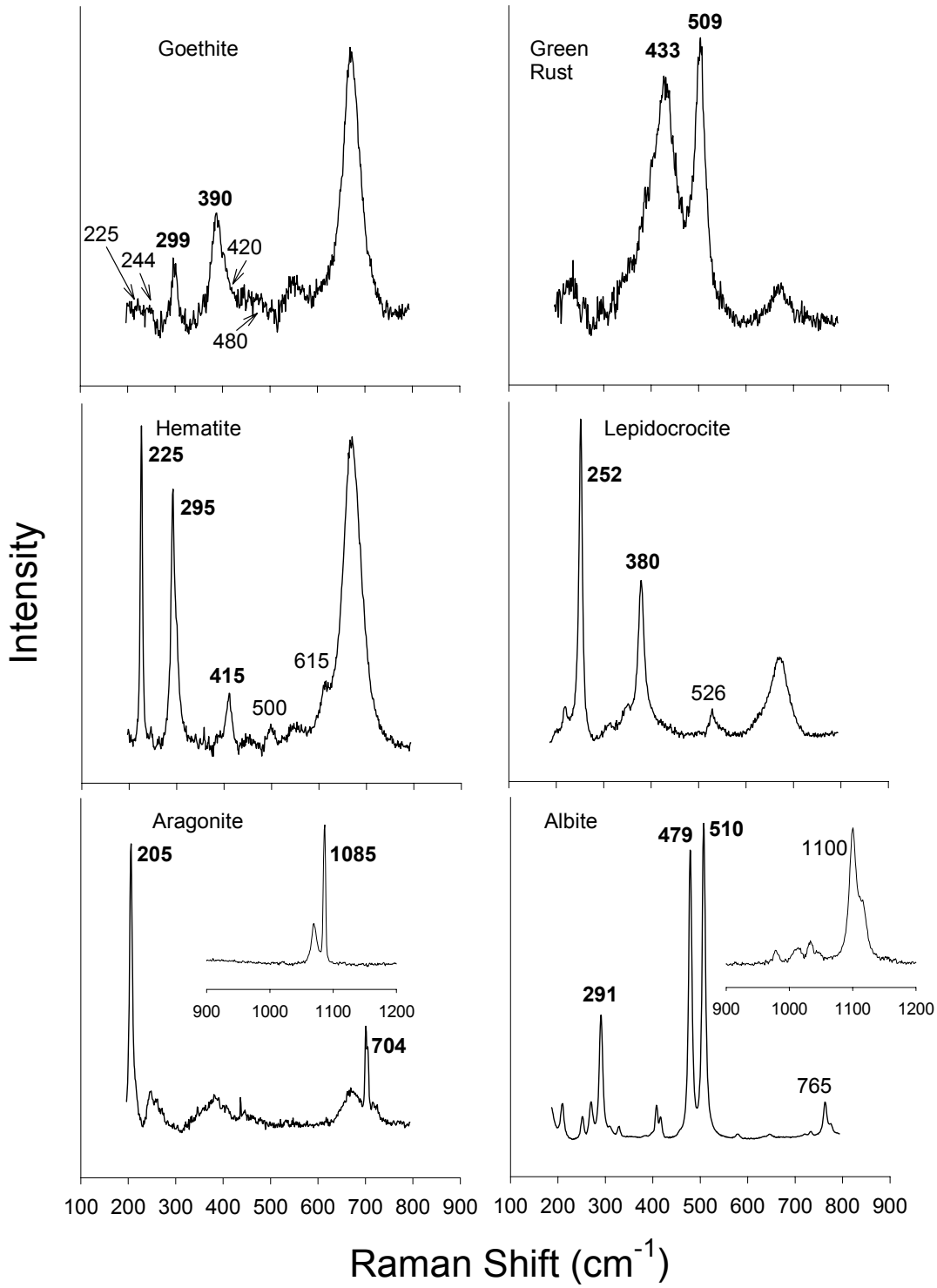

Figure 5.29 Representative Raman spectra for goethite, green rust, hematite, lepidocrocite, aragonite, and albite. With the exception of albite, all of the spectra were obtained from individual points on various iron grains and thus represent crystalline phases that had formed on the iron surface. The strongest bands are given in **bold**. As discussed within the text, the peak at ~ 670 cm^{-1} is attributed to a mixture of magnetite and maghemite.

study also exhibit characteristic Raman signatures: aragonite (peaks at 205, 703, and 1085 cm^{-1}) and albite (peaks at 291, 479, 510, and 1100 cm^{-1}).

For illustrative purposes, all of the Raman spectra depicted in Fig. 5.29 exhibited sharp peaks at the characteristic Raman shifts of a given precipitate phase. For most of the samples from the columns, however, the Raman bands were considerably less sharp. For these samples, the lack of sharpness can be attributed to impurities in the crystal phases or to the amorphous character of the surface layer (Oblonsky and Devine, 1995).

Characterization of Raw Master Builder Iron

To properly characterize the species that form on the surface of the iron as it reacts with water and other reducible species, it was first necessary to examine the surface composition of the raw unreacted iron. As shown in Fig. 5.30, the surface of the iron was initially coated by an oxide layer composed of hematite (peaks at 223, 287, 408, and 498 cm^{-1}) and magnetite/maghemite (peaks at 602, 665, and 702 cm^{-1}). This surface composition is similar to that observed previously for Master Builder iron (Odziemkowski and Gillham, 1997).

Interfacial Composition as a Function of Position in a Column

Because reactivity changed with distance along the column (i.e., was slightly lower near the inlet relative to the outlet) and because the geochemistry of the porewater also changed with distance, it was hypothesized that different surficial phases would be present within the different portions of the column. To test this hypothesis we utilized Raman spectroscopy to examine sets of iron grains extracted from columns G-J on day 288. By comparing the resultant spectra, it was possible to examine this variability. Within this section, we present Raman spectra deemed to be representative of the majority of the scans obtained for samples extracted from a given port.

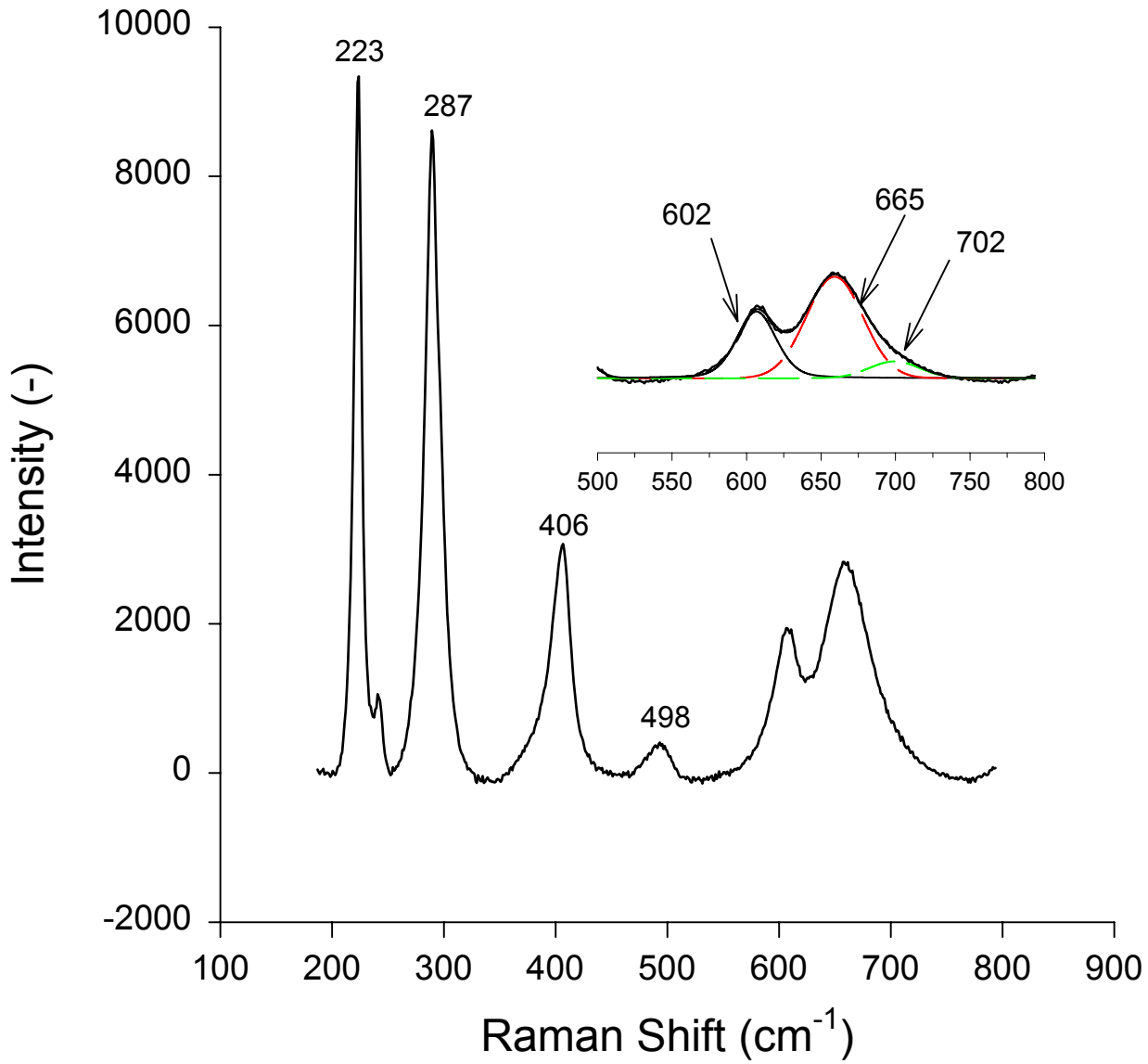

Figure 5.30 Raman spectrum for as-received Master Builder iron. The band pattern indicates that the surface is coated by a mixture of hematite (peaks at 223, 287, 406, 498, and 602 cm^{-1}) and magnetite/maghemite (peaks at 665 and 702 cm^{-1}).

As such, these spectra provide a picture of the predominant phases present at any point along the column.

Column G – 100% Master Builder iron, influent pH 7.5, buffered with $CaCO_3/CO_2$

Representative Raman spectra of iron grains obtained from ports located ~ 5, 30, 80, and 340 cm from the inlet to column G are shown in Fig. 5.31. A visual comparison of the spectra indicates that the interfacial composition of the iron grains changed significantly between the inlet and the outlet of the column. For grains extracted from port 1 (near the inlet), two strong Raman bands at 672 and 1069 cm^{-1} and several smaller bands at 371, 450, and 550 cm^{-1} were observed. As discussed previously, the bands at 672 and 550 cm^{-1} reflect the A_{1g} and the T_{2g} modes of magnetite. Additionally, due to the large width of the peak at 672 cm^{-1} (FWHM ~ 45 cm^{-1}) it again appears that maghemite was present. The weak band at 371 cm^{-1} is attributed to goethite. The band at 450 cm^{-1} is not consistent with any known iron (hydr)oxide species, but it has previously been attributed to the E_g stretch of Fe^{III}-OH_2 associated with the electrical double layer present at the (hydr)oxide surface (Bonin et al., 2000a).

Many of the Raman bands located in the 1000-1100 cm^{-1} region reflect the presence of carbonate species present either in solution or as precipitated materials. Accordingly, the band at 1069 cm^{-1} corresponds to the symmetric stretch of the CO_3^{2-} present in solution yet associated with the surface (i.e., within the double layer) (Bonin et al., 2000b).

Proceeding to Ports 2 and 3, at ~ 30 mm and ~ 80 mm, respectively, these peaks (with the exception of the small band at 550 cm^{-1}) are still apparent and additional major peaks at 207, 705, and 1085 cm^{-1} are observed. These additional peaks indicate the presence of aragonite ($CaCO_3$), with the peaks corresponding to the $E_{g,ext}$, $E_{g,int}$, and A_{1g} modes of the carbonate anion within the crystal lattice, respectively (Herman et al., 1987). Additional smaller peaks at 249 and

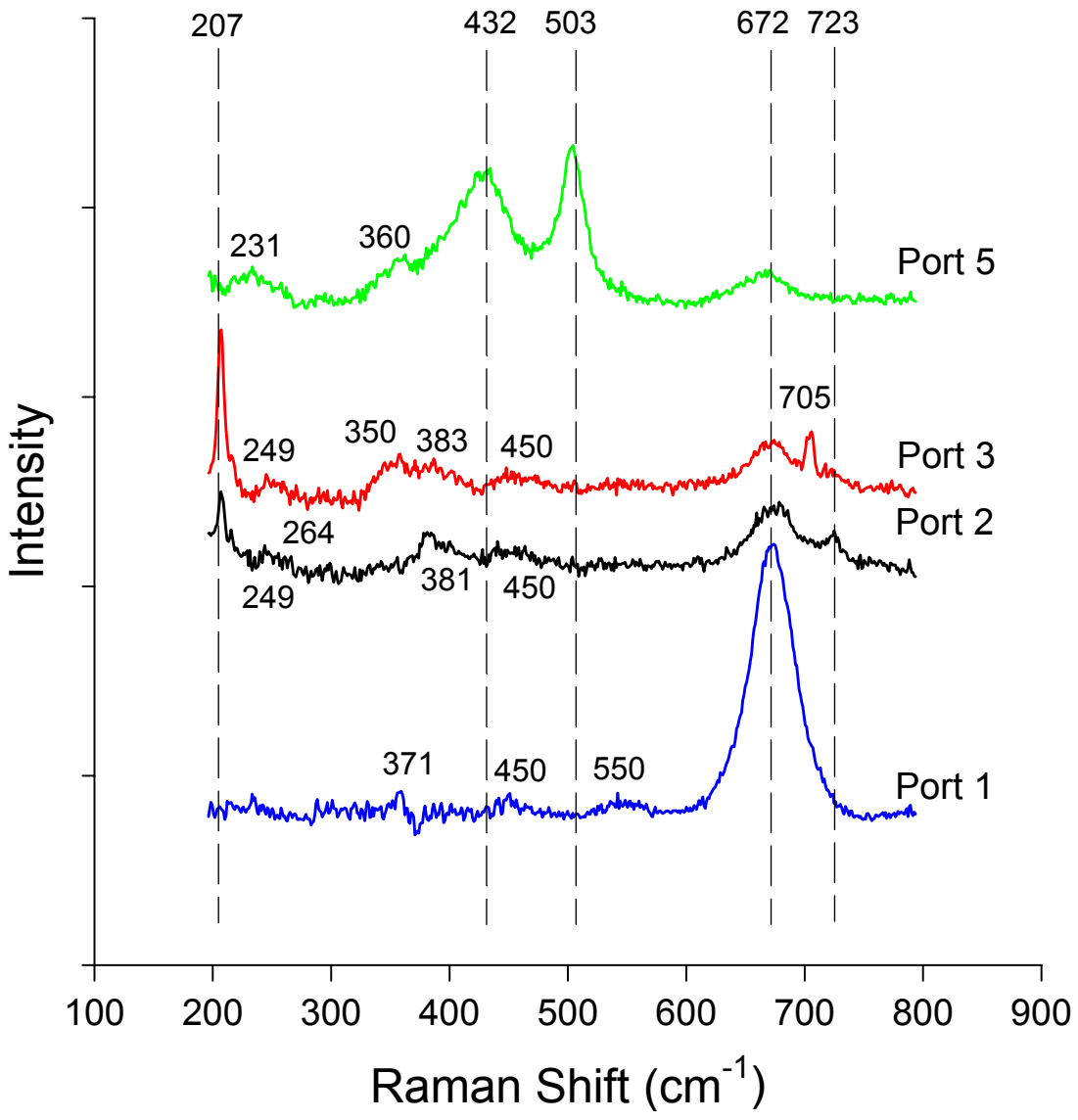

Figure 5.31 Raman spectroscopic results for column G. Sample grains were extracted from the column on day 288. Vertical lines indicate Raman shifts for high intensity bands. As noted, some less intense bands are also identified.

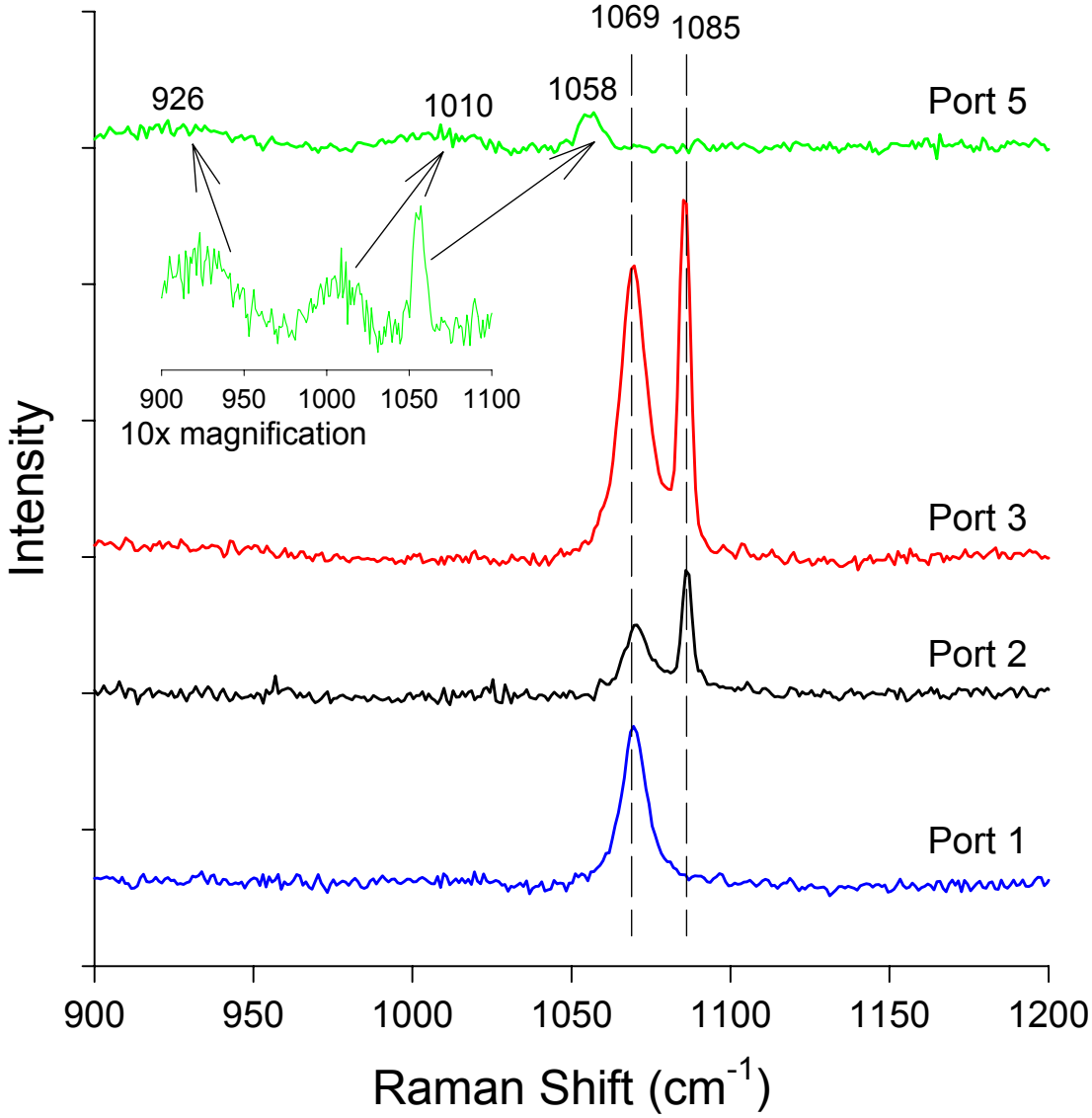

Figure 5.31 Continued

264 cm^{-1} further reflect this assignment. Were calcite present instead of aragonite we would have expected a strong Raman band at 281 cm^{-1}. The formation of aragonite instead of calcite in granular iron systems is consistent with modeling studies on the geochemistry of a PRB (Yabusaki et al., 2001) and with previous Raman measurements (Odziemkowski et al., 1998).

Near the column outlet (Port 5), the peaks at 207, 1069, and 1085 cm^{-1} have disappeared, while major peaks at 432, 503, and 1058 cm^{-1} have appeared. The peaks at 432 and 503 cm^{-1} are characteristic of the Fe^{II}-OH and Fe^{III}-OH stretches, respectively, of green rust compounds (Boucherit et al., 1991; Bonin et al., 2000b; Legrand et al., 2001b). Green rusts, mixed valence Fe^{II}-Fe^{III} layered double hydroxide compounds of the pyroaurite class (Refait et al., 1998b), have previously been observed to form as an iron corrosion product (Boucherit et al., 1991; Abdelmoula et al., 1996; Bonin et al., 2000b; Legrand et al., 2001b; Simard et al., 2001). These species are composed of brucite-like sheets of $Fe^{II}(OH)_6$ in which some of the structural Fe(II) is replaced by Fe(III). The inclusion of Fe(III) into the sheet results in a positive charge that is balanced by negatively charged anions (i.e., Cl^-, SO_4^{2-}, CO_3^{2-}, OH^-) in the interlayer space (Abdelmoula et al., 1996). In general, two types of green rust species have been identified: those involving planar anions such as Cl^- and CO_3^{2-} are referred to as green rust one (GR1; e.g., GR1(Cl^-) and GR1(CO_3^{2-})) and those involving three dimensional anions are referred to as green rust two (e.g., GR2(SO_4^{2-})).

With Raman spectroscopy, it is possible to discern amongst the different interlayer ions, as the Cl^-, CO_3^{2-}, and SO_4^{2-} species present within the interlayer exhibit characteristic Raman shifts that differentiate them from non-interlayer species (Simard et al., 2001). Within the columns, both carbonate (present in the feed solutions) and chloride (a product of the dechlorination reactions) are present and therefore they have the potential to be found within the

interlayer. For the grains extracted from Column G, the Raman spectra appear to indicate that both species were present. Chloride present within the interlayer has been reported to have a Raman band at ~ 220 cm^{-1} (Simard et al., 2001) and interlayer carbonate has a Raman band at ~ 1053 cm^{-1} (Bonin et al., 2000b; Legrand et al., 2001b). From the Raman spectra depicted in Fig. 5.31, it is apparent that peaks at ~ 231 and 1058 cm^{-1} have appeared and we attribute them to the presence of chloride and carbonate, respectively, within the interlayer. The simultaneous detection of multiple types of interlayer ions has been previously observed and has been attributed to the rapid interchange that can occur amongst different interlayer ions (Refait and Génin, 1994).

The ratio of the intensities of the Fe^{II}-OH and Fe^{III}-OH peaks reflect the relative proportions of Fe^{II} and Fe^{III} within the structures. For a natural GR ($[Fe^{II}Fe^{III}(OH)_4]^+[OH^-]$) a ratio of 1:1 has been observed, while for GR1(CO_3^{2-}) ($[Fe_4^{II}Fe_2^{III}(OH)_{12}]^{2+}[CO_3 \cdot 2\ H_2O]^{2-}$ a ratio of 2:1 has been found (Trolard et al., 1997). For the carbonate GR produced by the electrochemical oxidation of iron, a ratio of 1:1 was observed (Legrand et al., 2001b). In this column, for the 10 spots (out of 12 total at port 5) where GR was detected, a ratio of 0.99:1 ($\pm$ 0.08 at 95% confidence level) was observed. In accord with Legrand et al., we hypothesize that the green rust present within this column has structural formulas of $Fe^{II}_2Fe^{III}_2(OH)_8^{2+}[CO_3^{2-}]$ and $Fe^{II}_2Fe^{III}_2(OH)_9Cl$.

Column H – 92% Master Builder iron/8% albite, influent pH 7.5, buffered with $NaHCO_3/CO_2$

Representative Raman spectra of iron grains obtained from column H are shown in Fig. 5.32. As was the case with column G, a visual comparison of the spectra indicates that the interfacial composition of the grains changed significantly between the inlet and the outlet of the column. Iron grains extracted from port 1 exhibit three significant Raman bands: a broad

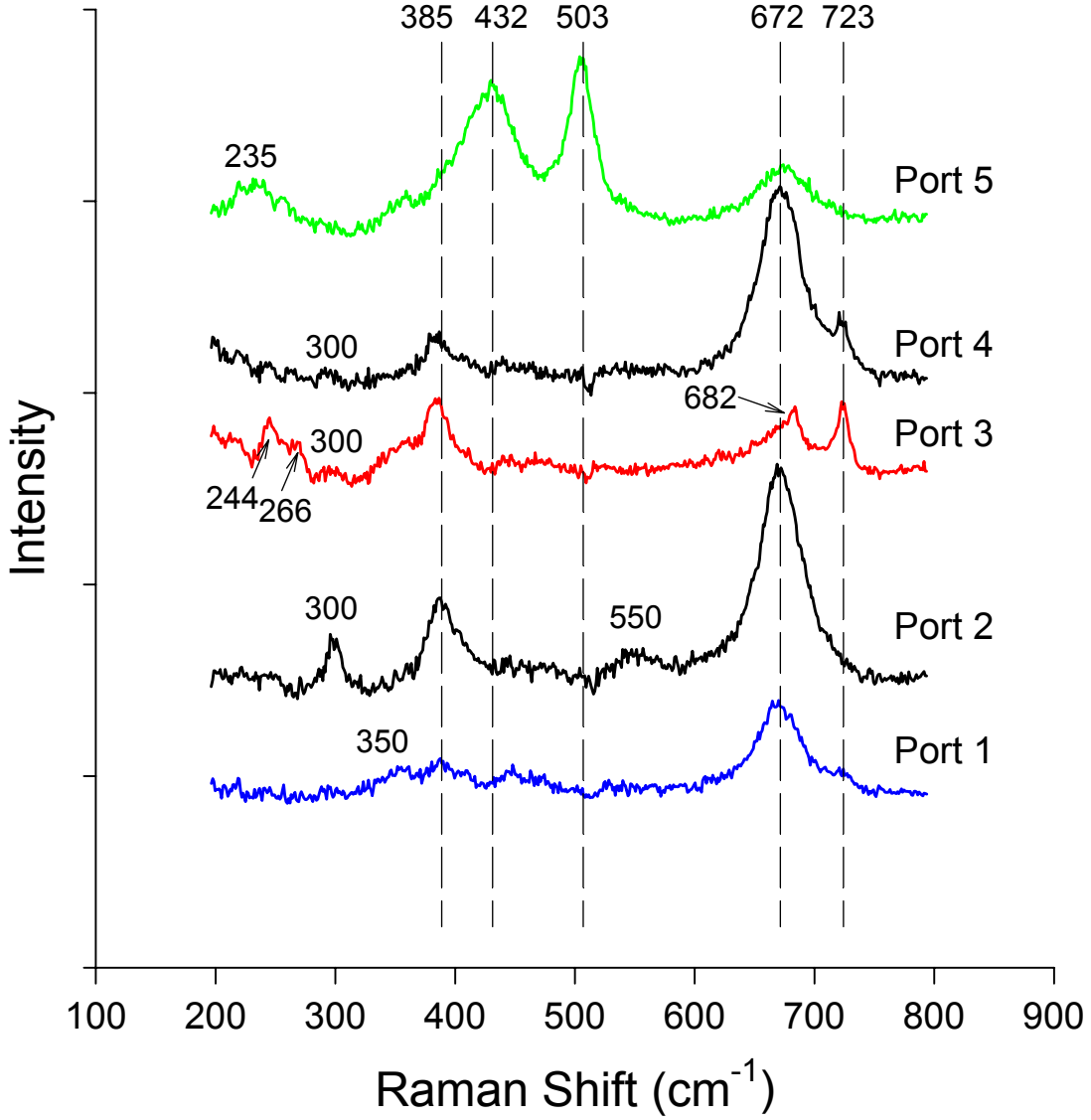

Figure 5.32 Raman spectroscopic results for column H. Sample grains were extracted from the column on day 288. Vertical lines indicate Raman shifts for high intensity bands. As noted, some less intense bands are also identified.

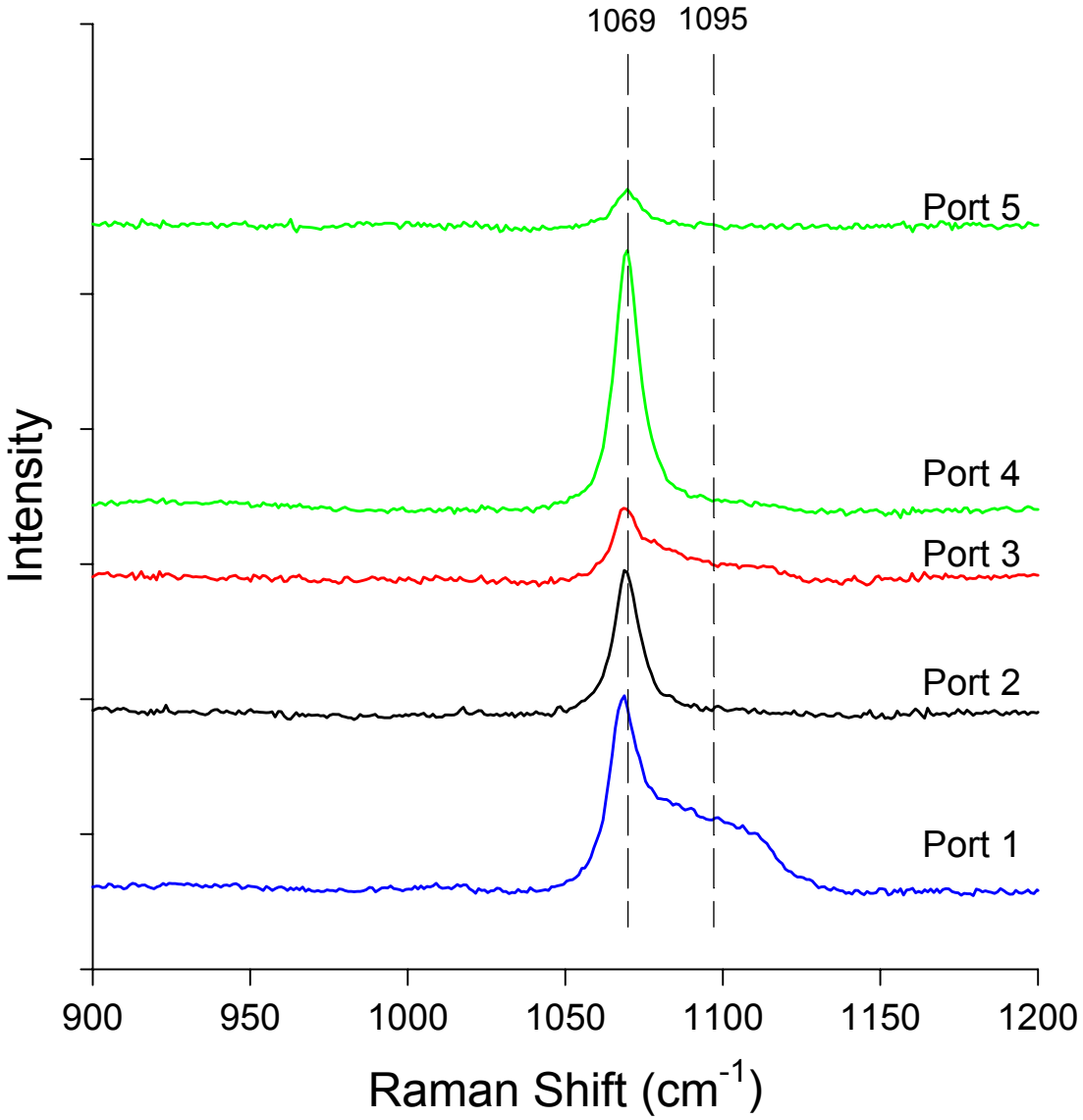

Figure 5.32 Continued.

peak at ~ 390 cm^{-1} that is attributed to goethite, a peak at 672 cm^{-1} attributed to magnetite/maghemite, and the peak at 1069 attributed to the symmetric stretch of solution phase CO_3^{2-}. In addition to these major peaks, bands at 723 and 1095 cm^{-1} were also observed. These peaks are attributed to the $E_{g,int}$ and the $A_{1g,int}$ modes of siderite (Herman et al., 1987). These peaks both occur within Raman shift ranges where carbonate mineral phases exhibit intense Raman bands and do not correspond to any known iron (hydr)oxide phases. The broadness of the peak at 1095 cm^{-1} suggests, however, a high degree of amorphous character (Oblonsky and Devine, 1995).

Moving further into the column, we note that the Raman bands corresponding to goethite (bands at 300, 385, 550 cm^{-1}) become more apparent. At port 3, two unidentified peaks occur at 244 and 266 cm^{-1}, these peaks could possibly indicate hematite formation, however, this is unlikely since no band at ~ 500 cm^{-1} was observed. Because the admixed albite had partially dissolved (as detailed within Chapter 4) it is conceivable that these peaks reflect the presence of amorphous silicate phases. Nevertheless, these peaks do not correspond to amorphous silica, fayalite (Fe_2SiO_4), or the parent albite material.

As with column G, green rust was detected near the column outlet (peaks at 432 and 503 cm^{-1}). Due to the lack of any discernable peaks at ~ 1058 cm^{-1} it does not appear that sufficient quantities of carbonate existed within the interlayer space to be detectable. Based on the appearance of the peak at 235 cm^{-1}, however, it does appear that chloride was present within the interlayer space. For the 11 spots (out of 12 sampled points at port 5) where GR was detected, a ratio of 0.95:1 ($\pm$ 0.13 at 95% confidence level) was observed. This ratio once again suggests a 1:1 stoichiometry between Fe(II) and Fe(III) (e.g., $Fe^{II}_2Fe^{III}_2(OH)_9Cl$).

Interestingly, very few Raman bands that correspond to any known silicate or iron-silicate minerals were detected. Out of the 60 spots analyzed on the grains from this column, only 1-2 appeared to indicate the presence of albite precipitates on the iron surface. It is extremely unlikely, however, that albite would re-precipitate on the iron surface from solution and therefore the presence of this signal is presumed to be an artifact resulting from the association between an original albite grain and the iron itself.

Although little evidence suggests that Raman detectable silicate phases formed at the iron surface, there is evidence that iron-bearing phases did form on the albite grains themselves. As shown in Fig. 5.33, albite grains extracted from Ports 1, 4, and 5 exhibit different characteristics. Near the column inlet, the Raman spectra is quite clean with the major albite peaks at 292, 482, 510, 785, and 1099 cm^{-1} clearly visible. Proceeding further into the column, these bands are still evident, however, the Raman signals have become increasingly noisy and the magnetite/maghemite peak (672 cm^{-1}) has become apparent. In addition, the relative intensities of the peaks have decreased significantly, indicating that the albite has weathered (Frogner et al., 1998). Near the column inlet, where the pH was considerably lower (~ 7.5) than at the outlet (~ 9.3), the effects of weathering were minimal, an observation supported by previous studies suggesting that high pH values accelerate albite dissolution relative to circumneutral pH values (Blum and Lasaga, 1988).

Column I – 100% Master Builder iron, influent pH 7.5, buffered with $NaHCO_3/CO_2$

Within this column, a variety of iron (hydr)oxides were detected: goethite (peaks at 297 and 390 cm^{-1}) at ports 1 and 3, magnetite/maghemite (peak at 672 cm^{-1}) at all ports, lepidocrocite (peaks at 250, 300, 350, and 382 cm^{-1}) at port 5, $Fe(OH)_2$ at ports 1 and 3, and green rust at port 5 (Fig. 5.34). The presence of $Fe(OH)_2$ was indicated by the broad bands at 460 and 550 cm^{-1}

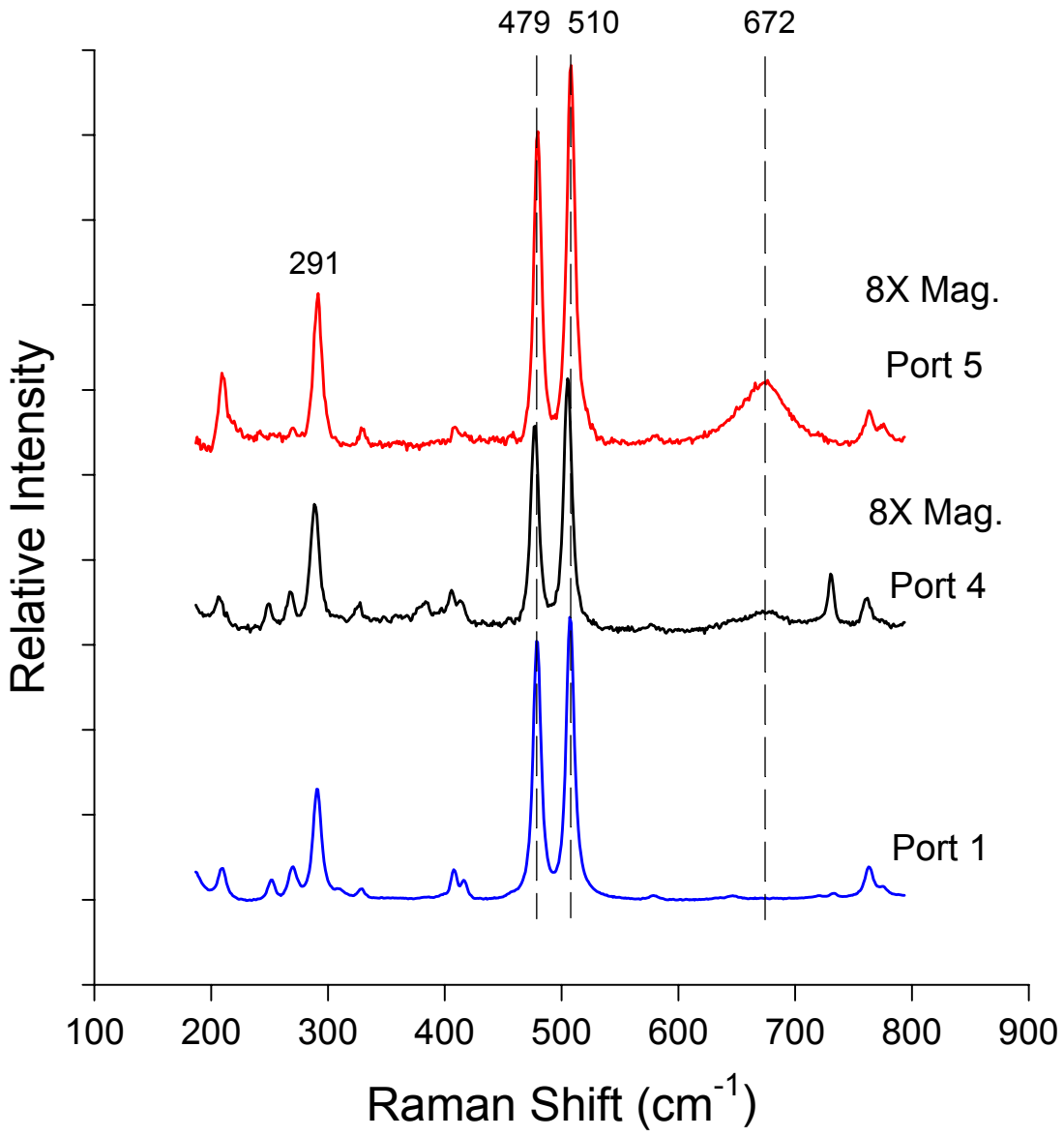

Figure 5.33 Raman spectra for albite grains extracted from ports 1, 4, and 5 from column H.

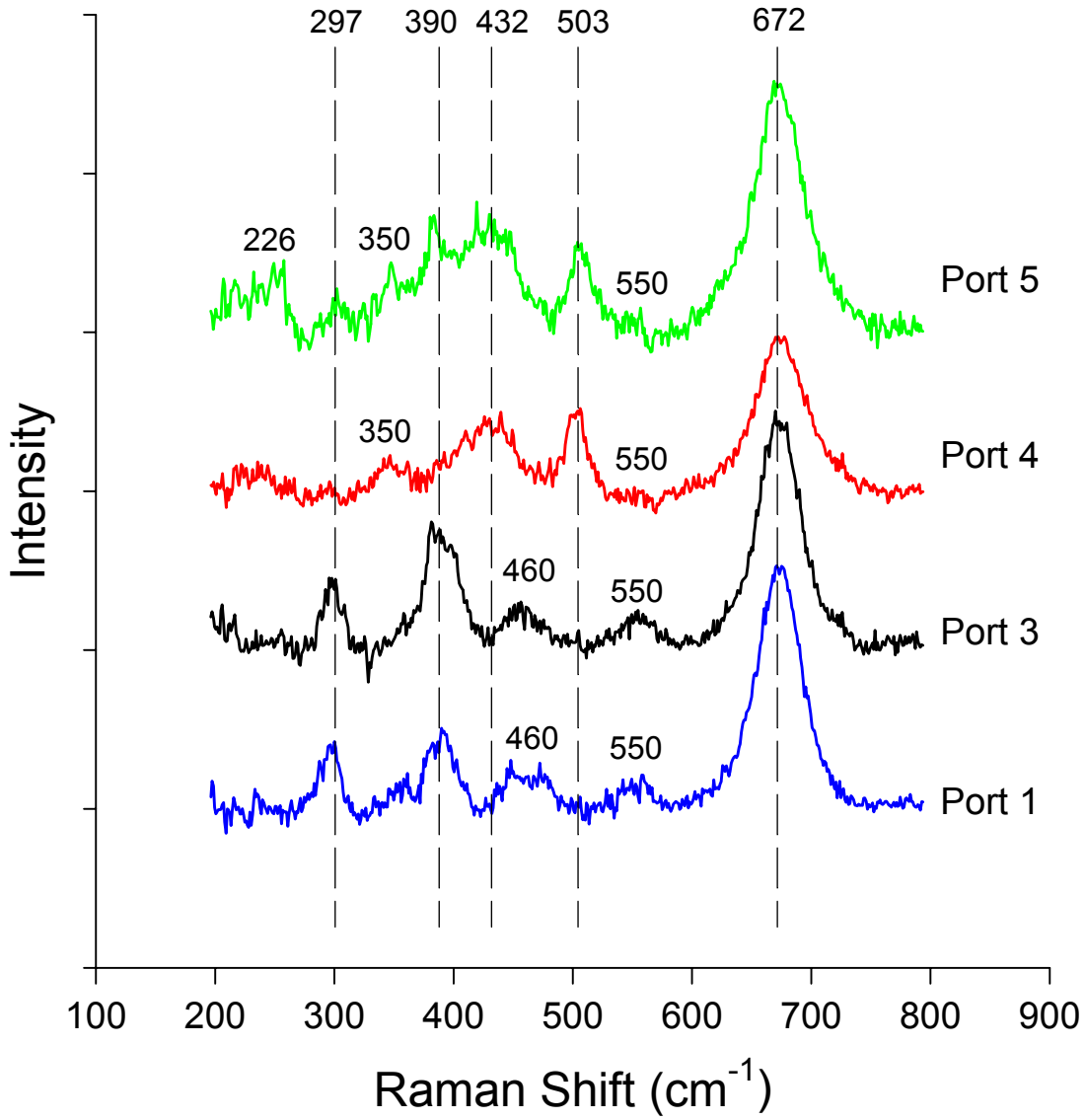

Figure 5.34 Raman spectroscopic results for column I. Sample grains were extracted from the column on day 288. Vertical lines indicate Raman shifts for high intensity bands. As noted, some less intense bands are also identified.

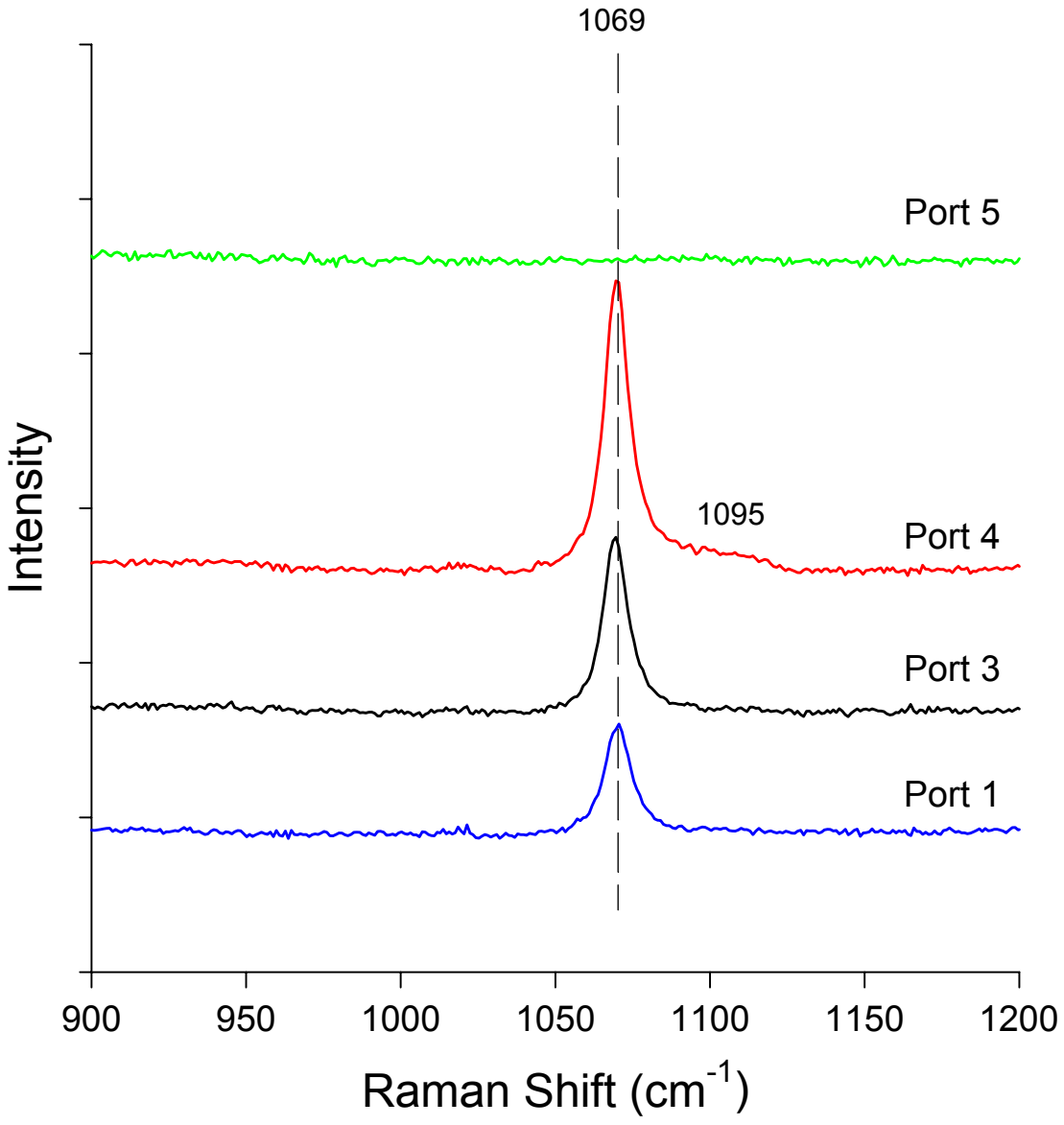

Figure 5.34 Continued.

observed for the grains extracted from Ports 1 and 3. The simultaneous occurrence of these bands as well as the observation that the band at 550 cm^{-1} is much wider than the T_{2g} band of magnetite (Odziemkowski et al., 1998) clearly suggest the presence of this phase. The occurrence of green rust near the column outlet was indicated by the presence of peaks at 432 and 503 cm^{-1}. In addition, the peak at 226 cm^{-1} indicated that Cl^- was present within the interlayer of the green rust. The ratio of the intensities of the Fe^{II}-OH and Fe^{III}-OH peaks was 1.22 ± 0.28, again suggesting a 1:1 ratio between Fe^{II} and Fe^{III}.

Other than the CO_3^{2-} stretch at ~ 1069 cm^{-1}, no significant carbonate bands were observed. Interestingly, we saw no evidence of this carbonate peak for any of the grains extracted from Port 5. This possibly suggests a deficit of surface complexed carbonate ions near the oxide surface for grains present within the distal portion of the column.

Column J – 100% Master Builder iron, influent pH 9.3, buffered with $NaHCO_3/CO_2$

Within this column, few Raman detectable oxides other than magnetite/maghemite (peak at 672 cm^{-1}) were found near the column inlet (i.e., ports 1 and 2; Fig. 5.35). Other than this peak, the only other significant one occurred at 1069 cm^{-1}, corresponding to double-layer CO_3^{2-}. For grains extracted from ports 3, 4, and 5, however, green rust species (peaks at 432 and 503 cm^{-1}) were detected. The ratio of intensities for these two peaks was 1.04 ± 0.253 at port 3, 0.832 ± 0.041 at port 4, and 0.913 ± 0.085 at port 5. These ratios again suggest a 1:1 ratio between Fe^{II} and Fe^{III}. Peaks at 225 and 1056 cm^{-1} suggest that the interlayer anions for the green rust in this column are chloride and carbonate, respectively.

Interestingly, in this column green rust compounds were detected nearer the inlet than in columns G-I. This spatial variability between the columns is potentially the result of the lower

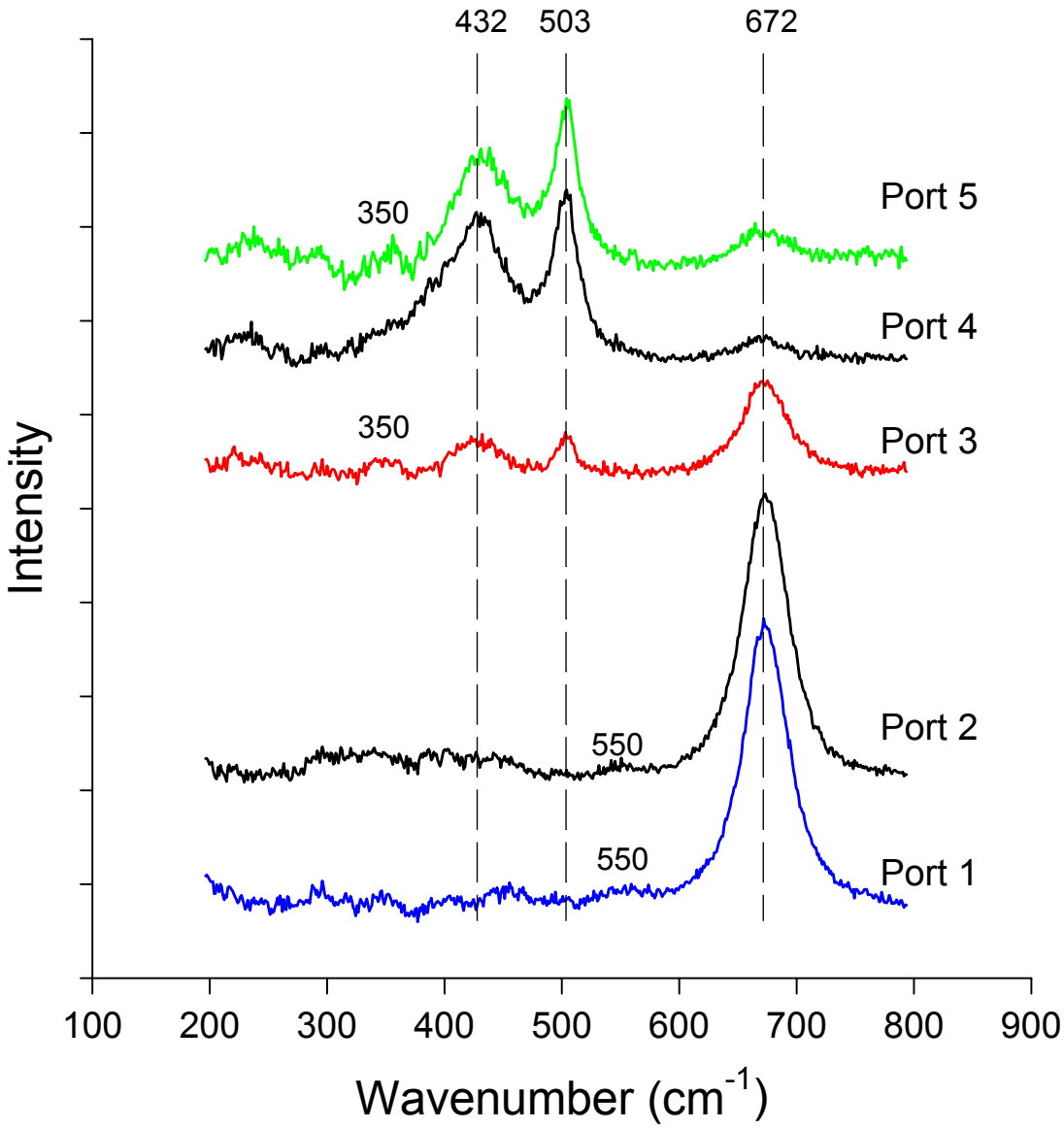

Figure 5.35 Raman spectroscopic results for column J. Sample grains were extracted from the column on day 288. Vertical lines indicate Raman shifts for high intensity bands. As noted, some less intense bands are also identified.

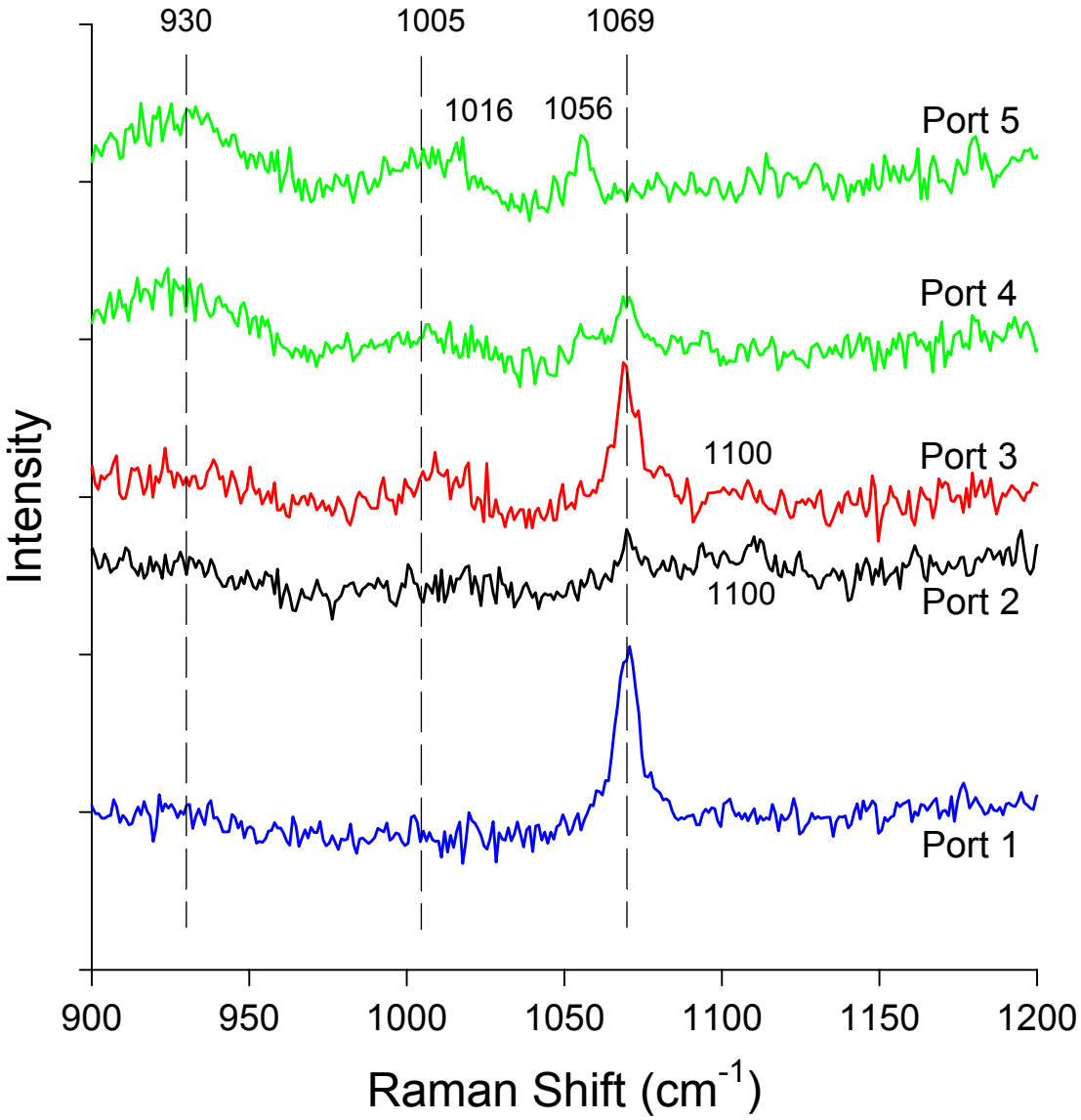

Figure 5.35 Continued.

influent pH (~ 7.5) of columns G-I. Predominance area diagrams for both GR1(Cl^-) and GR1(CO_3^{2-}) suggest that both species are thermodynamically stable under pH (pH = 7.5-9.5) and redox (E_h = -0.3 to –0.7 V) conditions similar to those found within the columns (Génin et al., 1998). Further examination of these diagrams, however, indicates that the green rusts are slightly more stable at higher pH values. Because the porewater pH in columns G-I did not reach ~ 9.3 until the last third of each column, the green rusts may have been thermodynamically unstable and therefore did not form.

Interfacial Composition as a Function of Column Age.

Fig. 5.36 depicts Raman spectra for samples obtained from ports 5 and 30 mm from the inlet of column F after 308 and 921 days. As shown, the interfacial composition of the iron grains extracted from port 2 changed significantly as the column aged, whereas those extracted from port 1 did not. At 308 days, the strong Raman bands at 425 and 504 cm^{-1} that are indicative of green rust were clearly present for the grains from port 2. After 921 days, however, the bands for green rust have disappeared leaving three Raman bands at 390, 460, and 672 cm^{-1}, corresponding to the species goethite and magnetite/maghemite. These differences indicated that the interfacial composition changes with time. As the column aged, the green rust was no longer detected at port 2, suggesting that the spatial variations observed in columns G-J are temporal as well.

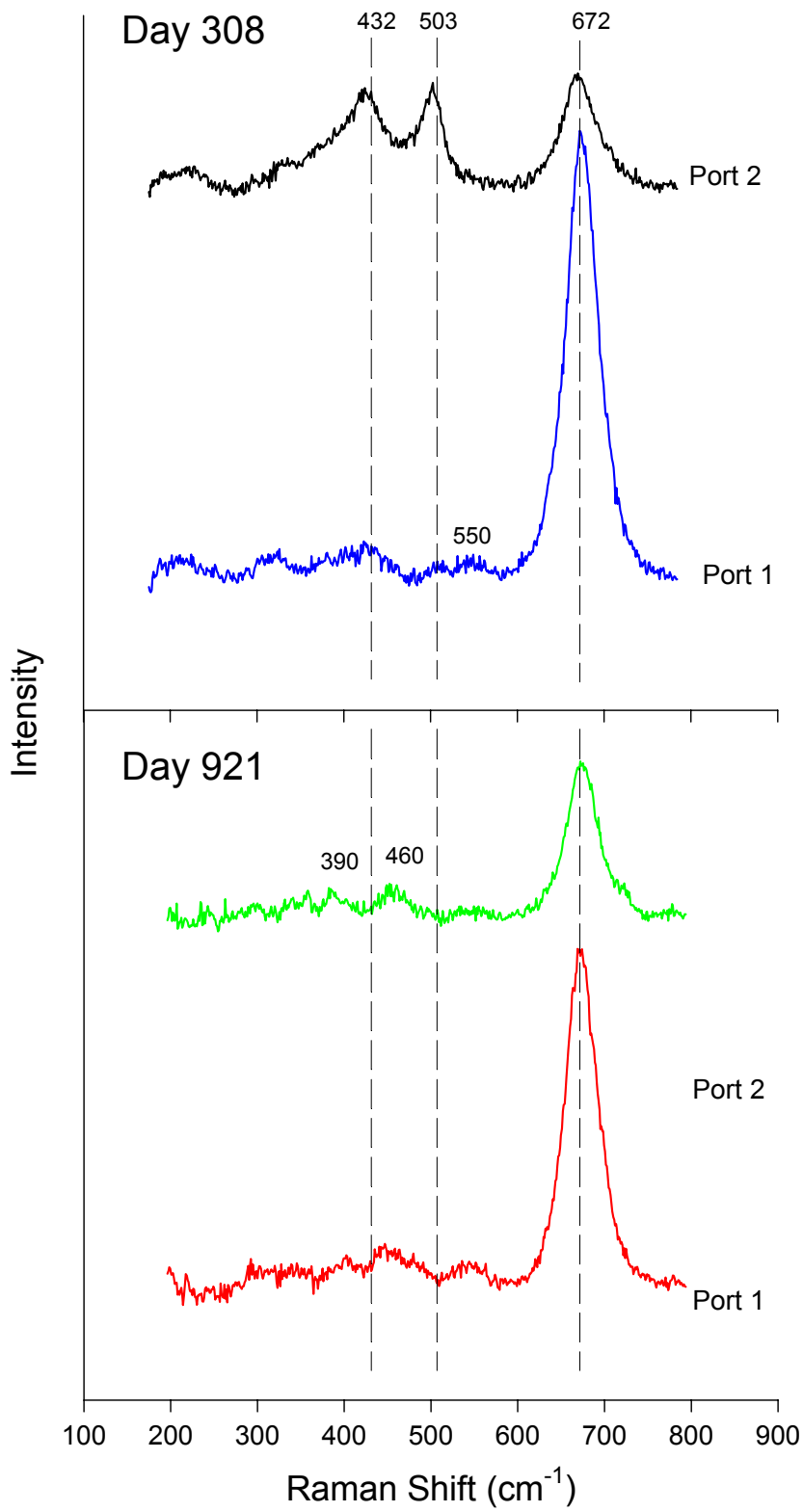

Figure 5.36 Comparison of representative Raman spectra for column F. Grains were extracted on days 308 and 921. Vertical lines indicate Raman shifts for high intensity bands. As noted, some less intense bands are also identified.

CHAPTER 6 – ELECTROCHEMICAL PROBE RESULTS

As noted within Chapter 2, two different types of electrochemical probe experiments were conducted. The first type involved the use of in-situ probes containing five individual iron grains serving as working electrodes, an Ag/AgCl reference electrode, and a platinum counter-electrode. These probes were attached to columns G-J and were used for the first ~ 120 days of column operation. Once it became apparent, however, that the performance of these probes was unsatisfactory, as detailed in the sections that follow, a series of ex-situ experiments were conducted.

IN-SITU ELECTROCHEMICAL PROBES

The response of the electrochemical probes was monitored by measuring the open circuit potential (OCP) as a function of time and through the use of impedance spectroscopy. The results obtained from the OCP measurements suggest that the response is characteristic of the local chemistry in the probes and not representative of the location in column. Similar problems with reproducibility were noted for the impedance spectroscopy.

Open-Circuit Potential Measurements

OCP measurements were obtained from each of the twelve in-situ electrochemical probes (three probes each for columns G-J). Each of these probes was used to acquire two types of OCP measurements: the potential measured at the iron grain surface relative to a reference electrode (Ag/AgCl) and the potential of one iron grain relative to another. The voltage measured relative to a reference electrode is the potential at the corroding iron surface and may provide some insight into the processes occurring therein. The voltages measured between two different iron

grains provide information about dissimilarities in the reactivity of the grains. Figs. 6.1 to 6.12 illustrate the voltages measured using both of these techniques. Each figure contains three panels, the left-most panel depicts the OCP measurements relative to the reference electrode and the center and right-most panels depict the potential measurements of grains 2 and 3 versus grain 1, respectively.

Grain 1 vs. Reference Electrode Measurements

In general, the open circuit potential, measured with respect to the reference electrode decreased to about -0.3 V to -0.4 V in the first 20 -30 days and then gradually increased to about 0 to -0.1 V after 120 days. The large fluctuations seen for all the grains suggest periods of active corrosion followed by the build up of corrosion products. The frequency of these events is particularly noticeable during the first 20 - 30 days. The gradual increase in potential to -0.1 V suggests the slow build up of precipitates at the surface of the grain.

Comparison of the open circuit potentials shows that there is no obvious difference for electrodes at different locations in each column. It is likely that the restricted flow into and out of the probes isolated the grains in the probe from the grains in the column, so that the response does not reflect the electrochemical behavior at a given location in the column.

Prior results suggest that the measured OCP at a corroding iron electrode should be in the –0.4 to –0.5 V vs. Ag/AgCl range (Farrell et al., 2000; Ritter et al., 2002). The average measured OCP value for the in-situ probes in columns G-J was in this range only for a relatively short period, typically from 20 – 30 days. The increase in potential at longer times is consistent with the build up of corrosion products and precipitates in the occluded regions of the probes.

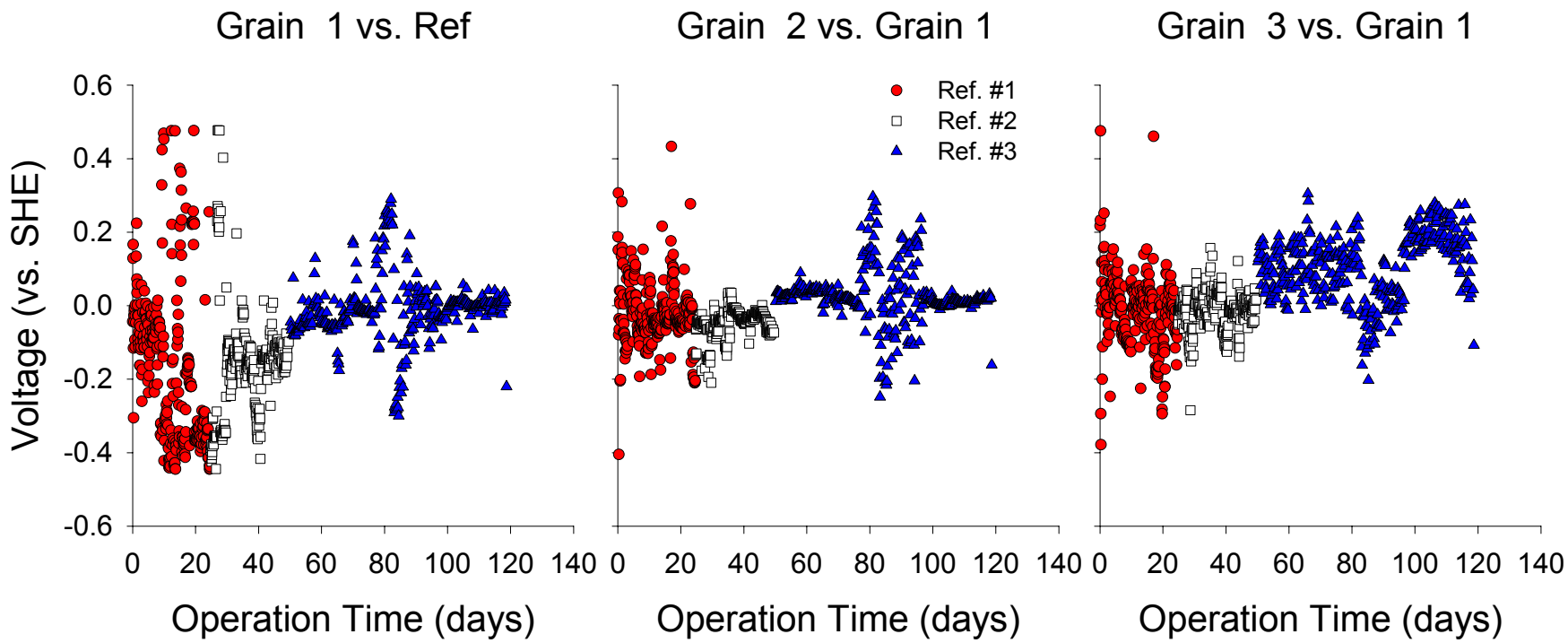

Figure 6.1 Electrochemical results – probe G1. As noted, three different reference electrodes were used during the course of these experiments.

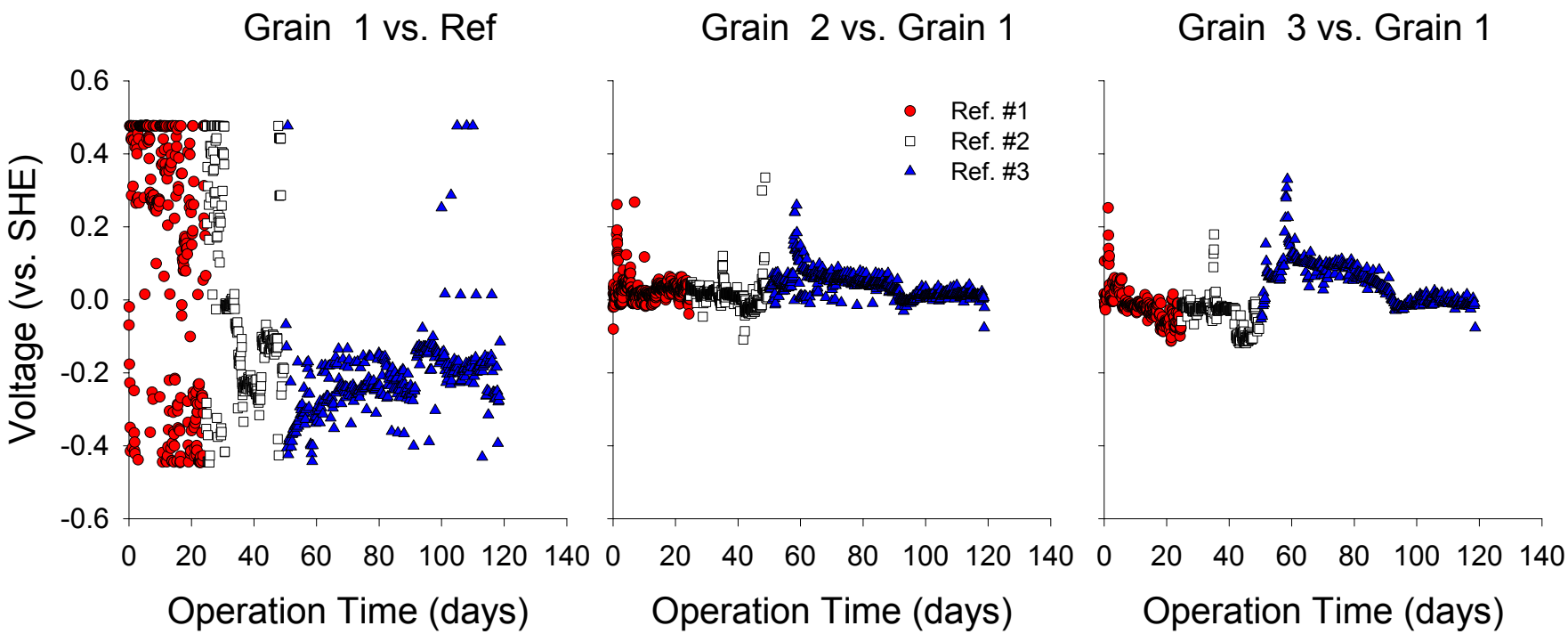

Figure 6.2 Electrochemical results – probe G2. As noted, three different reference electrodes were used during the course of these experiments.

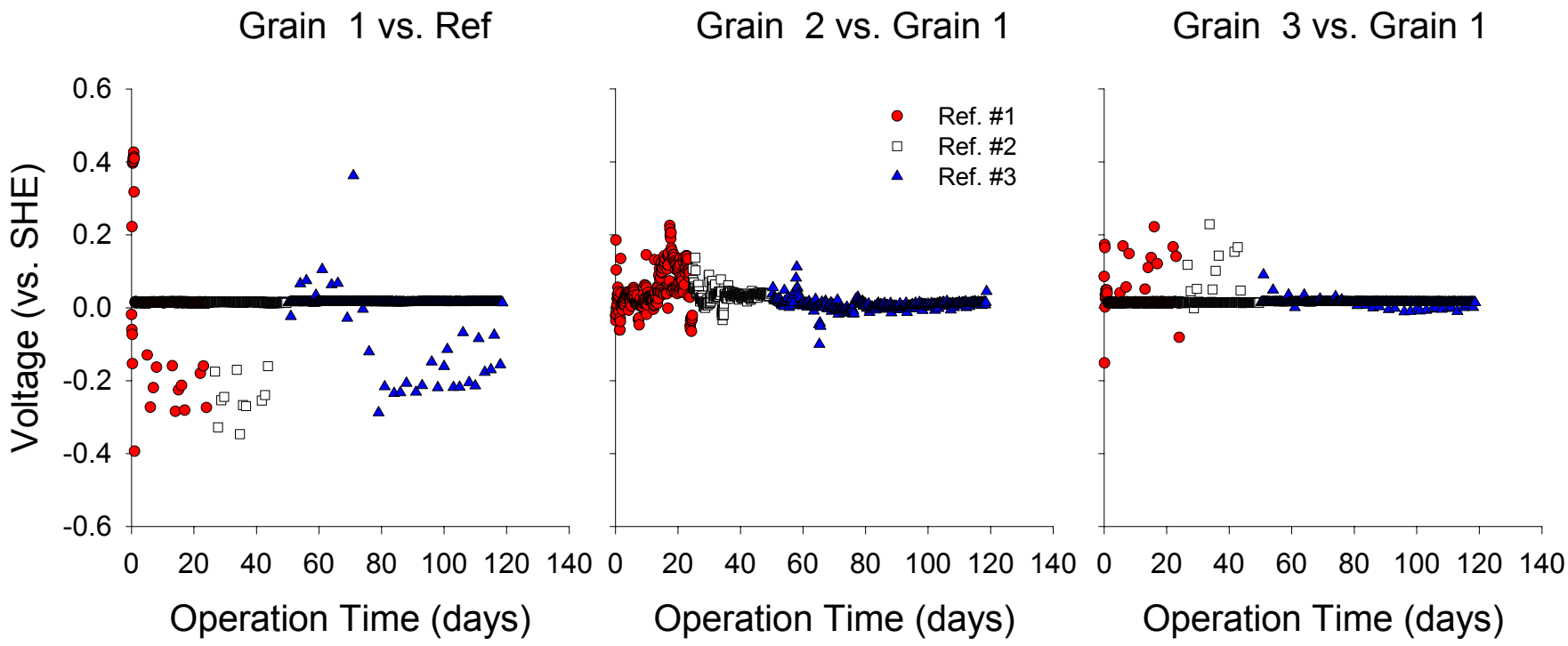

Figure 6.3 Electrochemical results – probe G3. As noted, three different reference electrodes were used during the course of these experiments.

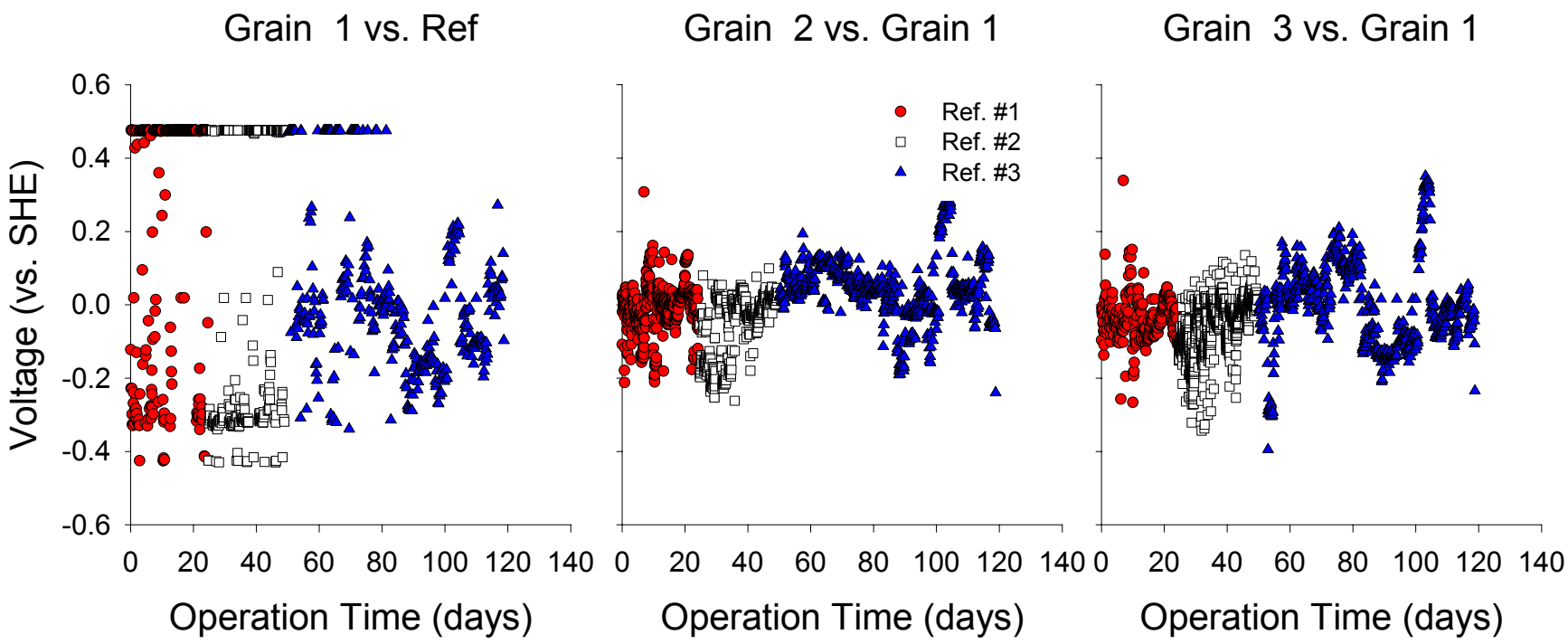

Figure 6.4 Electrochemical results – Probe H1. As noted, three different reference electrodes were used during the course of these experiments.

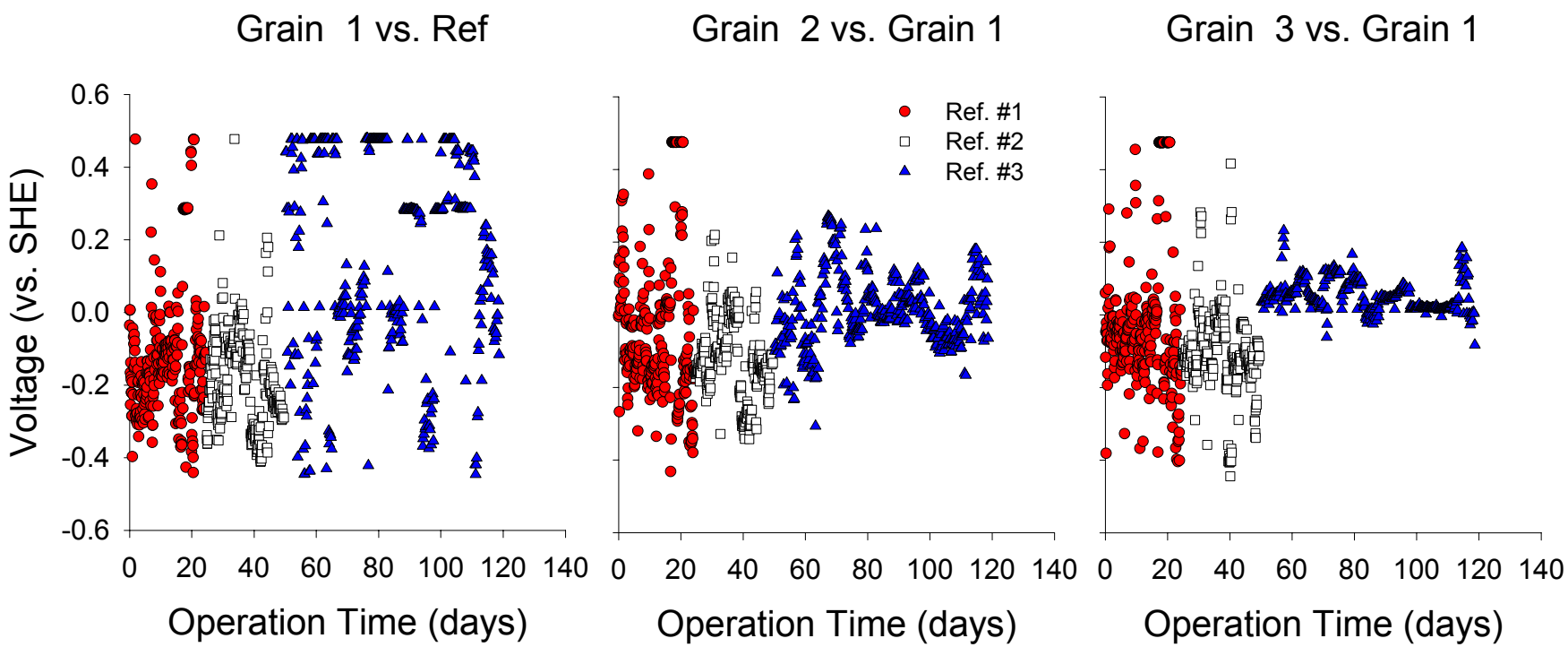

Figure 6.5 Electrochemical results – Probe H2. As noted, three different reference electrodes were used during the course of these experiments.

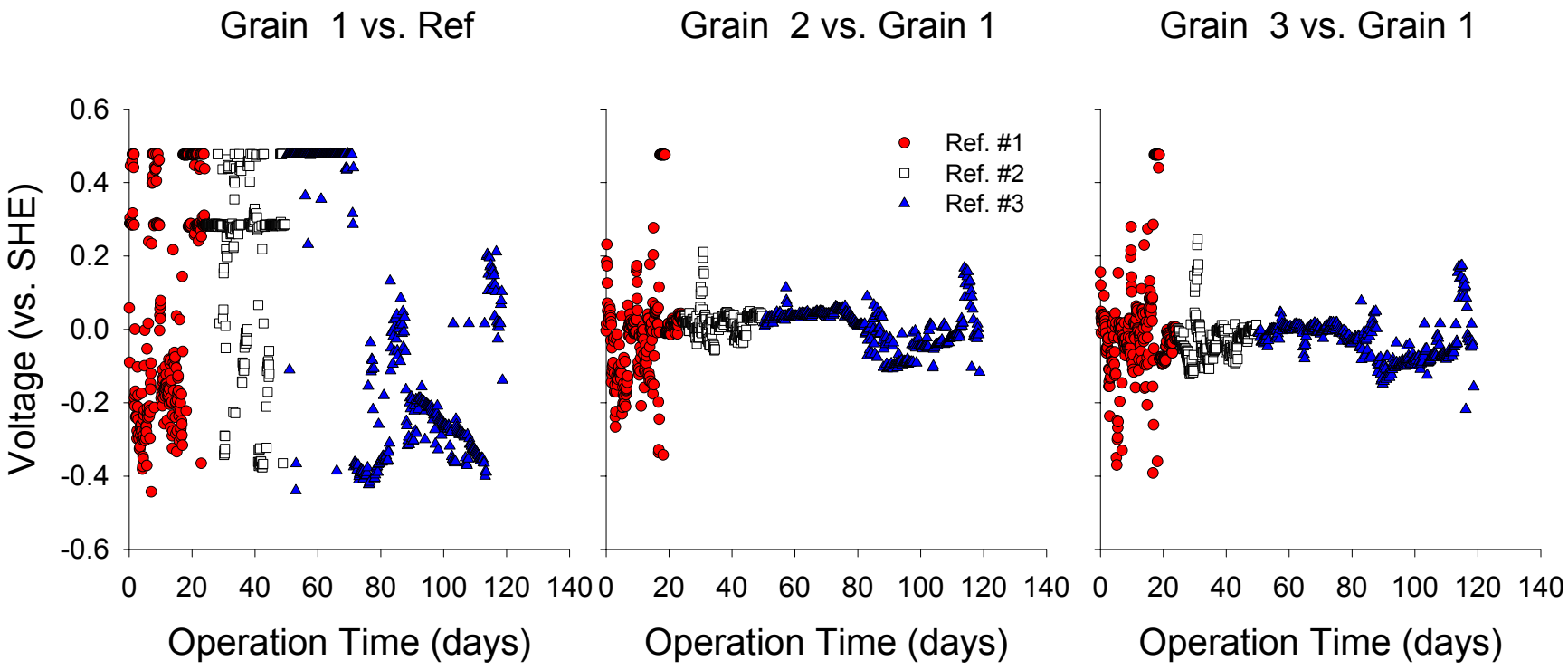

Figure 6.6 Electrochemical results - Probe H3. As noted, three different reference electrodes were used during the course of these experiments.

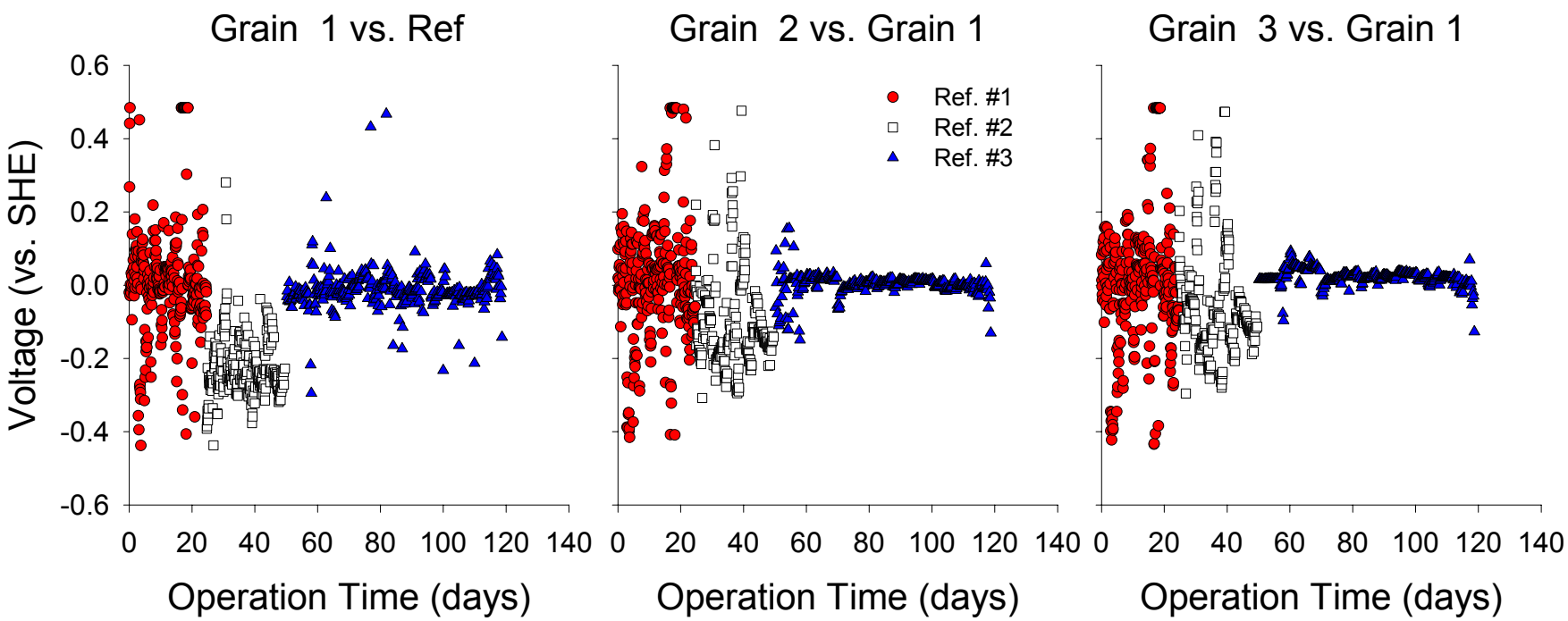

Figure 6.7 Electrochemical results – Probe I1. As noted, three different reference electrodes were used during the course of these experiments.

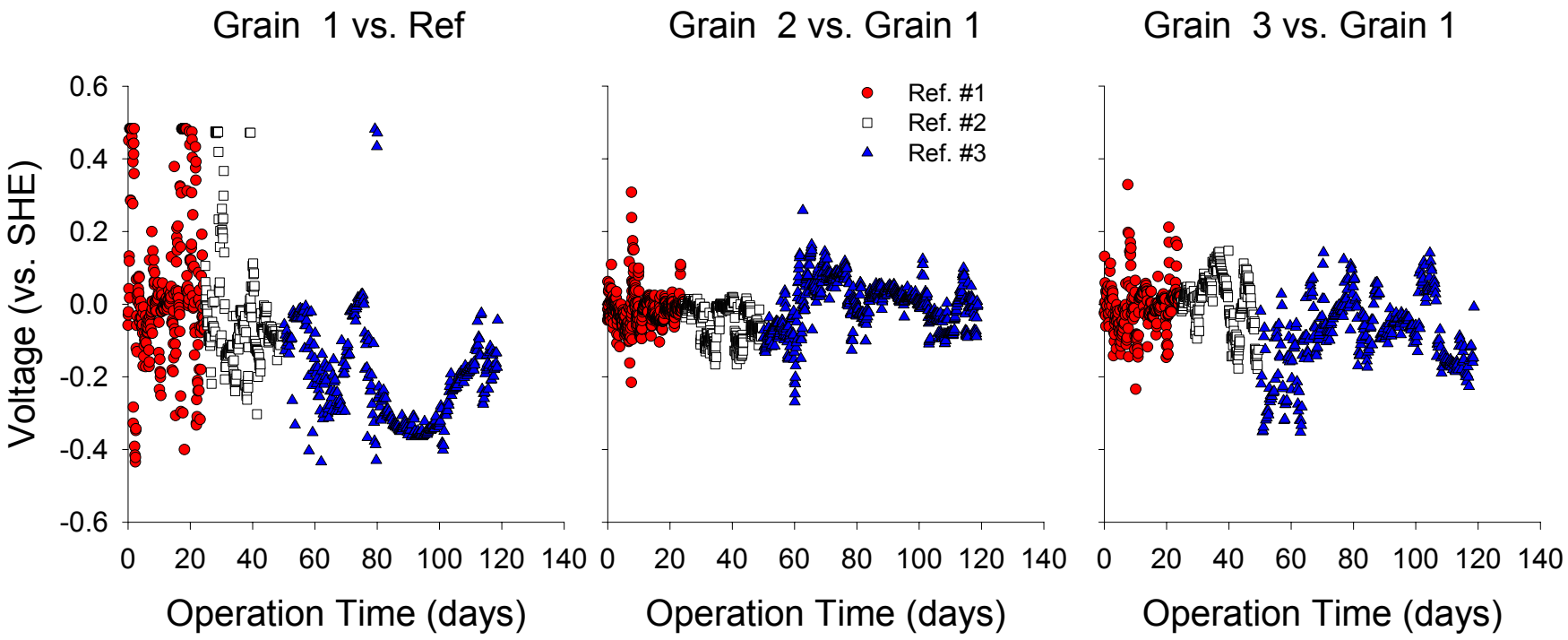

Figure 6.8 Electrochemical results - Probe I2. As noted, three different reference electrodes were used during the course of these experiments.

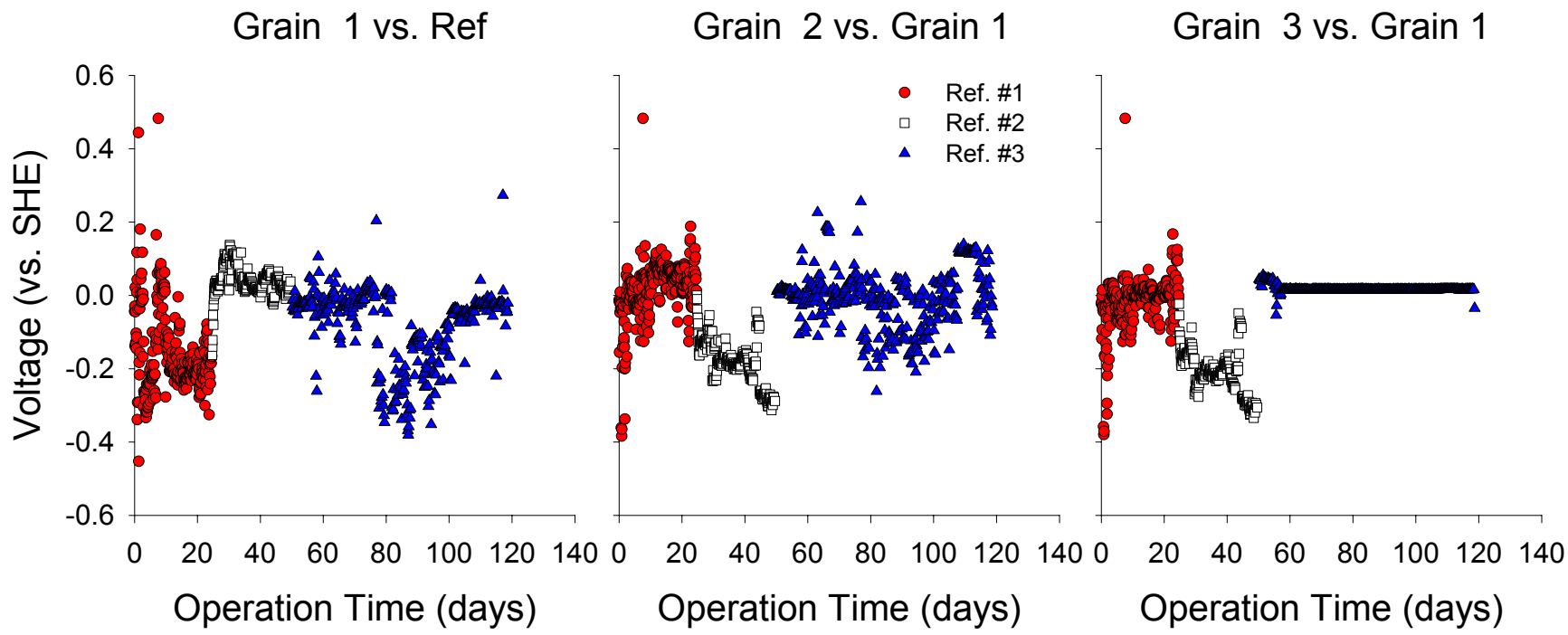

Figure 6.9 Electrochemical results - Probe I3. As noted, three different reference electrodes were used during the course of these experiments.

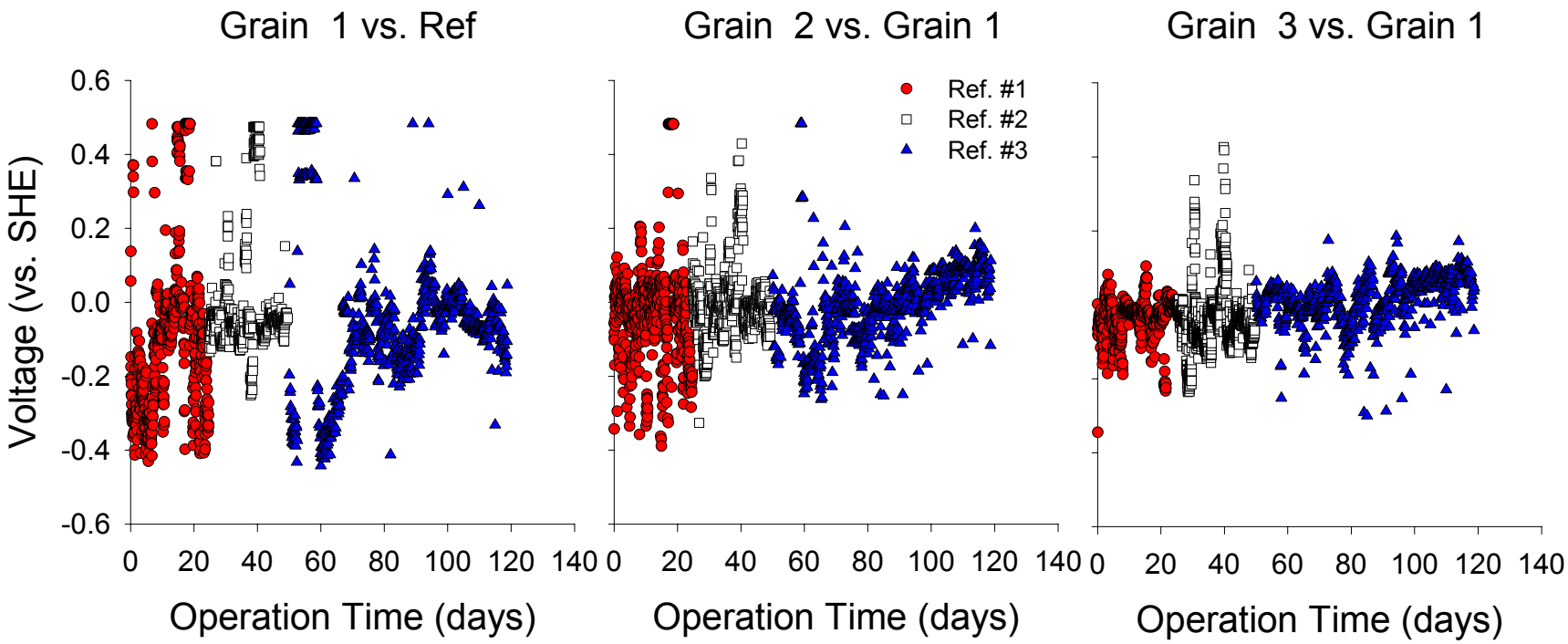

Figure 6.10 Electrochemical data – Probe J1. As noted, three different reference electrodes were used during the course of these experiments.

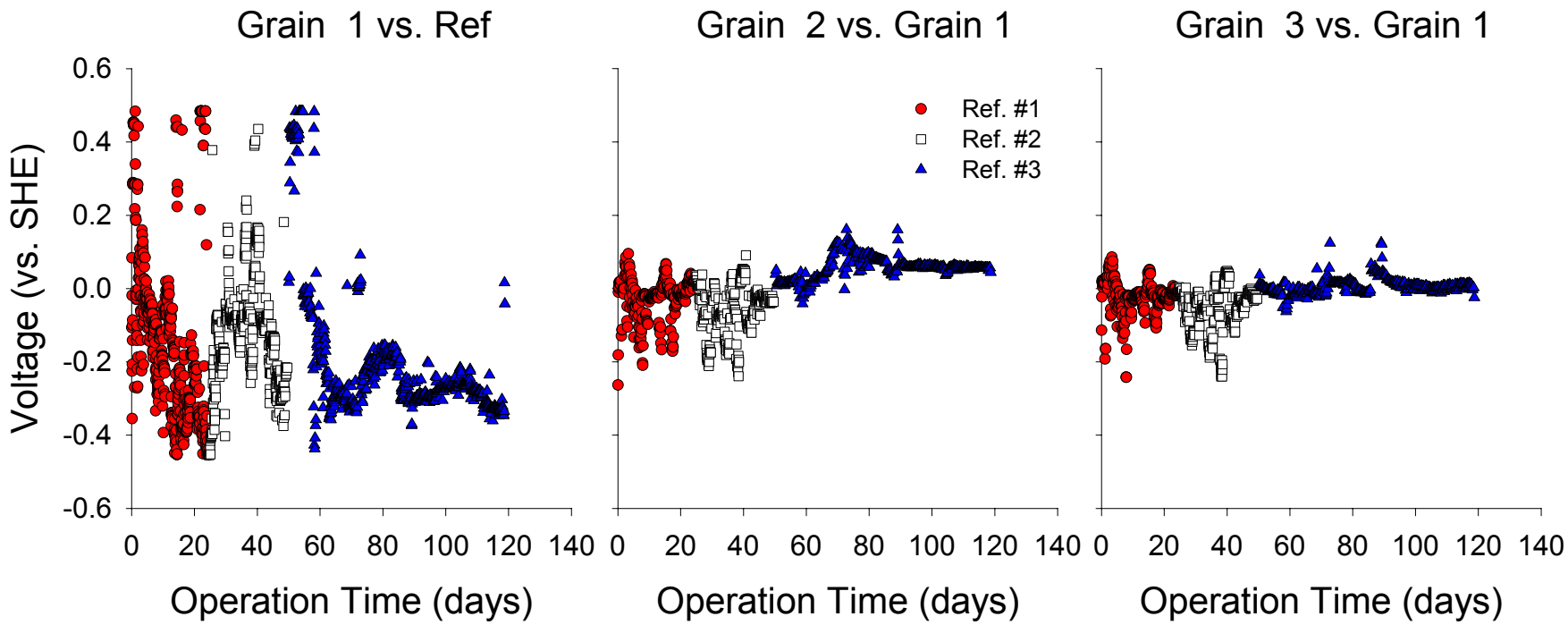

Figure 6.11 Electrochemical data - Probe J2. As noted, three different reference electrodes were used during the course of these experiments.

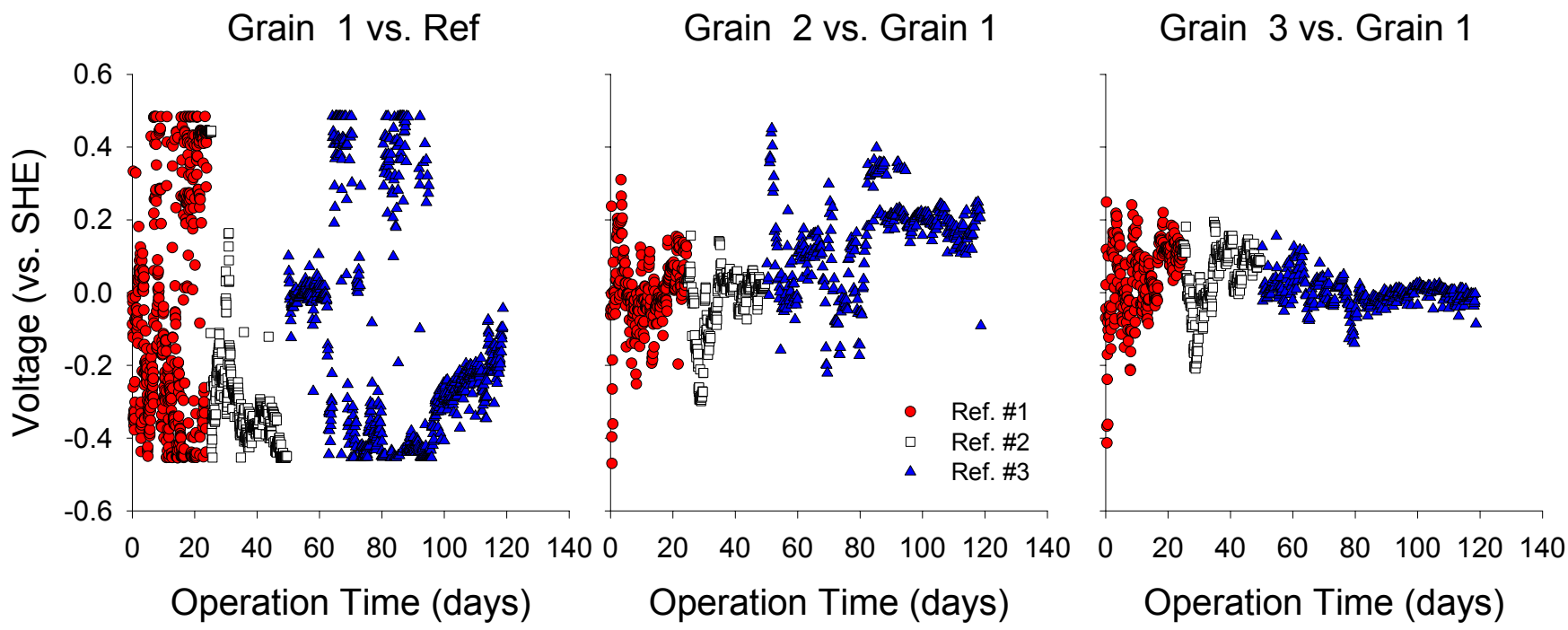

Figure 6.12 Electrochemical data – Probe J3. As noted, three different reference electrodes were used during the course of these experiments.

Although the measured OCPs for the different iron grains exhibited a great deal of scatter and no trends could be discerned for a given probe, for the sake of completeness the responses of the different probes within a given column were compared (Figs. 6.13 to 6.16). As shown, there were no observable trends in the OCP values measured between the probes at the influent and the effluent ends of the column.

Iron Grain to Iron Grain Comparison of Electrochemical Response

As noted previously, the observed variations in the measured OCP values could possibly be due to the contamination of the reference electrode or to variations in the response of the individual iron grains. To address this second possibility, the voltages measured between grain two and grain one and between grain three and grain one were examined. Because these voltages compare the electrochemical response between electrodes of similar composition it is expected that the measured voltages would be ~ 0.0 V if the two grains behaved similarly. In general, as shown in Figs. 6.1 to 6.12, this was observed. This suggests that within each probe that the grains exhibited similar behavior. An additional comparison of the voltages measured between grain 2 and grain 1 and between grain 3 and grain 1 was made for each of the probes (Fig. 6.17). In this type of comparison, if the iron grains were behaving similarly then the response would fall on the given forty-five degree lines. Any deviations from this line reflect differences in the reactivity of one grain relative to the other. As shown, for most of the grains there was a general correlation between in the response of the grains 2 and 3 relative to grain 1. These correlations reflect that similar processes were affecting the potential measured at the iron grain surface.

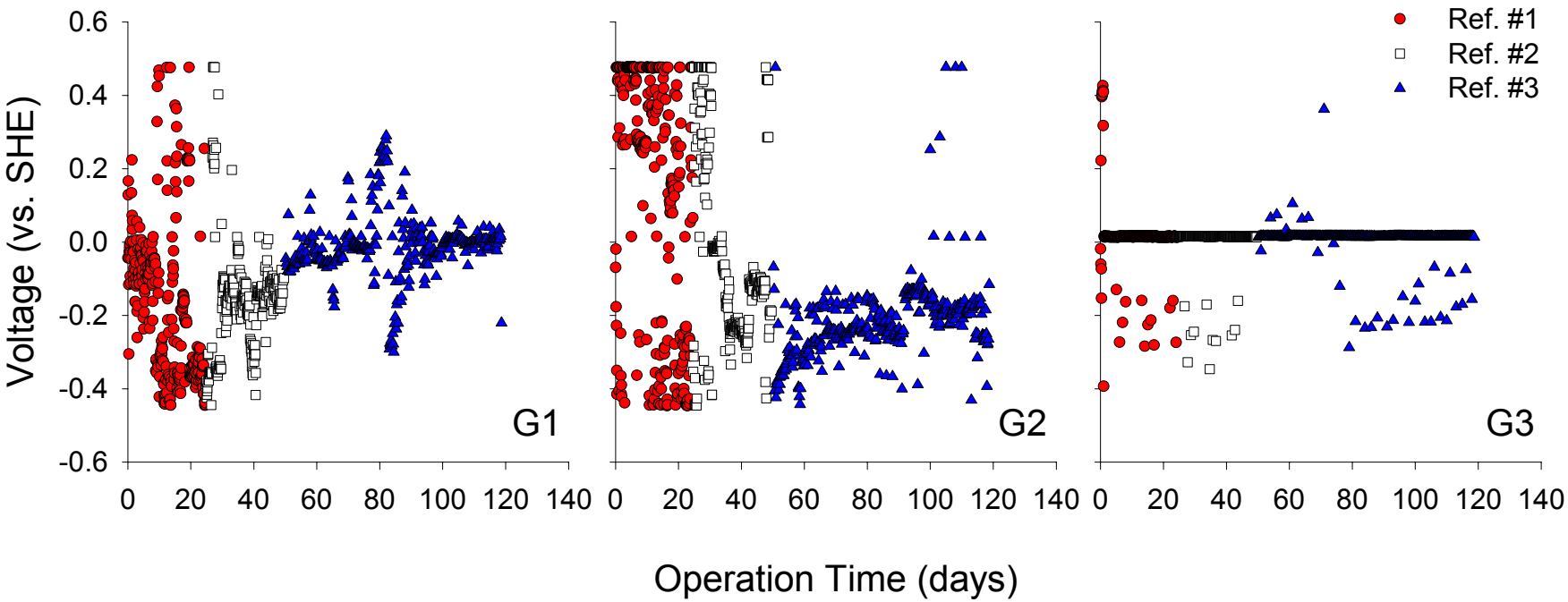

Figure 6.13 Electrochemical results - comparison of Probes G1, G2, and G3 (Grain 1 vs. reference). As noted, three different reference electrodes were used during the course of these experiments.

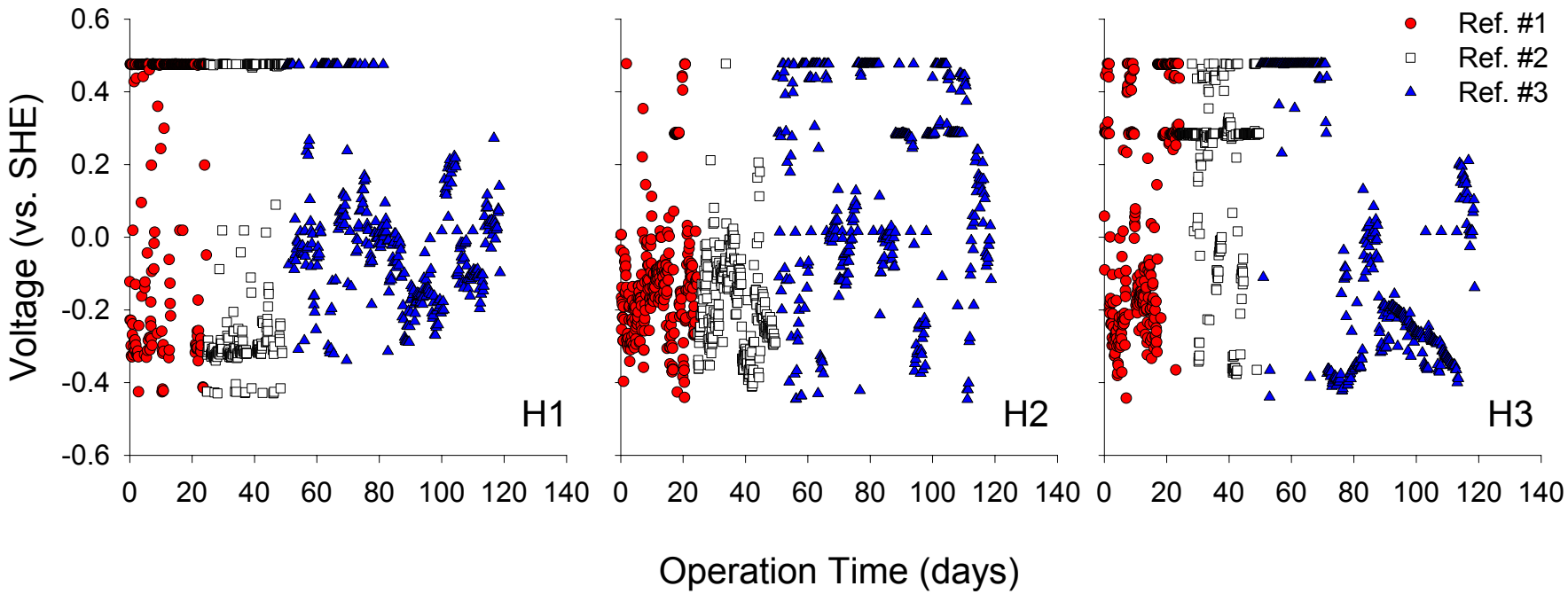

Figure 6.14 Electrochemical results - comparison of Probes H1, H2, and H3 (Grain 1 vs. reference). As noted, three different reference electrodes were used during the course of these experiments.

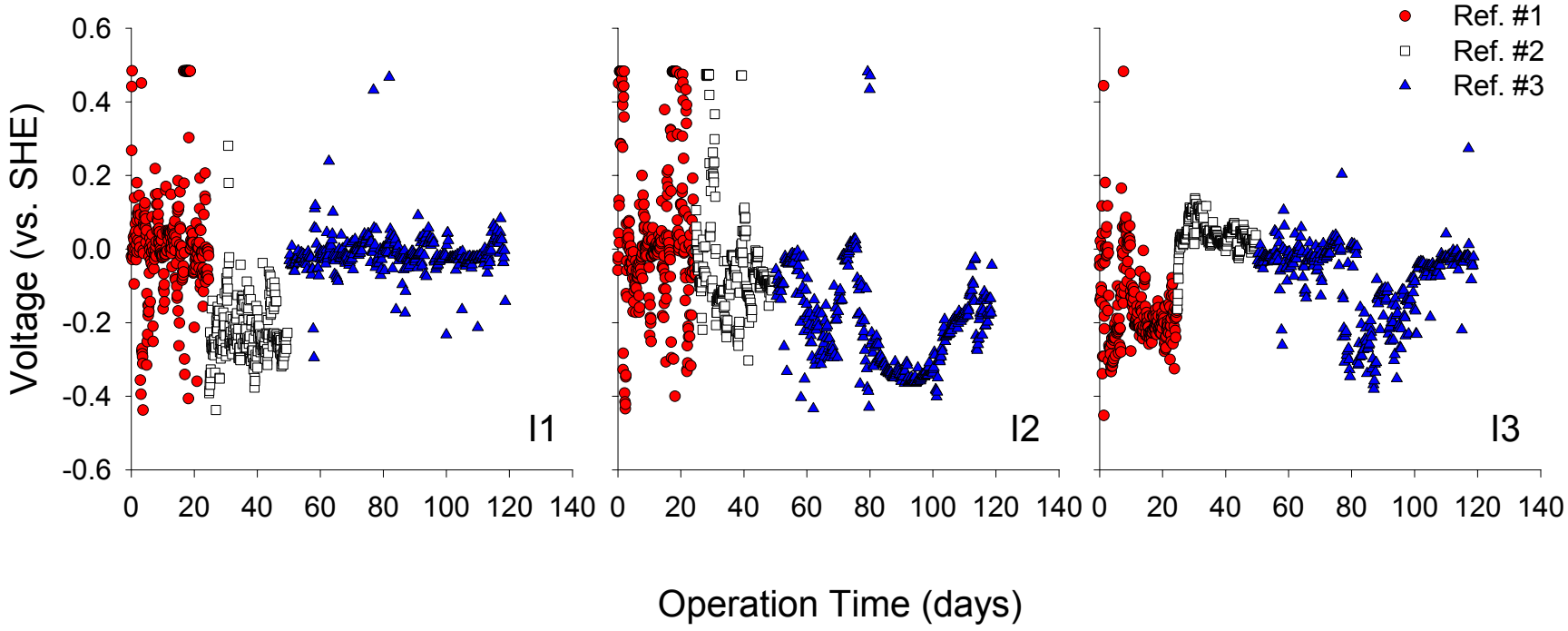

Figure 6.15 Electrochemical results - comparison of Probes I1, I2, and I3 (Grain 1 vs. reference). As noted, three different reference electrodes were used during the course of these experiments.

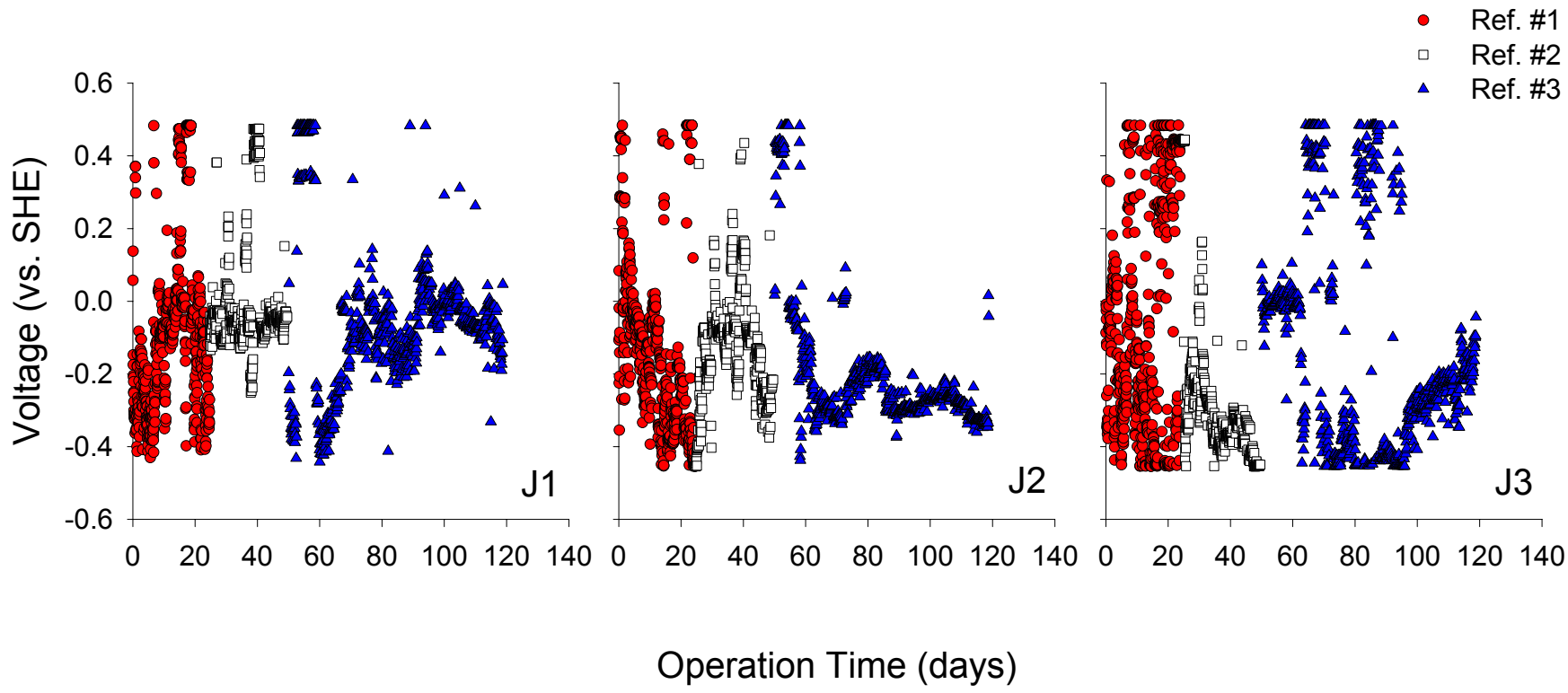

Figure 6.16 Electrochemical results - comparison of Probes J1, J2, and J3 (Grain 1 vs. reference). As noted, three different reference electrodes were used during the course of these experiments.

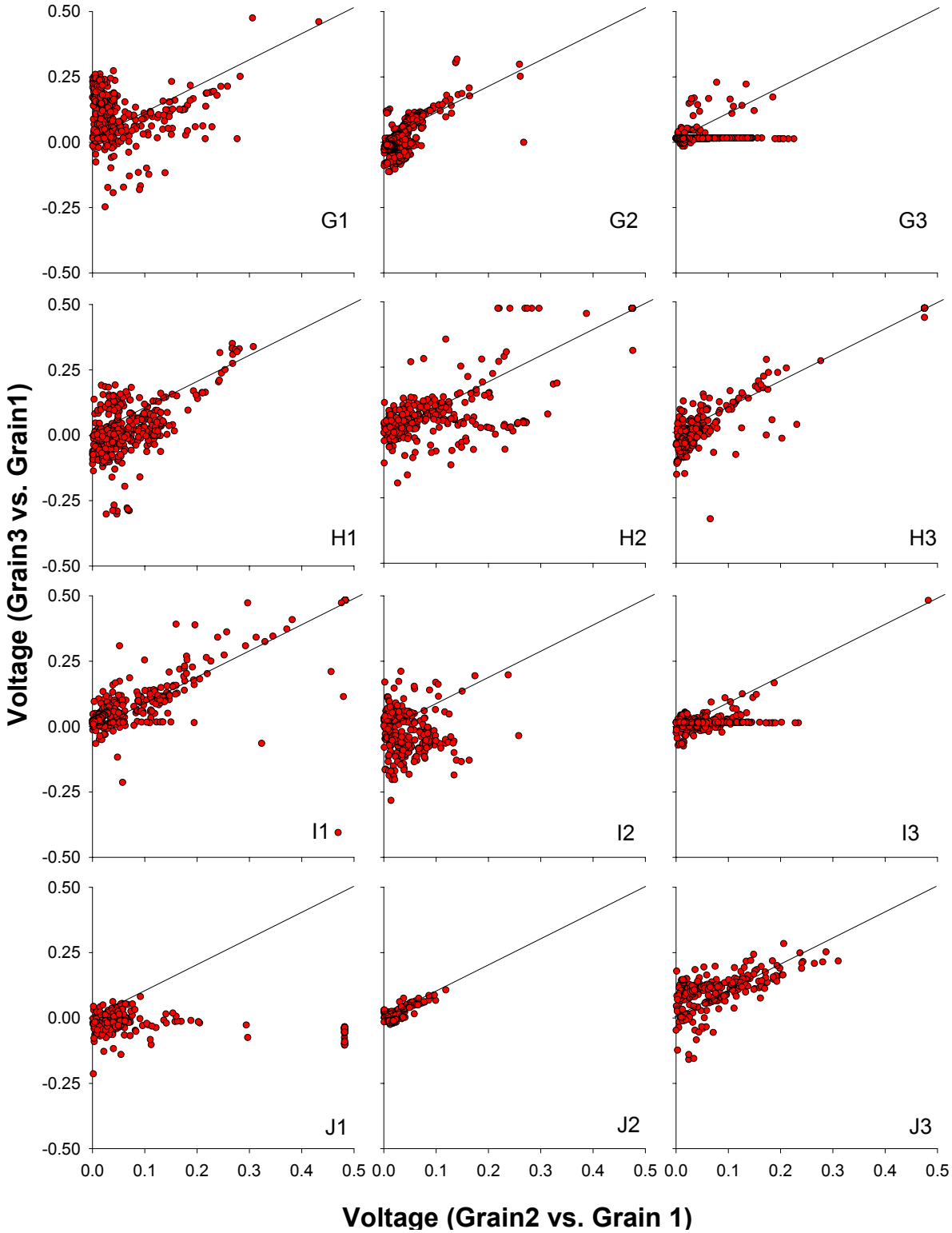

Figure 6.17 Comparison of differential voltages for Grain 3 (vs. Grain 1) and Grain 2 (vs. Grain 1). The given 45-degree line illustrates a perfect correlation between the two measurements

Impedance Spectroscopy

Impedance spectra were obtained from each of the twelve columns once a week. Unfortunately, none of the spectra gave results that could be readily interpreted. A typical Nyquist plot obtained from the in-situ probes is shown in Fig. 6.18. As can be seen in this figure, the data is widely scattered. The typical half-circle features expected in the Nyquist plots cannot be discerned. Therefore, no conclusions can be drawn from this part of the electrochemical study.

Several sources can be named for the problems we encountered with impedance spectroscopy. The electrical contact between the grains and the wires may have been insufficient or entirely disrupted. Problems with the stability of the reference electrodes also may have contributed to the poor data quality. Furthermore, a stable OCP is desirable before taking an impedance spectrum. As discussed in the previous paragraph, the OCP measurements for our in-situ probes fluctuated considerably.

Impedance spectroscopy is preferably performed on smooth, well-defined surfaces (Bard and Faulkner, 1980). An inhomogeneous surface, like our grain surface, makes it difficult to propose an equivalent circuit for the entire grain. Furthermore, it disrupts the uniformity of the current and leads to a frequency dispersion (Amaral and Muller, 1999). Spectra obtained from an electrochemical cell using an iron grain electrode gave satisfactory results. In the electrochemical cell the electrical connections and the grain surface could be observed by eye and potential problems could be minimized. The in-situ probes, however, were subject to many alterations inaccessible to our control and therefore the data quality was poor.

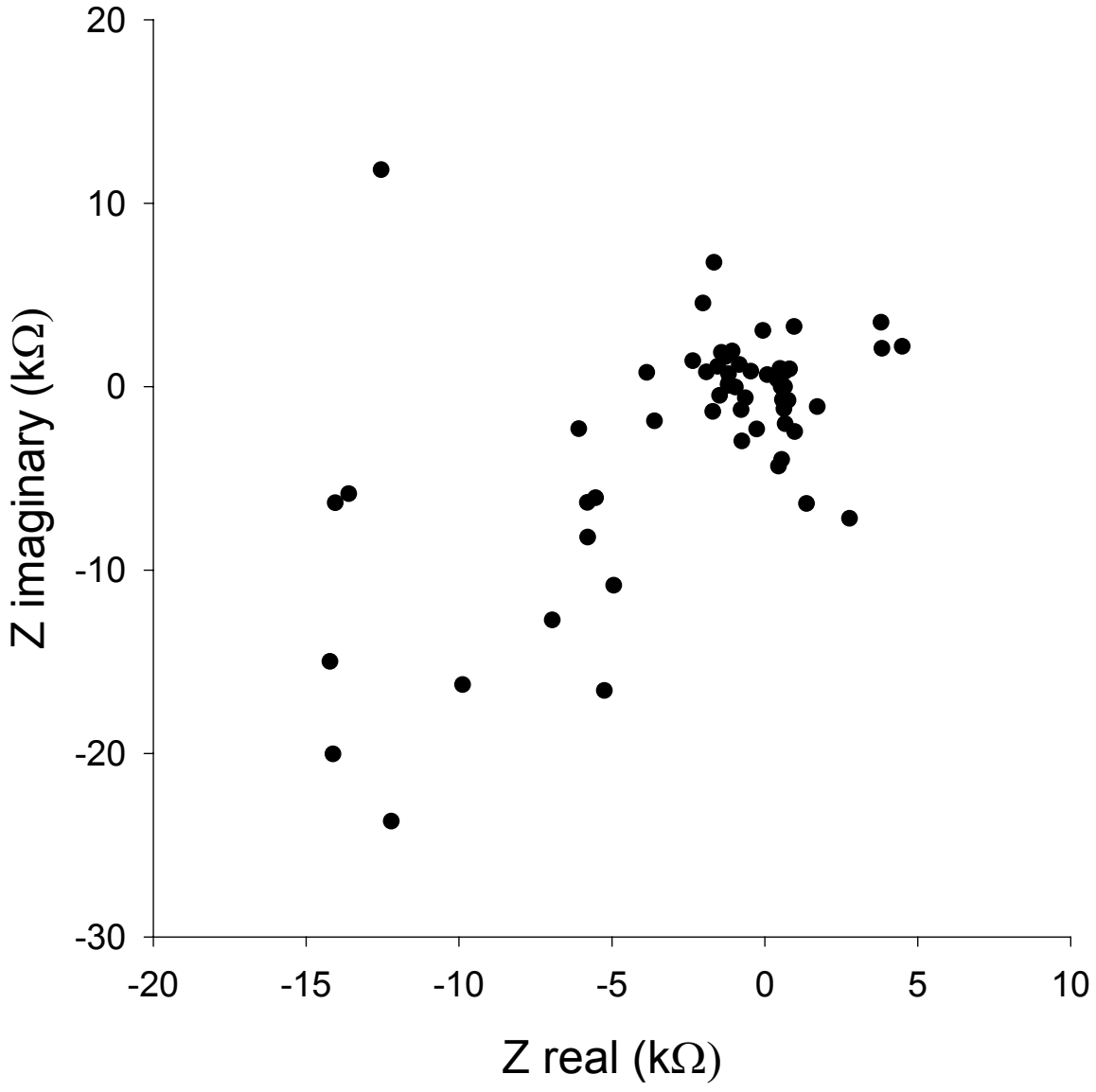

Figure 6.18 Nyquist plot of an impedance measurement on an in-situ probe

EX-SITU ELECTROCHEMICAL PROBE RESULTS

In order to provide a comparison to the in-situ column experiments, a set of trial experiments was conducted to examine the viability of the probe concept. Accordingly, an experiment was conducted to examine the effect of silica addition on the OCP. For this experiment, the silica content of a reactor was increased and it was observed that the OCP increased rapidly (Fig. 6.19). This increase is consistent with the passivation of the iron surface by the presence of silica.

To further simplify the system, experiments measuring the OCP of only one grain at a time versus the reference electrode were conducted. A flow-through cell was set up in an airtight plastic container with transparent walls. This enabled us to detect air-bubble formation and corrosion of the grain during the experiment. The electrodes as well as the inlet and outlet ports of the feed solution entered the cell through openings in the top. The openings were sealed with O-rings and silicone to minimize the entrance of oxygen to the system. Experiments were conducted over the course of several days. As for the in-situ probes, the flow rate was 0.5 ml/min, and OCP measurements were obtained every ten seconds. In an effort to minimize the noise in the signal, a relatively high electrolyte concentration (0.05 M NaCl) was used in these experiments. The solution furthermore was buffered with 4 mM $NaHCO_3$.

Open Circuit Potential Under Standard Conditions

The first experiment performed consisted of a grain exposed to solution containing only the buffer and the electrolyte. The OCP was measured over 10 days (240 hours) as depicted in Fig. 6.20. This part of the measured OCP was used as the baseline for comparison with grains exposed to varying solution conditions. It can be seen that the signal initially decreased sharply

from –0.57 V to –0.65 over the course of a few hours and then it stabilized around – 0.65 V. The signal fluctuated to slightly higher values around 130 hours, and then decreased back to its original OCP. This behavior may result from the breaking off of small pieces of the grain, which could be seen at the bottom of the cell.

Effect of Silica

Since no rusting of the grain was observed after 10 days, the experiment was continued. The feed solution was switched to a solution containing 50 mg/L SiO_2, in addition to the buffer and the electrolyte. As can be seen in Fig. 6.20 the addition of silica lead to a rapid increase in the OCP of more than 0.1 V. Unfortunately, the pH of the silica-containing feed solution readjusted itself to 10.04, whereas the pH of the initial feed solution was only 9.24. This difference in pH is at least in part responsible for the increase of the OCP.

To avoid this pH effect, a second experiment was performed where silica was added to the solution and the pH was kept constant. The result of this experiment is shown along with the first 10 days of the initial experiment in Fig. 6.21. A new grain was exposed to only buffer and electrolyte at pH 9.3 for 91 hours. The measured OCP coincides well with the OCP measured in the first experiment. Its slightly higher value can be explained by the small pH difference between the feed solutions. After 91 hours, the feed solution was switched to a solution containing 50 mg/L SiO_2. The pH was regularly monitored and adjusted to 9.3. It can be seen that the OCP steadily increased up to –0.55 V over the next days. Unfortunately, several rusty spots were observed on the grain, which may have contributed to the increase in OCP.

Effect of High Bicarbonate Concentrations

In addition to silica, high bicarbonate concentrations had a detrimental effect on the reactivity of the columns, as discussed in Chapter 4. Therefore an OCP experiment at a higher bicarbonate concentration was performed. The result of this experiment is shown in Fig. 6.23, along with the initial experiment at 4 mM bicarbonate. A new grain was exposed from the start to a solution containing the electrolyte and 20 mM HCO_3^- at pH 8.97. It can be seen that the OCP of this grain at first also decreased sharply, but steadied at a higher value (-0.62 V) than the initial grain, in spite of the lower pH of the solution. The OCP never stabilized but exhibited a slowly increasing trend up to –0.60 V after 4 days. At this point, the experiment was terminated due to difficulties with the reference electrode. Neither rusting nor breaking of the grain was observed over this time-period.

From the ex-situ experiments discussed above, we conclude that bicarbonate and silica have a passivating influence on iron grains and that the effect is manifested in an increased OCP. Unfortunately, rusting and breaking of the grains and instabilities of the reference electrodes inhibited us from further quantifying the effects of these two co-solutes.

OVERVIEW OF ELECTROCHEMICAL PROBE DEVELOPMENT

In light of the experimental difficulties associated with the development of the electrochemical probes, we concluded that although the concept of using electrochemistry to examine PRB longevity is viable *theoretically* that in *practice* that the concept is flawed. Because of gas and precipitate accumulation, it is difficult to know exactly what is occurring at the iron electrode surface. Changes in the OCP or impedance spectra that result from these processes were random in nature and extremely difficult to understand.

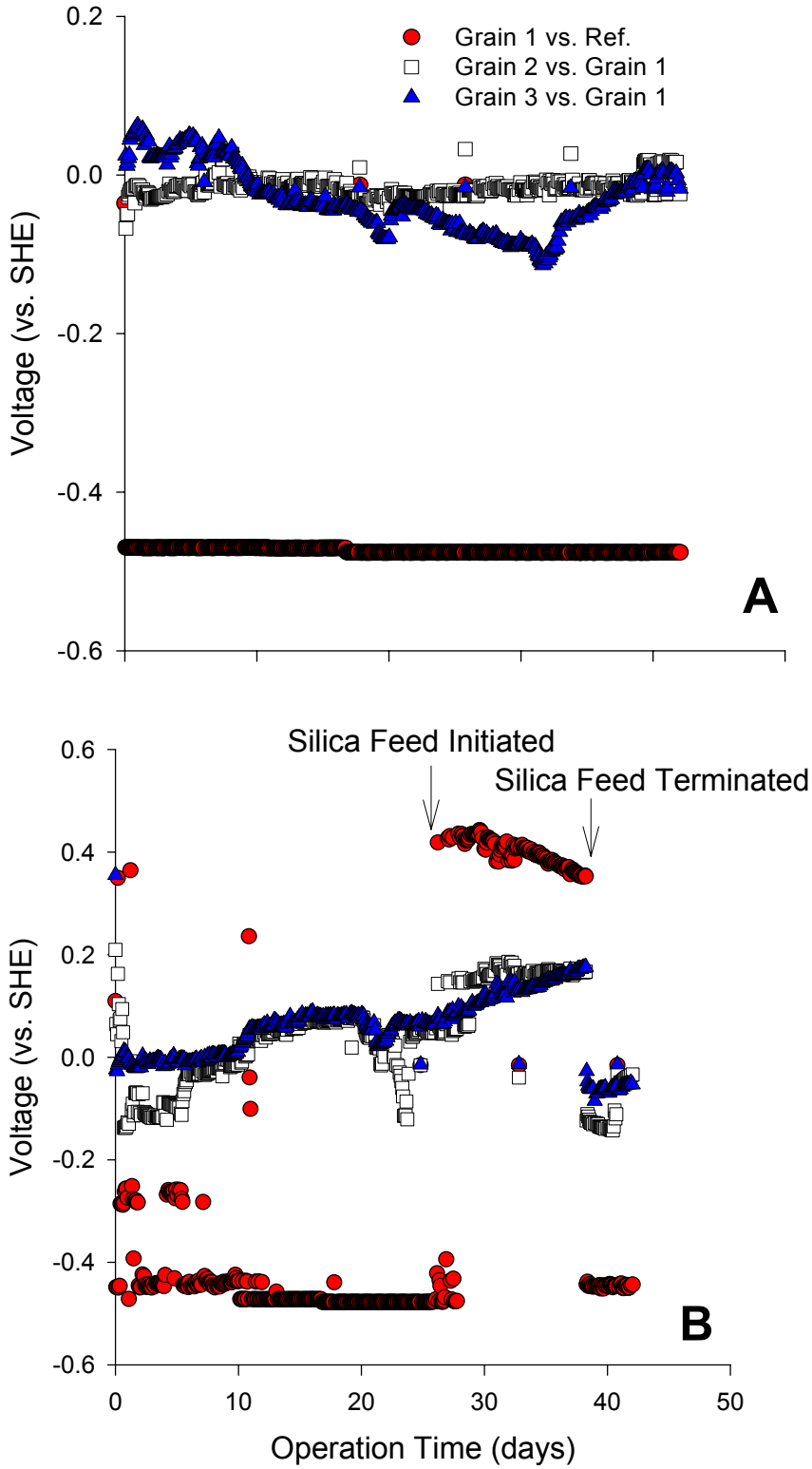

Figure 6.19 Ex-situ probe experimental results. Effect of silica addition on the open circuit potential.

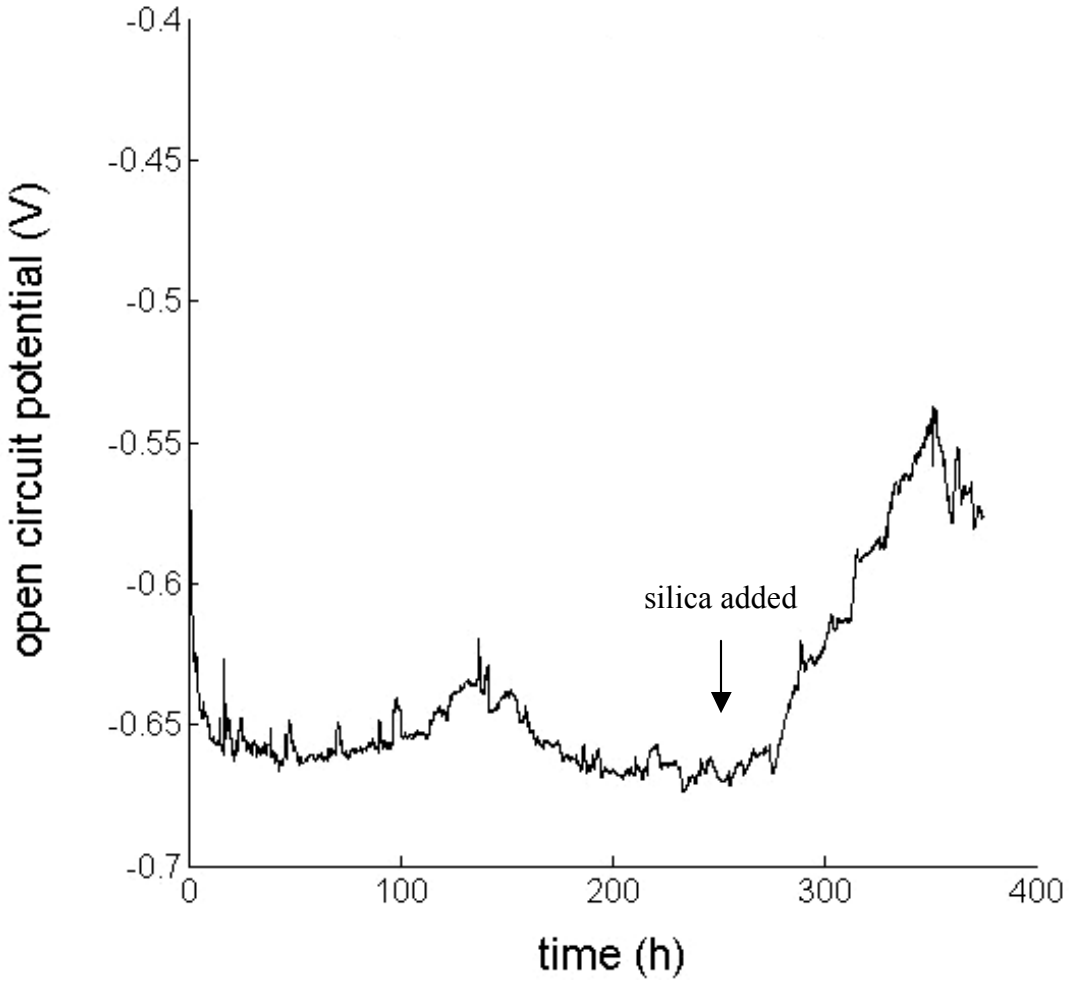

Figure 6.20 Ex-situ probe results: Effect of silica addition on the open circuit potential. 50 mg/L SiO_2 was added after 261 hours.

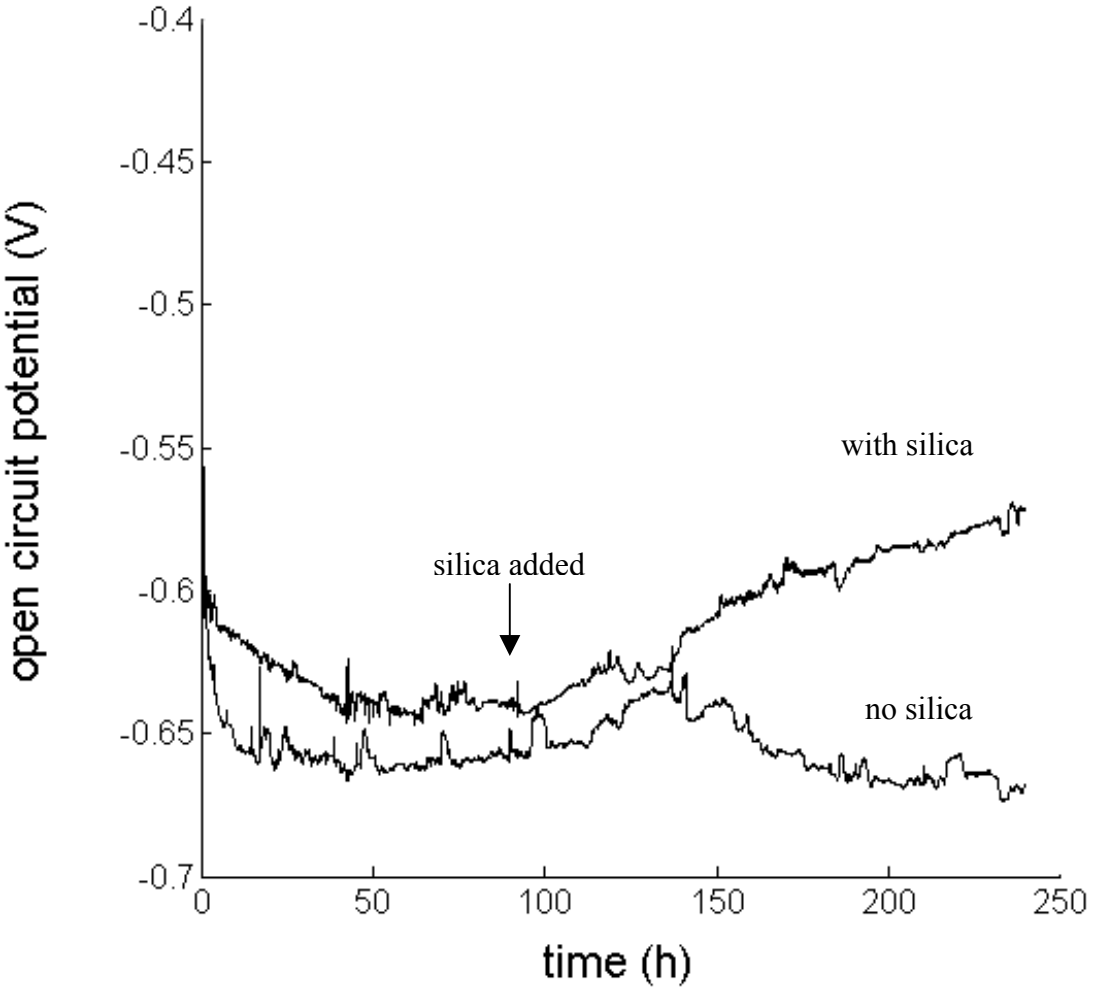

Figure 6.21 Comparison of the open circuit potentials of a grain exposed to 50 mg/L silica and a grain exposed to no silica over the course of 10 days.

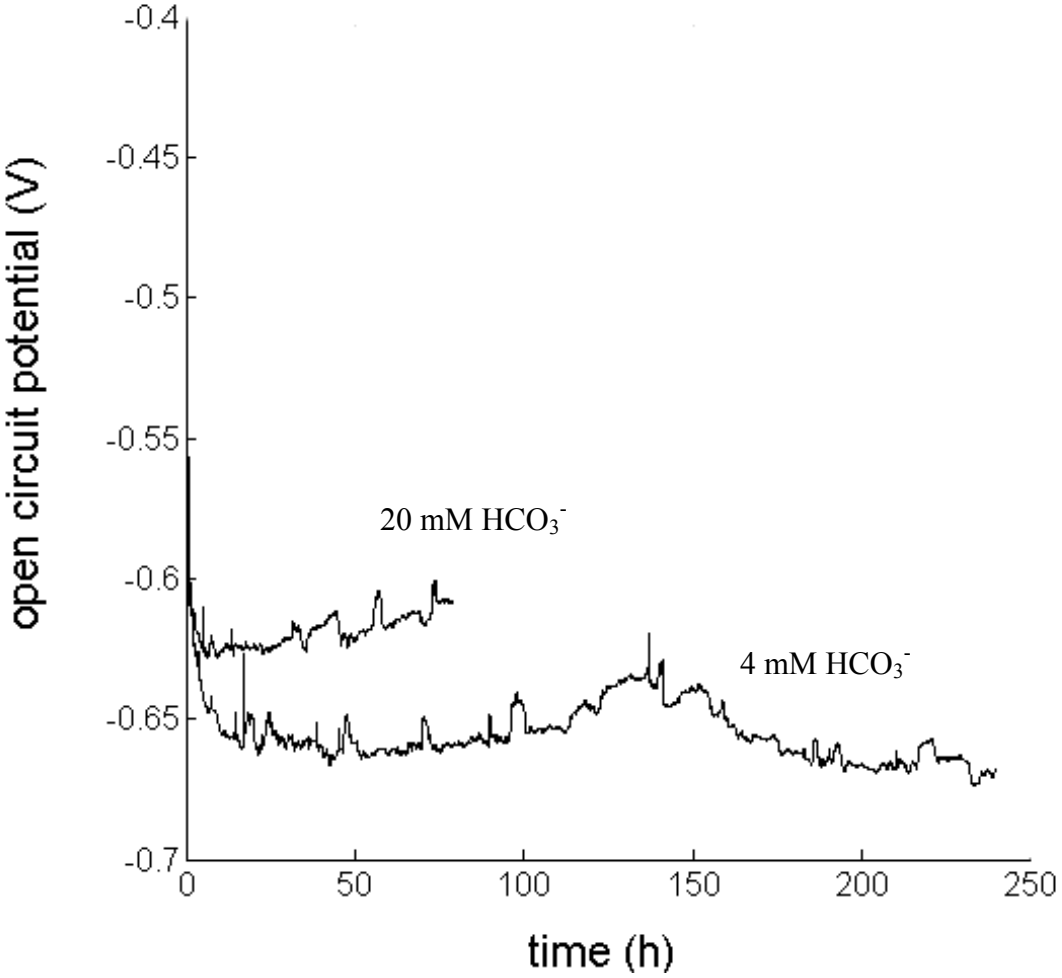

Figure 6.22 Open circuit potentials of two iron grains in solutions of high (20 mM) and low (4 mM) bicarbonate concentration.

CHAPTER 7 – IMPLICATIONS OF RESULTS TO BARRIER DESIGN

OVERVIEW

Barrier width is one of the key design variables that must be considered when PRBs are installed in the field. To achieve a desired level of contaminant attenuation while maintaining sufficient safeguards against the breakthrough of contaminants (or degradation products), investigators will often conduct preliminary laboratory column experiments using site groundwater to determine the appropriate barrier width. Owing to the short-term nature of these tests, however, they may fail to account for long-term changes in the transport properties of the porous media, such as those described in Chapter 3, or the reactivity of the surface, as described in Chapter 4. Unless an appropriate safety factor has been incorporated into the PRB design, the long-term viability of many treatment walls may be compromised. Data from a number of PRBs currently emplaced in the field (Duran et al., 2000; Morkin et al., 2000) suggest that factors that could lead to long-term deterioration of performance should be more fully considered when designing PRBs.

In general, the long-term operation of a barrier is expected to affect the rate of a solute's transformation through the combined impact of (1) changes in flow properties within the porous medium, and (2) changes in surface speciation over time (owing to combined effects of iron oxidation and adsorption or precipitation of solutes at the interfacial region). Each of these processes is of course influenced by the quality of incoming groundwater (as emphasized by our study objectives and design). For the transport conditions of our column studies (*i.e.*, constant flow in a vertically upward direction) and for the specific groundwater compositions investigated herein, we have decoupled these two processes by periodically obtaining independent

assessments of hydraulic residence time distributions (Chapter 3). In this context, our studies were not designed to mimic certain aspects of field-scale conditions, such as horizontal flow under unconfined conditions (with the potential for transverse gas migration) or three-dimensional flow driven by the imposed hydraulic gradient (which need not maintain a constant average longitudinal flow velocity). Nevertheless, the results obtained over the course of this work have important implications for field-scale design, as discussed in the sub-sections that follow. We begin (in the first sub-section below) with a discussion of the projected effects of solute transport property changes under conditions of constant flow, and we compare these with expectations for overall changes in reactivity, as based on our own observations and as therefore limited to the conditions of this study. We follow this discussion (in the second sub-section below) with a more general exploration of co-solute effects on reactivity change. We conclude with a general discussion of pertinent safety factors for permeable barrier design.

PROJECTIONS OF THE RELATIVE IMPACTS ON PERFORMANCE OWING TO CHANGES IN SOLUTE TRANSPORT

To simulate some possible effects of changes in transport properties and surface reactivity on TCE degradation, we coupled equations of solute transport and mass transfer with the surface reaction model developed by Burris et al. (1998) for Master Builder iron. This model hypothesizes that TCE sorbs to both reactive and non-reactive sites on the iron surface. The sorption of TCE to the reactive sites and the subsequent degradation of TCE at those sites is modeled using a pseudo-first-order kinetic coefficient (λ_a) that is expressed as a function of the aqueous phase TCE concentration. Not only does λ_a account for TCE degradation at the iron

surface, but it also considers mass transfer to that surface. Sorption to non-reactive sites, hypothesized to represent graphitic inclusions in the granular iron, is described by a non-linear Freundlich isotherm (K_F = 15.6 (nmol/g)/(nmol/mL)^m with m = 0.36).

For these model simulations, the dual-region model described in Chapter 3 was extended to include terms that describe surface reactivity and TCE sorption to non-reactive sites (van Genuchten and Wierenga, 1976; van Genuchten and Wagenet, 1989):

$$\left(\theta_m + f\rho_b K_d\right)\frac{\partial c_m}{\partial t} = \theta_m D_m \frac{\partial^2 c_m}{\partial x^2} - v_m \theta_m \frac{\partial c_m}{\partial x} - k_{mt,TCE}(c_m - c_{im}) - \theta_m \lambda_a c_m \tag{7-1}$$

$$\left(\theta_{im} + \left(1-f\right)\rho_b K_d\right)\frac{\partial c_{im}}{\partial t} = k_{mt,TCE}(c_m - c_{im}) - \theta_{im}\lambda_a c_{im} \tag{7-2}$$

Here, f represents the fraction of adsorption sites that equilibrate with the mobile phase, ρ_b is the bulk density of the iron within the PRB (= 2.97 g/mL), and K_d [L/g] is an empirical distribution coefficient describing sorption to the unreactive sites. For the purpose of our simulations, f was set equal to β (the immobile water content as defined in Chapter 3), based on an assumption that similar adsorption characteristics apply to solids adjacent to the mobile and immobile fluid. To simplify the model it is assumed that the same value of λ_a describes the surface reactivity of both the mobile and immobile regions. The parameter $k_{mt,TCE}$ is related to our measured values of k_{mt} (the mass transfer coefficient for ^3H_2O) by the relative magnitudes of the diffusion coefficients for TCE and ^3H_2O (Brusseau et al., 1989; Young and Ball, 1997):

$$k_{mt,TCE} = k_{mt}\frac{D_{TCE}}{D_{^3H_2O}} \tag{7-3}$$

Here, D_{TCE} (= 8.8 × 10^{-6} cm^2/sec) and $D_{3_{H_2O}}$ (= 3 × 10^{-5} cm^2/sec) are the diffusion coefficients determined for TCE and water at 20 °C using the Wilke-Chang approximation (Cussler, 1997).

An approximate value for K_d (= 6.3 L/g) was obtained by fitting the linear range of the Burris et al. (1998) sorption isotherm.

Assuming a steady input of 1000 μM (131.4 mg/L) TCE, we simulated steady state TCE degradation in a granular iron PRB with a thickness of 1000 cm. Fourteen different simulations were conducted and grouped into the following three categories: A) fixed reaction rate (λ_a) and variable transport properties (v_m, D_m, β, $k_{mt,TCE}$); B) variable reaction rate and variable transport properties; C) variable reaction rate and fixed transport properties. For categories A and B, the transport properties were varied systematically and were intended to illustrate the impact of changes in the HRTD on TCE degradation. Accordingly, the transport properties were varied so that they followed the same general trends we observed in our laboratory column experiments. For categories B and C, parameters were varied to illustrate the effect of decreasing surface reaction rates on PRB efficacy. As with the transport properties, variations in reaction rate coefficients were selected so as to follow the same general trends we observed over the course of our column study.

For the simulations using a fixed reaction rate, λ_a was set to 20.66 d^{-1} as determined by Burris et al. (1998). This value was employed because it is representative of the rate coefficients obtained from short-term column studies (Environmetal Technologies Inc., 2002) and is therefore a reasonable starting point for many PRB design calculations. It is also in reasonable agreement with our own short-term results. For the simulations for which the TCE degradation rate was varied (Categories B and C), the values for the reaction rate coefficient, λ_a, were varied from 20.66 to 2.5 d^{-1}. This range was used because it spans the four-fold decrease in the observed rate coefficients that we have obtained with our iron-filled columns over three years of operation. The transport properties (v_m, D_m, β, $k_{mt,TCE}$) were systematically varied to account for

changes in the HRTD of the PRB over time. Accordingly, these values were varied from a simulation with uniform flow (v_m = 180 cm/d, D_m = 5 cm^2/d, β = 0.99, $k_{mt,TCE}$ = 35.0 d^{-1}) to a simulation with increased preferential flow (v_m = 240 cm/d, D_m = 150 cm^2/d, β = 0.5, $k_{mt,TCE}$ = 0.037 d^{-1}). In this manner, we attempted to illustrate the effects of solute precipitation and gas accumulation on TCE degradation over time, based on our own conditions of operation. Of course, precipitate formation and gas accumulation in the field should be expected to vary as a function of many parameters, and most especially the influent water quality (e.g., for groundwater quality conditions outside the range studied in this work). Moreover, the impacts of precipitate formation and gas accumulation on solute transport will be different under conditions of field flow, where a constant average groundwater discharge (and hence average linear velocity) need not be maintained, and where larger domains of three-dimensional transport may provide additional opportunities for "short-circuiting," especially as related to differing transport effects at proximal and distal locations within the barrier. Nevertheless, our predictions of overall (column-averaged) transport under constant flow conditions represent an interesting case that may be largely applicable to major portions of a barrier.

The results of our model simulations are shown in Fig. 7.1; the model parameters used to generate these simulations are provided in Table 7.1. Based on these simulations it is apparent that changes in transport characteristics within the range of our observations do affect our predictions of TCE removal efficiency. As shown in Fig. 7.1a, the variation in the transport properties alters the barrier thickness required to attain drinking water standards for TCE, with the required dimension increasing from ~ 100 to ~ 300 cm as preferential flow paths develop (immobile water content increases) and mean pore water velocity increases. Sensitivity analyses (data not shown) indicate that these effects stem from the simultaneous variation of all of the

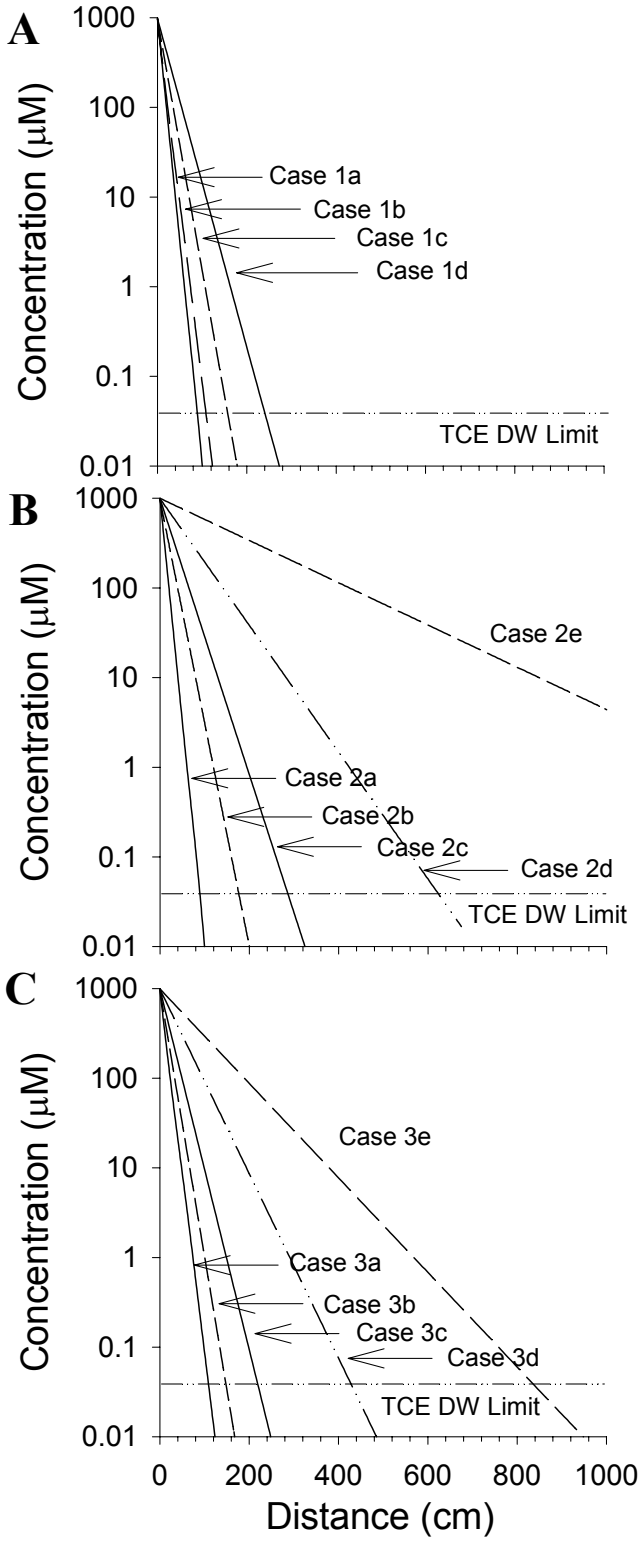

Figure 7.1 Simulations of steady state TCE concentrations through a 10 m thick iron (Master Builder) PRB. A) Fixed reaction rate, variable transport properties, B) Variable reaction rate, variable transport properties, C) Variable reaction rate, fixed transport properties. Descriptions of the conditions for each simulation are provided in Table 7.1. (1000 μM TCE = 131.4 mg/L)

Table 7.1 Input parameters for model simulations of TCE transport and reaction within an iron PRB. PRB thickness = 1000 cm, K_d = 6.3 L/g.

	Case	v_m [cm/d]	D_m [cm^2/d]	β [–]	$k_{mt,TCE}$ [1/d]	λ_a [1/d]
Fixed reaction	1a	180	5	0.99	35.2	20.66
Variable transport	1b	200	50	0.9	0.352	20.66
	1c	220	100	0.7	0.073	20.66
	1d	240	150	0.5	0.037	20.66
Variable reaction	2a	180	5	0.99	35.2	20.66
Variable transport	2b	210	75	0.8	0.22	15
	2c	215	87.5	0.75	0.147	10
	2d	220	100	0.7	0.073	5
	2e	240	150	0.5	0.037	2.5
Variable reaction	3a	200	50	0.9	0.352	20.66
Fixed transport	3b	200	50	0.9	0.352	15
	3c	200	50	0.9	0.352	10
	3d	200	50	0.9	0.352	5
	3e	200	50	0.9	0.352	2.5

transport properties, with no single parameter predominating. We note that the effects of HRTD on chemical conversions in engineered reactors can be strongly dependent on the reaction mechanism and rate law assumed (Fogler, 1999). For example, if a reaction order higher than first-order were assumed, the impact of changes in dispersion and mass transfer would increase; conversely, a reaction order closer to zero would tend to diminish the effects of HRTD changes.

Figs. 7.1b and 7.1c indicate that the simulated changes in surface reactivity would clearly have a very large impact on PRB efficacy. As the apparent surface reactivity decreases from 20.66 to 2.5 d^{-1}, the barrier thickness required to meet drinking water standards for TCE increases and eventually exceeds the 1000-cm dimension employed in these simulations. A comparison of Figs. 7.1b and 7.1c indicates that changes in the transport properties further alter the TCE profiles. The predicted effects of transport property variations are of smaller magnitude, however, relative to those directly attributable to alterations in surface reactivity.

Although the simple model used here does consider the partitioning of TCE to both reactive and unreactive sorption sites, it does not consider any partitioning of volatile TCE to gas pockets that may exist within the porous media (Cirpka and Kitanidis, 2001). Nor does the model consider the complexities of heterogeneous reactions that could lead to behavior other than that characterized by pseudo-first-order irreversible kinetics. For example, competition of parent species and products for a limited number of reactive surface sites has been previously reported, with associated impacts on overall rates of reaction and PRB efficiency (Arnold and Roberts, 2000b). Because of these and other limitations (some of which have been previously discussed), the results of this modeling exercise should not be considered as necessarily representative of any specific field situation. Instead, the results should be viewed as a condition-dependent illustration of the potential magnitude of "longevity" effects on PRB efficiency and as an illustration of the means by which independently obtained knowledge about transport can be incorporated into design calculations.

At this point, it is useful to reiterate some important differences between our column conditions and those that are more likely to be encountered in the field. In column studies such as those described here, in which the flow rate was precisely controlled, changes in the water-filled porosity that occur as a result of precipitate formation and gas accumulation are manifested by changes in the distribution of pore water velocities and, thus, hydraulic residence time. In contrast, if the porosity of a barrier emplaced in the field is diminished, the resulting alterations in hydraulic conductivity could modify groundwater flowpaths and flow velocities not only within the barrier itself but also within in the aquifer both upgradient and downgradient of the barrier. Depending on the barrier configuration (e.g., continuous wall vs. funnel-and-gate), this may reduce the capture zone, or it may result in other types of deleterious effects on barrier

performance. Recent results from hydraulic "slug" tests and monitoring studies conducted on a PRB installed in the field have illustrated that permeability changes can vary with location within the porous medium (Kiilerich et al., 2000), and that these changes can affect contaminant remediation. In contrast, our results provide a much more precisely controlled measure of "overall" porous medium changes at the scale of a laboratory column. Additional laboratory and field studies are needed to more fully evaluate the range of effects that may be observed (e.g., at proximal versus distal locations in a barrier) and to more fully explore the ramifications of such column-scale effects on transport and reaction under field conditions.

IMPACTS OF CO-SOLUTES ON TCE DEGRADATION

Our results indicate that the design of a PRB for TCE should not only consider the level of treatment needed for organic contaminants and the potential for both inter- and especially intraspecies competition of contaminants and their daughter products for reactive surface sites; Arnold and Roberts, 2000a), but it also must weigh the effect of other co-solutes present in the site groundwater, such as inorganic species and dissolved natural organic matter. To adequately account for the diverse array of possible interactions it is critical that bench-scale column studies be conducted using site groundwater, with contaminants introduced at concentrations comparable to levels occurring at the site in question. Because the effects of many co-solutes may not manifest themselves immediately, such studies should be of sufficient duration that long-term declines in reactivity are fully evident.

Unfortunately, the length of time required for bench-scale studies to provide reliable long-term results may be prohibitively long in comparison to planning horizons for many engineered PRB installations. As illustrated in Fig. 7.2, the fraction of TCE that passed unreacted through three of our columns increased dramatically during the early months of

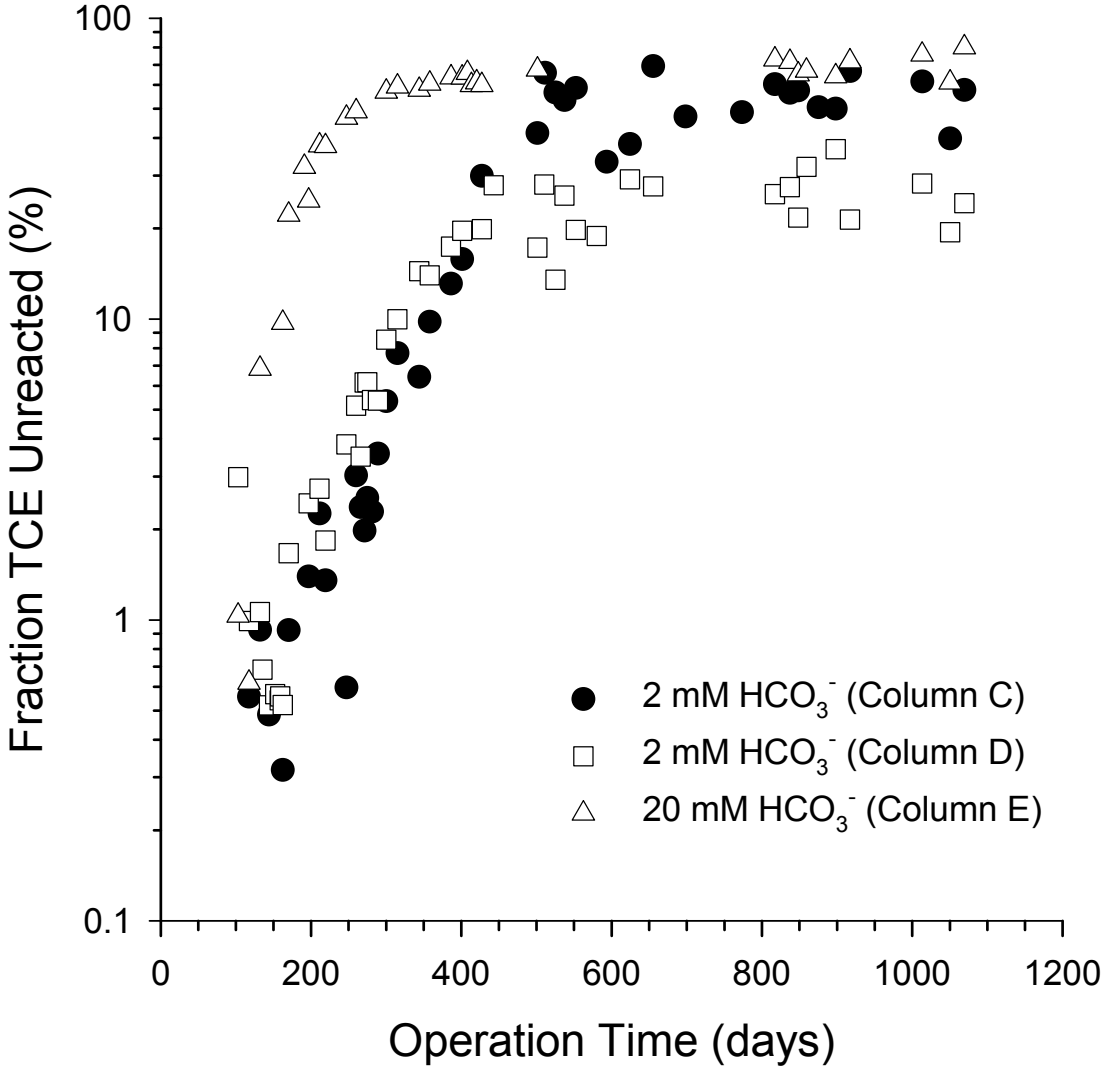

Figure 7.2 Variation in TCE removal over time as a result of surface passivation and the formation of an apparent unreactive zone near the column inlets. Fraction of TCE unreacted = $(TCE_{effluent}/TCE_{influent,est})\times100\%$. $TCE_{effluent}$ is the TCE concentration measured at the column outlet, $TCE_{influent,est}$ is the estimated influent TCE concentration determined via non-linear regression of contaminant profile data and was used in place of the measured influent concentration ($TCE_{influent}$) to minimize the effects of sampling errors on the analysis. On day 409 the feed to column C was augmented with 100 μM silica and this resulted in the observed decline in column reactivity relative to column D.

column operation, only leveling off after 300 to 400 days for Columns E and D, respectively, depending on the bicarbonate concentration. (Although it might appear that Column C required an even longer period to produce a consistent level of TCE removal, this likely stems from the addition of silica from day 409 to day 538.) At the flow rates employed herein, columns E and D required ~1200 to ~1600 pore volumes to reach quasi-steady-state TCE removal rates. This volume is considerably greater than that typically employed in bench scale feasibility testing for TCE treatment (30-40 pore volumes; Arun Gavaskar, personal communication).

An alternative to long-term bench-scale testing would be to incorporate a safety factor to account for anticipated declines in reactivity. Such a safety factor must be selected judiciously in order to provide for the requisite longevity and to properly assess the cost-effectiveness of PRBs relative to other treatment or containment techniques. Unfortunately, the dependence of long-term reactivity on feedwater composition makes it impossible to recommend a 'generic' safety factor to account for attenuations in reactivity. Our results indicate that certain solutes, such as silica, NOM, and relatively high concentrations of bicarbonate can have a particularly deleterious effect on long-term reactivity. Differences between reactivity in columns continuously exposed to organohalides, and those only intermittently exposed, suggest that contaminant concentration also plays a role in granular iron passivation and thus should also be considered in selection of an appropriate safety factor. Although high concentrations of chloride initially enhanced reactivity in our studies, this effect was relatively short-lived. In this light, short-term column experiments may be especially misleading at sites where groundwater contains appreciable chloride. The selection of higher safety factors may be prudent in such cases.

Fortunately, the effect of diminishing k_{obs} on requisite barrier width is less pronounced than the effect of k_{obs} on "fraction of TCE untreated" (Fig. 7-2). For quantitative estimation of

the effects of k_{obs} on safety factor, we consider the following equation for barrier width design (Eykholt et al., 1999):

$$W_d = -\nu \times CF_D \times \ln\left(\frac{C_{design}}{C_{influent}}\right) \times \frac{FS_w}{k_{obs}} \tag{7-4}$$

where W_d is the requisite PRB width, v is the groundwater seepage velocity, CF_D is a correction factor for dispersion, C_{design} is the target effluent concentration, $C_{influent}$ is the influent concentration of the contaminant requiring treatment, and FS_w is a safety factor for barrier width. This expression can be applied if the parent compound, rather than a daughter product, dictates PRB design. For any given safety factor, a twofold decrease in k_{obs} translates quite simply to a doubling of W_d. Conversely, a two-fold increase in safety factor would be warranted if the assumed (short-term design estimate) of k_{obs} is two times lower than that which is ultimately anticipated. In this context, our results with the columns fed 2 mM bicarbonate (C, D, and K) indicate that our Master Builder iron reactivity toward TCE decreased approximately four-fold between day 50 and day 300 of column operation. Similar declines in reactivity have been reported (Arun Gavaskar, personal communication) for column tests of somewhat shorter duration (~1300 pore volumes) conducted with site groundwater and either Master Builders iron (fourfold decrease in reaction rate) or Peerless iron (twofold decrease in reaction rate).

Although more work will be required to ascertain the relative importance of iron type versus groundwater composition in dictating longevity, our results suggest that safety factors on the order of 4 may suffice to account for declines in reactivity toward TCE such as those we observed over a three-year period on exposure of Master Builders iron to bicarbonate (in the absence of NOM or silica). Commensurately larger safety factors may be needed to account for the affects of NOM and silica (see Chapter 4). Even greater safety factors may be needed to account for uncertainties in hydraulic parameters (*e.g.*, natural variability in groundwater seepage

velocities; alterations in seepage velocity resulting from progressive alterations in PRB permeability; and changes in hydraulic residence time distributions resulting from increased dispersion and the development of zones of "immobile water", depending on the hydrogeology of the site). We stress, moreover, that the requisite safety factor may be quite different for contaminants whose mode of attenuation differs significantly from that observed for TCE. For example, it should be apparent that our TCE reactivity results will not apply to contaminants that undergo attenuation by different mechanisms or which interact with different surface species. Additional studies examining long-term changes in removal efficiencies would undoubtedly be necessary in such cases.

REFERENCES CITED

Abdelmoula, M., P. Refait, S. H. Drissi, J. P. Mihe and J.-M. R. Génin (1996). "Conversion Electron Mössbauer Spectroscopy and X-Ray Diffration Studies of the Formation of Carbonate-Containing Green Rust One by Corrosion of Metallic Iron in $NaHCO_3$ and ($NaHCO_3$ + NaCl) Solutions." Corrosion Science **38**(4): 623-633.

Agrawal, A., P. G. Tratnyek, P. Stoffyn-Egli and L. Liang (1995). Processes Affecting Nitro Reduction by Iron Metal: Mineralogical Consequences of Precipitation in Aqueous Carbonate Environments. 209th American Chemical Society National Meeting, Anaheim, CA, ACS.

Amonette, J. E., D. J. Workman, D. W. Kennedy, J. S. Fruchter and Y. A. Gorby (2000). "Dechlorination of Carbon Tetrachloride by Fe(II) Associated with Goethite." Environmental Science and Technology **34**(21): 4606-4613.

Arnold, W. A. (1999). Kinetics and Pathways of Chlorinated Ethylene and Chlorinated Ethane Reaction with Zero-Valent Metals. Geography and Environmental Engineering. Baltimore, MD, The Johns Hopkins University.

Arnold, W. A., W. P. Ball and A. L. Roberts (1999). "Polychlorinated Ethane Reaction with Zero-Valent Zinc: Pathways and Rate Control." Journal of Contaminant Hydrology **40**: 183-200.

Arnold, W. A. and A. L. Roberts (2000a). "Inter- and Intraspecies Competitive Effects in Reactions of Chlorinated Ethylenes with Zero-Valent Iron in Column Reactors." Environmental Engineering Science **17**(5): 291-302.

Arnold, W. A. and A. L. Roberts (2000b). "Pathways and Kinetics of Chlorinated Ethylene and Chlorinated Acetylene Reaction with Fe(0) Particles." Environmental Science and Technology **34**(9): 1794-1805.

Avena, M. J. and L. K. Koopal (1998). "Desorption of Humic Acids from an Iron Oxide Surface." Environmental Science and Technology **32**(17): 2572-2577.

Banerjee, G. and S. N. Malhotra (1992). "Contribution to Adsorption of Aromatic-Amines on Mild-Steel Surface from Hcl Solutions by Impedance, Uv, and Raman- Spectroscopy." Corrosion **48**(1): 10-15.

Bard, A. J. and L. R. Faulkner (1980). Electrochemical Methods: Fundamentals and Applications. New York, John Wiley and Sons.

Bear, J. (1972). Dynamics of Fluids in Porous Media. New York, Elsevier.

Bear, J. (1979). Hydraulics of Groundwater. New York, McGraw-Hill.

Becker, U., K. M. Rosso and M. F. Hochella, Jr. (2001). "The Proximity Effect on Semiconducting Mineral Surfaces: A New Aspect of Mineral Surface Reactivity and Surface Complexation Theory?" Geochimica et Cosmochimica Acta **65**(16): 2641-2649.

Benali, O., M. Abdelmoula, P. Refait and J.-M. R. Genin (2001). "Effect of Orthophosphate on the Oxidation Products of Fe(II)-Fe(III) Hydroxycarbonate: The Transformation of Green Rust to Ferrihydrite." Geochimica et Cosmochimica Acta **65**(11): 1715-1726.

Blowes, D. W., C. J. Ptacek and J. L. Jambor (1997). "*In-Situ* Remediation of Cr(VI)-Contaminated Groundwater Using Permeable Reactive Walls: Laboratory Studies." Environmental Science and Technology **31**(12): 3348-3357.

Blum, A. and A. Lasaga (1988). "Role of Surface Speciation in the Low-Temperature Dissolution of Minerals." Nature **331**: 431-433.

Blum, A. E. and L. L. Stillings (1995). Feldspar Dissolution Kinetics. Chemical Weathering Rates of Silicate Minerals. A. F. White and S. L. Brantley. Washington, D.C., Mineralogical Society of America. **Volume 31:** 291-351.

Boltz, D. F. and M. G. Mellon (1947). "Determination of Phosphorous, Germanium, Silicon, and Arsenic by the Heteropoly Blue Method." Analytical Chemistry **16**: 873-877.

Bonin, P. M., M. S. Odziemkowski and R. W. Gillham (1998). "Influence of Chlorinated Solvents on Polarization and Corrosion Behavior of Iron in Borate Buffer." Corrosion Science **40**(8): 1391-1409.

Bonin, P. M. L., W. Jedral, M. S. Odziemkowski and R. W. Gillham (2000a). "Electrochemical and Raman Spectroscopic Studies of the Influence of Chlorinated Solvents on the Corrosion Behavior of Iron in Borate Buffer and in Simulated Groundwater." Corrosion Science **42**: 1921-1939.

Bonin, P. M. L., M. S. Odziemkowski, E. J. Reardon and R. W. Gillham (2000b). "*In Situ* Identification of Carbonate-Containing Green Rust on Iron Electrodes in Solutions Simulating Groundwater." Journal of Solution Chemistry **29**(10): 1061-1074.

Boucherit, N. and A. Hugot-Le Goff (1992). "Localized Corrosion Processes in Iron and Steels Studied by *in situ* Raman Spectroscopy." Faraday Discussions **94**: 137-147.

Boucherit, N., A. Hugot-Le Goff and S. Joiret (1991). "Raman Studies of Corrosion Films Grown on Fe and Fe-6Mo in Pitting Conditions." Corrosion Science **32**(5/6): 497-507.

Brusseau, M. L., R. E. Jessup and P. S. C. Rao (1989). "Modeling the Transport of Solutes Influenced by Multiprocess Nonequilibrium." Water Resources Research **25**(9): 1971-1988.

Brusseau, M. L., R. E. Jessup and P. S. C. Rao (1992). "Modeling Solute Transport Influenced by Multiprocess Nonequilibrium and Transformation Reactions." Water Resources Research **28**(1): 175-182.

Buerge, I. J. and S. J. Hug (1999). "Influence of Mineral Surfaces on Chromium(VI) Reduction by Iron(II)." Environmental Science and Technology **33**(23): 4285-4291.

Bunting, W. E. (1944). "Determination of Soluble Silica in Very Low Concentrations." Industrial and Engineering Chemistry **16**(612-615).

Burke, D. P. and R. L. Higginson (2000). "Characterisation of Multicomponent Scales by Electron Back Scattered Diffraction (EBSD)." Scripta materialia **42**: 277-281.

Burris, D. R., R. M. Allen-King, V. S. Manoranjan, T. J. Campbell, G. A. Loraine and B. Deng (1998). "Chlorinated Ethene Reduction by Cast Iron: Sorption and Mass Transfer." Journal of Environmental Engineering **124**(10): 1012-1019.

Carlson, A. B. and C. V. Banks (1952). "Spectrophotometic Determination of Silicon." Analytical Chemistry **24**(3): 472-477.

Casey, F. X. M., S. K. Ong and R. Horton (2000). "Degradation and Transformation of Trichloroethylene in Miscible-Displacement Experiments through Zerovalent Metals." Environmental Science and Technology **34**(23): 5023-5029.

Castro, E. B., J. R. Vilche and A. J. Arvia (1991). "Iron Dissolution and Passivation in K_2CO_3-$KHCO_3$ Solutions. Rotating Ring Disc Electron and XPS Studies." Corrosion Science **32**(1): 37-50.

Charlet, L., E. Liger and P. Gerasimo (1998). "Decontamination of TCE- and U-Rich Waters by Granular Iron: Role of Sorbed Fe(II)." Journal of Environmental Engineering **124**(1): 25-30.

Cirpka, O. A. and P. K. Kitanidis (2001). "Transport of Volatile Compounds in Porous Media in the Presence of a Trapped Gas Phase." Journal of Contaminant Hydrology **49**(3-4): 263-285.

Colon, D., E. J. Weber and J. L. Anderson (1997). Role of Natural Organic Matter in the Mineral-Mediated Reduction of Organic Chemicals. American Chemical Society Annual Conference, San Francisco.

Colon, D., E. J. Weber and J. L. Anderson (1998). Role of Natural Organic Matter in the Reductive Transformation of Nitroaromatics. American Chemical Society Annual Conference, Boston.

Cornell, R. M. and U. Schwertmann (1996). The Iron Oxides: Structure, Properties, Reactions, Occurrence and Uses. Weinheim, Germany, VCH.

Crittenden, J. C., N. J. Hutzler, D. G. Geyer, J. L. Oravitz and G. Friedman (1986). "Transport of Organic Compounds With Saturated Groundwater Flow: Model Development and Parameter Sensitivity." Water Resources Research **22**(3): 271-284.

Cussler, E. L. (1997). Diffusion: Mass Transfer in Fluid Systems. Cambridge, UK, Cambridge University Press.

Davis, C. C., W. R. Knocke and M. Edwards (2001). "Implications of Aqueous Silica Sorption to Iron Hydroxide: Mobilization of Iron Colloids and Interference with Sorption of Arsenate and Humic Substances." Environmental Science and Technology **35**(15): 3158-3162.

Davis, J. A. (1982). "Adsorption of Natural Dissolved Organic Matter at the Oxide/Water Interface." Geochimica et Cosmochimica Acta **46**: 2381-2393.

de Faria, D. L. A., S. Venâncio Silva and M. T. de Oliveira (1997). "Raman Microspectroscopy of Some Iron Oxides and Oxyhydroxides." Journal of Raman Spectroscopy **28**(11): 873-878.

Dempsey, B. A. and C. O'Melia (1983). Proton and calcium complexation of four fulvic acid fractions. Aquatic and Terrestrial Humic Materials. E. Christman and E. Gjessing. Ann Arbor, MI, Ann Arbor Science.

Deng, B., S. Hu and D. R. Burris (1998). Effect of Iron Corrosion Inhibitors on Trichloroethylene Reduction. Physical, Chemical, and Thermal Technologies:

Remediation of Chlorinated and Recalcitrant Compounds. G. B. Wickramanayake and R. E. Hinchee. Columbus, OH, Battelle Press**:** 341-346.

Devlin, J. F., J. Klausen and R. P. Schwarzenbach (1998). "Kinetics of Nitroaromatic Reduction on Granular Iron in Recirculating Batch Experiments." Environmental Science and Technology **32**(13): 1941-1947.

Devlin, J. F., M. Morkin and C. Repta (2000). Incorporating Surface Saturation Effects Into Iron Wall Design Calculations. Chemical Oxidation and Reactive Barriers: Remediation of Chlorinated and Recalcitrant Compounds. G. B. Wickramanayake, A. R. Gavaskar and A. S. C. Chen. Columbus, OH, Battelle Press**:** 393-400.

Drissi, S. H., P. Refait, M. Abdelmoula and J.-M. R. Genin (1995). "The Preparation and Thermodynamic Properties of Fe(II)-Fe(III) Hydroxide-Carbonate (Green Rust 1); Pourbaix Diagram of Iron in Carbonate-Containing Aqueous Media." Corrosion Science **37**(12): 2025-2041.

Duran, J. M., J. Vogan and J. R. Stening (2000). Reactive Barrier Performance in a Complex Contaminant and Geochemical Environment. Chemical Oxidation and Reactive Barriers: Remediation of Chlorinated and Recalcitrant Compounds. G. B. Wickramanayake, A. R. Gavaskar and A. S. C. Chen. Columbus, OH, Battelle Press**:** 401-408.

Dzombak, D. A. and F. M. M. Morel (1990). Surface Complexation Modeling: Hydrous Ferric Oxide. New York, John Wiley and Sons.

EnviroMetal Technologies, Inc. (2002). "Field Applications" [Online]. Available: http://www.eti.ca/ (access date May 29, 2002).

Erbs, M., H. C. B. Hansen and C. E. Olsen (1999). "Reductive Dechlorination of Carbon Tetrachloride Using Iron(II) Iron(III) Hydroxide Sulfate (Green Rust)." Environmental Science and Technology **33**(2): 307-311.

Eykholt, G. R., S. S. Baghel, T. M. Sivavec, P. D. Mackenzie, D. Haitko and D. Horney (1995). Conservative Flow Tracers for Iron Column Studies. Nat. Meet.-Am. Chem. Soc., Div. Environ. Chem., Anaheim, CA.

Eykholt, G. R., C. R. Elder and C. H. Benson (1999). "Effects of Aquifer Heterogeneity and Reaction Mechanism Uncertainty on a Reactive Barrier." Journal of Hazardous Materials **68**: 1999.

Farrell, J., M. Kason, N. Melitas and T. Li (2000). "Investigation of the Long-Term Performance of Zero-Valent Iron for Reductive Dechlorination of Trichloroethylene." Environmental Science and Technology **34**(3): 514-521.

Focht, R. M. (1994). Bench-Scale Treatability Testing to Evaluate the Applicability of Metallic Iron for Above-Ground Remediation of 1,2,3-trichloropropane Contaminated Groundwater. Earth Sciences. Waterloo, Ontario, Canada, University of Waterloo**:** 58.

Fogler, H. S. (1999). Elements of Chemical Reaction Engineering. Upper Saddle River, NJ, Prentice Hall PTR.

Frogner, P., C. Broman and S. Lindblom (1998). "Weathering Detected by Raman Spectroscopy Using Al-Ordering in Albite." Chemical Geology **151**: 161-168.

Génin, J.-M. R., G. Bourrié, F. Trolard, M. Abdelmoula, A. Jaffrezic, P. Refait, V. Maitre, B. Humbert and A. Herbillon (1998). "Thermodynamic Equilibria in Aqueous Suspensions of Synthetic and Natural Fe(II)-Fe(III) Green Rusts: Occurrences of the Mineral in Hydromorphic Soils." Environmental Science and Technology **32**(8): 1058-1068.

Génin, J.-M. R., A. A. Olowe, P. Refait and L. Simon (1996). "On the Stoichiometry and Pourbaix Diagram of Fe(II)-Fe(III) Hydroxy-Sulphate or Sulphate-Containing Green Rust 2: An Electrochemical and Mossbauer Spectroscopy Study." Corrosion Science **38**(10): 1751-1762.

Gillham, R. W. and S. F. O'Hannesin (1994). "Enhanced Degradation of Halogenated Aliphatics by Zero-Valent Iron." Ground Water **32**(6): 958-967.

Gotpagar, J., S. Lyuksyutov, R. Cohn, E. Grulke and D. Bhattacharyya (1999). "Reductive Dehalogenation of Trichloroethylene with Zero-Valent Iron: Surface Profiling Microscopy and Rate Enhancement Studies." Langmuir **15**(24): 8412-8420.

Gout, R., E. H. Oelkers, J. Schott and A. Zwick (1997). "The Surface Chemistry and Structure of Acid-Leached Albite: New Insights on the Dissolution Mechanism of the Alkali Feldspars." Geochimica et Cosmochimica Acta **61**(14): 3013-3018.

Greenberg, A. E., A. D. Eaton and L. S. Clesceri, Eds. (1992). Standard Methods for the Examination of Water and Wastewater. Washington, D.C., APHA.

Gu, B., T. J. Phelps, L. Liang, M. J. Dickey, Y. Roh, B. L. Kinsall, A. V. Palumbo and G. K. Jacobs (1999). "Biogeochemical Dynamics in Zero-Valent Iron Columns: Implications for Permeable Reactive Barriers." Environmental Science and Technology **33**(13): 2170-2177.

Gu, B., J. Schmitt, Z. Chen, L. Liang and J. F. McCarthy (1994). "Adsorption and Desorption of Natural Organic Matter on Iron Oxide: Mechanisms and Models." Environmental Science and Technology **28**(1): 38-46.

Gui, J. and T. M. Devine (1995). "A SERS Investigation of the Passive Films Formed on Iron in Mildly Alkaline Solutions of Carbonate/Bicarbonate and Nitrate." Corrosion Science **37**(8): 1177-1189.

Haderlein, S. B. and K. Pecher (1998). Pollutant Reduction in Heterogeneous Fe(II)-Fe(III) Systems. Mineral-Water Interfacial Reactions. D. L. Sparks and T. J. Grundl. Washington D.C., American Chemical Society**:** 342-357.

Hansen, H. C. B., C. B. Koch, H. Nancke-Krogh, O. K. Borggaard and J. Sorensen (1996). "Abiotic Nitrate Reduction to Ammonium: Key Role of Green Rust." Environmental Science & Technology **30**: 2053-2056.

Hansen, H. C. B., T. P. Wetche, K. Raulund-Rasmussen and O. K. Borggaard (1994). "Stability Constants for Silicate Adsorbed to Ferrihydrite." Clay Minerals **29**: 341-350.

Hardy, L. I. and R. W. Gillham (1996). "Formation of Hydrocarbons from the Reduction of Aqueous CO_2 by Zero-Valent Iron." Environmental Science and Technology **30**(1): 57-65.

Hering, J. G. (1995). Interaction of Organic Matter with Mineral Surfaces: Effects on Geochemical Processes at the Mineral-Water Interface. Aquatic Chemistry: Interfacial

and Interspecies Processes. C. P. Huang, C. R. O'Melia and J. J. Morgan. Washington, D.C., ACS Books. **244:** 95-110.

Herman, R. G., C. E. Bodgan, A. J. Sommer and D. R. Simpson (1987). "Discrimination Among Carbonate Minerals by Raman Spectroscopy Using the Laser Microprobe." Applied Spectroscopy **41**(3): 437-440.

Hladky, K., L. M. Callow and J. L. Dawson (1980). "Corrosion Rates from Impedance Measurements: An Introduction." British Corrosion Journal **15**(1): 20-25.

Hochella, M. F. J., J. N. Moore, U. Golla and A. Putnis (1999). "A TEM Study of Samples from Acid Mine Drainage Systems: Metal-Mineral Association with Implications for Transport." Geochimica Cosmochimica Acta **63**(19/20): 3395-3406.

Hofstetter, T. B. (1999). Reduction of Polynitroaromatic Compounds by Reduced Iron Species - Coupling Biogeochemical Processes with Pollutant Transformation. EAWAG. Dübendorf, Switzerland, Swiss Federal Institute of Technology**:** 117.

Hubaux, A. and G. Vos (1970). Analytical Chemistry **42**: 849-855.

Jenko, M., B. Korousic, D. Mandrino and V. Presern (2000). "HRAES Study of Oxide Scale Formation by Decarburization of Non-Oriented Electrical Steel Sheets." Vacuum **57**: 295-305.

Johnson, T. L., W. Fish, Y. A. Gorby and P. G. Tratnyek (1998). "Degradation of Carbon Tetrachloride by Iron Metal: Complexation Effects on the Oxide Surface." Journal of Contaminant Hydrology **29**: 379-398.

Johnson, T. L., M. M. Scherer and P. G. Tratnyek (1996). "Kinetics of Halogenated Organic Compound Degradation by Iron Metal." Environmental Science and Technology **30**(8): 2634-2640.

Kiilerich, O., J. W. Larsen, C. Nielsen and L. Deigaard (2000). Field Results from the Use of a Permeable Reactive Wall. Chemical Oxidation and Reactive Barriers: Remediation of Chlorinated and Recalcitrant Compounds. G. B. Wickramanayake, A. R. Gavaskar and A. S. C. Chen. Columbus, OH, Battelle Press**:** 377-384.

Klausen, J., J. Ranke and R. P. Schwarzenbach (2001). "Influence of Solution Composition and Column Aging on the Reduction of Nitroaromatic Compounds by Zero-Valent Iron." Chemosphere **44**(4): 511-517.

Klausen, J., S. P. Tröber, S. B. Haderlein and R. P. Schwarzenbach (1995). "Reduction of Substituted Nitrobenzenes by Fe(II) in Aqueous Mineral Suspensions." Environmental Science and Technology **29**(9): 2396-2404.

Klein, C. and C. S. Hurlblut (1985). Manual of Mineralogy. New York, John Wiley & Sons, Inc.

Legrand, L., M. Abdelmoula, A. Gehin, A. Chausse and J. M. R. Genin (2001a). "Electrochemical formation of a new Fe(II)-Fe(III) hydroxy- carbonate green rust: characterisation and morphology." Electrochimica Acta **46**(12): 1815-1822.

Legrand, L., G. Sagon, S. Lecomte, A. Chausse and R. Messina (2001b). "A Raman and infrared study of a new carbonate green rust obtained by electrochemical way." Corrosion Science **43**(9): 1739-1749.

Legrand, L., S. Savoye, A. Chausse and R. Messina (2000). "Study of Oxidation Products Formed on Iron in Solutions Containing Bicarbonate Carbonate." Electrochimica Acta **46**: 111-117.

Liger, E., L. Charlet and P. Van Cappellen (1999). "Surface Catalysis of Uranium(VI) Reduction by Iron(II)." Geochimica et Cosmochimica Acta **63**(19/20): 2939-2955.

Lovley, D. R. and E. J. P. Phillips (1986). "Organic Matter Mineralization with Reduction of Ferric Iron in Anaerobic Sediments." Applied and Environmental Microbiology **51**(4): 683-689.

Mac Berthouex, P. and L. C. Brown (1994). Statistics for Environmental Engineers. Boca Raton, Fla., Lewis Publishers.

MacDonald, D. D. (1991). Application of Electrochemical Impedance Spectroscopy in Electrochemistry and Corrosion Science. Techniques for Characterization of Electrodes and Electrochemical Processes. R. Varma and J. R. Selman. New York, John Wiley and Sons, Inc.**:** 515-580.

MacDougall, B. and M. J. Graham (1995). Growth and Stability of Passive Films. Corrosion Mechanisms in Theory and Practice. P. Marcus and J. Oudar. New York, Marcel Dekker, Inc.**:** 143-173.

Mackenzie, P. D., D. P. Horney and T. M. Sivavec (1999). "Mineral Precipitation and Porosity Losses in Granular Iron Columns." Journal of Hazardous Materials **68**(1-2): 1-17.

Marmier, N. and F. Fromage (2000). "Sorption of Cs(I) on Magnetite in the Presence of Silicates." Journal of Colloid and Interface Science **223**: 83-88.

Matheson, L. J. and P. G. Tratnyek (1994). "Reductive Dehalogenation of Chlorinated Methanes by Iron Metal." Environmental Science and Technology **28**(12): 2045-2053.

McMahon, P. B., K. F. Dennehy and M. W. Sandstrom (1999). "Hydraulic and Geochemical Performance of a Permeable Reactive Barrier Containing Zero-Valent Iron, Denver Federal Center." Ground Water **37**(3): 396-404.

Meites, L., P. Zuman, et al. (1982). CRC Handbook Series in Organic Electrochemistry. Boca Raton, FL, CRC Press, Inc.

Morkin, M., J. F. Devlin, J. F. Barker and B. J. Butler (2000). "In Situ Sequential Treatment of a Mixed Contaminant Plume." Journal of Contaminant Hydrology **45**(3-4): 283-302.

Munz, C. and P. V. Roberts (1986). "Effects of Solute Concentration and Cosolvents on the Aqueous Activity Coefficient of Halogenated Hydrocarbons." Environmental Science and Technology **20**(8): 830-836.

Murphy, E. M., J. M. Zachara and S. C. Smith (1990). "Influence of Mineral-Bound Humic Substances on the Sorption of Hydrophobic Organic Compounds." Environmental Science and Technology **24**(10): 1507-1516.

Oblonsky, L. J. and T. M. Devine (1995). "A Surface Enhanced Raman Spectroscopic Study of the Passive Films Formed in Borate Buffer on Iron, Nickel, Chromium, and Stainless Steel." Corrosion Science **37**(1): 17-41.

Odziemkowski, M., J. Flis and D. E. Irish (1994). "Raman Spectal and Electrochemical Studies of Surface Film Formation on Iron and Its Alloys With Carbon in $Na_2CO_3/NaHCO_3$ Solution With Reference to Stree Corrosion Cracking." Electrochimica Acta **39**(14): 2225-2236.

Odziemkowski, M. S. and R. S. Gillham (1997). Surface Redox Reactions on Commercial Grade Granular Iron (Steel) and Their Influence on the Reductive Dechlorination of Solvent. Micro Raman Spectroscopic Studies. ACS National Meeting, San Francisco, CA, ACS.

Odziemkowski, M. S., T. T. Schumacher, R. W. Gillham and E. J. Reardon (1998). "Mechanism of Oxide Film Formation on Iron in Simulating Groundwater Solutions: Raman Spectroscopic Studies." Corrosion Science **40**(2-3): 371-389.

O'Hannesin, S. F. and R. W. Gillham (1998). "Long-Term Performance of an In Situ "Iron Wall" for Remediation of VOCs." Ground Water **36**(1): 164-170.

Ohtsuka, T., K. Kubo and N. Sato (1986). "Raman Spectroscopy of Thin Corrosion Films on Iron at 100 to 150 C in Air." Corrosion **42**: 476-482.

Orth, W. S. and R. W. Gillham (1996). "Dechlorination of Trichloroethene in Aqueous Solution Using Fe^0." Environmental Science and Technology **30**(1): 66-71.

Parker, J. C. and M. T. van Genuchten (1984). "Flux-Averaged and Volume-Averaged Concentrations in Continuum Approaches to Solute Transport." Water Resources Research **20**(7): 866-872.

Pecher, K., S. B. Haderlein and R. P. Schwarzenbach (2002). "Reduction of Polyhalogenated Methanes by Surface-Bound Fe(II) in Aqueous Suspensions of Iron Oxides." Environmental Science and Technology **36**(8): 1734-1741.

Powell, R. M. and R. W. Puls (1997). "Proton Generation by Dissolution of Intrinsic or Augmented Aluminosilicate Minerals for in Situ Contaminant Remediation by Zero-Valence-State Iron." Environmental Science and Technology **31**(8): 2244-2251.

Puls, R. W., C. J. Paul and R. M. Powell (1999). "The Application of In-Situ Permeable Reactive (Zero-Valent Iron) Barrier Technology for the Remediation of Chromate-Contaminated Groundwater: A Field Test." Applied Geochemistry **14**: 989-1000.

Reardon, E. J. (1995). "Anaerobic Corrosion of Granular Iron: Measurement and Interpretation of Hydrogen Evolution Rates." Environmental Science and Technology **29**(12): 2936-2945.

Refait, P., M. Abdelmoula and J.-M. R. Génin (1998). "Mechanisms of Formation and Structure of Green Rust One in Aqueous Corrosion of Iron in the Presence of Chloride Ions." Corrosion Science **40**(9): 1547-1560.

Refait, P., S. H. Drissi, P. J. and J.-M. R. Genin (1997). "The Anionic Species Competition in Iron Aqueous Corrosion: Role of Various Green Rust Compounds." Corrosion Science **39**(9): 1699-1710.

Refait, P. and J.-M. R. Génin (1994). "The Transformation of Chloride-Containing Green Rust One Into Sulphated Green Rust Two by Oxidation in Mixed Cl^- and SO_4^{2-} Aqueous Media." Corrosion Science **36**(1): 55-65.

Ritter, K., M. S. Odziemkowski and R. W. Gillham (2002). "An In-situ Study of the Role of Surface Films on Granular Iron in the Permeable Iron Wall Technology." Journal of Contaminant Hydrology **55**: 87-111.

Roberts, A. L., L. A. Totten, W. A. Arnold, D. R. Burris and T. J. Campbell (1996). "Reductive Elimination of Chlorinated Ethylenes by Zero-Valent Metals." Environmental Science and Technology **30**(8): 2654-2659.

Roberts, P. V., P. Cornel and R. S. Summers (1985). "External mass-transfer rate in fixed-bed adsorption." Journal of Environmental Engineering **111**(6): 891-904.

Roberts, P. V., M. N. Goltz, R. S. Summers, J. C. Crittenden and P. Nkedi-Kizza (1987). "The Influence of Mass Transfer on Solute Transport in Column Experiments with an Aggregated Soil." Journal of Contaminant Hydrology **1**: 375-393.

Roden, E. E. and J. M. Zachara (1996). "Microbial Reduction of Crystalline Iron(III) Oxides: Influence of Oxide Surface Area and Potential for Cell Growth." Environmental Science and Technology **30**(5): 1618-1628.

Roh, Y., S. Y. Lee and M. P. Elless (2000). "Characterization of corrosion products in the permeable reactive barriers." Environmental Geology **40**(1-2): 184-194.

Roos, B. W. (1969). Analytical functions and distributions in physics and engineering. New York, Wiley.

Sass, B., A. Gavaskar and W.-S. Yoon (2001). Analysis of Corrosion Compound Associated with Permeable Reactive Barriers and Their Impact on Barrier Longevity. American Chemical Society Annual Conference, San Diego.

Sastri, V. S. (1998). Corrosion Inhibitors: Principles and Applications. New York, John Wiley and Sons.

Scherer, M. M., B. A. Balko and P. G. Tratnyek (1998). The Role of Oxides in Reduction Reactions at the Metal-Water Interface. Mineral-Water Interfacial Reactions: Kinetics and Mechanisms. D. L. Sparks and T. J. Grundl. Washington, D.C., American Chemical Society**:** 301-322.

Scherer, M. M., K. M. Johnson, J. C. Westall and P. G. Tratnyek (2001). "Mass transport effects on the kinetics of nitrobenzene reduction by iron metal." Environmental Science & Technology **35**(13): 2804-2811.

Scherer, M. M., J. C. Westall, M. Ziomek-Moroz and P. G. Tratnyek (1997). "Kinetics of Carbon Tetrachloride Reduction at an Oxide-Free Iron Electrode." Environmental Science and Technology **31**(8): 2385-2391.

Schwarzenbach, R. P., P. M. Gschwend and D. M. Imboden (1993). Environmental Organic Chemistry. New York, John Wiley and Sons, Inc.

Schwarzenbach, R. P., T. B. Hofstetter, M. Elsner and S. B. Haderlein (2000). Probing the Reactivity of Mineral-Bound Ferrous Iron by Using Nitroaromatic and Polyhalogenated Compounds. ACS National Meeting: Division of Environmental Chemistry Preprints of Extended Abstracts.

Schwarzenbach, R. P., R. Stierli, K. Lanz and J. Zeyer (1990). "Quinone and Iron Porphyrin Mediated Reduction of Nitroaromatic Compounds in Homogeneous Aqueous Solution." Environmental Science and Technology **24**(10): 1566-1574.

Sigg, L. and W. Stumm (1981). "The Interaction of Anions and Weak Acids with the Hydrous Goethite (α-FeOOH) Surface." Colloids and Surfaces **2**: 101-117.

Simard, S., H. Ménard and L. Brossard (1998). "Localized corrosion of 1024 mild steel in slightly alkaline bicarbonate solution with Cl- ions." Journal of Applied Electrochemistry **28**(2): 151-160.

Simard, S., M. Odziemkowski, D. E. Irish, L. Brossard and H. Ménard (2001). "*In Situ* micro-Raman Spectroscopy to Investigate Pitting Corrosion Product of 1024 Mild Steel in Phosphate and Bicarbonate Solutions Containing Chloride and Sulfate Ions." Journal of Applied Electrochemistry **31**: 931-920.

Simpson, L. J. (1998). "Electrochemically Generated $CaCO_3$ Deposits on Iron Studied with FTIR and Raman Spectroscopy." Electrochimica Acta **43**(16-17): 2543-2547.

Simpson, L. J. and C. A. Melendres (1996). "Temperature Dependence of the Surface Enhanced Raman Spectroelectrochemistry of Iron in Aqueous Solutions." Electrochimica Acta **41**(10): 1727-1730.

Sivavec, T. M. and D. P. Horney (1996). "Reductive dechlorination of chlorinated solvents by zero-valent iron, iron oxide and iron sulfide minerals." Abstracts of Papers of the American Chemical Society **211**: 50-COLL.

Sivavec, T. M., D. P. Horney, P. D. Mackenzie and J. J. Salvo (1995). Zero-Valent Iron Treatability Study for Groundwater Contaminated with Chlorinated Organic Solvents at the Paducah Gaseous Diffusion Plant (PGDP) Site - Final Report. Schenectady, NY, GE Corporate Research and Development**:** 181.

Sorel, D., S. D. Warner, B. L. Longino, J. H. Honniball and L. A. Hamilton (2001). Dissolved Hydrogen Measurements at a Permeable Zero-Valent Iron Reactive Barrier. American Chemical Society Meeting, San Diego, CA, ACS.

Stookey, L. L. (1970). "Ferrozine--A New Spectrophotometric Reagent for Iron." Analytical Chemistry **42**(7): 779-781.

Stumm, W. (1992). Chemistry of the Solid-Water Interface, John Wiley and Sons.

Swedlund, P. J. and J. G. Webster (1999). "Adsorption and Polymerisation of Silicic Acid on Ferrihydrite, and Its Effect on Arsenic Adsorption." Water Research **33**(16): 3413-3422.

Taniguchi, S., K. Yamamoto, D. Megumi and T. Shibata (2001). "Characteristics of Scale/Substrate Interface Area of Si-Containing Low-Carbon Steels at High Temperatures." Materials Science & Engineering A **A308**: 250-257.

Thierry, D., D. Persson, C. Leygraf, N. Boucherit and A. Hugot-LeGoff (1991). Corrosion Science **32**: 273.

Tipping, E. (1981). "Adsorption by Goethite (α-FeOOH) of Humic Substances from Three Different Lakes." Chemical Geology **33**: 81-89.

Toride, N., F. J. Leij and M. T. Van Genuchten (1993). "A Comprehensive Set of Analytical Solutions for Nonequilibrium Solute Transport With First-Order Decay and Zero-Order Production." Water Resources Research **29**(7): 2167-2182.

Toride, N., F. J. Leij and M. T. van Genuchten (1995). The CXTFIT Code for Estimating Transport Parameters from Laboratory or Field Tracer Experiments. Riverside, U.S. Salinity Laboratory, Agriculture Research Service, U.S. Department of Agriculture.

Tratnyek, P. G., M. M. Scherer, B. Deng and S. Hu (2001). "Effects of Natural Organic Matter, Anthropogenic Surfactants, and Model Quinones on the Reduction of Contaminants by Zero-Valent Iron." Water Research **35**(18): 4435-4443.

Trolard, F., J.-M. R. Génin, M. Abdelmoula, G. Bourrié, B. Humbert and A. Herbillon (1997). "Identification of a Green Rust Mineral in a Reductomorphic Soil by Mossbauer and Raman Spectroscopies." Geochmica et Cosmochimica Acta **61**(5): 1107-1111.

van Aken, P. A., V. J. Styrsa, B. Liebscher, A. B. Woodland and G. J. Redhammer (1999). "Microanalysis of Fe^{3+}/Sigma Fe in Oxide and Silicate Minerals by Investigation of Electron Energy-Loss Near Edge Structures (ELNES) at the Fe M-2,M-3 Edge." Physics and Chemistry of Minerals **26**(7): 584-590.

van Genuchten, M. T. and J. C. Parker (1984). "Boundary Conditions for Displacement Experiments Through Short Laboratory Soil Columns." Soil Science Society of America Journal **48**(4): 703-708.

van Genuchten, M. T. and R. J. Wagenet (1989). "Two-Site/Two-Region Models for Pesticide Transport and Degradation: Theoretical Development and Analytical Solutions." Soil Science Society of America Journal **53**(5): 1303-1310.

van Genuchten, M. T. and P. J. Wierenga (1976). "Mass Transfer Studies in Sorbing Porous Media I. Analytical Solutions." Soil Science Society of America Journal **40**(4): 473-480.

Vikesland, P. J. (1998). Monochloramine Loss in the Presence of Ferrous Iron: Kinetics, Mechanism, and Products. CEE. Iowa City, Iowa, The University of Iowa**:** 300.

Vikesland, P. J., J. Klausen, H. Zimmermann, W. P. Ball and A. L. Roberts (2000). Contaminant Reduction by Fe(0): Evaluation of Transport Properties and Chemical Reactivity Over Time. Abstracts of Papers of the American Chemical Society, Washington D.C.

Vikesland, P. J. and R. L. Valentine (2002). "Iron-Oxide Surface Catalyzed Reduction of Monochloramine by Ferrous Iron: Implications of Oxide Type and Carbonate on Reactivity." Environmental Science and Technology **36**(3): 512-519.

Vogan, J. L., R. M. Focht, D. K. Clark and S. L. Graham (1999). "Performance Evaluation of a Permeable Reactive Barrier for Remediation of Dissolved Chlorinated Solvents in Groundwater." Journal of Hazardous Materials **68**: 97-108.

Wang, Y. X. and E. J. Reardon (2001). "A siderite/limestone reactor to remove arsenic and cadmium from wastewaters." Applied Geochemistry **16**(9-10): 1241-1249.

Williams, A. G. B. and M. M. Scherer (2001). "Kinetics of Cr(VI) Reduction By Carbonate Green Rust." Environmental Science and Technology **35**(17): 3488-3494.

Wilson, R. D. and D. M. Mackay (1993). "The Use of Sulphur Hexafluoride as a Conservative Tracer in Saturated Sandy Media." Ground Water **31**(5): 719-724.

Wranglén, G. (1985). An Introduction to Corrosion and Protection of Metals. London, Chapman and Hall.

Wüst, W. F., R. Köber, O. Schlicker and A. Dahmke (1999). "Combined Zero- and First-Order Kinetic Model of the Degradation of TCE and cis-DCE with Commerical Iron." Environmental Science and Technology **33**(23): 4304-4309.

Yabusaki, S., K. Cantrell, B. Sass and C. Steefel (2001). "Multicomponent reactive transport in an in situ zero-valent iron cell." Environmental Science & Technology **35**(7): 1493-1503.

Young, D. F. and W. P. Ball (1997a). "Effects of Column Conditions on the First-Order Rate Modeling of Nonequilibrium Solute Breakthrough: Cylindrical Macropores Versus Spherical Media." Water Resources Research **33**(5): 1149-1156.

Young, D. F. and W. P. Ball (1997b). "Injection Mode Effects on Tracer Experiments in Columns." Journal of Hydrologic Engineering **2**(3): 113-119.

Young, D. F. and W. P. Ball (2000). "Column Experimental Design Requirements for Estimating Model Parameters from Temporal Moments Under Nonequilibrium Conditions." Advances in Water Resources **23**(5): 449-460.